Faculteit Wetenschappen
Departement Fysica

Novel mesoscopic effects and topological states in chiral *p*-wave superconductors

---

Nieuwe mesoscopische effecten en topologische toestanden in chirale *p*-wave supergeleiders

Proefschrift ingediend tot het behalen van de graad van
Doctor in de Wetenschappen: Fysica
aan de Universiteit Antwerpen, te verdedigen door

Víctor Leonardo FERNÁNDEZ BECERRA

Promotor
Prof. dr. Milorad Milošević

Antwerpen, June 2017

Members of the Jury:

Chairman
Prof. dr. Jacques Tempere, Universiteit Antwerpen, Belgium
Promotor
Prof. dr. Milorad Milošević, Universiteit Antwerpen, Belgium
Members
Prof. dr. Sara Bals, Universiteit Antwerpen, Belgium
Prof. dr. Wim Magnus, Universiteit Antwerpen, Belgium
Prof. dr. Alejandro Silhanek, Université de Liège, Belgium
Prof. dr. Joris Van de Vondel, Katholieke Universiteit Leuven, Belgium

Contact Information
Víctor Leonardo Fernández Becerra
Universiteit Antwerpen
Departement Fysica
G. U. 210
Groenenborgerlaan 171
2020 Antwerpen
België
vickthor31@gmail.com

To the loving memory of my brother
José Wilder

Acknowledgement

First of all, I would like to express my sincere gratitude to my supervisor Prof. Milorad Milošević for giving me the opportunity to work on such interesting topic. I am thankful for his encouragement, support, and patience along all the stages of my PhD. I admire his ability to see potentially interesting problems from far ahead, and the way that he materializes them in concrete works. I greatly benefitted from this process of unravelling the basic principles behind exciting topics in condensed matter physics.

I also would like to thank the head of the group, Prof. François Peeters, for the nice atmosphere that he encourages in the group and for shaping it with such talented minds with whom I have had the pleasure to work with during the last years. My special thanks go to Dr. Lingfeng Zhang and Dr Lucian Covaci, for their collaboration that broadened my knowledge in superconductivity. Prof. Edson Sardella from Brazil is another collaborator with whom I am indebted for his thoughtful guidance.

I am very greatful to Hilde Evans and Véronique Van Herck for their unlimited help with the paperworks of the uncountable registration offices at the most varied instances (academic and non-academic ones). I am also greatful to the support team of the computational facilities at the university where all the simulations of this work were performed.

I kindly thank to all my friends from the CMT group and outside of it. The Brazilians (the Diegos, the Jorges, Lucas, Silvia, Ariel and Rodolpho), the Serbians (Slaviša, Dean, Željko, Miša, and Marko), my fellow Colombians (William, Jagger and the Jesus'), the Iranians (Massoud, Davoud and the Mohammads), the locals (Vincent, Ben, Jonas, Sam and Mario), my officemates Hossein and Erpan, and my dear Nina.

I lovely thank my family for all the effort to keep us connected despite of the distance and the technological gaps, especially my parents who nowadays are more active in the social media than I am. My deep thanks go to my brothers and their families. The memories in my mind with you remain immutable.

Last, but by no means least, I owe a special thank to my enchanting girlfriend Rebeca. You have been a lifesaver to me. Your patience, support, encouragement, and company strengthened me when I most needed it. To you the spanish verses that once I told you, and the stories that I want to write next to you after this thesis.

Table of Contents

List of Abbreviations

1D	One dimensional
2D	Two dimensional
μ**SR**	Muon spin relaxation
ABM	Anderson-Brinkmann-Morel
ARPES	Angle-resolved photoemission spectroscopy
BCS	Bardeen-Cooper-Schrieffer
BdG	Bogoliubov-de Gennes
BEC	Bose-Einstein condensate
BSCCO	Bismuth-Strontium-Calcium-Copper-Oxygen
BW	Balian-Werthamer
CLV	coreless vortex
DOS	Density of States
DW	Domain walls
FV	Full vortex
GLB	Geshkenbein-Larkin-Barone
GL	Ginzburg-Landau
HQV	Half quantum vortex
HTS	High temperature superconductors
LDOS	Local density of states
OP	order parameter
QH	Quantum Hall effect
QSH	Quantum spin Hall effect
SQUID	Superconducting quantum interference device
SRO	Strontium ruthenate
SS	Spin singlet
STM	Scanning Tunneling Microscopy
ST	Spin triplet
TEM	Transmission electron microscopy
TDGL	Time-dependent Ginzburg-Landau
TRS	Time reversal symmetry
YBCO	Ytrium-Barium-Copper-Oxygen

1
Introduction

1.1 Introduction to superconductivity

Superconductivity is a phenomenon in condensed matter physics where a material looses its electrical resistivity below some critical temperature T_c. The phenomenon was discovered in 1911 by the Dutch physicist Heike Kamerlingh Onnes when measuring the electrical resistance of Mercury [see Fig. 1.1(a)] [1]. Being the first one to liquify Helium in 1908, Kamerlingh Onnes was studying the behavior of pure metals at temperatures close to the absolute zero, when he observed that below 4.2 K the resistance of a mercury sample abruptly vanished. This finding, which was later reproduced in other materials such as tin and lead [2], convinced Kamerlingh Onnes that his measurements were revealing a completely new state of matter. He coined it as "supraconductivity", later to be changed to "superconductivity".

Another characteristic of superconductivity is the perfect diamagnetism, i.e. the total expulsion of applied magnetic fields independently of the history of the process. This behavior is referred to as the Meissner-Ochsenfeld effect, after its discoverers Walther Meissner and Robert Ochsenfeld who observed it first in 1933 [see Fig. 1.1(b)] [3]. One is tempted to claim that the origin of the Meissner-Ochsenfeld effect lies exclusively in the zero resistance of the superconducting state [4]. If a superconductor is cooled down below its T_c and later a magnetic field is applied, a current is generated that flows without dissipation to induce a magnetic field opposite to the external one, compensating it inside the sample, in agreement with Lenz's law, i.e. the superconductor behaves as an ideal conductor. However, if one inverts the order and first applies the external field to subsequently cool down the superconductor below its T_c, the behavior followed by an ideal conductor differs from the actual behavior of a superconductor. While the ideal conductor keeps inside the same magnetic field below T_c that it had above T_c, the superconductor totally expels the external field below T_c.

On theoretical side, brothers Fritz and Heinz London were the pioneers that devised a model to capture the Meissner-Ochsenfeld effect in 1935 [5]. The model which was based on electromagnetism and early ideas about solids provided an equation for the magnetic field along with a characteristic scale for its spatial variation. This scale, denoted by λ_L is called the penetration depth of the applied field into the superconducting sample [4]. The values of λ_L are material specific, e.g. for Nb and Cd λ_L is 32 and $110\ \mathrm{nm}$, respectively. Another large breakthrough in superconductivity occurred in 1950 when Vitaly Ginzburg and Lev Landau formulated a theory based on Landau's theory of second-order phase transitions, to show that superconductivity depends on two different

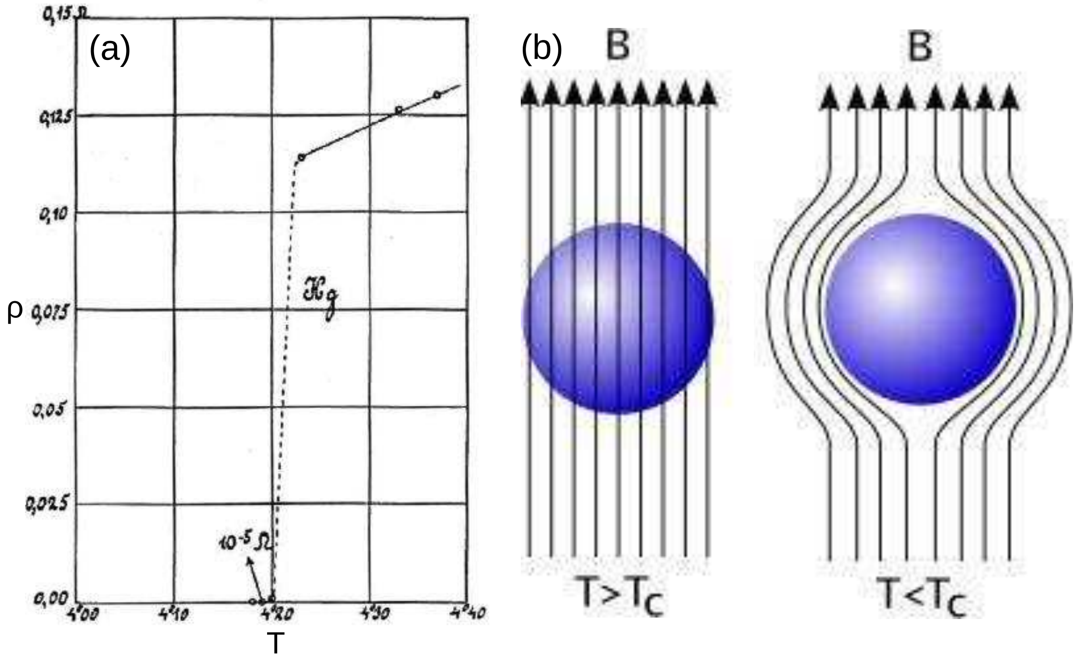

Figure 1.1: (a) The resistance of a mercury sample suddenly disappears below critical temperature $T_c = 4.2K$, indicating that the material became a superconductor. From Ref. [1]. (b) Depiction of the expulsion of an external magnetic field $\mathbf{B}$ by a spherical superconductor (the Meissner-Ochsenfeld effect).

length scales [6], λ_L and ξ. The new length in this model, the so-called coherence length (ξ), defines the scale for variation of the order parameter ψ whose square magnitude yields the local density of carriers of superconductivity ($\rho_s(\mathbf{r}) = |\psi(\mathbf{r})|^2$). The Ginzburg-Landau model achieved widespread recognition after (i) introducing two types of superconductors, namely type I and II, and (ii) its prediction of vortices and their subsequent experimental confirmation (see Fig. 1.2) [7, 8]. Vortices are localized defects where superconductivity is destroyed, and in which the magnetic field is compressed so that one vortex carries exactly one quantum of magnetic flux ϕ_0. Vortices arise in type-II superconductors to allow partial penetration of the applied magnetic field into the sample without completely destroying the superconductivity, as would be the case in type-I superconductors. Vortices form a triangular lattice, the so-called Abrikosov lattice, which defines a phase only in type II superconductors (called Shubnikov phase or the mixed state). Type I superconductors do not have mixed state, as they can not host vortices, unless due to finite size and demagnetization effects [4].

Despite of the success of the phenomenological theories to explain many of the main characteristics of superconductivity, there were still several features that remained puzzling to the scientific community. The discontinuity of the specific heat at the superconducting/normal state transition and its exponentially decaying behavior in the superconducting phase (see Fig. 1.3) were some of the features which were only understood after a microscopic theory of superconductivity came out in 1957. The BCS theory, called after its founders John Bardeen, Leon Cooper, and John Robert Schrieffer [10], emerged after Cooper realized that two electrons could form a bound state slightly above the Fermi surface provided that a weak attractive potential exists [11]. The bound state of electrons, the so-called Cooper pair, forms after the virtual exchange of phonons (lattice deformations of the ionic crystal structure propagating as a wave). This idea of an interaction between electrons mediated by phonons that could bind them was first suggested by Fröhlich in 1950 [12], and it was subsequently confirmed that same year through the discovery of the isotope effect [13], i.e. the dependence of T_c on the mass of the lattice ions. Finally, another important breakthrough in the theory of superconductivity came in 1959, when Lev Gor'kov derived the Ginzburg-Landau equations from the BCS theory [14]. This derivation not only validated the Ginzburg-Landau theory (in its limits), but also provided a relationship between the phenomenological coefficients of the Ginzburg-Landau

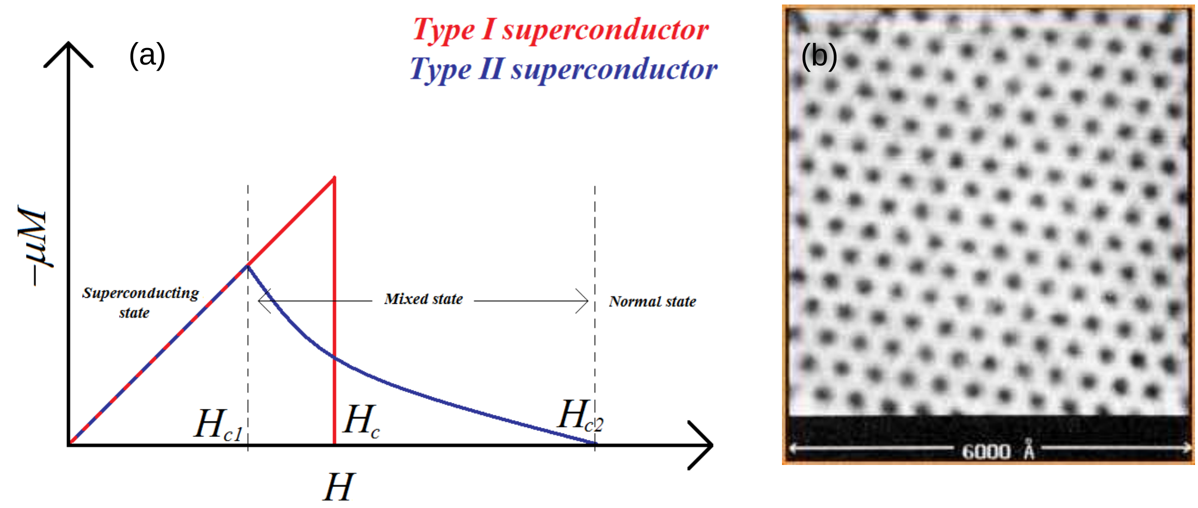

Figure 1.2: (a) Magnetization as a function of the external field showing the differences between bulk type I and II superconductors. While in the type I case there is an abrupt transition from superconducting to normal state, in the type II case there exists a mixed state so that superconductivity is gradually destroyed. (b) In the mixed state (also called Shubnikov phase) the external field partially penetrates the sample in the form of vortices, each carrying a quantized unit of flux, which form a triangular lattice known as the Abrikosov lattice. From Ref. [9].

theory and the microscopic parameters of a material such as its Fermi velocity and density of states.

With the BCS theory explaining the pairing mechanism in superconductors, and due to lack of new important discoveries of superconductivity in other materials, the research in superconductivity went to a slowdown in decades that followed the publication of Bardeen, Cooper and Schrieffer's work. However, the research took a major impulse in 1986 when Georg Bednorz and Alex Müller discovered superconductivity in a ceramic compound of lanthanum and copper oxide, doped with barium [16]. The discovery, that drew the attention of the broad community, reported for the first time superconductivity appearing in a non metallic compound rather than a chemical element or alloy. Besides, the T_c of this material (35 K) broke an implicit limit (30 K) established for the mechanism of Cooper pairing based on the virtual exchange of phonons. Within the subsequent few years more compounds containing copper-oxide planes were reported to superconduct with even higher T_c's, reaching to date the record of 153 K for the mercury barium calcium copper oxide ($HgBa_2Ca_2Cu_3O_8$) under pressure [17]. Regarding the pairing mechanism of this group of superconductors, widely known as cuprates, there is no consensus yet about what interaction provides the required attractive potential for the formation of the Cooper pairs. However, what has been widely accepted to date is that the superconducting gap has d-wave symmetry rather than the s-wave symmetry of conventional (low T_c) superconductors [18, 19]. The d-wave symmetry is manifested in the gap in the form of line nodes, i.e. regions where the gap in the phase space goes to zero, which modify important quantities such as the quasiparticle density of states (DOS) and the London penetration depth [20]. Precisely, in the DOS plot shown in Fig. 1.4(a), one sees the V-shape characteristic for high temperature superconductors (HTSs) [21], agreeing well with the expected behavior for gaps having line nodes (d-wave symmetry). This DOS was obtained by scanning tunneling microscopy whose fundamentals are shown in panels (b) and (c) of Fig. 1.4.

So far in this overview of superconductivity the existence of a unique gap developing at the Fermi surface has been implicitly assumed both in theories and experiments. However, recent experimental reports have revealed superconductivity with multiple gaps, namely multi-gap superconductivity, in compounds such as: magnesium diboride (MgB_2) [23], iron pnictides ($LaFeAsO_{1-x}F_x$) [24,25], iron chalcogenides ($FeTe_{1-x}Se_x$) [26], and iron-arsenic compounds (RFeAsO), with R standing for a rare earth element. These materials have Fermi surfaces with a rich topology that enable the formation

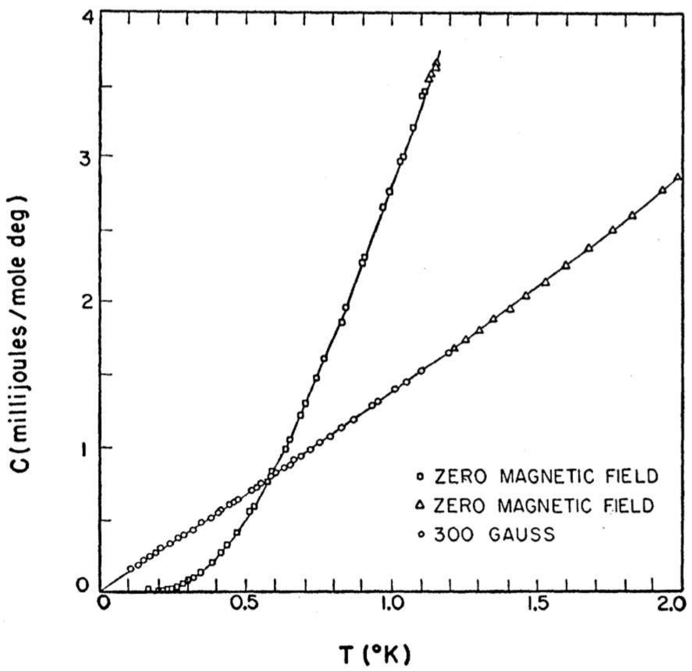

Figure 1.3: Heat capacity of aluminium in its superconducting and normal phases. In the normal phase the heat capacity has a polynomial dependence with temperature, i.e. $C_n = \gamma T + \beta T^3$*, while in the superconducting phase it has an exponential dependence, i.e.* $C_{es}/\gamma T_c = a \exp -bT_c/T$*, where* γ*,* β*,* a*,* b *and* T_c *are constants that are material specific. From Ref. [15].*

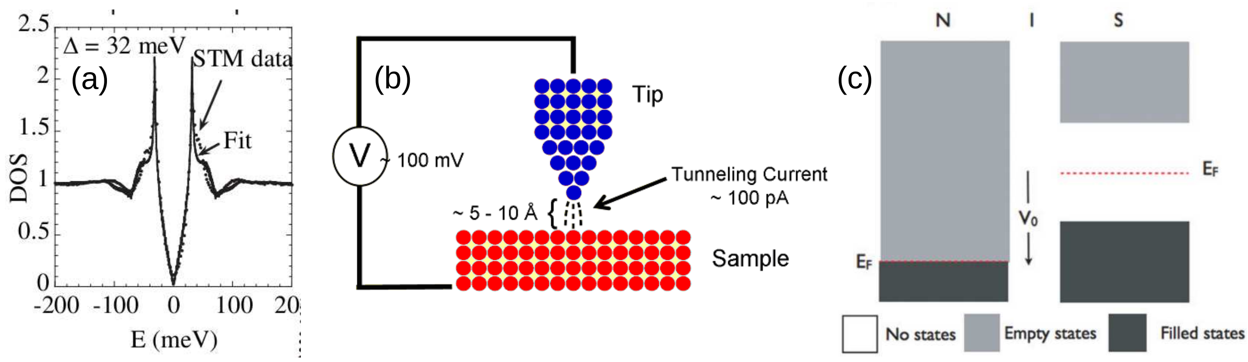

Figure 1.4: (a) Quasiparticle density of states, obtained with a scanning tunneling microscope (STM), for the high critical temperature superconductor $Bi_2Sr_2CaCu_2O_{8+\delta}$ *[21]. (b) Depiction of the STM along with (c) its corresponding diagram. Due to the potential difference between the tip (N) and the sample (S), electrons tunnel the insulating barrier (I) formed by vacuum that surrounds the device. From Ref. [22].*

of multiple superconducting gaps. As an example, Fig. 1.5 shows a 3D plot of the three superconducting gaps, namely α, β, and γ, of the compound $Ba_{0.6}K_{0.4}Fe_2As_2$ [27]. The corresponding Fermi sheets have an almost perfect cilindrical shape and are located at the highly symmetric points Γ and M of the two-dimensional Brillouin zone. The z direction displays the magnitude of the gaps. The Fermi surface, having three sheets and obtained with angle-resolved photoemission spectroscopy, is also shown at the bottom of the figure. Finally, the temperature dependence of the three gaps is shown in the inset.

The report of the first multigap iron-based superconductor drew the attention of the broad community since for long time persisted the antagonistic idea between ferromagnetism (inherent in iron) and superconductivity. However, with the following years this idea was slowly dismantled, owing to the appearance of more iron-based superconductors that directly or indirectly confirmed the in-

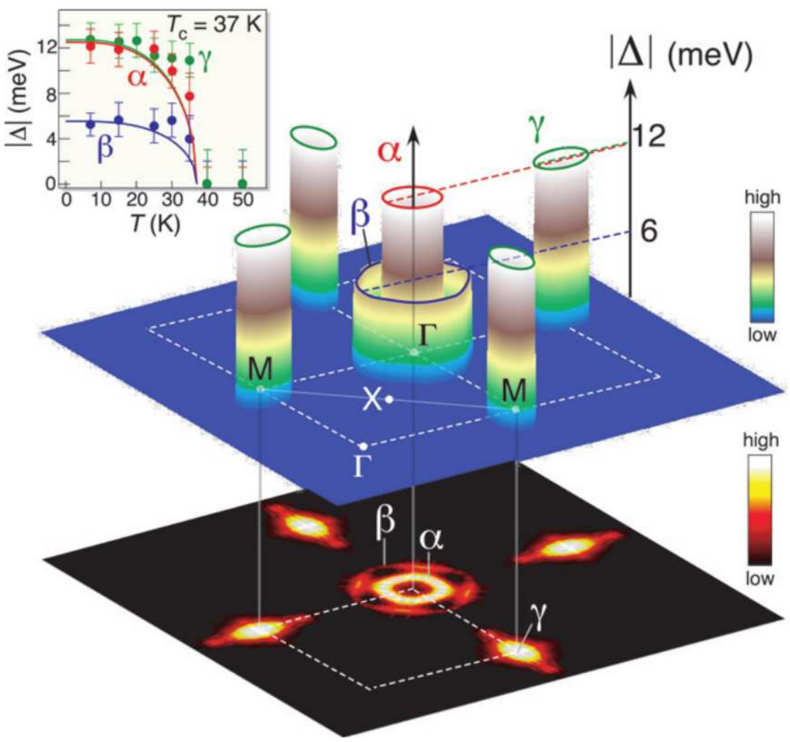

Figure 1.5: 3D plot of the superconducting gaps on the Fermi surface, α, β, and γ bands, of the iron-based superconductor $Ba_{0.6}K_{0.4}Fe_2As_2$. With the magnitude of the gaps being displayed along the z direction, one can note that the α and γ bands have roughly the same magnitude. The inset shows the temperature dependence of the magnitude of the gaps. The Fermi surface of $Ba_{0.6}K_{0.4}Fe_2As_2$, having three sheets and mapped with angle-resolved photoemission spectroscopy, is shown at the bottom of the figure. From Ref. [27].

terplay between strong correlation and superconductivity. Today, after the intense research carried out in iron-based superconductors there are solid evidences suggesting that the pairing symmetry in these superconductors is of the $s_{\pm}$-wave type [28]. On the other hand, regarding the pairing mechanism the debate is still open. There is no consensus yet on what is the exact interaction responsible for superconductivity in the iron-based materials.

We conclude this overview of superconductivity with a short description of a superconductor that has raised major expectations regarding reaching superconductivity at ambient temperatures. It is hydrogen sulphide (H_2S), a chemical compound that at ambient pressures is a gas easily recognized by its odor of rotten eggs. H_2S becomes a metallic conductor of electricity under pressures higher than 0.9 million of atmospheres (90 GPa), and at 1.5 million of atmospheres it breaks the record of the highest superconducting critical temperature with a T_c of 203 K (-70 ^oC) [29]. The wave of excitement spread within the scientific community might suggest that we are witnessing the epoch-making discovery in the field of superconductivity during the last decades.

1.2 The Ginzburg-Landau theory

The grounds of the Ginzburg-Landau (GL) theory of superconductivity lie in (i) the gauge invariant principle and (ii) the paradigmatic model of Landau of second order phase transitions [6]. That means that the theory requires a complex order parameter (ψ) in order to describe the continuous transition from the superconducting to the normal phase. Besides, ψ has to change smoothly from a finite value to zero along the superconducting/normal transition. The minimal free energy density fulfilling this requirement is

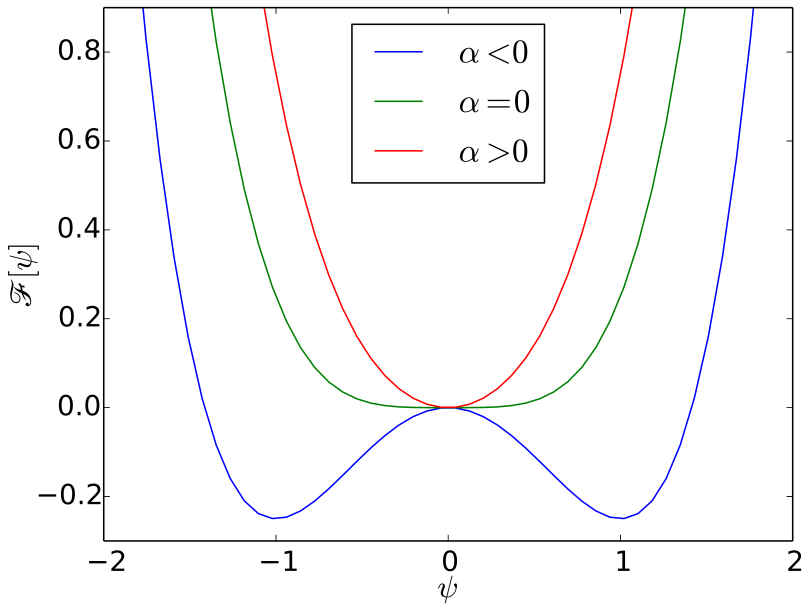

Figure 1.6: Free energy density for different values of the phenomenological parameter α, revealing the existence of two phases that are smoothly connected, i.e. without any abrupt discontinuity at the transition point, in agreement with the characteristics of second order phase transitions.

$$\mathscr{F}[\psi] = \alpha|\psi|^2 + \frac{\beta}{2}|\psi|^4 , \tag{1.1}$$

where α and β are phenomenological expansion coefficients. Minimization of Eq. 1.1 yields two solutions,

$$\psi = 0, \quad \text{and} \quad |\psi|^2 = \frac{-\alpha}{\beta} . \tag{1.2}$$

One can see that α and β have to be negative and positive respectively, in order for the free energy to be bounded from below (see Fig. 1.6). The coefficient α depends on temperature and drives the transition between the superconducting and the normal phase. Bearing in mind that Landau's theory of second order phase transitions is valid in the vicinity of the critical point (in superconductivity defined by T_c), the precise dependence of the coefficient α on temperature is reduced to first order, i.e. $\alpha(T) = \alpha(T - T_c)$. The coefficient β, unlike α, is temperature-independent. Fig. 1.6 shows plots of the free energy for different values of α. There one can see that as the temperature changes around T_c, equivalently to α changing around zero, the local minimum is established at either zero or at a finite value of the order parameter.

Spatial variations of the order parameter and coupling to the magnetic field are included in the free energy density 1.1 by adding two more terms,

$$\mathscr{F}[\psi, \mathbf{A}] = \mathscr{F}_{n0} + \alpha|\psi|^2 + \frac{\beta}{2}|\psi|^4 + \frac{1}{2m^*}\left|\left(\frac{\hbar}{i}\nabla - \frac{e^*}{c}\mathbf{A}\right)\psi\right|^2 + \frac{\mathbf{h}^2}{8\pi} , \tag{1.3}$$

where m^* and e^* are the mass and the electric charge of the carriers of superconductivity, respectively. $\mathbf{A}$ is the vector potential and $\mathbf{h}$ is the local magnetic field. The free energy density of the normal phase $\mathscr{F}_{n0}$ has also been added in Eq. 1.3 to complete the full expression of the GL free energy density. Minimization of $\mathscr{F}$ with respect to the fields ψ^* and $\mathbf{A}$ yields the two GL equations,

$$\frac{1}{2m^*}\Big(\frac{\hbar}{i}\nabla - \frac{e^*}{c}\mathbf{A}\Big)^2\psi + \alpha\psi + \beta|\psi|^2\psi = 0, \tag{1.4}$$

$$\mathbf{J} = \frac{c}{4\pi}\nabla\times\mathbf{h} = \frac{e^*}{m^*}\mathrm{Re}\Big\{\psi^*\Big(\frac{\hbar}{i}\nabla - \frac{e^*}{c}\mathbf{A}\Big)\psi\Big\}. \tag{1.5}$$

Eq. 1.4 resembles the Schrödinger equation of a free electron in a magnetic field, but with the nonlinear term $\beta|\psi|^2\psi$ as an interaction term in the first GL equation. On the other hand, Eq. 1.5 is the Ampère's law with $\mathbf{J}$ being the superconducting current density. The GL equations and the GL free energy density are gauge invariant by definition. They remain the same for other fields ψ' and $\mathbf{A}'$, provided that $\psi' = \psi e^{i\chi}$ and $\mathbf{A}' = \mathbf{A} + i\nabla\chi$, where χ is the arbitrary gauge. Finally, the boundary conditions that complement the GL equations are [4]

$$\Big(\frac{\hbar}{i}\nabla - \frac{e^*}{c}\mathbf{A}\Big)\psi\cdot\hat{n} = 0, \tag{1.6}$$

where $\hat{n}$ is a vector normal to the boundary surface. This boundary condition is appropriate for vacuum-superconductor (V-S) interfaces since it prohibits superconducting currents to flow perpendicularly to the interface. On the other hand, the appropriate condition for insulator-superconductor (I-S), metal-superconductor (M-S), and superconductor-superconductor (S'-S) interfaces is [30]

$$\Big(\frac{\hbar}{i}\nabla - \frac{e^*}{c}\mathbf{A}\Big)\psi\cdot\hat{n} = \frac{i\hbar}{b}\psi, \tag{1.7}$$

where b can be infinity, finite positive, and negative for the I-S, M-S, and S'-S interfaces, respectively.

1.2.1 Characteristic length scales

The GL equations 1.4 and 1.5 form the set of coupled nonlinear differential equations that describe superconductivity near the critical temperature T_c. Due to their complexity the available analytical solutions are scarce. However, from the analytical cases reported in the literature to date one can draw very important quantities, such as the natural length scale governing the spatial variation of the superconducting order parameter.

Consider a one-dimensional superconductor at zero external magnetic field and occupying the region $x \geq 0$. The first GL equation for this case becomes

$$\frac{\hbar^2}{2m^*|\alpha|}\frac{d^2\psi'}{dx^2} + \psi' - |\psi'|^2\psi' = 0, \tag{1.8}$$

where $\psi = \Delta(0)\psi'$, and $\Delta(0) = \sqrt{|\alpha|/\beta}$. One can notice in Eq. 1.8 that the quantity $\sqrt{\frac{\hbar^2}{2m^*|\alpha|}}$ has the unit of length. Therefore, one can expect that it defines the scale for the order parameter ψ, namely the superconducting coherence length. When one solves Eq. 1.8 with the conditions that $\psi(x\!=\!0) = 0$ and $\psi(x\!=\!\infty) = 1$, the order parameter takes the form

$$\psi(x) = \tanh\Big(\frac{x}{\sqrt{2}\xi}\Big), \tag{1.9}$$

where $\xi = \sqrt{\frac{\hbar^2}{2m^*|\alpha|}}$. In other words, $\psi(x)$ changes from zero to one in a short interval defined by the coherence length ξ [see Fig. 1.7(a)].

Another example of analytical solutions of the GL equations useful for the introduction of a second length scale, is the case of a superconductor filling half the real space, i.e. at $z \leq 0$, with an constant external magnetic field H_{ext} parallel to its surface at $z = 0$. Considering that the order parameter is constant and equal to $\Delta(0)$, Eq. 1.5 reduces to

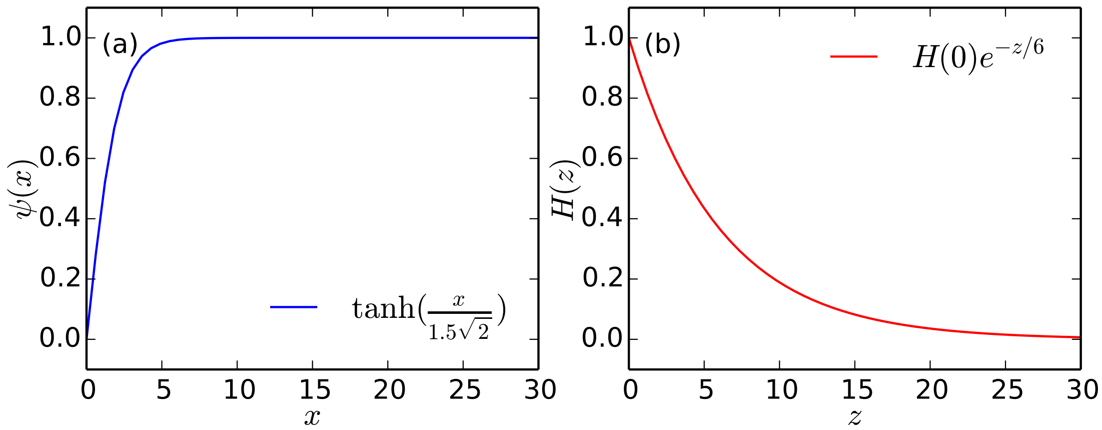

Figure 1.7: From the few analytical solutions existing for the Ginzburg-Landau equations, panel (a) plots the superconducting order parameter ψ of a one-dimensional superconductor for $\xi = 1.5$, and panel (b) the magnetic field h_x of a semi-infinite superconductor slab for $\lambda = 6$.

$$\nabla \times \mathbf{h} = -\frac{4\pi(e^*)^2\Delta(0)^2}{m^*c^2}\mathbf{A}. \tag{1.10}$$

Taking the rotational in both sides of the last equation and bearing in mind that $\mathbf{h} = \nabla \times \mathbf{A}$, one obtains the following equation for the magnetic field,

$$\nabla^2\mathbf{h} - \frac{4\pi(e^*)^2\Delta(0)^2}{m^*c^2}\mathbf{h} = 0. \tag{1.11}$$

Here one easily notices that the quantity $\sqrt{\frac{4\pi(e^*)^2\Delta(0)^2}{m^*c^2}}$ has the inverse units of length. One can choose $\mathbf{h} = h_x(z)\hat{e}_x$ for simplicity, without loosing the important results, and reduce further Eq. 1.11 to

$$\frac{d^2h_x}{dz^2} - \frac{4\pi(e^*)^2\Delta(0)^2}{m^*c^2}h_x = 0. \tag{1.12}$$

The particular solution of Eq. 1.12 with the boundary condition $h_x(0) = H_{ext}$ is

$$h_x(z) = h_x(0)e^{-z/\lambda}, \tag{1.13}$$

where $\lambda = \sqrt{\frac{m^*c^2}{4\pi(e^*)^2\Delta(0)^2}}$. This means that a constant magnetic field parallel to the surface of a superconductor penetrates the sample in a top layer of thickness λ. This is the reason why λ is called the penetration depth. Fig. 1.7(b) shows the plot of such penetrating magnetic field inside the superconductor.

1.2.2 The surface energy and types of superconductivity

To realize that there exist two types of superconductors one needs to calculate the difference of the Gibbs free energy (ΔG), in the superconducting state, at zero and at a nonzero value of the external field. One therefore starts from the definition of the Gibbs free energy density [31],

$$\mathscr{G}[T, \mathbf{H}] = \mathscr{F}[T, \mathbf{h}] - \frac{1}{4\pi}\mathbf{h} \cdot \mathbf{H}. \tag{1.14}$$

Unlike the Helmholtz free energy density $\mathscr{F}$ which depends on T and $\mathbf{h}$ (the temperature and the local field), the Gibbs free energy density $\mathscr{G}$ is a function of the independent variables T and $\mathbf{H}$, with

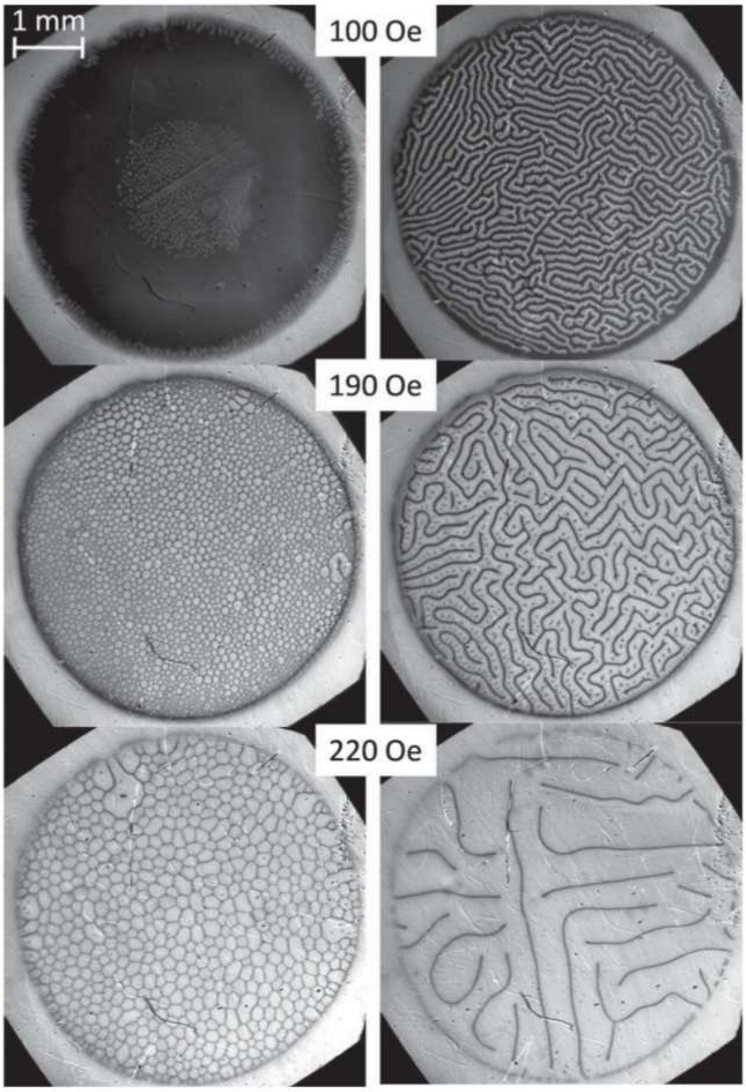

Figure 1.8: Domain structures formed in the type I superconductor (lead) having a disk-shape, after (left) zero field cooling, and (right) when field cooled. From Ref. [32].

the latter being the external magnetic field. Substituing Eq. 1.3 into Eq. 1.14, the expression for $\mathscr{G}$ at the external field $\mathbf{H}$ becomes

$$\mathscr{G}_{sH} = \mathscr{F}_{n0} + \alpha|\psi|^2 + \frac{\beta}{2}|\psi|^4 + \frac{1}{2m^*}\left|\left(\frac{\hbar}{i}\nabla - \frac{e^*}{c}\mathbf{A}\right)\psi\right|^2 + \frac{\mathbf{h}^2}{8\pi} - \frac{\mathbf{h}\cdot\mathbf{H}}{4\pi}, \tag{1.15}$$

whereas the Gibbs free energy density at zero field yields

$$\mathscr{G}_{s0} = \mathscr{F}_{s0}. \tag{1.16}$$

Calculating the difference $\Delta\mathscr{G} = \mathscr{G}_{sH} - \mathscr{G}_{nH}$, one easily obtains

$$\Delta\mathscr{G} = \alpha|\psi|^2 + \frac{\beta}{2}|\psi|^4 + \frac{1}{2m^*}\left|\left(\frac{\hbar}{i}\nabla - \frac{e^*}{c}\mathbf{A}\right)\psi\right|^2 + \frac{\mathbf{h}^2}{8\pi} - \frac{\mathbf{h}\cdot\mathbf{H}}{4\pi} + \frac{\mathbf{H}^2}{8\pi}, \tag{1.17}$$

which one can simplify even further to

$$\Delta\mathscr{G} = \alpha|\psi|^2 + \frac{\beta}{2}|\psi|^4 + \frac{1}{2m^*}\left|\left(\frac{\hbar}{i}\nabla - \frac{e^*}{c}\mathbf{A}\right)\psi\right|^2 + \frac{\left(\mathbf{h}-\mathbf{H}\right)^2}{8\pi}. \tag{1.18}$$

One can see that there exists some resemblance between the last expression and the first GL equation, and one can exploit this resemblance to obtain a reduced expression for $\Delta\mathscr{G}$. The multiplication of Eq. 1.5 by $\bar{\psi}$ gives

$$\bar{\psi}\frac{1}{2m^*}\Big(\frac{\hbar}{i}\nabla - \frac{e^*}{c}\mathbf{A}\Big)^2\psi + \alpha|\psi|^2 + \beta|\psi|^4 = 0. \tag{1.19}$$

Moreover, by using the chain rule it is straightforward to show that,

$$\bar{\psi}\Big(\frac{\hbar}{i}\nabla - \frac{e^*}{c}\mathbf{A}\Big)^2\psi = \Big|\Big(\frac{\hbar}{i}\nabla - \frac{e^*}{c}\mathbf{A}\Big)\psi\Big|^2 + \frac{\hbar}{i}\nabla\Big[\bar{\psi}\Big(\frac{\hbar}{i}\nabla - \frac{e^*}{c}\mathbf{A}\Big)\Big]. \tag{1.20}$$

The last equation after integration, since the last term on the right hand side is a surface term that with the proper boundary condition vanishes, becomes

$$\int d^3\mathbf{r}\,\bar{\psi}\Big(\frac{\hbar}{i}\nabla - \frac{e^*}{c}\mathbf{A}\Big)^2\psi = \int d^3\mathbf{r}\,\Big|\Big(\frac{\hbar}{i}\nabla - \frac{e^*}{c}\mathbf{A}\Big)\psi\Big|^2. \tag{1.21}$$

Therefore the integration of $\Delta\mathscr{G}$, after substitution of Eqs. 1.19 and 1.21, followed by some straightforward algebra yields

$$\Delta G = \int d^3\mathbf{r}\Big[-\frac{\beta}{2}|\psi|^4 + \frac{\big(\mathbf{h} - \mathbf{H}\big)^2}{8\pi}\Big] \tag{1.22}$$

which can be easily recast in the most useful form,

$$\Delta G = \frac{\mathrm{H}_c^2}{8\pi}\int d^3\mathbf{r}\Big[-\Big|\frac{\psi}{\Delta(0)}\Big|^4 + 2\kappa^2\Big(\frac{\mathbf{h}}{\mathrm{H}_{c2}} - \frac{\mathbf{H}}{\mathrm{H}_{c2}}\Big)^2\Big], \tag{1.23}$$

owing to the the relation between the thermodynamic critical field and the phenomenological parameters of the GL theory, $\mathrm{H}_c^2/8\pi = \alpha^2/2\beta$ [4]. The magnetic field is scaled to the uppper critical field, H_{c2}, and $\kappa = \lambda/\xi$ is the GL parameter, respecting $\mathrm{H}_{c2} = \sqrt{2}\kappa\mathrm{H}_c$. The integral of Eq. 1.23 has to be solved numerically since it involves simultaneous solutions of the two GL equations. One case that provides valuable information without loosing the important results of the theory is the one dimensional normal-superconducting interface. In that case one obtains that the surface energy can be positive or negative and that the crossover lies at $\kappa = 1/\sqrt{2}$ [6]. When the surface energy is negative, i.e. for $\kappa > 1/\sqrt{2}$, the superconductor maximizes the normal-superconducting interfaces which leads to multiple localized regions where the magnetic field partially penetrates the sample [7–9], i.e. vortex formation. On the other hand, when the surface energy is positive, i.e. for $\kappa < 1/\sqrt{2}$, the normal-superconducting interfaces become energetically unfavorable and the superconductor avoids them, or allows for larger domain structures, such as those shown in Fig. 1.8, appearing in specific cases where the demagnetization field is important. Superconductors with $\kappa > 1/\sqrt{2}$ are known as type II whereas those with $\kappa < 1/\sqrt{2}$ are called type I.

1.2.3 Flux quantization

The distinguishing property of type II superconductors is the existence of an intermediate state between the Meissner and the normal phase where vortices appear due to the negative energy of the superconducting-normal interface. Using the second GL equation, let us calculate the magnetic flux inside the area S of a type II superconductor enclosed by a path C. Writing the order parameter in the polar form of complex numbers, i.e. $\psi = |\psi|e^{i\phi}$, Eq. 1.5 becomes

$$\mathbf{J} = \frac{e^*\hbar}{m^*}|\psi|^2\Big(\nabla\phi - \frac{e^*}{\hbar c}\mathbf{A}\Big). \tag{1.24}$$

Calculating the line integral of the vector potential $\mathbf{A}$ along the closed path C, one obtains

$$\oint_C \mathbf{A}\cdot\mathbf{dl} = \int_S \mathbf{h}\cdot\mathbf{ds} = \frac{\hbar c}{e^*}\oint_C \nabla\phi\cdot\mathbf{dl} - \frac{m^* c}{e^{*2}}\oint_C \mathbf{j}\cdot\mathbf{dl}, \tag{1.25}$$

where $\mathbf{j} = \mathbf{J}/|\psi|^2$, and in the central equation the Stoke's theorem has been used. If one chooses the path C such that along it $\mathbf{j} = 0$, and one assumes that the order parameter is single valued, the magnetic flux inside the area S becomes

$$\Phi = n\Phi_0, \tag{1.26}$$

where n is an integer number and the quantity $\Phi_0 = hc/e^*$ is the minimal amount of flux penetrating the sample, i.e. the quantum of flux. It is noteworthy to point out that a first reading of Eq. 1.26 might lead us to interpret it as a quantization of the magnetic flux. However, formally speaking what is quantized is the fluxoid rather than the flux. Reorganizing Eq. 1.25 we see that

$$\int_S \mathbf{h}\cdot\mathbf{ds} + \frac{m^* c}{e^{*2}}\oint_C \mathbf{j}\cdot\mathbf{dl} = n\Phi_0, \tag{1.27}$$

where the quantity on the left side is the fluxoid. Nevertheless, notice that along the path C where $\mathbf{j} = 0$ the fluxoid and the flux are the same.

Finally, direct measurements of the flux quantization revealed that $e^* = 2e$, where e is the electronic charge, indicating that pairs of electrons rather than single electrons play the essential role in superconductivity. In the discussion of the microscopic theory of superconductivity this suggestion was most useful.

1.2.4 The Josephson effect

One of the archetypal consequences of the quantum behavior of electrons is their ability to tunnel through potential barriers. Similarly, the tunneling of Cooper pairs between two superconductors separated by a thin insulating or metallic layer has provided one of the hallmarks of the quantum nature of the Cooper pairs. However, the fact that the Cooper pairs form a highly coherent condensate, unlike electrons in a conduction band, allows the stabilization of an persistent flow between two weakly connected superconductors without any external drive (the Josephson effect) [33]. This effect, named after the theoretical prediction of Brian David Josephson in 1962, is one of the most successfully applied features of superconductivity in technology. In order to explain this effect, let us consider a junction where a thin layer separates two superconductors such as shown in Fig. 1.9. Moreover, consider the following appropriate boundary conditions for the junction [31]

$$\frac{\partial\psi_1}{\partial x} - \frac{ie^*}{\hbar c}A_x\psi_1 = \frac{\psi_2}{\zeta}, \qquad \text{and} \qquad \frac{\partial\psi_2}{\partial x} - \frac{ie^*}{\hbar c}A_x\psi_2 = \frac{\psi_1}{\zeta}, \tag{1.28}$$

where ζ is a phenomenological parameter associated to the insulating layer. Substituing the junction boundary condition in the x component of the superconducting current density given by Eq. 1.5, one obtains

$$J_x = \frac{e^*\hbar}{2m^* i}\Big[\psi_1^*\Big(\frac{\psi_2}{\zeta} + \frac{ie^*}{\hbar c}A_x\psi_1\Big) - \psi_1\Big(\frac{\psi_2^*}{\zeta} - \frac{ie^*}{\hbar c}A_x\psi_1^*\Big)\Big]. \tag{1.29}$$

In the last equation, where the time reversal invariance of the order parameter and the vector potential was assumed, the boundary coefficient ζ became real, along with the vector potential leading to the following simple form

$$J_x = \frac{e^*\hbar}{m^*\zeta}|\psi_1||\psi_2|\sin(\phi_2 - \phi_1), \tag{1.30}$$

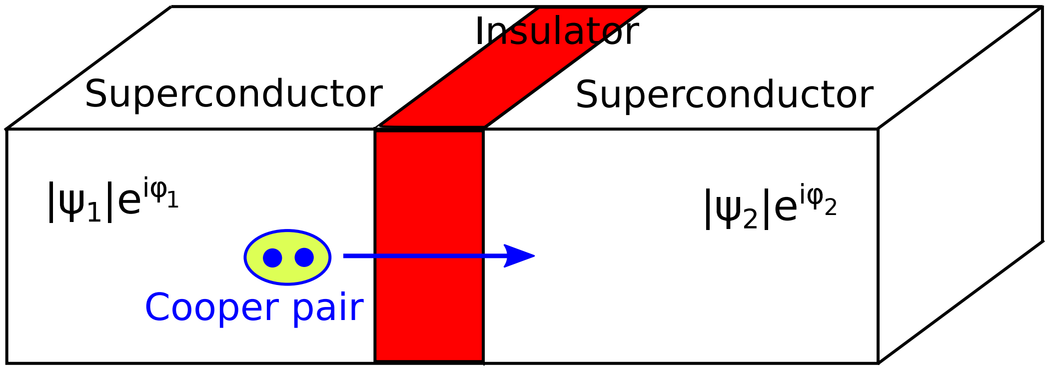

Figure 1.9: Cartoon of a Josephson junction with two superconductors with order parameters having angular phases ϕ_1 and ϕ_2, weakly connected through a thin insulating layer. Just as electrons are able to tunnel potential barriers, the Cooper pairs here tunnel through the insulating layer and establish Josephson current provided that there exists a difference between the angular phases ($\phi_1 \neq \phi_2$).

where the polar expressions of the superconducting order parameters have been used. If the two superconductors are the same material, the expression for this tunneling current becomes

$$J_x = J_m \sin \Phi_{21}, \tag{1.31}$$

where $J_m = \frac{e^* \hbar |\psi|^2}{m^* \zeta}$ is the maximal value of the Josephson current and $\Phi_{21} = \phi_2 - \phi_1$ is the phase difference between the two superconductors. Eq. 1.31 then tells us that due to tunneling of Cooper pairs between two weakly connected superconductors, a nonzero current density can appear on the junction provided that there exists an imbalance in phase between the two sides of the junction. Such imbalance can be achieved by e.g. applying a voltage to the junction or an external magnetic field.

1.3 BCS theory

Up to here superconductivity has been discussed in this thesis mostly from a phenomenological point of view. This description, although powerful and general, falls short in the analysis of the microscopic origins of superconductivity. Thus, to go beyond the phenomenological description of superconductivity of the Ginzburg-Landau model, in the following sections the microscopic theory will be presented.

1.3.1 Instability of the Fermi surface

Superconductivity arises after Cooper pairs condense into a coherent state of matter revealing the unique properties that have been discussed so far. It is of course not obvious, how two electrons can form a Cooper pair when the Coulomb repulsion between them is strong. One can naively think that there exists an attractive potential stronger than the Coulomb repulsion. Nevertheless, such argument is not required at all to explain the formation of Cooper pairs. Interestingly, what is required for the Cooper pair formation is a Fermi surface and a weak attractive interaction. In order to demonstrate this, consider two electrons with opposite spins, i.e. forming a singlet state, and consider the following Schrödinger equation for the orbital part of the pair

$$\left[\frac{\mathbf{p}_1^2}{2m} + \frac{\mathbf{p}_2^2}{2m} + V(\mathbf{r}_1, \mathbf{r}_2)\right] |\Psi(\mathbf{r}_1, \mathbf{r}_2)\rangle = (\varepsilon + 2E_F) |\Psi(\mathbf{r}_1, \mathbf{r}_2)\rangle \, , \tag{1.32}$$

where E_F is the energy of the Fermi surface and ε is the energy of the pair relative to E_F. Changing the coordinates from ($\mathbf{r}_1$, $\mathbf{r}_2$) to the coordinate of the center of mass ($\mathbf{R} = \frac{\mathbf{r}_1 + \mathbf{r}_2}{2}$) and the relative coordinate ($\rho = \mathbf{r}_1 - \mathbf{r}_2$), one can rewrite the kinetic terms of the Hamiltonian of Eq. 1.32 as

$$\frac{\mathbf{p}_1^2}{2m} + \frac{\mathbf{p}_2^2}{2m} = -\frac{\hbar^2}{2m}\big(\nabla_1^2 + \nabla_2^2\big) = -\frac{\hbar^2}{2m}\big(\frac{1}{2}\nabla_{\mathbf{R}}^2 + 2\nabla_\rho^2\big). \tag{1.33}$$

Next, considering that the potential V depends only on the relative coordinate ρ, one should notice the existence of two movements: one where the center of mass of the pair propagates freely, and other described by the following Hamiltonian,

$$\Big[-\frac{\hbar^2}{m}\nabla_\rho^2 + V(\rho)\Big]\left|\Psi(\rho)\right\rangle = (\varepsilon + 2E_F)\left|\Psi(\rho)\right\rangle. \tag{1.34}$$

The solution of Eq. 1.34 can be built by doing an expansion in terms of the complete basis $\{|\mathbf{k}\rangle\}$, whose infinite elements satisfy the eigenvalue equation $\nabla_\rho |\mathbf{k}\rangle = i\mathbf{k}\,|\mathbf{k}\rangle$, i.e. $|\Psi(\rho)\rangle = \sum g(\mathbf{k})\,|\mathbf{k}\rangle$. The complete basis $\{|\mathbf{k}\rangle\}$ is nothing less than the infinite set composed of plane waves $\{e^{i\mathbf{k}\cdot\rho}\}$. Substitution of the expanded wave function into Eq. 1.34 yields

$$\sum_{\mathbf{k}}\Big[\frac{\hbar^2k^2}{m} + V(\rho)\Big]g(\mathbf{k})\,|\mathbf{k}\rangle = (\varepsilon + 2E_F)\sum_{\mathbf{k}} g(\mathbf{k})\,|\mathbf{k}\rangle. \tag{1.35}$$

By projecting into the state $\langle\mathbf{k}'|$ and bearing in mind that the elements of the complete basis are orthogonal, i.e. $\langle\mathbf{k}'|\mathbf{k}\rangle = \delta_{\mathbf{k}',\mathbf{k}}$, one obtains

$$\frac{\hbar^2k'^2}{m}g(\mathbf{k}') + \sum_{\mathbf{k}} g(\mathbf{k})V_{\mathbf{k}',\mathbf{k}} = (\varepsilon + 2E_F)g(\mathbf{k}'), \tag{1.36}$$

where

$$V_{\mathbf{k}',\mathbf{k}} = \frac{1}{\Omega}\int V(\rho)e^{-i(\mathbf{k}'-\mathbf{k})\cdot\rho}d^3\rho. \tag{1.37}$$

The precise value of the matrix $V_{\mathbf{k}',\mathbf{k}}$ is complex and depends on the full knowledge of the potential $V(\rho)$, which in many cases is not available. However, a simplification of the problem, first suggested by Cooper [11], assumes $V_{\mathbf{k}',\mathbf{k}}$ is constant and nonzero only inside a narrow window around the Fermi surface as shown in Fig. 1.10,

$$V_{\mathbf{k}',\mathbf{k}} = \begin{cases} -\tilde{V}, & |\frac{\hbar^2k^2}{2m} - E_F| < \hbar\omega_D \quad and \quad |\frac{\hbar^2k'^2}{2m} - E_F| < \hbar\omega_D \\ 0, & elsewhere \end{cases} \tag{1.38}$$

with ω_D being the Debye frequency. By applying the Cooper simplification on matrix $V_{\mathbf{k}',\mathbf{k}}$, Eq. 1.36 becomes

$$\frac{-\tilde{V}\sum g(\mathbf{k})}{\varepsilon + 2E_F - \frac{\hbar^2k'^2}{m}} = g(\mathbf{k}'), \tag{1.39}$$

which can be reduced further by summing over $\mathbf{k}'$ on both sides of the equation and then factoring out the k-independent term $\sum g(\mathbf{k}')$, leading to

$$\tilde{V}\sum_{\mathbf{k}'}\frac{1}{\frac{\hbar^2k'^2}{m} - 2E_F - \varepsilon} = 1. \tag{1.40}$$

The sum over $\mathbf{k}'$ in the last equation can be transformed into an integral over $\epsilon = \hbar^2k'^2/2m - E_F$, with the corresponding introduction of the density of states per spin $N(\epsilon)$, so that

$$\tilde{V}\int_0^{\hbar\omega_D}\frac{N(\epsilon)d\epsilon}{2\epsilon - \varepsilon} = 1 = \frac{\tilde{V}}{2}N(0)\ln\Big(\frac{\varepsilon - 2\hbar\omega_D}{\varepsilon}\Big). \tag{1.41}$$

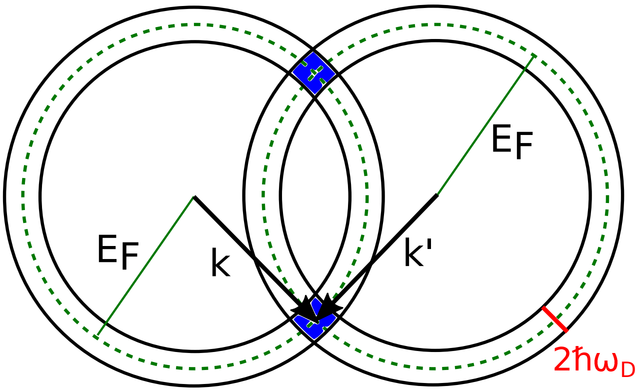

Figure 1.10: The simplification suggested by Cooper to the complex matrix $V_{\mathbf{k}',\mathbf{k}}$ replaces it by a constant and negative potential ($-\tilde{V}$) in the shaded areas shown in the figure, i.e. the interception of the rings around the Fermi surface E_F.

The assumption that $|\varepsilon| \ll \hbar\omega_D$ leads finally to the energy of the pair relative to the Fermi surface,

$$\varepsilon = -2\hbar\omega_D e^{-2/N(0)\tilde{V}}, \tag{1.42}$$

which is negative, i.e. represents a bound state, and divergent at $\tilde{V}$, explaining why a perturbative approach was not successful in the attempts prior to the Cooper work.

1.3.2 The BCS ground state

The fact that within the Debye window an attractive interaction between two electrons, immersed in a Fermi sea, leads to the formation of a state with negative energy, i.e. a bound state, suggested that the Fermi surface is unstable against Cooper pairing [11]. By extension one can then think that more electrons from the Debye window can also pair up and abruptly increase the number of Cooper pairs. The process stops when an equilibrium between the condensate of Cooper pairs and the Fermi surface is reached. With the condensate of Cooper pairs being a many-body state, one can attempt to describe it in terms of wave functions of electronic pairs. However, the many-body state has to be asymmetric under particle interchange in order to fulfill the Pauli principle. That is achieved by defining an operator $\hat{\mathcal{A}}$ which for the case of two particles has the following property,

$$\hat{\mathcal{A}}\,|\psi_1\rangle\otimes|\psi_2\rangle = |\psi_1\rangle\otimes|\psi_2\rangle - |\psi_2\rangle\otimes|\psi_1\rangle\,. \tag{1.43}$$

In order to give a practical example of a many-body wave function, let us consider two electrons and start the analysis from the spin sector. Each particle has the typical two spin states, either up or down. The asymmetric two particle state for these spins is

$$|s\rangle = \frac{1}{\sqrt{2}}\big(|1\uparrow\rangle\otimes|2\downarrow\rangle - |1\downarrow\rangle\otimes|2\uparrow\rangle\big), \tag{1.44}$$

where s denotes that the state is a singlet, i.e. the total angular momentum of the two-particle system is zero. Now, since the electrons also have orbital components, consider they are in quantum states $|\mathbf{k}_1\rangle$ and $|\mathbf{k}_2\rangle$, or equivalently, they are described by the plane waves $e^{\mathbf{k}_1\cdot\mathbf{r}_1}$ and $e^{\mathbf{k}_2\cdot\mathbf{r}_2}$. By imposing that the total linear momentum of the system is zero, the full asymmetric wave function of the two-electron state becomes

$$\Psi(\mathbf{r}_1,\mathbf{r}_2)_{\mathbf{k},s} = \frac{1}{\sqrt{2}}\big(e^{i\mathbf{k}\cdot(\mathbf{r}_1-\mathbf{r}_2)} + e^{-i\mathbf{k}\cdot(\mathbf{r}_1-\mathbf{r}_2)}\big)|s\rangle\,, \tag{1.45}$$

which one can easily prove to be asymmetric under particle interchange. Moreover, this state is time-reversal invariant, as required in conventional superconductivity due to the absence of spontaneous magnetic fields.

One can use the second quantization formalism of field theories to describe the many-body states of condensed matter in a more practical way. The building blocks of the second quantization formalism are the creation and annihilation operators, namely $\hat{c}^{\dagger}_{\mathbf{k}\alpha}$ and $\hat{c}_{\mathbf{q}\beta}$, satisfying the following properties:

$$\begin{aligned} \hat{c}^{\dagger}_{\mathbf{k}\alpha}\hat{c}^{\dagger}_{\mathbf{q}\beta} + \hat{c}^{\dagger}_{\mathbf{q}\beta}\hat{c}^{\dagger}_{\mathbf{k}\alpha} &= 0, \qquad (1.46) \\ \hat{c}_{\mathbf{k}\alpha}\hat{c}_{\mathbf{q}\beta} + \hat{c}_{\mathbf{q}\beta}\hat{c}_{\mathbf{k}\alpha} &= 0, \qquad (1.47) \end{aligned}$$

and

$$\hat{c}^{\dagger}_{\mathbf{k}\alpha}\hat{c}_{\mathbf{q}\beta} + \hat{c}_{\mathbf{q}\beta}\hat{c}^{\dagger}_{\mathbf{k}\alpha} = \delta_{\mathbf{k}\mathbf{q}}\,\delta_{\alpha\beta}. \qquad (1.48)$$

Here $\mathbf{k}$ and $\mathbf{q}$ label the orbital component of the state, while α and β label its spin part. From Eq. 1.46 one notices that when $\mathbf{k} = \mathbf{q}$ and $\alpha = \beta$, the product $\hat{c}^{\dagger}_{\mathbf{k}\alpha}\hat{c}^{\dagger}_{\mathbf{k}\alpha}$ vanishes, thus the creation of two particles occupying exactly the same quantum state is forbidden. On the other hand, the definition of the particle number operator as: $\hat{n}_{\mathbf{k}\alpha} = \hat{c}^{\dagger}_{\mathbf{k}\alpha}\hat{c}_{\mathbf{k}\alpha}$, along with the Eqs. 1.46 - 1.48, leads us to the distinguishing property $\hat{n}^2_{\mathbf{k}\alpha} = \hat{n}_{\mathbf{k}\alpha}$, which means that the electronic occupation of any quantum state is either one or zero. The combination of these results then indicates that the creation and annihilation operators $\hat{c}^{\dagger}_{\mathbf{k}\alpha}$ and $\hat{c}_{\mathbf{q}\beta}$ describe particles satisfying the Fermi-Dirac statistics. By using the second quantization formalism one can then rewrite the asymmetric two-particle state of Eq. 1.45 as,

$$|\mathbf{k}, s\rangle = \hat{c}^{\dagger}_{\mathbf{k}\uparrow}\hat{c}^{\dagger}_{-\mathbf{k}\downarrow}\,|\phi_0\rangle\,, \qquad (1.49)$$

where $|\phi_0\rangle$ represents the vacuum state of the system, i.e. the state defined by the equation $\hat{c}_{\mathbf{q}\beta}\,|\phi_0\rangle = 0$, for any $\mathbf{q}$ and β. By extension, one can also build a many-body wave function for N electrons out of $N/2$ time-reversal electronic pairs, as

$$|\Psi_N\rangle = \sum_{\mathbf{k}_1}\cdots\sum_{\mathbf{k}_{N/2}} g_{\mathbf{k}_1}\cdots g_{\mathbf{k}_{N/2}}\hat{c}^{\dagger}_{\mathbf{k}_1\uparrow}\hat{c}^{\dagger}_{-\mathbf{k}_1\downarrow}\cdots\hat{c}^{\dagger}_{\mathbf{k}_{N/2}\uparrow}\hat{c}^{\dagger}_{-\mathbf{k}_{N/2}\downarrow}\,|\phi_0\rangle\,, \qquad (1.50)$$

where for the case $N = 2$ it was demonstrated earlier that $g_{\mathbf{k}_1} = \frac{C_1}{2\xi-\epsilon}$, with C_1 a constant. Nevertheless, the wave function Ψ_N, which represents a state with fixed number of particles, is difficult to manipulate in the calculations of physical quantities. Bardeen, Cooper and Schrieffer then suggested a wave function not conserving the number of particles, but practical to unravel the properties derived from the BCS hamiltonian [10]:

$$|\Psi_{\mathrm{BCS}}\rangle = \prod_{\mathbf{k}}\left(\mu_{\mathbf{k}} + \nu_{\mathbf{k}}\hat{c}^{\dagger}_{\mathbf{k}\uparrow}\hat{c}^{\dagger}_{-\mathbf{k}\downarrow}\right)|\phi_0\rangle\,, \qquad (1.51)$$

where, the normalization $\left(\langle\Psi_{\mathrm{BCS}}|\Psi_{\mathrm{BCS}}\rangle = 1\right)$ implies that $|\mu_{\mathbf{k}}|^2 + |\nu_{\mathbf{k}}|^2 = 1$. The interpretation that $|\nu_{\mathbf{k}}|^2$ is the probability of an electronic pair ($\mathbf{k}\uparrow$,$-\mathbf{k}\downarrow$) being occupied, while $|\mu_{\mathbf{k}}|^2$ is the probability of the pair being unoccupied is easily derived from this normalization condition.

1.3.3 The superconducting gap

The reduced Hamiltonian of the BCS theory that arises after the imposition of Cooper pairing in a Hamiltonian for interacting particles with a general pairwise potential reads [31]

$$\hat{\mathcal{H}}_{\rm red} = \sum_{\mathbf{k}\alpha} \frac{\hbar^2 k^2}{2m} \hat{c}^{\dagger}_{\mathbf{k}\alpha} \hat{c}_{\mathbf{k}\alpha} + \sum_{\mathbf{k},\mathbf{k}'} V_{\mathbf{k},\mathbf{k}'} \hat{c}^{\dagger}_{\mathbf{k}'\uparrow} \hat{c}^{\dagger}_{-\mathbf{k}'\downarrow} \hat{c}_{-\mathbf{k}\downarrow} \hat{c}_{\mathbf{k}\uparrow}, \tag{1.52}$$

where the first term represents the kinetic energy of the electrons in a parabolic band, and the second term is the electronic coupling responsible for the formation of the Cooper pairs. Since the BCS wave function of Eq. 1.51 does not conserve the number of particles [10], a Lagrange multiplier, namely the chemical potential, has to be included in the reduced Hamiltonian as follows,

$$\hat{\mathcal{H}}_{\rm BCS} = \hat{\mathcal{H}}_{\rm red} - \mu \hat{N}. \tag{1.53}$$

Here the chemical potential μ is nothing but the Fermi energy, and the total particle number operator is

$$\hat{N} = \sum_{\mathbf{k}\alpha} \hat{c}^{\dagger}_{\mathbf{k}\alpha} \hat{c}_{\mathbf{k}\alpha}. \tag{1.54}$$

In what follows, one needs to demonstrate that the BCS wave function of Eq. 1.51 is the variational ground state of the BCS Hamiltonian of Eq. 1.53. The details of the calculations are well documented elsewhere [4,31], so here we will outline just the most important findings. The expected value of the Hamiltonian 1.53 with the BCS wave function yields

$$\langle \hat{\mathcal{H}}_{\rm BCS} \rangle = 2 \sum_{\mathbf{k}} \xi_{\mathbf{k}} |\nu_{\mathbf{k}}|^2 + \sum_{\mathbf{k},\mathbf{k}'} V_{\mathbf{k},\mathbf{k}'} \nu^*_{\mathbf{k}} \mu_{\mathbf{k}} \nu^*_{\mathbf{k}'} \mu_{\mathbf{k}'} \,, \tag{1.55}$$

where $\xi_{\mathbf{k}} = \hbar^2 k^2/2m - \mu$. From the normalization condition $\left(|\mu_{\mathbf{k}}|^2 + |\nu_{\mathbf{k}}|^2 = 1\right)$ one can parametrize the amplitude densities as: $\mu_{\mathbf{k}} = \cos\theta_k$ and $\nu_{\mathbf{k}} = \sin\theta_k$. Then one minimizes the expected value 1.55 with respect to the parameter θ_k and obtains

$$2\xi_k \sin 2\theta_k + \cos 2\theta_k \sum_{k'} V_{k,k'} \sin 2\theta_{k'} = 0, \tag{1.56}$$

where it was assumed that the potential $V_{\mathbf{k},\mathbf{k}'}$ is symmetric, i.e. $V_{\mathbf{k},\mathbf{k}'} = V_{\mathbf{k}',\mathbf{k}}$. Defining the sum in the last equation as

$$\Delta_k = -\frac{1}{2} \sum_{k'} V_{k,k'} \sin 2\theta_{k'}, \tag{1.57}$$

Eq. 1.56 takes the simpler form

$$\tan 2\theta_k = \frac{\Delta_k}{\xi_k}. \tag{1.58}$$

By using the trigonometric identities one can see that

$$\cos 2\theta_k = \frac{\xi_k}{\sqrt{\xi_k^2 + \Delta_k^2}}, \quad \text{and} \quad \sin 2\theta_k = \frac{\Delta_k}{\sqrt{\xi_k^2 + \Delta_k^2}}, \tag{1.59}$$

or equivalently

$$\mu_k^2 = \frac{1}{2}\Big(1 + \frac{\xi_k}{\varepsilon_k}\Big), \quad \text{and} \quad \nu_k^2 = \frac{1}{2}\Big(1 - \frac{\xi_k}{\varepsilon_k}\Big), \tag{1.60}$$

where $\varepsilon_k = \sqrt{\xi_k^2 + \Delta_k^2}$ is the excitation energy of a quasi-particle with momentum $\hbar\mathbf{k}$. One can notice that there is a minimal amount of energy required to add an electron in the excited state, i.e. there exists a gap, namely Δ_k, which satisfies the following nonlinear integral equation,

$$\Delta_k = -\frac{1}{2}\sum_{k'} \frac{V_{k,k'}\Delta_{k'}}{\sqrt{\xi_{k'}^2 + \Delta_{k'}^2}}. \tag{1.61}$$

Normal solution

The simplest solution of the linear equation 1.56 is the trivial gap solution $\Delta_k = 0$. The excitation energy of the quasi-particles in this case becomes $\varepsilon_k = \pm\xi_k$, and the occupation coefficients are

$$\mu_k = 0, \qquad \nu_k = 1, \qquad \text{for } \xi_k < 0, \tag{1.62}$$

and

$$\mu_k = 1, \qquad \nu_k = 0, \qquad \text{for } \xi_k > 0. \tag{1.63}$$

Substituing the last coefficients into the BCS wave function of Eq. 1.51 one obtains,

$$|\Psi_{\text{BCS}}\rangle = \prod_{\mathbf{k}<k_F} \hat{c}^\dagger_{\mathbf{k}\uparrow}\hat{c}^\dagger_{-\mathbf{k}\downarrow}\,|\psi_0\rangle\,, \tag{1.64}$$

which is the usual ground-state wavefunction of a filled Fermi surface (also called the Fermi vacuum) [31].

Isotropic gap solution

Using the Cooper simplification for the attractive potential (see Eq. 1.38) and the important assumption that the gap is constant in the reciprocal space, one can analytically solve the integral gap equation 1.61 to obtain

$$1 = \frac{\tilde{V}}{2}\sum_{k'} \frac{1}{\sqrt{\xi_{k'}^2 + \Delta_{k'}^2}}, \tag{1.65}$$

which in the continuum limit becomes

$$N(0)\tilde{V}\int_0^{\hbar\omega_D} \frac{d\xi}{\sqrt{\xi^2+\Delta^2}} = 1 = N(0)\tilde{V}\sinh^{-1}\Big(\frac{\hbar\omega_D}{\Delta}\Big), \tag{1.66}$$

with $N(0)$ the density of states at the Fermi energy. The fact that in many superconductors $\Delta \ll \hbar\omega_D$, allows one to approximate the last result and obtain for the gap the following value

$$\Delta \approx 2\hbar\omega_D e^{-1/N(0)\tilde{V}}, \tag{1.67}$$

which resembles the energy of the bound state discussed in Eq. 1.42. Rewriting the expectation value of the BCS Hamiltonian, i.e. the energy of the superconducting state (see Eq. 1.55), with the aid of the practical notation introduced through Eq. 1.60 yields

$$\langle\hat{\mathcal{H}}_{\text{BCS}}\rangle = 2\sum_k \frac{\xi_k}{2}\Big(1 - \frac{\xi_k}{\varepsilon_k}\Big) + \frac{1}{4}\sum_{k,k'} V_{k,k'}\frac{\Delta_k\Delta_{k'}}{\varepsilon_k\varepsilon_{k'}}. \tag{1.68}$$

The detailed calculation of this energy can be found in Ref. [31]. Here we present and discuss the following relation,

$$\langle\hat{\mathcal{H}}_{\text{BCS}}\rangle - \langle\hat{\mathcal{H}}_{\Delta=0}\rangle = -\frac{1}{2}N(0)\Delta^2, \tag{1.69}$$

which means that the BCS wave function of Eq. 1.51 has lower energy than the normal state solution of Eq. 1.64, i.e. $|\Psi_{\text{BCS}}\rangle$ is the ground state of the BCS Hamiltonian 1.53.

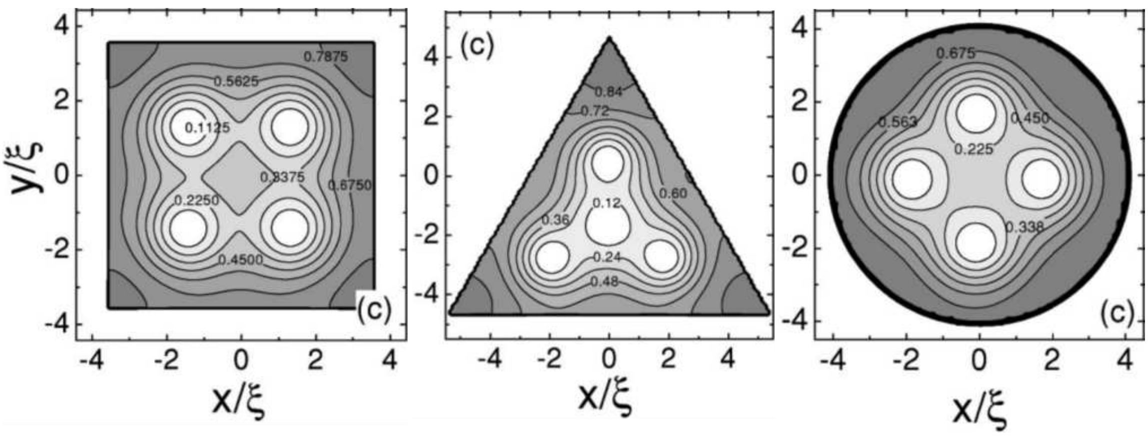

Figure 1.11: Contour plots of the Cooper-pair density of mesoscopic samples of different shapes. Notice that despite of the samples having the same number of vortices the vortex configuration changes. From Ref. [34].

1.4 Mesoscopic superconductivity

We discussed in section 1.2.1 the existence of two length scales, ξ and λ, governing the spatial variation of the fields ψ and $\mathbf{h}$, respectively. Also, in section 1.2.2 it was demonstrated that the ratio between these two scales ($\kappa = \lambda/\xi$) determines the magnetic behavior of the superconductor, and classifies it as type I or II. The limiting case of an extreme type II superconductor, i.e. a case where $\lambda \gg \xi$, is known as the London limit [4], where the linear relationship between the magnetic field and the superconducting density current can be generalized, resulting in an expression useful for our present purpose

$$\frac{4\pi\lambda^2}{c}\nabla \times \mathbf{J} + \mathbf{h} = \Phi_0\hat{\mathbf{k}}\delta_2(\mathbf{r}\,). \tag{1.70}$$

Here $\delta_2(\mathbf{r}\,)$ is the 2D Dirac delta distribution function that introduces the fluxoid quantization. Taking the curl of the second GL equation 1.5 and substituing the Eq. 1.70 there, one obtains the following differential equation for the magnetic field,

$$\nabla^2\mathbf{h} - \lambda^{-2}\mathbf{h} = -\lambda^{-2}\Phi_0\hat{\mathbf{k}}\delta_2(\mathbf{r}\,). \tag{1.71}$$

The solution of Eq. (1.71) is

$$h(r) = \frac{\Phi_0}{2\pi\lambda^2}K_0\Big(\frac{r}{\lambda}\Big), \tag{1.72}$$

where K_0 is the zeroth order modified Bessel function. From Eq. 1.72 and the use of energy arguments it is straightforward to calculate the interaction energy between two vortices with single vorticity [4, 31], as

$$U(r) = \frac{\Phi_0^2}{8\pi^2\lambda^2}K_0\Big(\frac{r_{12}}{\lambda}\Big), \tag{1.73}$$

where r_{12} is the distance between the two vortices. Since this potential energy is monotonically decreasing, the interaction between vortices is repulsive. In a bulk superconductor this type of interaction leads to the formation of a triangular lattice of vortices, the Abrikosov lattice [7–9]. However, in mesoscopic superconductors, i.e. in those with dimensions comparable to the characteristic length scales ξ and λ, the spatial configuration of vortices changes depending on the sample shape [34]. For example, we show in the Fig. 1.11 the contour plots of the Cooper-pair density illustrating that the vortex configuration of square, triangular and circular samples differ for the same vorticity.

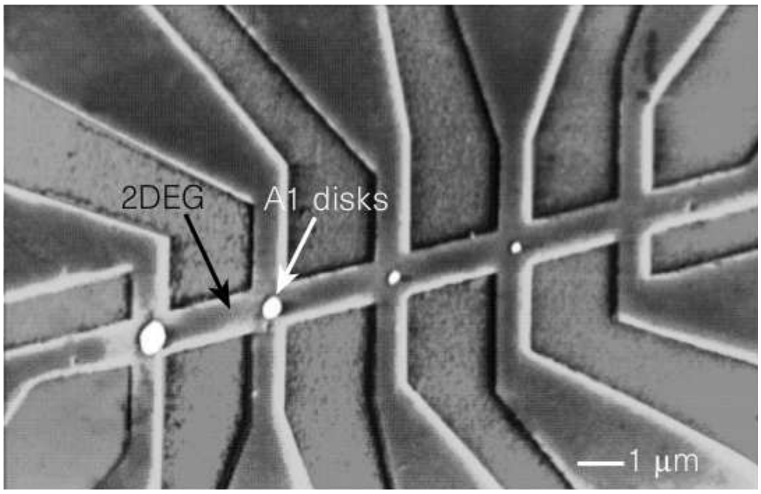

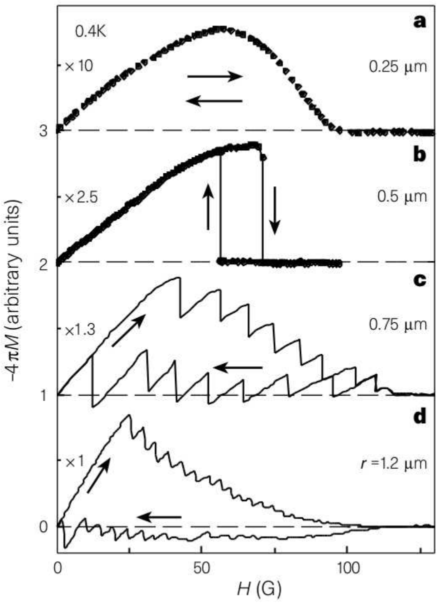

Figure 1.12: (a) Scanning electron micrograph of Hall probes on which disks of aluminum of different radii were placed. The Hall probes measure the average magnetic field emanating from the aluminum disks. (b) Measured magnetization loops as a function of the external magnetic field for the superconducting disks of (a). The plots reveal distinct behavior in the magnetization as the sample size is changed. From Ref. [35]

The behavior of the magnetization in mesoscopic superconducting samples also differs from the one in bulk samples [35]. For instance one can easily see the effect of the sample size of several mesoscopic disks on the magnetization plots in Fig. 1.12. There, in the loops of the magnetization against the external field H, jumps occur due to transitions between superconducting states with different vorticities. Thus, one can infer from these jumps that there exists a barrier for the penetration and exit of vortices which has to be surpassed. This barrier depends on the size and geometry of the sample [36, 37], and the electromagnetic properties of vortices [38], and causes the irreversibility in the magnetization loops in the mesoscopic case.

Another interesting effect that emerges in mesoscopic superconductivity is the stabilization of superconducting states unattainable in bulk superconductors. In Fig. 1.2(b) it was shown that vortices in bulk $\mathrm{NbSe_2}$ form the triangular lattice characteristic of type II superconductors [9], i.e. the Abrikosov lattice. These vortices, which each carry a single quantum of flux, minimize the free energy by forming this lattice [7]. However, in mesoscopic superconductivity, vortices with vorticity higher than one (from here on called giant vortices) can be stabilized due to geometric confinement provided by the boundaries [39]. A giant vortex is not attainable in bulk superconductors because its kinetic energy is far higher than that of a sum of single-quantum vortex. The geometric confinement therefore provides the mechanism for the reduction of its energy as one can see in Fig. 1.13(a).

For a defined vorticity and at certain value of H, Fig. 1.13(a) shows that configurations of vortices (multivortex states) have higher energy than giant vortex states, e.g. for vorticity $L = 3, 4, 5$. Moreover, it also shows continuous transitions from multivortex to giant vortex configurations, that in the heat capacity appear as jumps [Fig. 1.13(b)], suggesting an universal method for the indirect detection of giant vortices [40]. Directly, giant vortices have been imaged in mesoscopic superconductors by e.g. STM [41].

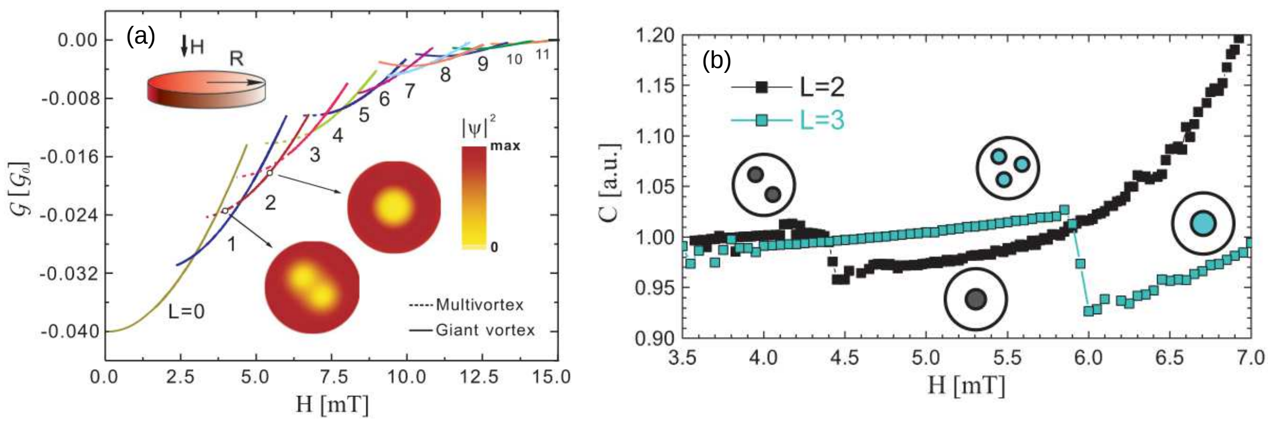

Figure 1.13: (a) Free energy of a mesoscopic disk with radius $R = 10\xi$ as a function of the external magnetic field H. Each colored line represents a superconducting state with defined vorticity L. In some states one finds continuous transitions from multivortex (dashed lines) to giant vortex (straight lines) states. (b) Heat capacity as a function of H corresponding to the states with $L=2$ and $L=3$, and revealing discontinuities in the multivortex to giant vortex transitions. From Ref. [40].

1.5 Unconventional superconductivity

The theoretical description of superconductivity that has been provided up to here was entirely devoted to superconductors with an isotropic gap and spin zero (singlet) Cooper pairs, the so-called conventional or s-wave superconductors. In this section we briefly discuss other materials that have been proven to superconduct but do not support the conventional picture of singlet Cooper pairs with an isotropic gap.

1.5.1 The cuprates

In superconductivity, the name cuprates designates the class of materials having a perovskyte structure with planes of copper oxide ($\mathrm{CuO_2}$) being alternated with layers of ions such as lanthanum, barium and strontium. These materials are superconducting in a broad range of temperature and chemical doping. Precisely, this broad range of temperature, that can reach 170 K in certain materials under pressure, is the responsible for their alternative name, high temperature superconductors (HTS). The superconductivity in the cuprates is highly anisotropic owing to their layered structure. In fact, many experiments point out that superconducting order is developed in the $\mathrm{CuO_2}$ so that the HTS phenomenon is two-dimensional. Nevertheless, this 2D-superconductivity is different from the conventional superconductivity discussed so far in this work.

The superconductivity in cuprates is of d-wave type rather than the s-wave type of conventional superconductors, according to three different analyses, namely penetration depth measurements [43], angle-resolved photoemission spectroscopy (ARPES) [44, 45], and phase-sensitive experiments [18, 19]. In Fig. 1.15(a) the inverse square of the penetration depth as a function of temperature for an YBCO crystal shows that at low temperatures λ^{-2} linearly depends on T, behaving distinctly different from the s-wave BCS behavior of conventional superconductors (also shown in the figure). This distinct behavior is a consequence of quasiparticle DOS being proportional to the energy, i.e. a line node as expected in the case of d-wave symmetry.

With ARPES, a technique devised to measure the distribution of electrons inside a solid, experimentalists have measured the band structure, Fermi surfaces, and most importantly for this work, the superconducting gap of the cuprates. In Fig. 1.15(b) the superconducting gap as a function of the angle along the Fermi surface is shown for the HTS $\mathrm{Bi_2Sr_2CaCu_2O_{8+\delta}}$ (BSCCO). There one notices that the gap has a node at $\theta = \pi/4$, in agreement with what is expected for the case of d-wave

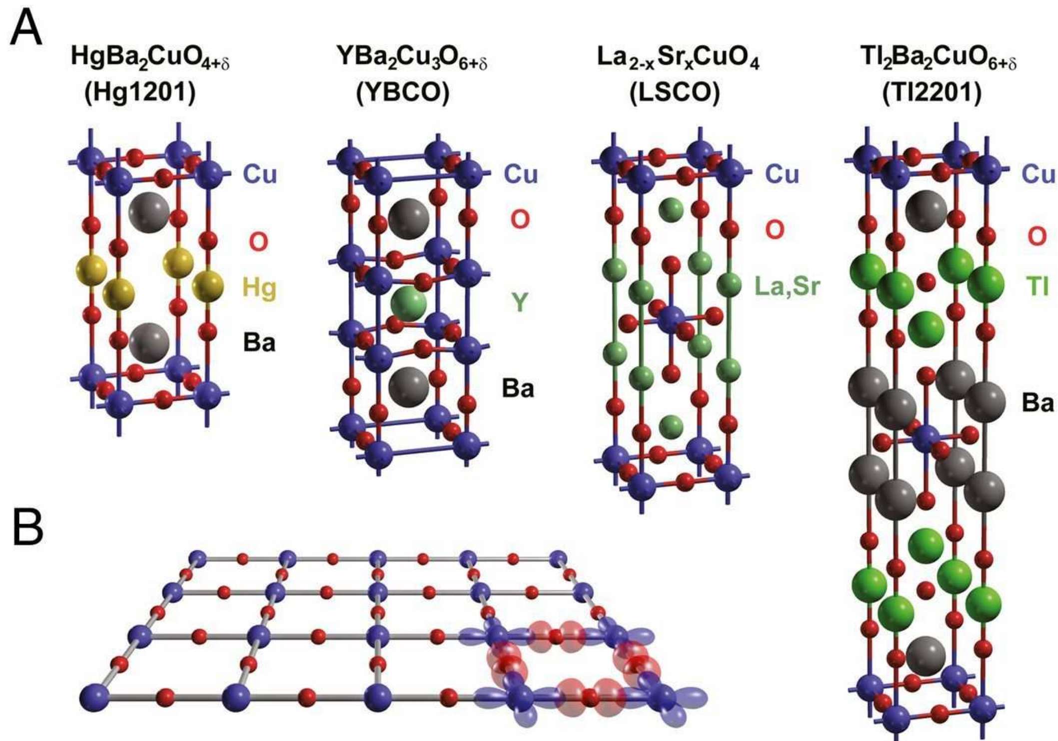

Figure 1.14: (a) Crystal structure of several cuprates. (b) The copper (blue) and oxygen (red) atoms form a square lattice in the layers where superconducting order emerges. From Ref. [42].

symmetry.

Finally, the phase-sensitive measurements in the cuprates were the smoking gun evidence that proved the gap in these materials has the d-wave symmetry. These measurements exploited the Josephson effect in a double junction device, such as one shown in Fig. 1.15(c), to detect the constructive or destructive interference in the critical current stemming from the spatial anisotropy of the superconducting gap. The device resembles the standard superconducting quantum interference devices (SQUIDs) used widely to measure small magnetic fields. In SQUIDs the critical current that circulates along the device is a periodic function of the flux penetrating the area enclosed by it,

$$I_c(\Phi) = 2I_0 \left| \cos\left(\pi \frac{\Phi}{\Phi_0}\right) \right|. \tag{1.74}$$

However, for the device of Fig. 1.15(c) the junctions are perpendicular to each other in such a way that while one junction is aligned with one of the positive lobes of the gap, the another junction is aligned with the negative one. This results in a destructive interference that is manifested in the critical current as a minimum at zero external field [see panel (d)]. The experiments with the device of 1.15(c) and with other devices with different geometries all confirmed the d-wave symmetry of the cuprates.

1.5.2 Strontium ruthenate

Strontium ruthenate ($\mathrm{Sr_2RuO_4}$), the first superconductor with a structure similar to the cuprates, but without copper as the key element, was reported eight years after the discovery of superconductivity in the cuprates. It has a layered perovskyte structure, as shown in Fig. 1.16(a), where octahedrons containing oxygen atoms in the corners surround the atoms of ruthenium. Very quickly it was realized that superconductivity in strontium ruthenate (SRO) and the cuprates was different, since the critical temperature of the former was just $1.5\,K$, nearly two orders of magnitude lower with respect

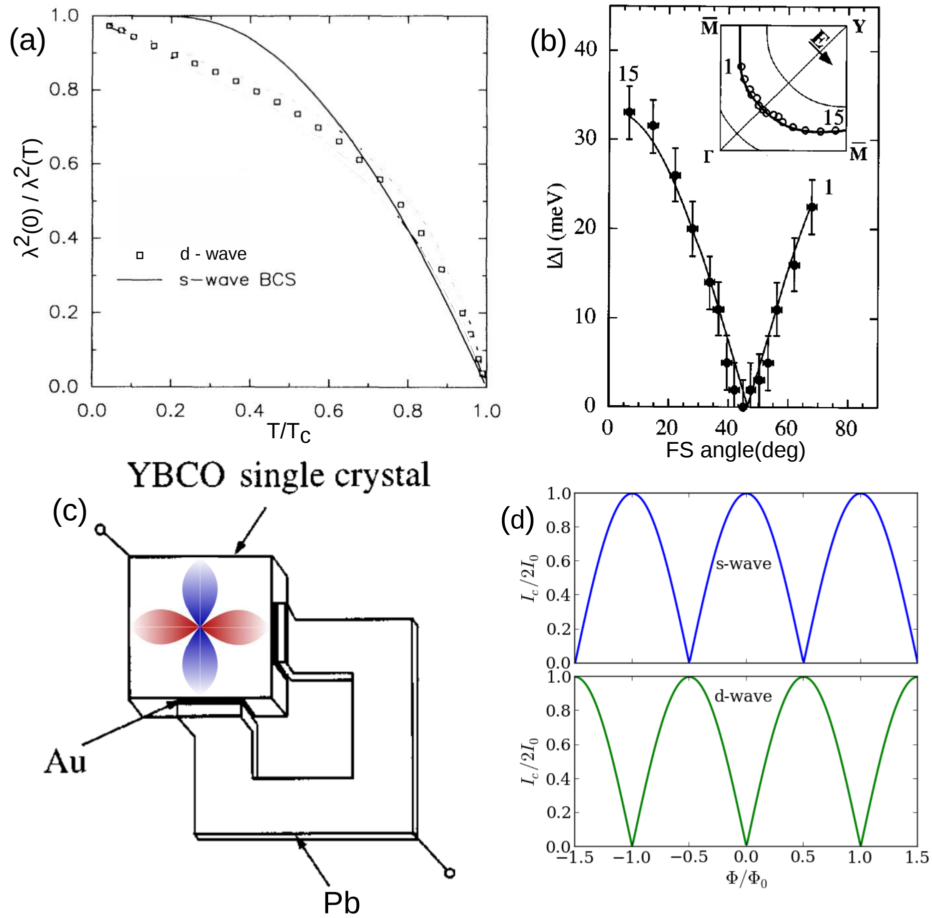

Figure 1.15: (a) Inverse square of the penetration depth, plotted as a function of temperature, for the Yttrium-Barium-Copper-Oxygen (YBCO) compound, revealing at low T a linear dependence. Adapted from Ref. [43]. (b) The superconducting gap as a function of the angle along the Fermi surface (FS) shows the existence of a node at $\theta = \pi/2$ in the HTS $\mathrm{Bi_2Sr_2CaCu_2O_{8+\delta}}$. From Ref. [44]. (c) Double junction device, having in one corner a single crystal of YBCO, to measure (through interference) the anisotropy of the gap in this material. Adapted from Ref. [18]. (d) Critical current as a function of the magnetic flux for superconducting quantum interference devices (SQUIDs) made of s-wave and d-wave superconductors.

to the latter. Moreover, the fact that the parent compound $\mathrm{SrRuO_3}$ is an itinerant ferromagnet provided another difference between the cuprates and SRO.

Spin-triplet superconductor

One of the first experiments that confirmed the unconventional superconductivity in SRO, and that suggested the possibility of spin-triplet superconductivity, was the Knight shift experiment of Ref. [47]. Before going further in this issue, some essential aspects of SRO required an explanation in order to understand better the Knight-shift results. The Fermi surface of SRO is shown in Fig. 1.16(b), containing three sheets: two of the electron type (α and γ), and one of the hole type (β) [46]. The three Fermi sheets are approximately cylindrical. Relevant quantities of these Fermi sheets, obtained via the de Haas-van Alphen effect, are presented in Table 1.1. Those are the quasiparticle effective mass m^*, the Fermi wave vector k_F, and the Fermi velocity v_F. Note that the quasiparticle effective mass in the γ sheet is 16 times larger the electron rest mass. For comparison, the effective masses of two good conductors namely, gold and copper, are only $1.10m_e$ and $1.01m_e$, respectively. The considerable enhancement of the effective mass in SRO demonstrates that the electronic correlations are strong in this material. Specific heat measurements in the normal phase corroborate this enhancement of the effective mass. Moreover, they also suggest that the normal phase in SRO is

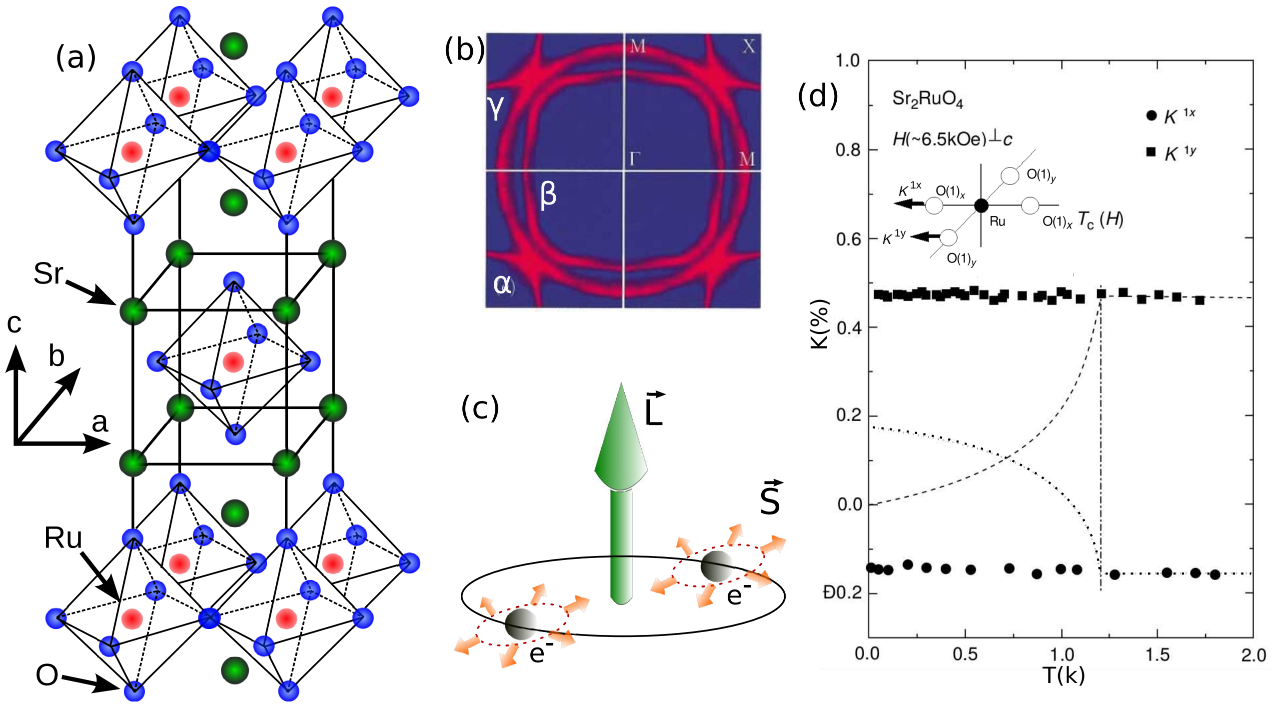

Figure 1.16: (a) Crystal structure of strontium ruthenate. (b) The Fermi surface of strontium ruthenate has three sheets, labelled α, β and γ. Among them two are of the electron type (β and γ), whereas the remaining one is of the hole type (α). From Ref. [46]. (c) Depiction of a Cooper pair with the spin of the electrons represented by small arrows, while the angular momentum of the pair is represented by the large arrow. (d) Knight-shift experiment showing the spin susceptibility is invariant across T_c. Adapted from Ref. [47].

Fermi-surface sheet	α	β	γ
m^* (m_e)	3.3	7.0	16.0
k_F (Å^{-1})	0.304	0.622	0.753
v_F (ms^{-1})	1.0 x 10^5	1.0 x 10^5	5.5 x 10^4

Table 1.1: Microscopic parameters of strontium ruthenate, obtained via the de Haas-van Alphen effect. m^* is the quasiparticle effective mass, m_e is the electron rest mass, and v_F (k_F) is the Fermi velocity (wave vector).

well described by the Fermi liquid theory.

Superconducting order was theoretically predicted to appear in the γ band and to be of the spin-triplet type [48]. That means that the Cooper pairs, instead of forming singlets as in conventional superconductors and the cuprates, form triplet states in the spin part of their wave functions. Due to the Pauli principle the spin-triplets, which are symmetric under particle interchange, require asymmetric states in the orbital part. That is achieved with odd parity states, where parity $[P=(-1)^L]$ is defined through the orbital angular momentum L. The odd parity state with the lowest L, i.e. $L = 1$, is called a p-wave state, in analogy with the orbitals of the hydrogen atom. Fig. 1.16(c) depicts a Cooper pair with the spins (**S**) of the two electrons represented by small arrows and the angular momentum (**L**) represented by the large one.

The superconductivity in SRO is as anisotropic as in the HTS. From Table 1.2 one can see a substantial difference between the upper critical magnetic field in and out of the basal plane, both at zero temperature, $H_{c2}(0)$. Similar anisotropic behavior that is also found in other superconducting parameters such as the coherence length $\xi(0)$, the penetration depth $\lambda(0)$, and the GL parameter κ. Based on the GL parameter the superconductivity is of type II independently of the crystallographic direction. However, while out of the basal plane SRO is a strong type II superconductor, in the basal plane it is soft type II.

Parameter		ab	c
T_c (K)	1.50		
$\mu_0 H_{c2}(0)$ (T)		1.50	0.075
$\xi(0)$ (Å)		660	33
$\lambda(0)$ (Å)		1900	3.0×10^4
κ		2.6	46
ξ_{ab}/ξ_c	20		

Table 1.2: Superconducting parameters for strontium ruthenate. T_c is the critical temperature, H_{c2} is the upper critical field, ξ is the superconducting coherence length, λ is the penetration depth, and $k = \lambda/\xi$ is the Ginzburg-Landau parameter.

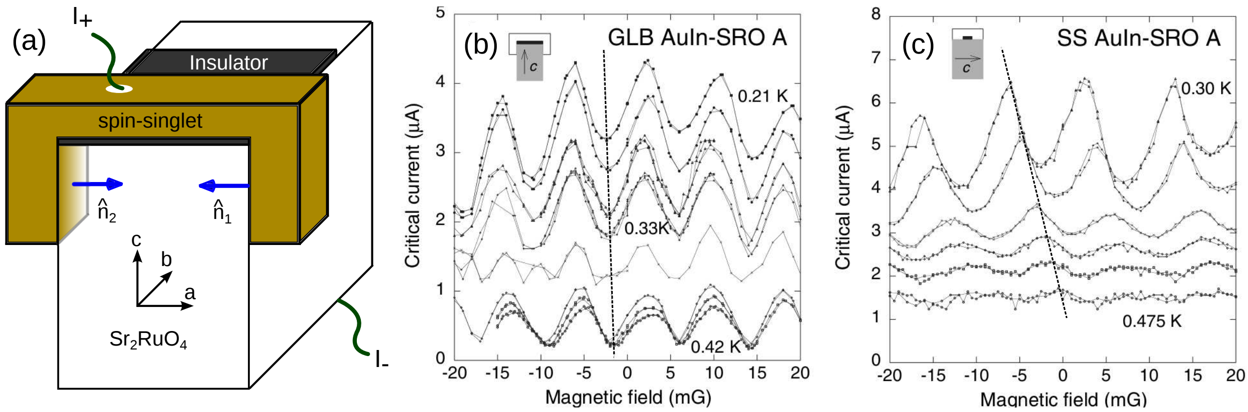

Figure 1.17: (a) Device with two opposite junctions of strontium ruthenate and a spin-singlet superconductor to test if the former is a spin-triplet superconductor (Geshkenbein-Larkin-Barone experiment). Critical currents as a function of the applied magnetic field for an opposite and a same-direction junctions are shown in panels (b) and (c) respectively. From Ref. [49].

The Knight-shift effect provides an estimate of the local magnetic field at the ions of a crystal produced by the magnetization of the conduction electrons, i.e. it indirectly measures the magnetic susceptibility of the conduction electrons. When a material becomes superconducting, in the conventional case and the cuprates, singlet states arise due to the formation of Cooper pairs. As a function of temperature the spin susceptibility of the superconductor decreases as the temperature decreases below T_c [see dashed line in Fig. 1.16(d)]. This happens because the singlet states are first destroyed than polarized. However, for a spin-triplet superconductor the electronic spin susceptibility, as a function of temperature, across the superconducting critical temperature is expected to remain constant for an in-plane external magnetic field [48]. Interestingly, Fig. 1.16(d) shows exactly that behavior. The Knight-shift effect at two different oxygen ions in the ab plane reveals that the spin susceptibility, for an external field parallel to this plane, remains constant above and below T_c, indicating spin-triplet superconductivity in SRO.

Another experiment that demonstrated the spin-triplet superconductivity in strontium ruthenate used a Geshkenbein-Larkin-Barone (GLB) interference device [49]. The principle behind this experiment relies on the Josephson effect between a spin-singlet (SS) and a spin-triplet (ST) superconductor. In a junction of SS and ST superconductors the Josephson current was demonstrated to be [50, 51],

$$j_s = \langle \mathrm{Re}(c_{21} s_{21}^*) \mathrm{Im}\{\Delta^* \mathbf{d} \cdot (\hat{n} \times \mathbf{k})\} \rangle_{FS} \tag{1.75}$$

where c_{21} and s_{21} represent the transmission amplitudes stemming from the spin-orbit and the spin-independent interactions, Δ is the gap of the SS superconductor, $\mathbf{d}$ is a vector perpendicular to the

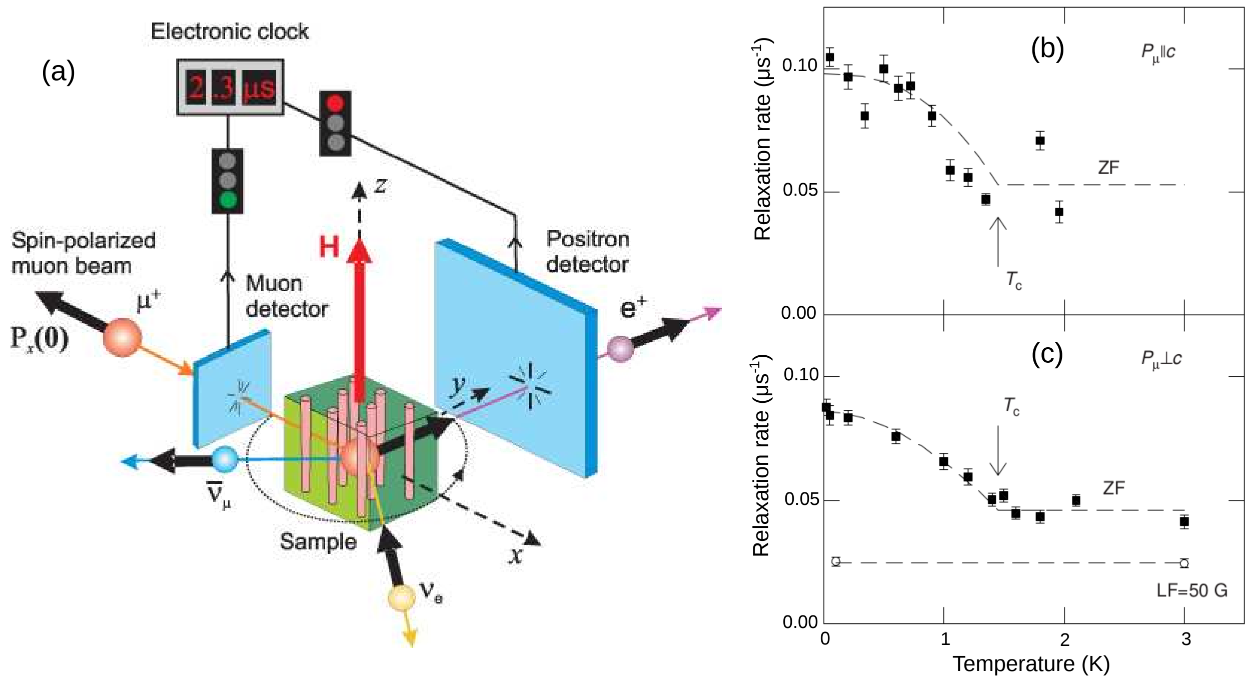

Figure 1.18: (a) Setup of the muon spin relaxation spectrometer enabling one to measure the internal magnetic fields inside a material, after statistically analyzing the decay of implanted muons into positrons. (b) For strontium ruthenate the muon-spin relaxation measurements reveal the existence of a spontaneous magnetic field that coincides with the emergence of superconducting order. From Ref. [52]

spin of the Cooper pairs in the ST superconductor, $\hat{n}$ is the vector normal to the boundary, $\mathbf{k}$ is the wave vector, and $\langle\,\rangle_{FS}$ denotes average over the Fermi surface.

In an experiment where the direction of the normal vectors in a GLB device is the opposite, such as shown in Fig. 1.17(a), the Josephson currents at the junctions will be opposite as well, since j_s is odd under mirror symmetry of vector $\hat{n}$. This leads to destructive interference in the critical current. On the other hand, in a GLB device where the normal vectors of the junctions point in the same direction, from Eq. 1.75 one expects constructive interference in the critical current. Interestingly, what has been reported in experiments agrees well with the previous analysis. Fig. 1.17(b) shows a minimum in the critical current for a GLB experiment with the two Josephson junctions opposite to each other (see the small inset for a depiction). The minimum is not localized exactly at zero field due to minor issues with trapped vortices and self-inductance of the device. On the other hand, for the GLB experiment with two junctions pointing in the same direction [see Fig. 1.17(c)], the maximum of the critical current remains close to zero, within the accuracy of the experiment, thus confirming the constructive interference. These two interference patterns then prove that the superconductivity in SRO is of the spin-triplet type.

Time reversal symmetry

Another interesting experiment that shed light on the unconventional properties of SRO is the test of time-reversal symmetry (TRS), carried out with the muon-spin relaxation (μSR) technique [52]. Muons are fundamental particles that decay into one positron and two neutrinos. In a μSR experiment muons are implanted in a sample and after they decay the positrons are registered in a detector [see Fig. 1.18(a)]. The positrons, which carry information about the magnetic order inside the sample, are statistically analyzed, and for the case of SRO they revealed the existence of a magnetic distribution at zero external field and for the two polarizations of the muons ($P_\mu \parallel c$ and $P_\mu \perp c$) [see Fig. 1.18(b) and (c)]. This means that the TRS is broken, since spontaneous magnetic fields arise when this symmetry breaks. Another experiment that confirmed the breaking of TRS in SRO

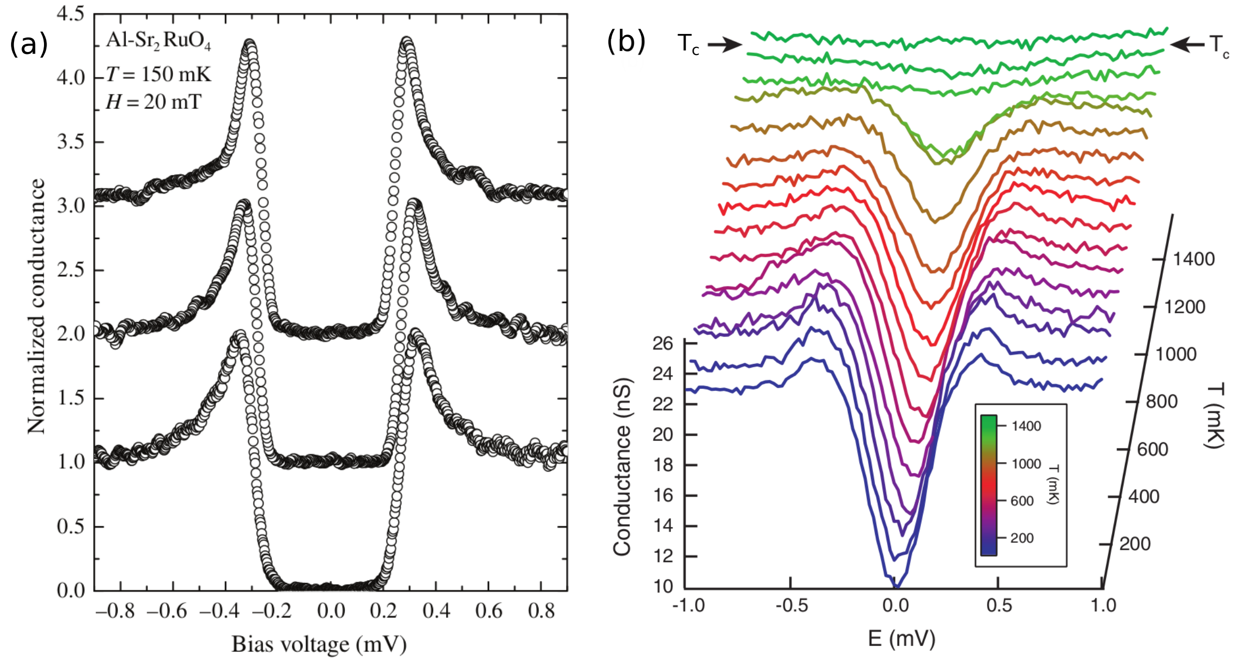

Figure 1.19: (a) Tunneling conductance in SRO as a function of the bias voltage for different positions of the STM tip over the sample. From Ref. [54]. (b) Differential conductance in SRO as a function of the bias voltage, and for temperatures between 200 mK and 1.5 K. From Ref. [55].

exploited the effect that samples with broken TRS have on circularly polarized beams of light, the magneto-optical Kerr effect [53]. To date the experiments with the μSR and the Kerr effect remain the most convincing evidence of TRS breaking in SRO.

Gap structure

It was discussed in Sec. 1.5.1 that the linear dependence of λ^{-2} with T at low temperatures was a consequence of a line node in the superconducting gap. Another physical quantity that reveals the existence of a line node in the superconducting gap is the specific heat. At low temperatures the dependence of the specific heat is exponential for nodeless superconducting gaps, while for superconductors with line nodes is that of a power law. The physical quantity that is behind the temperature dependence of penetration depth and the specific heat is the quasiparticle density of states (DOS). In superconductors the DOS can be directly measured with STM or point contact tunneling microscopy. For strontium ruthenate the STM measurements found in the literature seem to be contradictory. While Ref. [54] reported a nodeless, or equivalently a fully open, superconducting gap, Ref. [55] indicated the existence of a linear node or a near node in the superconducting gap of SRO [see Figs. 1.19(a) and (b)]. These two reports of STM measurements are therefore inconclusive about the gap structure in SRO and more studies are required, or another experiment where valuable information of the DOS can be obtained indirectly.

The evidence available to date about SRO indicates that it is an unconventional superconductor of the spin-triplet type, which apparently breaks TRS. The breaking of TRS is a controversial issue, since its manifestation has not been confirmed in any of the magnetic imaging experiments carried out to date [59–62]. Faced with this worrying history and the inconclusive results with STM, measurements of the penetration depth and the specific heat appear to indicate a depletion rather than a supression in the superconducting gap. In Fig. 1.20(a), the dependence of λ^{-2} with T, at low temperatures, shows that the superconducting gap in SRO is neither of a conventional BCS superconductor (s-wave), nor of a superconductor with line nodes (d-wave). The specific heat measurements of SRO, shown in Fig. 1.20(b), present similar conclusions. The behavior of the gap in SRO is not

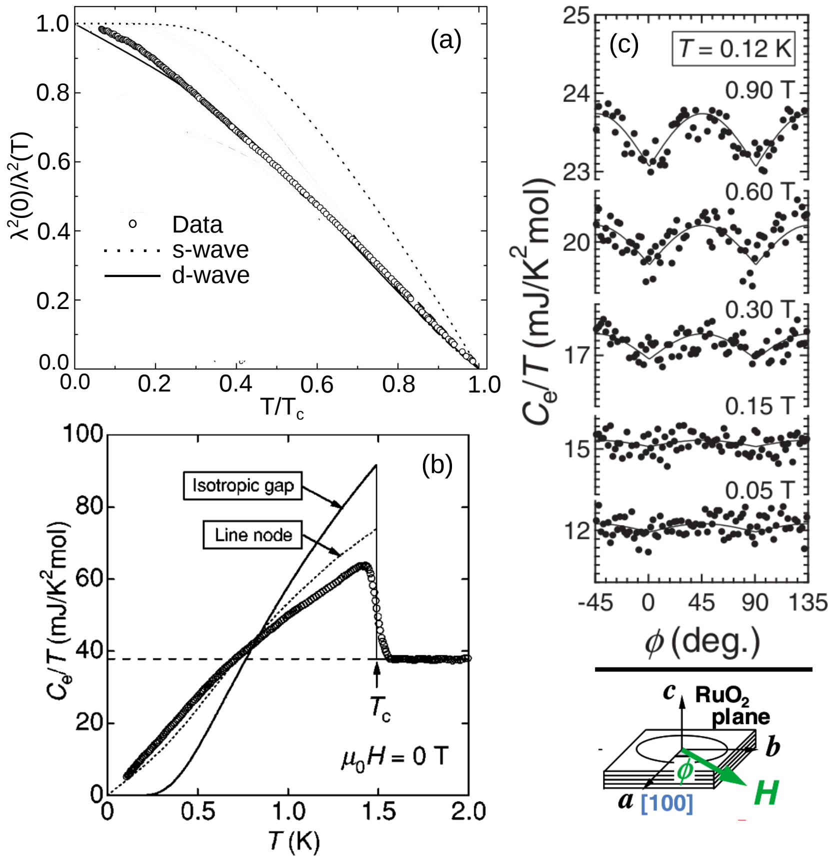

Figure 1.20: (a) For strontium ruthenate (SRO), the inverse square of the penetration depth (λ^{-2}) shows that the superconducting gap is neither of a conventional BCS (s-wave) superconductor, nor of a superconductor with line nodes (d-wave). Adapted from Ref. [56]. (b) Temperature dependence of the specific heat for SRO. At low temperatures the behavior is not exactly of an isotropic gap, neither of a gap with line nodes. From Ref. [57]. (c) Specific heat measurements depending on the orientation of the magnetic field, revealing an oscillating behavior with the polar angle ϕ that can be well fitted with the function $f_4(\phi) = 2|\sin 2\phi| - 1$. From Ref. [58].

exactly of an isotropic gap, neither of a gap with line nodes. In that respect, measurements of the field-orientation-dependent specific heat go further in this dichotomy, and suggest an anisotropic gap with a mininum along the crystallographic [100] direction [58, 63]. At values of H between 0.15 T and 0.90 T, Fig. 1.20(c) shows four-fold oscillations in the specific heat, well described by the function $f_4(\phi) = 2|\sin 2\phi| - 1$, that imply the emergence of a modulated superconducting gap in the γ band [58]. On the other hand, below 0.15 T the field dependence of the specific heat, not shown in the figure but presented in Ref. [58], reveals superconducting order in the α and β bands. That superconducting order is passive, being induced by the γ band. Thus, the field-orientation-dependent specific heat measurements indicate multiband superconductivity in SRO. More works are expected in the future to corroborate these findings.

The 3K phase

Single crystals of SRO are grown by the floating-zone method [57]. The onset of superconductivity in crystals with the lowest concentration of imperfections is found at temperature of 1.5 K. To date the majority of experiments reported in the literature have been conducted in crystals with dimensions in the mm scale. Thin films of SRO appear difficult to synthesize. Only one work has reported the fabrication of a thin film to date [64]. The ubiquitous presence of disorder in SRO was demonstrated to affect the superconducting properties. For example, in crystals where Ru atoms are

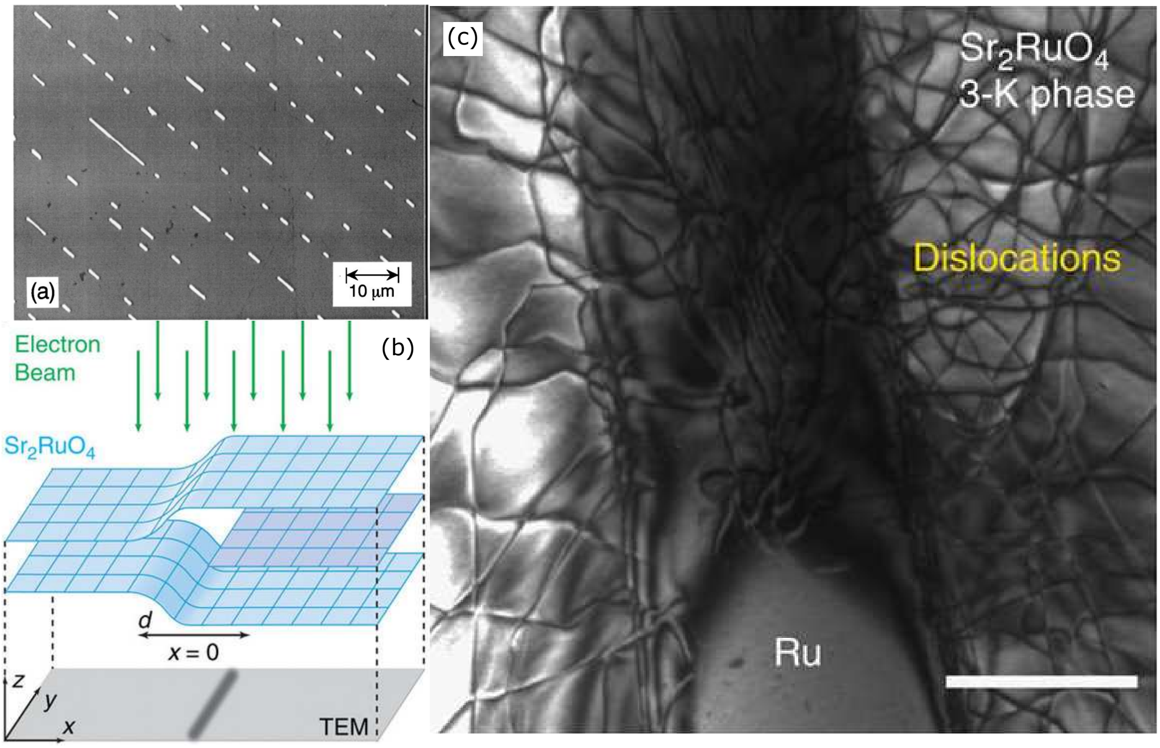

Figure 1.21: (a) Crystalline islands of Ru embedded in a matrix of strontium ruthenate. The islands appear bright. The islands of Ru form a periodic pattern characteristic of eutectic solidification. From Ref. [65]. (b) In strontium ruthenate two adjacent layers of RuO are dislocated by the insertion of a third one. The dislocation appears as a dark line in transmission electron microscopy (TEM). (c) TEM image of strontium ruthenate showing a crystalline islands of Ru and a large number of dislocations. From Ref. [68].

in excess, the T_c is twice larger and the superconducting properties are substantially changed [65]. This new phase, known as the 3K phase, was shown later to be composed by crystalline islands of Ru embedded in SRO. The islands of Ru form a periodic pattern characteristic of eutectic solidification [see Fig. 1.21(a)]. Despite of a couple of theoretical works explaining the origin of the 3K phase [66, 67], there are some features that remain unsolved. Thus, more extensive works providing an unifying explanation of the reported phenomena are expected.

Another type of imperfection in SRO forms when two adjacent layers of RuO are dislocated by a third one, as shown in Fig. 1.21(b). These dislocations break the symmetry of the crystal and simultaneously increase the critical temperature up to about twice the bulk T_c [68]. The dislocations appear in transmission electron microscopy (TEM) as dark lines owing to the peculiar scattering of electrons. Dislocations and crystalline islands of Ru are simultaneously found in SRO [see Fig. 1.21(c)]. Both imperfections reveal an increase in the critical temperature. A fact that demonstrates the superconductivity in SRO is unconventional since this behavior is expected in spin triplet superconductors, known to have multi-component order parameters.

1.5.3 Topological superconductors

In conventional (s-wave) superconductors the superconducting gap is isotropic in the phase space. That means that in order to destroy Cooper pairs, or conversely create quasiparticle states, one needs to provide the condensate with an energy at least greater than Δ for all the possible directions of the wave vector k [see the top panels of Fig. 1.22]. In topological superconductors a gap also exists, like in the conventional case, but it is limited to the bulk of the sample [69, 70]. At the edges of the sample the gap vanishes and allows the formation of surface bound states having a linear dispersion

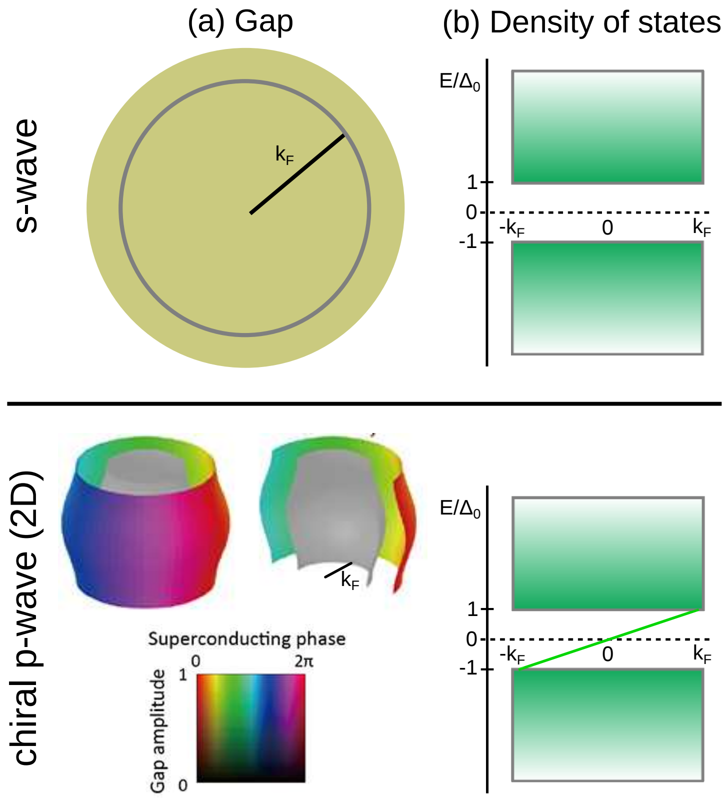

Figure 1.22: (a) Comparison of the superconducting gaps for (i) the conventional BCS case [top panel], and (ii) the 2D chiral p-wave case [bottom panel]. The Fermi surface in both cases is shown in gray. (b) Comparison of the corresponding density of states.

relation in the energy as shown in Fig. 1.22(b) (bottom panel) [71, 72]. The phenomenon is similar to that of topological insulators, which behave as insulators in the bulk of the sample and as metals at the edges [73]. However, the two phenomena are noteworthy different, since the nature of the gap in two cases is completely distinct.

One of the archetypal examples of topological superconductivity is the model for spinless (spin polarized) p-wave superconductors, which besides of breaking the time-reversal symmetry is known as the chiral p-wave model [69]. The bottom panel of Fig. 1.22(a) shows the gap corresponding to this model for a cylindrical Fermi surface. The chiral p-wave model differs from the spinfull case (known as helical), which is the archetypal example of a time-reversal-symmetric topological superconductor. The edge states in these cases are different. While in the helical superconductors two counterpropagating modes exist, with the spin of the quasiparticles locked perpendicular to the direction of motion, in the chiral case only one mode exists (owing to the break of TRS) [73]. Fig. 1.23(a) shows the differences between chiral and helical superconductivity, as well as the comparison with the quantum/quantum-spin Hall effect (QH/QSH). The edge states in the chiral p-wave model have spontaneous magnetic fields [76, 77], and in finite samples these fields should be detectable with the state-of-the-art magnetic probes. However, none of these spontaneous fields have been directly detected in SRO, the leading candidate to have chiral p-wave superconductivity [59–62], although the edge states have been measured in tunneling spectroscopy [78]. To explain the discrepancies between theory and experiment in SRO many works have considered the effects of multigap superconductivity [55, 79–81], disorder [82], and “robustness” [83, 84], on the edge states, but consensus has not been reached yet. On the other hand, STM measurements have recently detected edge states, but in a hybrid device rather than in a bulk superconductor [74]. The device consisted of magnetic Co adatoms forming a cluster under the surface of a s-wave superconductor, monolayer Pb on Si [see Fig. 1.23(b)]. Owing to the Zeeman field created by the Co cluster, the superconductivity in

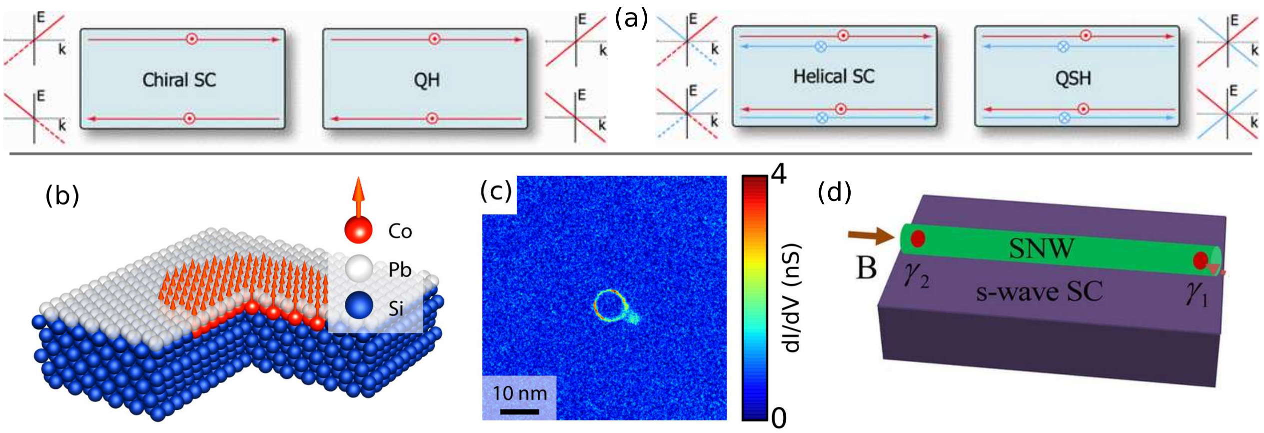

Figure 1.23: (a)Analogies between chiral/helical superconductors (SC), and the quantum/quantum-spin Hall effect (QH/QSH). Despite of the similarities of the edge states in the topological superconductors and the quantum Hall systems, the fact that in the former the particle-hole symmetry is present and in the latter not, makes them crucially different. From Ref. [73]. (b) Magnetic adatoms (Co) deposited on the surface of a monolayer of Pb grown on top of Si. (c) Conductance map over the hybrid device of panel (b) showing the experimental observation of the edge states of a topological superconductor. From Ref. [74]. (d) Semiconductor nanowire situated on top of a conventional s-wave superconductor. This hybrid device is predicted to realize p-wave superconductivity, where two Majorana quasiparticles emerge at the edges of the nanowire. From Ref. [75].

the monolayer of Pb/Si becomes topological. The edge states are shown in Fig. 1.23(c) in the conductance map of the hybrid device.

The search for topological superconductivity in materials without the need of any external drive (bulk TS), or in hybrid structures where topological superconductivity can be induced [85–88], is motivated by the prediction of Majorana quasiparticles [70]. These are excitations that resemble the particle introduced by the Italian physicist Ettore Majorana [89], and which has the exotic characteristic of being its own antiparticle. One hybrid device presenting topological superconducting order is shown in Fig. 1.23(d). The figure depicts a semiconductor nanowire situated on top of a conventional$s$-wave superconductor. The combination of the superconducting proximity effect, strong spin-orbit coupling in the nanowire, and an external magnetic field, results in the emergence of p-wave superconducting order in the nanowire [86, 87]. This system can be described according to the Kitaev model, where Majorana quasiparticles are demonstrated to exist at their two edges [90].

Majorana quasiparticles are predicted to exist in the cores of vortices of chiral p-wave superconductors [91, 92]. The energy of a Majorana quasiparticle is zero due to its duality between particle and antiparticle [69]. In 2D, Majorana quasiparticles present statistical properties distinctly different from those of fermions. For example, when two fermions (bosons) are interchanged they acquire a phase $e^{i\theta}$, where $\theta = \pi$ ($\theta = 0$). Strictly speaking, the interchange affects the quantum state of the pair ($|\psi_1\psi_2\rangle$) yielding $|\psi_1\psi_2\rangle = e^{i\theta}\,|\psi_2\psi_1\rangle$. For a set of degenerate Majorana quasiparticles the phase becomes a matrix and the statistics that stems from this peculiar phase is non-Abelian [91]. That implies that interchanging Majorana quasiparticles changes the state of the system in a way that depends only on the way that the exchange is executed. The importance of the realization of Majorana quasiparticles in a topological superconductor relies on the aplication of its non-Abelian statistical property to provide a set of robust quantum gates with topological protection [91–93]. Such gates are crucial for fault-tolerant quantum computation. Therefore, topological superconductivity is an active research field with outlooks that if materialized could revolutionize the technology as we know today.

1.6 Organization and contribution of the thesis

As discussed above, superconducting pairing is not solely of the s-wave type. There is a large number of unconventional superconductors being investigated by the broad community, and interested in unraveling novel phenomena with potential applications to technology. One of those examples is strontium ruthenate, the spin-triplet superconductor that breaks time-reversal symmetry (TRS), and in which evidence suggests the symmetry of the gap is of the chiral p-wave type. Interestingly, this type of gap is proven to be the archetypal example of a topological superconductor breaking TRS. This feature draws a lot of interest since zero-energy modes (the condensed matter equivalent of Majorana fermions) are predicted to emerge in the cores of vortices of chiral p-wave superconductors. Such and similar predictions form the bridge between unconventional superconductivity and technological applications owing to the idea of using Majorana fermions to build a fault-tolerant quantum computer. However, the materialization of a quantum computer based on the unconventional superconductivity of SRO is yet to be confirmed since the spontaneous magnetic fields predicted to exist in this superconductor due to TRS breaking have remained elusive so far.

In this thesis, we study chiral p-wave superconductivity to reveal the novel superconducting configurations that emerge in mesoscopic samples, where confinement is of particular importance. Furthermore, we discuss how the revealed magnetic, electronic and electric properties of the states reported in this thesis facilitate the identification of chiral p-wave superconductivity in a candidate material. These features, namely the magnetic profile, the density of states, and the voltage-current characteristic, can be compared with results from Hall probe microscopy, scanning tunneling microscopy, and resistance measurements. The approach used in this thesis comprises the phenomenological Ginzburg-Landau theory and the microscopic Bogoliubov-de Gennes formalism. Since we consider single band superconductivity, the phenomenological and microscopic theories employed in this thesis are a minimal model of unconventional superconductivity in SRO. More elaborated models for SRO, including superconducting order in multi-bands, have been recently proposed. However, consensus in this respect has not been reached yet.

The thesis is organized as follows.

In **chapter** 1, we present an introduction to superconductivity, where we described its main properties and two fundamental theories, one phenomenological (Ginzburg-Landau) and one microscopic (Bardeen-Cooper-Schrieffer). Next, we presented an overview of mesoscopic superconductivity where the dimensions of the sample are comparable to the characteristic length scales ξ and λ. Finally, we concluded the chapter with a brief description of superconductors that do not obey the conventional picture of the original Bardeen-Cooper-Schrieffer (BCS) theory, i.e. the unconventional superconductors.

In **chapter** 2, we employ the mean-field approach to calculate the BCS Hamiltonian of spin-triplet superconductivity. Then, we derive the corresponding Bogoliubov-de Gennes (BdG) equations which later on are required for the calculations in the specific case of chiral p-wave superconductivity. Finally, the phenomenological theories for three cases of unconventional superconductivity are obtained using group theory analyses and the self-consistent equations for the superconducting gap. Among the cases considered, there exist two that break the time-reversal symmetry (chiral p-wave and $s+id$-wave), and one that preserves it ($d+s$-wave).

In **chapter** 3, we describe the numerical methods used in this thesis to solve the BdG and the Ginzburg-Landau (GL) equations of chiral p-wave superconductivity. The description of the algorithm that solves the phenomenological equations for the $d+s$ and $a+id$ types of superconductivity is also provided.

In **chapter** 4, we solve the GL equations for mesoscopic chiral p-wave superconducting samples in absence of any applied magnetic field. We reveal stable multichiral states with domain walls separating regions with different chiralities, as well as monochiral states with spontaneous currents flowing along the edges. The effect of confinement on these states is investigated - we show that it provides stabilization to the multichiral states, but at the same time it can overshadow the magnetic signatures characteristic of chiral domain walls.

In **chapter** 5, we continue investigating mesoscopic chiral p-wave superconducting samples with the GL theory, but this time with an out-of-plane applied magnetic field. The states that we obtain at finite magnetic field are composed of several unique configurations of conventional vortices, edge states and skyrmions, all of them identified not only by their magnetic signatures, but also by their topological properties. Moreover, the reconfiguration of the states with varied magnetic field and the anisotropy parameters of the Fermi surface is also discussed. Finally, novel temporal and field-induced transitions between vortical and skyrmionic states reveal the remarkable role that confinement has on the stabilization of states, but also on the reported novel transitions.

In **chapter** 6, motivated by the stabilization of skyrmions reported in chapter 5, we solve the self-consistent BdG equations of chiral p-wave superconductivity, and show the electronic properties of the reported states, namely edge states, conventional vortices, and skyrmions. We reveal the link between the local density of states (LDOS) of the novel topological states and the behavior of the domain wall that separates regions with different chiralities, enabling direct identification of those states in scanning tunneling microscopy. Finally, the magnetic field and temperature dependence of the properties of a skyrmion show that this topological defect can be surprisingly large in size, and can be pinned by an artificially indented non-superconducting closed path in the sample, thus facilitating the experimental observation of skyrmionic states.

In **chapter** 7, we investigate the dynamic response of the topological states reported in chapters 4 and 5 to an external applied current. Using the time-dependent GL equations we obtain voltage-current characteristics for nano-bridges of chiral p-wave superconductors that enable us to reveal new fingerprints for the identification of these novel topological states.

Finally we conclude the thesis in **chapter** 9 and present an outlook for future studies.

2

Theories of chiral p-wave superconductivity

2.1 BCS theory of spin-triplet superconductors

The generalization of the reduced Hamiltonian for spin-singlet Cooper pairs to the spin-dependent case reads [94, 95],

$$\mathscr{H} = \sum_{\mathbf{k},s} \xi_{\mathbf{k}} c^{\dagger}_{\mathbf{k}s} c_{\mathbf{k}s} + \frac{1}{2} \sum_{\mathbf{k},\mathbf{k}'} \sum_{s_1,s_2,s_3,s_4} V_{\mathbf{k},\mathbf{k}';\,s_1,s_2,s_3,s_4} c^{\dagger}_{\mathbf{k}s_1} c^{\dagger}_{-\mathbf{k}s_2} c_{-\mathbf{k}'s_3} c_{\mathbf{k}'s_4}, \tag{2.1}$$

where, unlike in Eq. (1.52), $V_{\mathbf{k},\mathbf{k}';\,s_1,s_2,s_3,s_4}$ is a spin-dependent atractive potential defined within an energy range around the Fermi surface E_{F} by a cutoff ε_c, i.e. $V_{\mathbf{k},\mathbf{k}';\,s_1,s_2,s_3,s_4}$ is nonzero for $-\varepsilon_c < \xi_{\mathbf{k}}, \xi_{\mathbf{k}'} < \varepsilon_c$, and $\varepsilon_c \ll E_{\mathrm{F}}$. The spin subindices s_i, with $i = 1 - 4$, are either $\uparrow$ or $\downarrow$. Moreover, this potential satisfies the following properties, owing to the fermionic anticommutation rules of the creation and annihilation operators,

$$V_{\mathbf{k},\mathbf{k}';\,s_1,s_2,s_3,s_4} = -V_{-\mathbf{k},\mathbf{k}';\,s_2,s_1,s_3,s_4} = -V_{\mathbf{k},-\mathbf{k}';\,s_1,s_2,s_4,s_3} = V_{-\mathbf{k},-\mathbf{k}';\,s_2,s_1,s_4,s_3}. \tag{2.2}$$

The Hamiltonian of Eq. (2.1) is treated within the mean field approach, where the products of two creation and annihilation operators are replaced by the following mean values plus a small deviation, denoted in parentheses,

$$\begin{aligned} c_{-\mathbf{k}'s_3} c_{\mathbf{k}'s_4} &= b_{\mathbf{k}',s_3s_4} + \left\{ c_{-\mathbf{k}'s_3} c_{\mathbf{k}'s_4} - b_{\mathbf{k}',s_3s_4} \right\}, \\ c^{\dagger}_{\mathbf{k}s_1} c^{\dagger}_{-\mathbf{k}s_2} &= b^{*}_{\mathbf{k},s_2s_1} + \left\{ c^{\dagger}_{\mathbf{k}s_1} c^{\dagger}_{-\mathbf{k}s_2} - b^{*}_{\mathbf{k},s_2s_1} \right\}. \end{aligned} \tag{2.3}$$

The following correlation function has been introduced in last equations,

$$b_{\mathbf{k},ss'} = \langle c_{-\mathbf{k}s} c_{\mathbf{k}s'} \rangle\,, \tag{2.4}$$

with $\langle\, A \,\rangle$ denoting the statistical average $\mathrm{tr}[e^{-\beta\mathscr{H}} A]/\mathrm{tr}[e^{-\beta\mathscr{H}}\,]$, and $\beta = 1/k_{\mathrm{B}}T$. The effective or BCS Hamiltonian resulting from Eq. (2.1) after the mean-field treatment reads [94, 95],

$$\begin{aligned}\mathscr{H}_{\text{eff}} &= \sum_{\mathbf{k},s} \xi_{\mathbf{k}} c^{\dagger}_{\mathbf{k}s} c_{\mathbf{k}s} + \frac{1}{2}\sum_{\mathbf{k},s_1 s_2}\left[\Delta_{\mathbf{k},s_1 s_2} c^{\dagger}_{\mathbf{k}s_1} c^{\dagger}_{-\mathbf{k}s_2} - \Delta^{*}_{-\mathbf{k},s_1 s_2} c_{-\mathbf{k}s_1} c_{\mathbf{k}s_2}\right] \\ &- \frac{1}{2}\sum_{\mathbf{k},s_1 s_2} \Delta_{\mathbf{k},s_1 s_2} b^{*}_{\mathbf{k},s_2 s_1},\end{aligned} \tag{2.5}$$

where

$$\Delta_{\mathbf{k},ss'} = \sum_{\mathbf{k}',s_3 s_4} V_{\mathbf{k},\mathbf{k}';s,s',s_3,s_4} b_{\mathbf{k}',s_3 s_4}, \tag{2.6}$$

and

$$\Delta^{*}_{-\mathbf{k}',ss'} = -\sum_{\mathbf{k},s_1 s_2} V_{-\mathbf{k}',\mathbf{k};s,s',s_2,s_1} b^{*}_{\mathbf{k},s_2 s_1}. \tag{2.7}$$

Using the symmetry properties of the two-pair potential, Eq. (2.2), one can derive that the gap holds the following relation,

$$\Delta_{\mathbf{k},ss'} = -\Delta_{-\mathbf{k},s's}, \quad \text{or in matrix notation} \quad \widehat{\Delta}(\mathbf{k}) = -\widehat{\Delta}^{T}(-\mathbf{k}). \tag{2.8}$$

2.1.1 Parity of the superconducting gap

Since the superconducting gap is related to the correlation function of two electrons with zero total momentum [see Eqs. (2.4) and (2.6)], i.e. the Cooper pairs, one can decompose it into an orbital and a spin part. For the spin part, one finds two possibilites, namely singlet and triplet states. While the singlet state is asymmetric under the exchange of the spin indexes, the triplet state is symmetric. These two states read

$$|\text{Singlet}\rangle = \frac{1}{\sqrt{2}}(|\uparrow\downarrow\rangle - |\downarrow\uparrow\rangle), \tag{2.9}$$

$$|\text{Triplet}\rangle = \begin{cases} |\uparrow\uparrow\rangle \\ \frac{1}{\sqrt{2}}(|\uparrow\downarrow\rangle + |\downarrow\uparrow\rangle) \\ |\downarrow\downarrow\rangle \end{cases}. \tag{2.10}$$

On the other hand, in the orbital part there are also two possible states with a well defined symmetry, namely the parity. These states are the odd and the even parity states and their properties are [94],

$$\psi(\mathbf{k}) = \psi(-\mathbf{k}), \qquad \text{for the even case}, \tag{2.11}$$

and

$$\mathbf{d}(\mathbf{k}) = -\mathbf{d}(-\mathbf{k}), \qquad \text{for the odd case}. \tag{2.12}$$

In order to satisfy the Pauli principle the superconducting gap has to be antisymmetric under particle interchange. This is achieved by the combination of a singlet and an even parity state, or a triplet and an odd parity state. In the literature, the spin-singlet and even-parity superconductivity, as well as spin-triplet and odd-parity superconductivity, are terms which are used interchangeably.

To sum up, the superconducting gap satisfies the following properties,

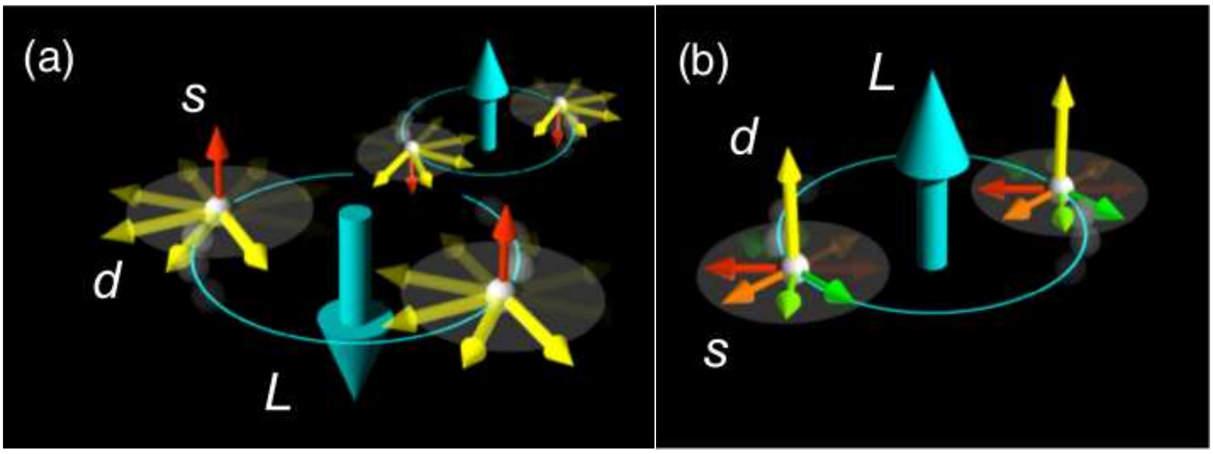

Figure 2.1: Orientations of the $\mathbf{d}$ vector, the spins of the Cooper pairs, and the angular momentum ($\mathbf{L}$), in spin-triplet superconductors. The spins of the Cooper pairs are defined orthogonally to the direction of $\mathbf{d}$. (a) The $\mathbf{d}$ vector is orthogonal to vector $\mathbf{L}$. (b) The $\mathbf{d}$ vector is parallel to vector $\mathbf{L}$. From Ref. [96].

$$\Delta_{\mathbf{k},ss'} = -\Delta_{-\mathbf{k},s's} = \begin{cases} \Delta_{-\mathbf{k},ss'} = \Delta_{\mathbf{k},ss'}, & \text{even parity,} \\ \Delta_{-\mathbf{k},ss'} = -\Delta_{\mathbf{k},ss'}, & \text{odd parity,} \end{cases} \tag{2.13}$$

which lead to the following parametrizations of the gap, useful to dinstinguish the even and odd parity states, respectively,

$$\widehat{\Delta}_{\mathbf{k}} = \begin{pmatrix} \Delta_{\mathbf{k},\uparrow\uparrow} & \Delta_{\mathbf{k},\uparrow\downarrow} \\ \Delta_{\mathbf{k},\downarrow\uparrow} & \Delta_{\mathbf{k},\downarrow\downarrow} \end{pmatrix} = \begin{pmatrix} 0 & \psi(\mathbf{k}) \\ -\psi(\mathbf{k}) & 0 \end{pmatrix} = i\hat{\sigma}_y\psi(\mathbf{k}), \tag{2.14}$$

and

$$\begin{aligned} \widehat{\Delta}_{\mathbf{k}} &= \begin{pmatrix} \Delta_{\mathbf{k},\uparrow\uparrow} & \Delta_{\mathbf{k},\uparrow\downarrow} \\ \Delta_{\mathbf{k},\downarrow\uparrow} & \Delta_{\mathbf{k},\downarrow\downarrow} \end{pmatrix} \\ &= \begin{pmatrix} -d_x(\mathbf{k})+id_y(\mathbf{k}) & d_z(\mathbf{k}) \\ d_z(\mathbf{k}) & d_x(\mathbf{k})+id_y(\mathbf{k}) \end{pmatrix} = i\big(\mathbf{d}(\mathbf{k})\cdot\hat{\sigma}\big)\hat{\sigma}_y. \end{aligned} \tag{2.15}$$

In last equations $\psi(\mathbf{k})$ and $\mathbf{d}(\mathbf{k})$ are even scalar and odd vectorial functions. Moreover, the plane where the spins in the triplet pairing case lie is defined orthogonally to the direction of $\mathbf{d}(\mathbf{k})$ [57,96]. Fig. 2.1 illustrates two cases of the orientations taken by the $\mathbf{d}$ vector and the spins of the Cooper pair. In Fig. 2.1(a), the $\mathbf{d}$ vector is in-plane (denoted by yellow arrows), while the spins are out-of-plane (denoted by red arrows). In Fig. 2.1(b) the case is the opposite, where the $\mathbf{d}$ vector is out-of-plane, and the spins are in-plane. Vector $\mathbf{L}$, denoted by the largest arrow in the figure, is the orbital angular momentum and in both cases is out-of-plane. If the spin-triplet superconductor under consideration possesses a layered structure, vector $\mathbf{L}$ is perpendicular to the layers.

Defining the square magnitude of the gap as half the trace of the matrix product, i.e. $|\widehat{\Delta}_{\mathbf{k}}|^2 = \frac{1}{2}\mathrm{tr}(\widehat{\Delta}_{\mathbf{k}}\widehat{\Delta}_{\mathbf{k}}^{\dagger})$, one obtains for the even parity and odd parity states,

$$\begin{aligned} \widehat{\Delta}_{\mathbf{k}}\widehat{\Delta}_{\mathbf{k}}^{\dagger} &= |\psi(\mathbf{k})|^2\hat{\sigma}_0, \\ \widehat{\Delta}_{\mathbf{k}}\widehat{\Delta}_{\mathbf{k}}^{\dagger} &= |\mathbf{d}|^2\hat{\sigma}_0 + i(\mathbf{d}\times\mathbf{d}^*)\cdot\hat{\sigma}. \end{aligned} \tag{2.16}$$

Note that for the even and for certain odd parity states the last matrix product is proportional to σ_0. In literature these types of states are widely known as unitary pairing states. On the other

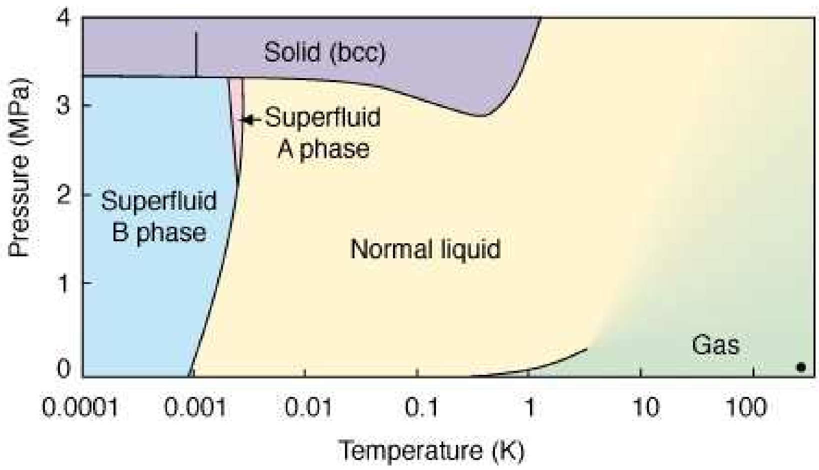

Figure 2.2: Phase diagram of ^{3}He showing two superfluid phases, namely A (Anderson-Brinkmann-Morel), and B (Balian-Werthamer).

hand, the states with $\mathbf{d}^* \neq \mathbf{d}$ are known as non-unitary states since the product $\widehat{\Delta}_{\mathbf{k}}\widehat{\Delta}^{\dagger}_{\mathbf{k}}$ is no longer proportional to σ_0 [57, 94–96]. In what follows, some examples of odd parity states, unitary and non-unitary, will be presented.

Balian-Werthamer state

^{3}He is an isotope of helium having two protons and one neutron [95]. Due to the odd number of fermions that compose it, ^{3}He is a fermion, unlike ^{4}He (or helium) which is a boson due to its two protons and two neutrons. Helium is widely known for its superfluid properties at low temperatures that stems from its bosonic properties. However, and despite of its fermionic nature, ^{3}He is also a superfluid at extremely low temperatures and high pressures [95]. The superfluidity in helium relies roughly on the Bose-Einstein condensation, meanwhile in ^{3}He it relies on the instability of the Fermi surface towards the formation of Cooper pairs.

In Fig. 2.2 the pressure vs. temperature diagram of bulk ^{3}He shows two superfluid phases, namely the A or Anderson-Brinkmann-Morel (ABM) phase, and the B or Balian-Werthamer (BW) phase. The superfluid gap in the BW phase is represented in the d-vector notation by [31, 95],

$$\mathbf{d}(\mathbf{k}) = \frac{\Delta_0}{k_{\mathrm{F}}}(\hat{\mathbf{x}}k_x + \hat{\mathbf{y}}k_y + \hat{\mathbf{z}}k_z), \tag{2.17}$$

where k_{F} is the Fermi wave vector, and where the corresponding magnitude of the gap is,

$$|\widehat{\Delta}_{\mathbf{k}}|^2 = \frac{1}{2}\mathrm{tr}\big(\widehat{\Delta}_{\mathbf{k}}\widehat{\Delta}^{\dagger}_{\mathbf{k}}\big) = |\Delta_0|^2, \tag{2.18}$$

meaning that the BW phase is fully gapped in its phase space.

Anderson-Brinkmann-Morel state

Another example of a unitary state of odd parity is provided by the superfluid ABM phase of ^{3}He. In this phase the corresponding d-vector is [31, 95],

$$\mathbf{d}(\mathbf{k}) = \frac{\Delta_0}{k_{\mathrm{F}}}\hat{\mathbf{z}}(k_x \pm ik_y), \tag{2.19}$$

and the magnitude of the gap becomes

$$|\widehat{\Delta}_{\mathbf{k}}|^2 = \frac{1}{2}\mathrm{tr}\left\{\frac{|\Delta_0|^2}{k_{\mathrm{F}}^2}|k_x \pm ik_y|^2\hat{\sigma}_0\right\} = |\Delta_0|^2\sin^2\theta. \tag{2.20}$$

This gap has point nodes at $\mathbf{k} = (0, 0, \pm 1)$, and a finite orbital angular momentum along the $\hat{z}$ direction [31], from which originates its widely used label as a chiral p-wave state.

Non-unitary state

One example of a non-unitary state in odd parity superconductivity is given within the d-vector representation as,

$$\mathbf{d}(\mathbf{k}) = \frac{\Delta_0}{k_{\mathrm{F}}}(\hat{\mathbf{x}} - i\hat{\mathbf{y}})k_z, \tag{2.21}$$

with the corresponding gap

$$\widehat{\Delta}_{\mathbf{k}} = \frac{2\Delta_0}{k_{\mathrm{F}}}\begin{pmatrix} 0 & 0 \\ 0 & k_z \end{pmatrix}. \tag{2.22}$$

Comparing last equation and Eq. (2.15) one can see that this state has pairing only in the spin down-down channel, so it is an example of a spin-polarized coupling state.

The phase diagram of ^{3}He confined to mesoscopic scales differs from the phase diagram of bulk ^{3}He. The main feature that appears in the diagram is the stabilization of more phases between the bulk BW and ABM phases [97]. The novel phases, possessing Cooper pairing different from the bulk phases, can be identified with nuclear magnetic resonance spectroscopy [97, 98].

2.1.2 The Bogoliubov-Valatin transformation in unitary states

Returning to the Hamiltonian of Eq. (2.5), one can write it in a more compact form useful to find the quasiparticle states of this Hamiltonian,

$$\begin{aligned}\mathscr{H} &= \frac{1}{2}\sum_{\mathbf{k}}(c^{\dagger}_{\mathbf{k}\uparrow}, c^{\dagger}_{\mathbf{k}\downarrow}, c_{-\mathbf{k}\uparrow}, c_{-\mathbf{k}\downarrow})\begin{bmatrix} \xi_{\mathbf{k}} & & \Delta_{\mathbf{k},\uparrow\uparrow} & \Delta_{\mathbf{k},\uparrow\downarrow} \\ & \xi_{\mathbf{k}} & \Delta_{\mathbf{k},\downarrow\uparrow} & \Delta_{\mathbf{k},\downarrow\downarrow} \\ \Delta^*_{\mathbf{k},\uparrow\uparrow} & \Delta^*_{\mathbf{k},\downarrow\uparrow} & -\xi_{\mathbf{k}} & \\ \Delta^*_{\mathbf{k},\uparrow\downarrow} & \Delta^*_{\mathbf{k},\downarrow\downarrow} & & -\xi_{\mathbf{k}} \end{bmatrix}\begin{pmatrix} c_{\mathbf{k}\uparrow} \\ c_{\mathbf{k}\downarrow} \\ c^{\dagger}_{-\mathbf{k}\uparrow} \\ c^{\dagger}_{-\mathbf{k}\downarrow} \end{pmatrix} \\ &+ K,\end{aligned} \tag{2.23}$$

where

$$K = \sum_{\mathbf{k}}\xi_{\mathbf{k}} - \frac{1}{2}\sum_{\mathbf{k},s_1s_2}\Delta_{\mathbf{k},s_1s_2}b^*_{\mathbf{k},s_2s_1}, \tag{2.24}$$

and where for convenience the subindex "eff" has been removed. The BCS Hamiltonian of the spin-dependent Hamiltonian of Eq. (2.1) thus becomes [94],

$$\mathscr{H} = \frac{1}{2}\sum_{\mathbf{k}}\mathbf{C}^{\dagger}_{\mathbf{k}}\hat{\mathcal{E}}_{\mathbf{k}}\mathbf{C}_{\mathbf{k}} + K, \tag{2.25}$$

where

$$\hat{\mathcal{E}}_{\mathbf{k}} = \begin{bmatrix} \xi_{\mathbf{k}}\hat{\sigma}_0 & \widehat{\Delta}_{\mathbf{k}} \\ \widehat{\Delta}^{\dagger}_{\mathbf{k}} & -\xi_{\mathbf{k}}\hat{\sigma}_0 \end{bmatrix}, \quad \text{and} \quad \mathbf{C}_{\mathbf{k}} = (c_{\mathbf{k}\uparrow}, c_{\mathbf{k}\downarrow}, c^{\dagger}_{-\mathbf{k}\uparrow}, c^{\dagger}_{-\mathbf{k}\downarrow})^T. \tag{2.26}$$

Seeking a vector transformation, namely $\widehat{U}_{\mathbf{k}}$, one can diagonalize the matrix $\tilde{\mathcal{E}}_{\mathbf{k}}$, simplifying the complexity of the bilinear form in the Hamiltonian (2.25). The matrix that represents this transformation introduces a new vector, namely $\mathbf{A}_{\mathbf{k}} = (a_{\mathbf{k}\uparrow}, a_{\mathbf{k}\downarrow}, a^{\dagger}_{-\mathbf{k}\uparrow}, a^{\dagger}_{-\mathbf{k}\downarrow})^T$, which is related to the old vector as

$$\mathbf{C}_{\mathbf{k}} = \widehat{U}_{\mathbf{k}} \mathbf{A}_{\mathbf{k}} \,. \tag{2.27}$$

If $\widehat{U}_{\mathbf{k}}$ is an unitary matrix, i.e. $\widehat{U}^{\dagger}_{\mathbf{k}} \widehat{U}_{\mathbf{k}} = \widehat{U}_{\mathbf{k}} \widehat{U}^{\dagger}_{\mathbf{k}} = \mathbb{1}$, the diagonalized Hamiltonian becomes

$$\widehat{E}_{\mathbf{k}} = \widehat{U}^{\dagger}_{\mathbf{k}} \hat{\mathcal{E}}_{\mathbf{k}} \widehat{U}_{\mathbf{k}}, = \begin{bmatrix} E_{\mathbf{k}+} & & & \\ & E_{\mathbf{k}-} & & \\ & & -E_{-\mathbf{k}+} & \\ & & & -E_{-\mathbf{k}-} \end{bmatrix}, \tag{2.28}$$

and the elements of the new four vector $\mathbf{A}_{\mathbf{k}}$ are identified as the generalization for spin-dependent superconductors of the Bogoliubov-Valatin operators [95]. Moreover, these new operators $a_{\mathbf{k}s}$ and $a^{\dagger}_{\mathbf{k}s}$ satisfy the same algebra as $c_{\mathbf{k}s}$ and $c^{\dagger}_{\mathbf{k}s}$, i.e. the transformation is canonical. The BCS Hamiltonian in a diagonal base therefore reads

$$\mathscr{H} = \sum_{\mathbf{k}} \mathbf{A}^{\dagger}_{\mathbf{k}} \widehat{E}_{\mathbf{k}} \mathbf{A}_{\mathbf{k}} + K, \tag{2.29}$$

where $\widehat{U}_{\mathbf{k}}$ is composed of four 2×2 submatrices,

$$\widehat{U}_{\mathbf{k}} = \begin{bmatrix} \hat{u}_{\mathbf{k}} & \hat{v}_{\mathbf{k}} \\ \hat{v}^{*}_{-\mathbf{k}} & \hat{u}^{*}_{-\mathbf{k}} \end{bmatrix}. \tag{2.30}$$

These submatrices, and the diagonal elements of $\widehat{E}_{\mathbf{k}}$, are calculated from the slightly modified Eq. (2.28), $[\widehat{U}_{\mathbf{k}} \widehat{E}_{\mathbf{k}} = \hat{\mathcal{E}}_{\mathbf{k}} \widehat{U}_{\mathbf{k}}]$, and the assumption of unitary pairing. They read

$$\hat{u}_{\mathbf{k}} = \frac{(E_{\mathbf{k}} + \xi_{\mathbf{k}})\hat{\sigma}_0}{\sqrt{2E_{\mathbf{k}}(E_{\mathbf{k}} + \xi_{\mathbf{k}})}}, \qquad \hat{v}^{*}_{-\mathbf{k}} = \frac{\Delta^{\dagger}_{k}}{\sqrt{2E_{\mathbf{k}}(E_{\mathbf{k}} + \xi_{\mathbf{k}})}}, \tag{2.31}$$

where $E_{\mathbf{k}+} = E_{\mathbf{k}-} = E_{\mathbf{k}} = \sqrt{\xi^2_{\mathbf{k}} + |\Delta_{\mathbf{k}}|^2}$, or in more elegant way,

$$E_{\mathbf{k}} = \sqrt{\xi^2_{\mathbf{k}} + \frac{1}{2}\mathrm{tr}\big(\widehat{\Delta}_{\mathbf{k}} \widehat{\Delta}^{\dagger}_{\mathbf{k}}\big)}. \tag{2.32}$$

With the expressions for the submatrices that compose matrix $\widehat{U}_{\mathbf{k}}$, the gap equation (Eq. 2.6) becomes

$$\Delta_{\mathbf{k},ss'} = \sum_{\mathbf{k}',s_3,s_4,\theta,\gamma} V_{\mathbf{k},\mathbf{k}';s,s',s_3,s_4} \left[u_{\mathbf{k}',\theta s_3} v_{\mathbf{k}',s_4\gamma} \langle a_{-\mathbf{k}'\theta} a^{\dagger}_{-\mathbf{k}'\gamma} \rangle - v_{\mathbf{k}',\theta s_3} u_{\mathbf{k}',s_4\gamma} \langle a^{\dagger}_{\mathbf{k}'\theta} a_{\mathbf{k}'\gamma} \rangle \right]. \tag{2.33}$$

Replacing the two statistical averages (the terms in brakets), by the Fermi distribution function $f(E_{\mathbf{k}}) = 1/(e^{\beta E_{\mathbf{k}}} + 1)$, yields

$$\langle a^{\dagger}_{\mathbf{k}'\theta} a_{\mathbf{k}'\gamma} \rangle = \delta_{\theta\gamma} f(E_{\mathbf{k}}), \qquad \langle a_{-\mathbf{k}'\theta} a^{\dagger}_{-\mathbf{k}'\gamma} \rangle = \delta_{\theta\gamma}(1 - f(E_{\mathbf{k}})) \tag{2.34}$$

and the gap equation reduces to

$$\Delta_{\mathbf{k},ss'} = -\sum_{\mathbf{k}',s_3,s_4} V_{\mathbf{k},\mathbf{k}';s,s',s_3,s_4} \frac{\Delta_{\mathbf{k}',s_4 s_3}}{2E_{\mathbf{k}'}} \tanh\left(\frac{E_{\mathbf{k}'}}{2k_{\mathrm{B}}T}\right), \tag{2.35}$$

where the fact that $\hat{u}_{\mathbf{k}}$ and $\hat{v}_{\mathbf{k}}$ commute has been used.

2.2 Bogoliubov-de Gennes equations

To describe inhomogeneous superconducting systems, one can use the equations derived by Bogoliubov and de Gennes, where a Schrödinger-like equation has to be solved for the space-dependent functions u and v, along with a self-consistency condition for the superconducting gap. In what follows, the derivation of these equations for spin-triplet superconductors is shown.

2.2.1 General case

Within the second quantization formalism, i.e. within the space defined by the field operators $\hat{\psi}^{\dagger}_{\alpha}(\mathbf{r})$ and $\hat{\psi}_{\beta}(\mathbf{r}')$, which satisfy the following algebra,

$$\begin{gathered}\hat{\psi}^{\dagger}_{\alpha}(\mathbf{r})\hat{\psi}_{\beta}(\mathbf{r}')+\hat{\psi}_{\beta}(\mathbf{r}')\hat{\psi}^{\dagger}_{\alpha}(\mathbf{r})=\delta_{\alpha\beta}\delta(\mathbf{r}-\mathbf{r}'),\\ \hat{\psi}_{\alpha}(\mathbf{r})\hat{\psi}_{\beta}(\mathbf{r}')+\hat{\psi}_{\beta}(\mathbf{r}')\hat{\psi}_{\alpha}(\mathbf{r})=\hat{\psi}^{\dagger}_{\alpha}(\mathbf{r})\hat{\psi}^{\dagger}_{\beta}(\mathbf{r}')+\hat{\psi}^{\dagger}_{\beta}(\mathbf{r}')\hat{\psi}^{\dagger}_{\alpha}(\mathbf{r})=0,\end{gathered} \tag{2.36}$$

the Hamiltonian for a system of fermions interacting through a pairwise potential $V^{(2)}_{\delta,\gamma,\alpha,\beta}(\mathbf{r},\mathbf{r}')$ reads [31]

$$\begin{aligned}\hat{H} &= \int d^3r\,\hat{\psi}^{\dagger}_{\alpha}(\mathbf{r})\mathscr{H}_0\hat{\psi}_{\alpha}(\mathbf{r})\\ &+ \frac{1}{2}\int\int d^3rd^3r'\hat{\psi}^{\dagger}_{\delta}(\mathbf{r})\hat{\psi}^{\dagger}_{\gamma}(\mathbf{r}')V^{(2)}_{\delta\gamma,\alpha,\beta}(\mathbf{r},\mathbf{r}')\hat{\psi}_{\alpha}(\mathbf{r}')\hat{\psi}_{\beta}(\mathbf{r}),\end{aligned} \tag{2.37}$$

where the pairwise potential remains invariant under particle interchange in order to satisfy the algebra of the field operators,

$$V^{(2)}_{\delta,\gamma,\alpha,\beta}(\mathbf{r},\mathbf{r}')=V^{(2)}_{\gamma,\delta,\beta,\alpha}(\mathbf{r}',\mathbf{r}). \tag{2.38}$$

Introducing the spin and space dependent correlation function,

$$b_{\alpha,\beta}(\mathbf{r}',\mathbf{r})=\langle\hat{\psi}_{\alpha}(\mathbf{r}')\hat{\psi}_{\beta}(\mathbf{r})\rangle\,, \tag{2.39}$$

and treating the interaction term within the mean field approach, i.e. replacing the product of two creation and annihilation operators by the respective correlation function plus a deviation term in parentheses,

$$\begin{aligned}\hat{\psi}_{\alpha}(\mathbf{r}')\hat{\psi}_{\beta}(\mathbf{r}) &= b_{\alpha,\beta}(\mathbf{r}',\mathbf{r})+\left\{\hat{\psi}_{\alpha}(\mathbf{r}')\hat{\psi}_{\beta}(\mathbf{r})-b_{\alpha,\beta}(\mathbf{r}',\mathbf{r})\right\},\\ \hat{\psi}^{\dagger}_{\delta}(\mathbf{r})\hat{\psi}^{\dagger}_{\gamma}(\mathbf{r}') &= b^{*}_{\gamma,\delta}(\mathbf{r}',\mathbf{r})+\left\{\hat{\psi}^{\dagger}_{\delta}(\mathbf{r})\hat{\psi}^{\dagger}_{\gamma}(\mathbf{r}')-b^{*}_{\gamma,\delta}(\mathbf{r}',\mathbf{r})\right\},\end{aligned} \tag{2.40}$$

one obtains the following effective many-body Hamiltonian after discarding second-order terms in the deriviation [31],

$$\begin{aligned}\hat{H}_{\text{eff}} &= \int d^3r\,\hat{\psi}^{\dagger}_{\alpha}(\mathbf{r})\mathscr{H}_0\hat{\psi}_{\alpha}(\mathbf{r})\\ &+ \frac{1}{2}\int\int d^3rd^3r'\left[\Delta_{\alpha\beta}(\mathbf{r},\mathbf{r}')\hat{\psi}^{\dagger}_{\alpha}(\mathbf{r})\hat{\psi}^{\dagger}_{\beta}(\mathbf{r}')+\Delta^{*}_{\alpha\beta}(\mathbf{r},\mathbf{r}')\hat{\psi}_{\beta}(\mathbf{r}')\hat{\psi}_{\alpha}(\mathbf{r})\right]\\ &- \frac{1}{2}\int\int d^3rd^3r'\Delta^{*}_{\beta\alpha}(\mathbf{r},\mathbf{r}')b_{\alpha,\beta}(\mathbf{r}',\mathbf{r}),\end{aligned} \tag{2.41}$$

where

$$\Delta^*_{\beta\alpha}(\mathbf{r},\mathbf{r}') = V^{(2)}_{\delta,\gamma,\alpha,\beta}(\mathbf{r},\mathbf{r}')b^*_{\gamma,\delta}(\mathbf{r}',\mathbf{r}), \tag{2.42}$$

and

$$\Delta_{\alpha\beta}(\mathbf{r},\mathbf{r}') = V^{(2)}_{\alpha,\beta,\delta,\gamma}(\mathbf{r},\mathbf{r}')b_{\delta,\gamma}(\mathbf{r}',\mathbf{r}). \tag{2.43}$$

After a straightforward calculation, one can show that owing to the Eqs. (2.36) and (2.38) the gap satisfies the following property,

$$\Delta_{\alpha\beta}(\mathbf{r},\mathbf{r}') = -\Delta_{\beta\alpha}(\mathbf{r}',\mathbf{r}). \tag{2.44}$$

Expanding the field operators as

$$\hat{\psi}_\alpha(\mathbf{r}) = \sum_{n,\beta} u_n(\mathbf{r})_{\alpha\beta}\hat{\gamma}_{n,\beta} + v^*_n(\mathbf{r})_{\alpha\beta}\hat{\gamma}^\dagger_{n,\beta}, \tag{2.45}$$

$$\hat{\psi}^\dagger_\theta(\mathbf{r}') = \sum_{m,\tau} u^*_m(\mathbf{r}')_{\tau\theta}\hat{\gamma}^\dagger_{m,\tau} + v_m(\mathbf{r}')_{\tau\theta}\hat{\gamma}_{m,\tau}, \tag{2.46}$$

where $\hat{\gamma}_{n,\beta}$ and $\hat{\gamma}^\dagger_{m,\tau}$ are annihilation and creation operators of Bogoliubov quasiparticles [95], i.e. (i) the operators satisfy the typical algebra of fermions, and (ii) they diagonalize the Hamiltonian (2.41) [$\hat{H} = E_{0s} + \sum_{m,\alpha}\varepsilon_{m\alpha}\hat{\gamma}^\dagger_{m\alpha}\hat{\gamma}_{m\alpha}$], one can easily demonstrate that the commutator between the Hamiltonian and the Bogoliubov quasiparticle annihilation operator is

$$[\hat{H},\hat{\gamma}_{n\beta}] = -\varepsilon_{n\beta}\hat{\gamma}_{n\beta}. \tag{2.47}$$

On the other hand, the commutator between the Hamiltonian of Eq. (2.41) and the annihilation field operator gives

$$[\hat{H},\hat{\psi}_\alpha(\mathbf{r})] = -\mathscr{H}_0\hat{\psi}_\alpha(\mathbf{r}) - \int d^3r'\Delta_{\alpha\beta}(\mathbf{r},\mathbf{r}')\hat{\psi}^\dagger_\beta(\mathbf{r}'). \tag{2.48}$$

Replacing the expansions of the field operators according to Eqs. (2.45) and (2.46), one obtains the following equations for the components $u_n(\mathbf{r})_{\alpha\tau}$ and $v_n(\mathbf{r})_{\alpha\tau}$,

$$\varepsilon_{n\tau}u_n(\mathbf{r})_{\alpha\tau} = \mathscr{H}_0 u_n(\mathbf{r})_{\alpha\tau} + \int d^3r'\Delta_{\alpha\beta}(\mathbf{r},\mathbf{r}')v_n(\mathbf{r}')_{\tau\beta}, \tag{2.49}$$

$$-\varepsilon_{n\tau}v_n(\mathbf{r})_{\alpha\tau} = \mathscr{H}^*_0 v_n(\mathbf{r})_{\alpha\tau} + \int d^3r'\Delta^*_{\alpha\beta}(\mathbf{r},\mathbf{r}')u_n(\mathbf{r}')_{\tau\beta}, \tag{2.50}$$

where the self-consistent condition (2.43) for the superconducting gap becomes

$$\Delta_{\alpha\beta}(\mathbf{r},\mathbf{r}') = V_{\alpha\beta,\delta\gamma}(\mathbf{r},\mathbf{r}')\sum_{n\theta} u_n(\mathbf{r}')_{\delta\theta}\, v^*_n(\mathbf{r})_{\gamma\theta}(1-f_n) + v^*_n(\mathbf{r}')_{\delta\theta}\, u_n(\mathbf{r})_{\gamma\theta}f_n, \tag{2.51}$$

or in a more convenient way, after using the symmetry properties of the pairwise interaction potential and the gap, Eqs. (2.38) and (2.44),

$$\Delta_{\alpha\beta}(\mathbf{r},\mathbf{r}') = \frac{1}{2}V_{\alpha\beta,\delta\gamma}(\mathbf{r},\mathbf{r}')\sum_{n\theta}(1-2f_n)\left[u_n(\mathbf{r}')_{\delta\theta}\, v^*_n(\mathbf{r})_{\gamma\theta} - v^*_n(\mathbf{r}')_{\delta\theta}\, u_n(\mathbf{r})_{\gamma\theta}\right]. \tag{2.52}$$

To sum up, the Bogoliubov-de Gennes equations for spin-triplet superconductors are composed of the set of integro-differential equations (2.49) and (2.50), along with the self-consistent condition (2.52). Notice that the equations are for each spin index, so there are indeed four coupled integro-differential equations. The complexity of these equations is high and to circumvent this problem one needs more insight into the coupling paring in order to simplify them. In the next section that will be done after discussing what is the most convincing pairing in SRO that agrees well with the majority of experiments performed to date.

2.2.2 Chiral p-wave superconductivity

In superconductors the spin susceptibility of the electrons provides a powerful method to distinguish spin-singlet from spin-triplet superconductivity. Moreover, it can also determine the structure of the gap, i.e. the representation of the corresponding d-vector. As a function of temperature the spin susceptibility for the chiral phase: $\mathbf{d}(\mathbf{k}) = \Delta_0\hat{\mathbf{z}}(k_x+ik_y)$, reads [48, 99]

$$\chi(T) = \chi_P \left\{ \begin{array}{cc} Y^{\rm ABM}(T) & \mathbf{H} \,||\, \hat{z} \\ 1 & \mathbf{H} \perp \hat{z} \end{array} \right. , \tag{2.53}$$

where $\chi_P = 2\mu_B^2 N_0$ is the Pauli spin susceptibility of the normal state, and $Y^{\rm ABM}(T)$ is the Yoshida function for the ABM phase after integration over the Fermi surface. For a spin-triplet superconductor in the ABM phase the plot of the Knight shift [a technique that indirectly reveals the spin susceptibility function (2.53)], is depicted in the right panel of Fig. 2.3. The dots, representing the experimental measurements for SRO [47], match the theoretical line $\chi(T) = \chi_P$ and thus suggest that SRO is a chiral p-wave superconductor. For comparison, the left panel shows the Knight shift of YBCO, and reveals the typical behavior of the spin susceptibility for a singlet state.

Experimental data of the spin susceptibility in SRO, with the applied magnetic field along the $\hat{\mathbf{z}}$ direction, seems to contradict all the evidence pointing towards chiral p-wave superconductivity. The spin susceptibility remained constant before T_c, when the magnetic field was applied perpendicularly to the basal plane [100]. One is of course aware that the low upper critical field H_{c2} can affect the measurements due to the screening effect of the Meissner currents. However, this unexpected behavior was attributed to weak spin-orbit coupling that was unable to sustain the spins of the Cooper pairs into the basal plane [96]. More accurate and sophisticated techniques are required to confirm the role of the spin-orbit coupling or other possibilities in the spin susceptibility measurements.

This thesis primarily considers the case of chiral p-wave superconductivity. Therefore, it requires the derivation of the BdG equations for chiral p-wave superconductors. In such equations, the gap matrix that corresponds to the d-vector representation of the chiral p-wave phase [see Eq. (2.19)], reads

$$\widehat{\Delta}(\mathbf{r},\mathbf{r}\,') = \left(\begin{array}{cc} 0 & \Delta_{\uparrow\downarrow} \\ \Delta_{\downarrow\uparrow} & 0 \end{array} \right), \tag{2.54}$$

where $\Delta_{\uparrow\downarrow} = \Delta_{\downarrow\uparrow}$. The replacement of the superconducting gap (2.54) into the BdG equations (2.49) and (2.50) of spin-triplet superconductors, leads one to remove the spin indexes

$$\varepsilon_n u_n(\mathbf{r}) = \mathscr{H}_0 u_n(\mathbf{r}) + \int d^3r' \Delta(\mathbf{r},\mathbf{r}\,') v_n(\mathbf{r}\,'), \tag{2.55}$$

$$-\varepsilon_n v_n(\mathbf{r}) = \mathscr{H}_0^* v_n(\mathbf{r}) + \int d^3r' \Delta^*(\mathbf{r},\mathbf{r}\,') u_n(\mathbf{r}\,'). \tag{2.56}$$

Transforming the coordinates of the two particles to the relative and center of mass coordinates, respectively,

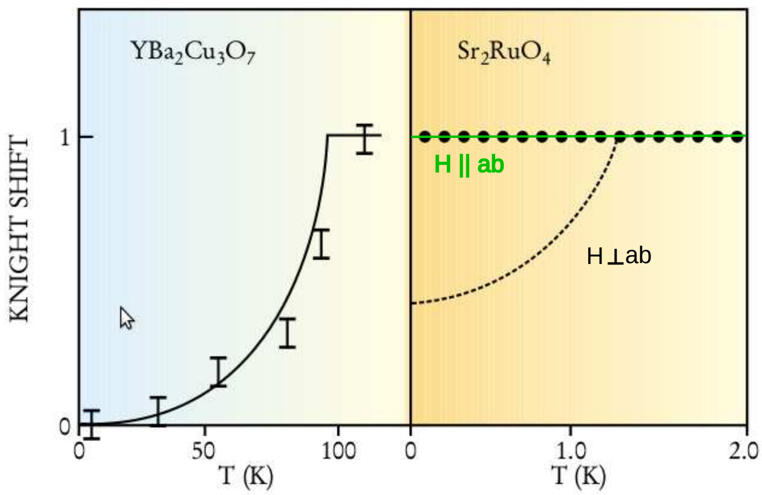

Figure 2.3: The Knight shift, an indirect measurement of the electronic spin susceptibility, shows here that the superconducting pairing for the Ytrium-Barium-Copper-Oxygen compound is of the singlet type, while for strontium ruthenate the pairing is suggested to be of the triplet type since the data (black dots) matched the theoretical prediction for the spin susceptibility with an in-plane field. From Ref. [101].

$$\mathbf{X} = \mathbf{r} - \mathbf{r}\,', \qquad \mathbf{R} = \frac{\mathbf{r} + \mathbf{r}\,'}{2}, \tag{2.57}$$

one can see that the following expression for the superconducting gap in the center of mass and reciprocal space coordinates is appropriate for chiral p-wave superconductivity,

$$\Delta(\mathbf{R}, \mathbf{k}) = \frac{\Delta_x(\mathbf{R})k_x + i\Delta_y(\mathbf{R})k_y}{k_{\mathrm{F}}}, \tag{2.58}$$

where k_{F} is the Fermi surface wave vector. The gap in terms of $\mathbf{R}$ and $\mathbf{X}$ consequently becomes,

$$\Delta(\mathbf{R}{,}\mathbf{X}) = \frac{1}{(2\pi)^3}\int d^3k e^{i\mathbf{k}\cdot\mathbf{X}}\Delta(\mathbf{R}, \mathbf{k}), \tag{2.59}$$

or after a straightforward calculation,

$$\Delta(\mathbf{R}{,}\mathbf{X}) = \frac{i}{k_{\mathrm{F}}}\left[\Delta_x(\mathbf{R})\,\partial_{x'} + i\Delta_y(\mathbf{R})\,\partial_{y'}\right]\delta(\mathbf{r}-\mathbf{r}\,'). \tag{2.60}$$

Replacing last expression of the gap back in Eqs. (2.55) and (2.56), one obtains the Bogoliubov-de Gennes equations for chiral p-wave superconductors,

$$\begin{aligned} \varepsilon_n u_n(\mathbf{r}\,) = \mathscr{H}_0 u_n(\mathbf{r}\,) \ &- \ \frac{i}{k_{\mathrm{F}}}\Big\{\Delta_x(\mathbf{r}\,)\partial_x + i\Delta_y(\mathbf{r}\,)\partial_y \\ &+ \ \frac{1}{2}\big[\partial_x\Delta_x(\mathbf{r}\,) + i\partial_y\Delta_y(\mathbf{r}\,)\big]\Big\}v_n(\mathbf{r}\,), \end{aligned} \tag{2.61}$$

and

$$\begin{aligned} -\,\varepsilon_n v_n(\mathbf{r}\,) = \mathscr{H}_0^* v_n(\mathbf{r}\,) \ &+ \ \frac{i}{k_{\mathrm{F}}}\Big\{\Delta_x^*(\mathbf{r}\,)\partial_x - i\Delta_y^*(\mathbf{r}\,)\partial_y \\ &+ \ \frac{1}{2}\big[\partial_x\Delta_x^*(\mathbf{r}\,) - i\partial_y\Delta_y^*(\mathbf{r}\,)\big]\Big\}u_n(\mathbf{r}\,). \end{aligned} \tag{2.62}$$

The self-consistency condition of the gap in the chiral case is derived from Eq. (2.52) by dropping out the spin labels in the matrices $u_n(\mathbf{r}\,')_{\delta\theta}$ and $v_n^*(\mathbf{r}\,)_{\gamma\theta}$, i.e.

$$\Delta(\mathbf{r},\mathbf{r}\,') = \frac{1}{2}V(\mathbf{r},\mathbf{r}\,')\sum_n(1-2f_n)\big[u_n(\mathbf{r}\,')\,v_n^*(\mathbf{r}\,)-v_n^*(\mathbf{r}\,')\,u_n(\mathbf{r}\,)\big]. \tag{2.63}$$

Moreover, one can reduce further this expression by relabelling the coordinates in the last term, and bearing in mind the asymmetry property of the potential when particles are interchanged, i.e. $V(\mathbf{r},\mathbf{r}\,') = -V(\mathbf{r}\,',\mathbf{r}\,)$,

$$\Delta(\mathbf{r},\mathbf{r}\,') = V(\mathbf{r},\mathbf{r}\,')\sum_n \tanh\left(\frac{E_n}{2T}\right)u_n(\mathbf{r}\,')\,v_n^*(\mathbf{r}\,). \tag{2.64}$$

Within the weak-coupling approach and the odd-parity attractive interaction ($V_p > 0$), the two particle potential in the reciprocal space reads,

$$V(\mathbf{k}-\mathbf{k}\,') = -V_p\frac{\mathbf{k}\cdot\mathbf{k}\,'}{k_{\mathrm{F}}^2}. \tag{2.65}$$

On the other hand, the corresponding attractive potential in the real space is given by the Fourier transform of $V(\mathbf{k}-\mathbf{k}\,')|_{\mathbf{k}\,'\to\mathbf{k}}$,

$$V(\mathbf{r},\mathbf{r}\,') = -\frac{V_p\Omega}{(2\pi)^3}\int d^3k e^{i\mathbf{k}\cdot\mathbf{X}}\frac{k^2}{k_{\mathrm{F}}^2}, \tag{2.66}$$

with Ω being the volume of the system. Defining for convenience the factor that multiplies the attractive potential in the self-consistency equation (2.64) as

$$D(\mathbf{r},\mathbf{r}\,') = \sum_n \tanh\left(\frac{E_n}{2T}\right)u_n(\mathbf{r}\,')\,v_n^*(\mathbf{r}\,), \tag{2.67}$$

the superconducting gap in terms of the center of mass and reciprocal space coordinates becomes

$$\begin{aligned}\Delta(\mathbf{R},\mathbf{k}\,) &= \int d^3X e^{-i\mathbf{k}\cdot\mathbf{X}}\Delta(\mathbf{r},\mathbf{r}\,') \qquad (2.68)\\ &= -V_p\Omega\int d^3k'\frac{k'^{\,2}}{k_{\mathrm{F}}^2}\left(\frac{1}{2\pi}\right)^2\int d^3X e^{i(\mathbf{k}'-\mathbf{k})\cdot\mathbf{X}}D\Big(\mathbf{R}+\frac{\mathbf{X}}{2},\mathbf{R}-\frac{\mathbf{X}}{2}\Big).\end{aligned}$$

Expanding the function D (defined in 2.67) in a Taylor series and taking the first two terms,

$$D\Big(\mathbf{R}+\frac{\mathbf{X}}{2},\mathbf{R}-\frac{\mathbf{X}}{2}\Big) \approx D(\mathbf{R},\mathbf{R}) + \left[\frac{\partial D(\mathbf{R},\mathbf{R}\,')}{\partial\mathbf{R}} - \frac{\partial D(\mathbf{R},\mathbf{R}\,')}{\partial\mathbf{R}'}\right]\Bigg|_{\mathbf{R}'\to\mathbf{R}}\cdot\frac{\mathbf{X}}{2}, \tag{2.69}$$

one obtains for the superconducting gap the zero and first order expansions,

$$\Delta_0(\mathbf{R},\mathbf{k}\,) = -V_p\Omega\frac{k^2}{k_{\mathrm{F}}^2}\sum_n \tanh\left(\frac{E_n}{2T}\right)u_n(\mathbf{R}\,)\,v_n^*(\mathbf{R}\,), \tag{2.70}$$

$$\Delta_I(\mathbf{R},\mathbf{k}\,) = -iV_p\Omega\frac{\mathbf{k}}{k_{\mathrm{F}}^2}\cdot\left[\frac{\partial}{\partial\mathbf{R}}-\frac{\partial}{\partial\mathbf{R}'}\right]\sum_n \tanh\left(\frac{E_n}{2T}\right)u_n(\mathbf{R}\,)\,v_n^*(\mathbf{R}\,')\Big|_{\mathbf{R}'\to\mathbf{R}}. \tag{2.71}$$

Here the zero order term is discarded since we are considereing only pure p-wave paring, and the first order term is compared with Eq. (2.58) to obtain the self-consistent condition for the two components of the gap

$$\Delta_x(\mathbf{r}\,) \;=\; -V_p\Omega\frac{i}{k_{\mathrm{F}}}\big(\partial_x-\partial_{x'}\big)\sum_n \tanh\left(\frac{E_n}{2T}\right)u_n(\mathbf{r}\,)\,v_n^*(\mathbf{r}\,')\big|_{\mathbf{r}\,'\to\mathbf{r}}\,, \tag{2.72}$$

$$\Delta_y(\mathbf{r}\,) \;=\; -V_p\Omega\frac{1}{k_{\mathrm{F}}}\big(\partial_y-\partial_{y'}\big)\sum_n \tanh\left(\frac{E_n}{2T}\right)u_n(\mathbf{r}\,)\,v_n^*(\mathbf{r}\,')\big|_{\mathbf{r}\,'\to\mathbf{r}}\,. \tag{2.73}$$

Finally, to conclude this section the calculation of the superconducting current density $\mathbf{j}(\mathbf{r}\,)$ is provided. Defining it as proportional to the real part of the statistical average of the kinetic momentum operator $\mathbf{p}$, one obtains

$$\begin{aligned}
\mathbf{j}(\mathbf{r}\,) &= \frac{e}{m}\mathrm{Re}\,\langle\hat{\psi}_\alpha^\dagger\Big(\frac{\hbar}{i}\nabla-\frac{e}{c}\mathbf{A}\Big)\hat{\psi}_\alpha\rangle\,,\\
&= \frac{e\hbar}{2im}\sum_n\Big\{\big[u_n^*(\mathbf{r}\,)\nabla u_n(\mathbf{r}\,)-c.c.\big]f_n+\big[v_n(\mathbf{r}\,)\nabla v_n^*(\mathbf{r}\,)-c.c.\big](1-f_n)\Big\}\\
&- \frac{e^2}{mc}\sum_n\big[|u_n(\mathbf{r}\,)|^2 f_n+|v_n(\mathbf{r}\,)|^2(1-f_n)\big]\mathbf{A},
\end{aligned} \tag{2.74}$$

where the field operators ($\hat{\psi}_\alpha^\dagger$ and $\hat{\psi}_\alpha$) have been replaced by their corresponding expansions (2.45) and (2.46) in the chiral case. The Ampère's law is thus introduced in its standard form

$$\nabla\times\nabla\times\mathbf{A}=\frac{4\pi}{c}\mathbf{j}(\mathbf{r}\,), \tag{2.75}$$

but with the current density stemming from the probability current of the quasiparticle states in the superconductor.

The BdG equations for chiral p-wave superconductivity are thus complemented with the self-consistent conditions (2.72) and (2.73), and Ampère's law (2.75). Their numerical solutions are computationally demanding and in the next chapter the procedure employed in this thesis to solve them is described.

2.3 Phenomenological theory

In this section the superconductivity of unconventional superconductors will be treated within the phenomenological formalism. The treatment is different from the microscopic one discussed in the previous sections, although the starting point is the self-consistent condition [see Eq. (2.35)] derived whithin the microscopic formalism.

2.3.1 Linearized gap equations

Superconductivity arises after the temperature of a material in its normal state is lowered below T_c, making the material undergo a second order (continuous) transition. The superconducting phase is characterized by an order parameter that represents the density of the Cooper pairs, and is vanishingly small closed to the critical temperature, as is the superconducting gap. One can then linearize the self-consistent gap equation (2.35) and thereby obtain the superconducting order parameter.

Replacing the spin-singlet superconducting gap of Eq. (2.14) into the self-consistent condition (2.35), yields

Bethe	Mulliken	Basis function	Direction of d	TRSB
Γ_1^-	A_{1u}	$\hat{\mathbf{x}}k_x + \hat{\mathbf{y}}k_y,\ \hat{\mathbf{z}}k_z$	$\mathbf{d}\|\|ab$, $\mathbf{d}\|\|c$	No
Γ_2^-	A_{2u}	$\hat{\mathbf{x}}k_y - \hat{\mathbf{y}}k_x$	$\mathbf{d}\|\|ab$	No
Γ_3^-	B_{1u}	$\hat{\mathbf{x}}k_x - \hat{\mathbf{y}}k_y$	$\mathbf{d}\|\|ab$	No
Γ_4^-	B_{2u}	$\hat{\mathbf{x}}k_y + \hat{\mathbf{y}}k_x$	$\mathbf{d}\|\|ab$	No
Γ_5^-	E_u	$\{\hat{\mathbf{z}}k_x,\ \hat{\mathbf{z}}k_y\}$, $\{\hat{\mathbf{x}}k_z,\ \hat{\mathbf{y}}k_z\}$	$\mathbf{d}\|\|c$, $\mathbf{d}\|\|ab$	Yes

Table 2.1: Table of the basis functions for the D_{4h} symmetry group within the d-vector representation for spin-triplets. The first two rows denotes the notations of Bethe and Mulliken, respectively.

$$\psi(\mathbf{k}) = -\sum_{\mathbf{k}'} V_{\mathbf{k},\mathbf{k}'} \frac{\psi(\mathbf{k}')}{2E_{\mathbf{k}'}} \tanh\left(\frac{E_{\mathbf{k}'}}{2k_{\mathrm{B}}T}\right). \tag{2.76}$$

In a first-order approach in terms of the superconducting gap, the quasiparticle energy $E_{\mathbf{k}'}$ is replaced by the kinetic energy $\epsilon_{\mathbf{k}'}$. Moreover, owing to the assumption that the attractive potential is nonzero only within the Debye window, one can transform the sum into an integral and separate it into a surface and an energy part,

$$\psi(\mathbf{k}) = -N(0) \int d\Omega\, V_{\mathbf{k},\mathbf{k}'} \psi(\mathbf{k}') \int_{-\epsilon_c}^{\epsilon_c} d\epsilon \frac{\tanh\left(\frac{\epsilon}{2k_{\mathrm{B}}T}\right)}{2\epsilon}, \tag{2.77}$$

where $N(0)$ is the density of states at the Fermi surface and ϵ_c is a cuttoff energy. In a more convenient way the linearized gap equation becomes

$$\Lambda_{\mathrm{S}} \psi(\mathbf{k}) = -N(0) \left\langle V_{\mathbf{k},\mathbf{k}'} \psi(\mathbf{k}') \right\rangle_{\mathrm{FS}}, \tag{2.78}$$

where the average is over the Fermi surface and

$$\frac{1}{\Lambda_{\mathrm{S}}} = \int_0^{\epsilon_c} d\epsilon \frac{1}{\epsilon} \tanh\left(\frac{\epsilon}{2k_{\mathrm{B}}T}\right). \tag{2.79}$$

In a similar way, replacing the spin-triplet superconducting gap of Eq. (2.15) into the self-consistent condition (2.35), one obtains

$$\mathbf{d}(\mathbf{k}) = -\sum_{\mathbf{k}'} V_{\mathbf{k},\mathbf{k}'} \frac{\mathbf{d}(\mathbf{k}')}{2E_{\mathbf{k}'}} \tanh\left(\frac{E_{\mathbf{k}'}}{2k_{\mathrm{B}}T}\right), \tag{2.80}$$

where the linearization process, described above for the spin-singlet case, can be applied again yielding

$$\Lambda_{\mathrm{T}} \mathbf{d}(\mathbf{k}) = -N(0) \left\langle V_{\mathbf{k},\mathbf{k}'} \mathbf{d}(\mathbf{k}') \right\rangle_{\mathrm{FS}}. \tag{2.81}$$

Eqs. (2.78) and (2.81) are eigenvalue equations with each eigenvalue Λ_S^a and Λ_{T}^a corresponding to an eigenvector $\psi^a(\mathbf{k})$ and $\mathbf{d}^a(\mathbf{k})$, respectively. The eigenvalues define different critical temperatures $\{T_c^{(1)}, T_c^{(2)}, \dots\}$, and the eigenvectors the corresponding representations of the gap.

Finding the eigenvectors of the linearized equation requires detailed knowledge of the interaction potential $V_{\mathbf{k},\mathbf{k}'}$, which in many cases is not available. Then, in order to circumvent the problem, one has to appeal to symmetry considerations and obtain the representations of the gap phenomenologically. For example, many of the HTSs as well as SRO have a tetragonal crystal structure represented by the D_{4h} symmetry group. One can then use the basis functions of this group and form an expansion of any physical quantity having this symmetry.

For the superconducting gap the same procedure applies, although one has to bear in mind that other symmetries need to be fulfilled such as: (i) the group of rotations generated by the total angular mometum $\mathbf{J} = \mathbf{L} + \mathbf{S}$, where $\mathbf{L}$ and $\mathbf{S}$ denote the orbital and spin angular momenta, and (ii) the continuous group of the gauge transformations $U(1)$,

$$\mathcal{G} = \mathcal{D}_{(\mathbf{J}\,)} \times D_{4h} \times U(1). \tag{2.82}$$

Let us consider first the basis functions of the group D_{4h} within the d-vector notation and leave the discussion of the gauge symmetry for later. There exist five different irreducible representations for this group (see Table 2.1). Among them four are one-dimensional and one two-dimensional, i.e. one that breaks the time-reversal symmetry. Since the basis functions of Table 2.1 are given within the d-vector notation, the symmetry generated by the total angular momentum $(\mathbf{J}\,)$ is included on them. The superconducting gap is thus given by an expansion in the irreducible representations of the group,

$$\mathbf{d}(\mathbf{k}\,) = \sum_m \psi(\Gamma, m)\mathbf{d}(\Gamma, m; \mathbf{k}\,), \tag{2.83}$$

where $\psi(\Gamma, m)$ are complex order parameters transforming like coordinates in the basis functions. When the expansion includes one single irreducible representation the gap is said to be in a "pure" state. This can happen when among the critical temperatures there is one that dominates the others, i.e. the highest T_c is much larger than the remaining $T_c\,'s$. On the other hand, when the critical temperatures of the irreducible representations are similar, an admixture of two or more representations may be realized. As the main example of the phenomenological theory of unconventional superconductors, the representation of the D_{4h} symmetry group breaking the time-reversal symmetry will be considered first, and the case of a gap with an admixture of two irreducible representations will be discussed later.

2.3.2 Chiral p-wave superconductivity

According to Table 2.1 the expansion of the superconducting gap in the basis of the irreducible representation E_u reads

$$\mathbf{d}(\mathbf{k}) = (\psi_x k_x + \psi_y k_y)\hat{\mathbf{z}}. \tag{2.84}$$

The calculation of the order parameters for this representation breaking the TRS has been reported elsewhere, so we only briefly outline the procedure. Following Landau's theory of second-order phase transitions, the order-parameter components Ψ_x and Ψ_y are demanded to minimize the free energy density

$$F = F_{\mathrm{N}} + \int d^3\mathbf{r}\Big[\mathscr{F}_{\mathrm{cond}} + \mathscr{F}_{\mathrm{kin}} + \frac{\mathbf{B}^2}{8\pi}\Big], \tag{2.85}$$

where F_N is the free energy of the normal state, $\mathscr{F}_{\mathrm{cond}}$ denotes the energy density of the condensate, $\mathscr{F}_{\mathrm{kin}}$ the kinetic energy density, and $\mathbf{B}$ the magnetic field. $\mathscr{F}_{\mathrm{cond}}$ is a combination of second order and fourth order terms in the order parameter, fulfilling the properties of the group $\mathcal{G}$, and with phenomenological parameters temperature-dependent or independent as dictated by Landau's theory:

$$\mathscr{F}_{\mathrm{cond}} = \alpha\big(|\psi_x|^2 + |\psi_y|^2\big) + \beta_1\big(|\psi_x|^2 + |\psi_y|^2\big)^2 + \beta_2\big(\psi_x^*\psi_y - \psi_x\psi_y^*\big)^2 + \beta_3|\psi_x|^2|\psi_y|^2. \tag{2.86}$$

The phenomenological parameters α and β_i, with $i = 1{-}3$, are material dependent constants, and one can demonstrate that microscopic quantities such as the shape of the Fermi surface, the Fermi

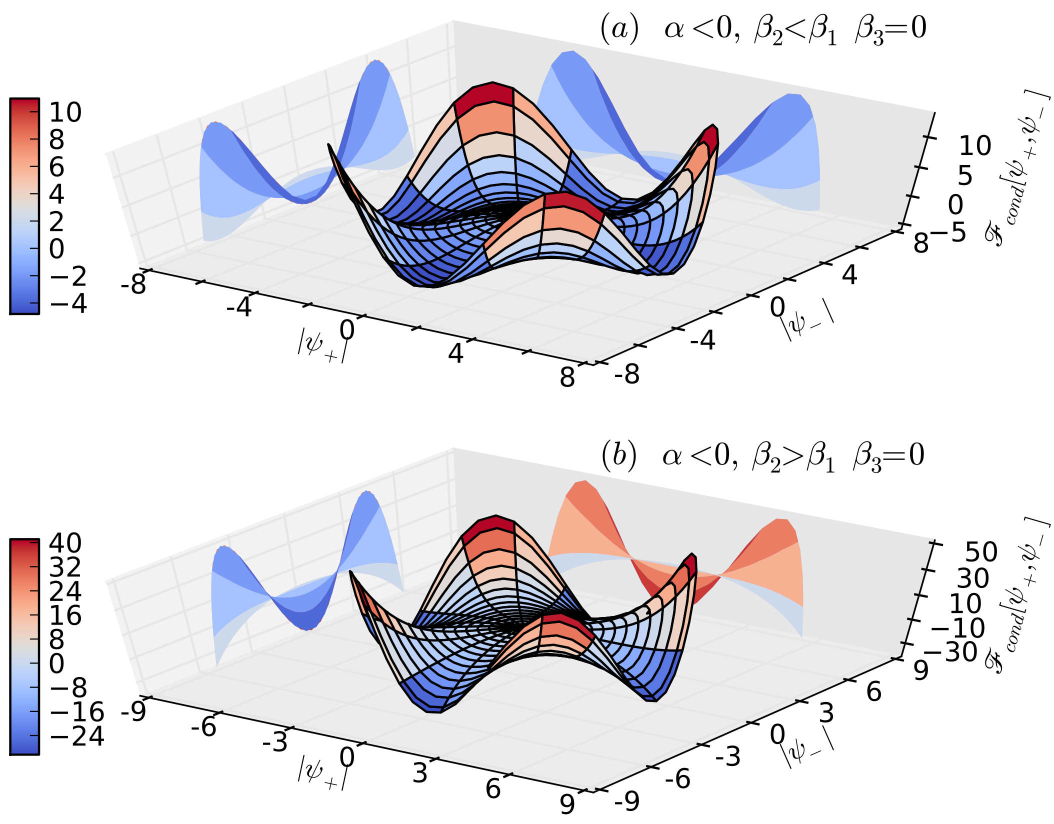

Figure 2.4: Contour plot of the condensation free energy density ($\mathscr{F}_{\text{cond}}$) for chiral p-wave superconductors. The energy density in panel (a) is bound from below and has two degenerated ground states, i.e. breaks the time-reversal-symmetry. On the other hand the energy density of panel (b) is not bound from below.

velocity and the electronic density of states define them [77, 102, 103]. In this section they will be treated as independent parameters and rather discussed based on general grounds. For example, writing the condensate free energy density in terms of the new order parameters $\psi_\pm = \psi_x \pm i\psi_y$, as

$$\begin{aligned}\mathscr{F}_{\text{cond}} = \tfrac{\alpha}{2}\left(|\psi_+|^2+|\psi_-|^2\right)+\tfrac{\beta_1}{4}\left(|\psi_+|^2+|\psi_-|^2\right)^2 \\ -\tfrac{\beta_2}{4}\left(|\psi_+|^2-|\psi_-|^2\right)^2+\tfrac{\beta_3}{16}\left[\left(|\psi_+|^2+|\psi_-|^2\right)^2-\left(\psi_+\psi_-^*+\psi_-\psi_+^*\right)^2\right],\end{aligned} \tag{2.87}$$

one can show in Fig. 2.4 two distinct shapes of $\mathscr{F}_{\text{cond}}$ for two different combinations of the phenomenological parameters. For ilustration purposes we took $\beta_3 = 0$, and extended the contour plot from the quadrant where $|\psi_\pm| > 0$ to the entire Cartesian plane. When $\beta_2 < \beta_1$, $\mathscr{F}_{\text{cond}}$ is bound from below and has two local minima at: (i) $(|\psi_+|, \psi_-) = (\sqrt{|\alpha|/(\beta_1-\beta_2)}, 0)$, and (ii) $(\psi_+, |\psi_-|) = (0, \sqrt{|\alpha|/(\beta_1-\beta_2)})$. On the other hand, when $\beta_2 > \beta_1$, $\mathscr{F}_{\text{cond}}$ has only a saddle point at $\psi_+ = \psi_- = 0$ and consequently it is not bound from below.

The kinetic energy density of Eq. (2.85) is obtained following the same procedure that was applied previously to the condensation free energy density. However, one has to bear in mind that these terms contain gradients of the order parameters, such as in the conventional case [see Eq. (1.3)], that one has to treat properly in order to make them invariant under the set of operations of the group $\mathcal{G}$. For example, let us consider the covariant derivative $\mathbf{D} = \frac{\hbar}{i}\nabla - \frac{e^*}{c}\mathbf{A}$, and try to build a $U(1)$ invariant term out of it and the two order parameters $\psi_{x,y}$. A first guess is $D_i\psi_j(D_m\psi_n)^*$, where one can easily check that this term is indeed invariant under the transformation $\psi_a = e^{-i\frac{e^*}{\hbar c}\chi}\tilde{\psi}_a$, provided that the vector potential transforms as: $\tilde{A}_a = A_a - \partial_a\chi$. However, the term $D_i\psi_j(D_m\psi_n)^*$ is not invariant under the set of operations of the group D_{4h}. The list of terms which are invariant are shown below, taken from Ref. [94]. They read

$$\begin{aligned}\mathscr{F}_{\text{kin}} = k_0\big[|D_x\psi_x|^2 + |D_y\psi_y|^2\big] + k_1\big[|D_x\psi_y|^2 + |D_y\psi_x|^2\big] + \\ k_2\big[(D_x\psi_x)^*(D_y\psi_y) + \text{c.c.}\big] + k_3\big[(D_x\psi_y)^*(D_y\psi_x) + \text{c.c.}\big] + \\ k_4\big[|D_z\psi_x|^2 + |D_z\psi_y|^2\big],\end{aligned} \tag{2.88}$$

where k_i, with $i = 0 - 4$, are phenomenological constants related to microscopic quantities, but treated here as independent variables. The method that relates the phenomenological parameters to the microscopic quantities uses Gor'kov's theory of weakly coupled superconductors. This method, besides providing an alternative derivation of the free energy density of chiral p-wave superconductors, yields

$$\alpha(T) = -\frac{\mathcal{N}(0)}{2}\ln\Big(\frac{T}{T_c}\Big), \quad \frac{\beta_1}{3} = \beta_2 = \frac{7\zeta(3)}{64}\frac{\mathcal{N}(0)}{(\pi k_{\text{B}}T_c)^2}, \quad \frac{k_0}{3} = k_1 = k_2 = k_3 = \frac{7\zeta(3)}{128}\Big(\frac{\hbar v_{\text{F}}}{\pi k_{\text{B}}T_c}\Big)^2\mathcal{N}(0), \tag{2.89}$$

where $\mathcal{N}(0)$ is the density of states per spin at the Fermi level, and $\zeta(s)$ is the Riemann zeta function. In order to see that the kinetic energy density possesses the symmetry of the group $\mathcal{G}$, one can integrate this density over the sample volume $\big(\int \mathcal{F}_{\text{kin}} d^3\mathbf{r} = F_{\text{kin}}\big)$ to subsequently transform the resultant free energy (F_{kin}) to the reciprocal space. The transformation, conveniently applied in the notation of the new order parameters, requires the kinetic energy density given in this notation,

$$\begin{aligned}\mathscr{F}_{\text{kin}} = \tfrac{k_0+k_1}{4}\big\{|\mathbf{D}\psi_+|^2 + |\mathbf{D}\psi_-|^2\big\} + (k_2+k_3)\text{Re}\big\{\Pi_+\psi_-(\Pi_-\psi_+)^*\big\} + \\ \tfrac{k_2-k_3}{2}\text{Re}\Big\{i\Big[D_x\psi_+(D_y\psi_+)^* - D_x\psi_-(D_y\psi_-)^*\Big]\Big\} + \tfrac{k_4}{2}\big\{|D_z\psi_+|^2 + |D_z\psi_-|^2\big\},\end{aligned} \tag{2.90}$$

where $\Pi_\pm = (D_x \pm iD_y)/\sqrt{2}$. The Fourier transform of F_{kin} at zero magnetic field yields

$$F_{\text{kin}} = \frac{\hbar^2}{4}\int d^2\mathbf{k}\big(\tilde{\psi}_+^*(\mathbf{k}), \tilde{\psi}_-^*(\mathbf{k})\big)\begin{bmatrix} (k_0+k_1)\mathbf{k}^2 & (k_2+k_3)k_+^2 \\ (k_2+k_3)k_-^2 & (k_0+k_1)\mathbf{k}^2 \end{bmatrix}\begin{pmatrix} \tilde{\psi}_+(\mathbf{k}) \\ \tilde{\psi}_-(\mathbf{k}) \end{pmatrix}, \tag{2.91}$$

where $k_\pm = k_x \pm ik_y$, $k_2 = k_3$, the dimension of the problem has been reduced to two, and $\tilde{\psi}_\pm(\mathbf{k})$ are the Fourier transforms of $\psi_\pm(\mathbf{r})$,

$$\tilde{\psi}_\pm(\mathbf{k}) = \frac{1}{(2\pi)^2}\int d^2\mathbf{r}e^{i\mathbf{k}\cdot\mathbf{r}}\psi_\pm(\mathbf{r}). \tag{2.92}$$

The integrand of Eq. (2.91) is a complex bilinear form. Finding it reduces to solve the following algebraic equation,

$$\big[(k_0+k_1)\mathbf{k}^2 - \omega^p\big]^2 - (k_2+k_3)^2(k_+k_-)^2 = 0, \tag{2.93}$$

derived from the eigenvalue problem $\widehat{A}X = \omega^p X$, with $X = (\tilde{\psi}_+(\mathbf{k}), \tilde{\psi}_-(\mathbf{k}))^T$, and $\widehat{A} = \begin{bmatrix} (k_0+k_1)\mathbf{k}^2 & (k_2+k_3)k_+^2 \\ (k_2+k_3)k_-^2 & (k_0+k_1)\mathbf{k}^2 \end{bmatrix}$. From the two roots of Eq. (2.93) we pick up the positive one, i.e. $\omega_+^p = \sum_{i=0}^{3} k_i\,\mathbf{k}^2$, and we plot it in Fig. 2.5(a). One can see that this kinetic contribution to the free energy is isotropic, resembling to what is expected in s-wave superconductors. However, there

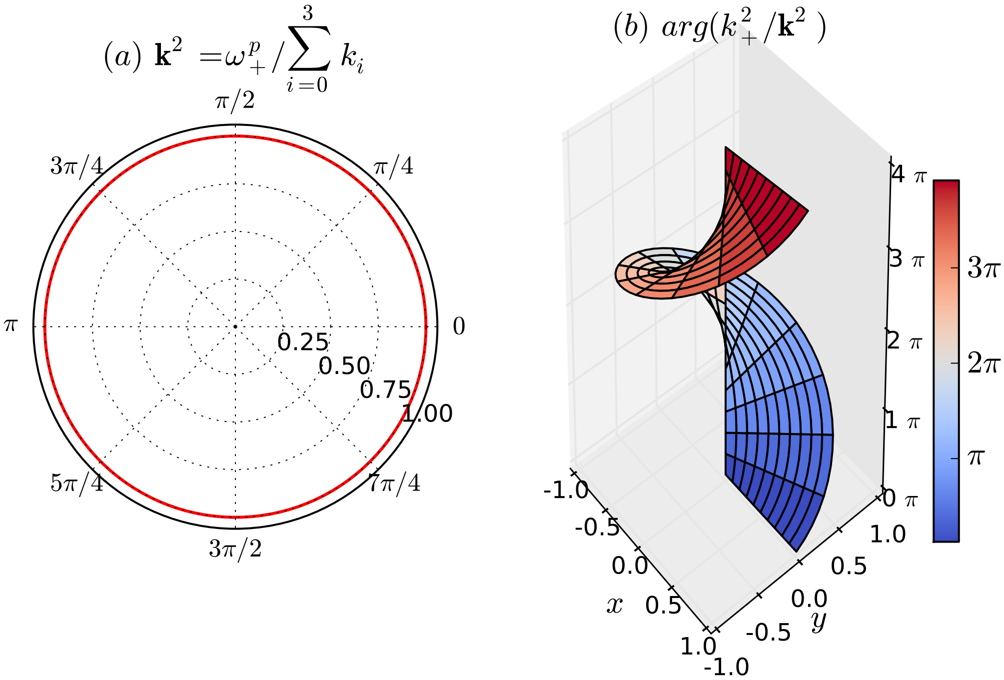

Figure 2.5: (a) Plot of one of the eigenvalues stemming from the bilinear form of the kinetic energy density for chiral p-wave superconductors after Fourier transformation (see main text). The plot, revealing that this eigenvalue is isotropic, is complemented with panel (b), which shows the relative phase between the components $\tilde{\psi}_+(\mathbf{k})$ and $\tilde{\psi}_-(\mathbf{k})$.

is an inherent phase which is the main characteristic of the chiral p-wave case, and which one can obtain by replacing ω_+^p back in the eigenvalue problem. This solution, not uniquely defined, is only given as the ratio

$$\frac{\tilde{\psi}_+(\mathbf{k})}{\tilde{\psi}_-(\mathbf{k})} = \frac{k_+^2}{\mathbf{k}^2} = e^{2i\phi}, \tag{2.94}$$

meaning that although the magnitude of the gap is constant (fully gapped), the phase of it is changing [see Fig. 2.5(b)].

2.3.3 $d+s$-wave superconductivity

The phase-sensitive experiments of Refs. [18, 19] showed that the symmetry of the superconducting gap in the HTS was of the d-wave type. This fact subsequently raised the question of how this symmetry was reflected in the vortex matter. The first answers came from theoretical works [104, 105], which suggested that the d-wave symmetry component was not the only component present in the HTS. In fact, they pointed out that an admixture of a s-wave component complemented the dominant d-wave order parameter.

Among the implications on the vortex matter of having a superconductor with multiple order parameters one can name two: (i) the lattice that form the vortices and which differs from the conventional Abrikosov lattice, and (ii) the bound states that emerge inside the cores of the vortices and which are distinct from the Caroli-Matricon bound states. Works have demonstrated that the vortex lattice is oblique for the d-wave order parameter with the admixture of a s-wave component [106, 107], namely the $d+s$-wave superconductor. Moreover, it has also been shown for a single vortex that the shape of the superconducting density from the s-wave component is not rotational

Bethe	Mulliken	Basis function	Location of line nodes	TRSB
Γ_1^+	A_{1g}	$1,\, k_x^2+k_y^2,\, k_z^2$	$\cdots$	No
Γ_2^+	A_{2g}	$k_xk_y(k_x^2-k_y^2)$	$x=y=0,\; y=\pm x$	No
Γ_3^+	B_{1g}	$k_x^2-k_y^2$	$y=\pm x$	No
Γ_4^+	B_{2g}	k_xk_y	$x=y=0$	No
Γ_5^+	E_g	$\{k_xk_z, k_yk_z\}$	$z=0$	Yes

Table 2.2: Table of the basis functions for the D_{4h} symmetry group within the d-vector representation for spin-singlets. The first two rows denotes the notations of Bethe and Mulliken, respectively.

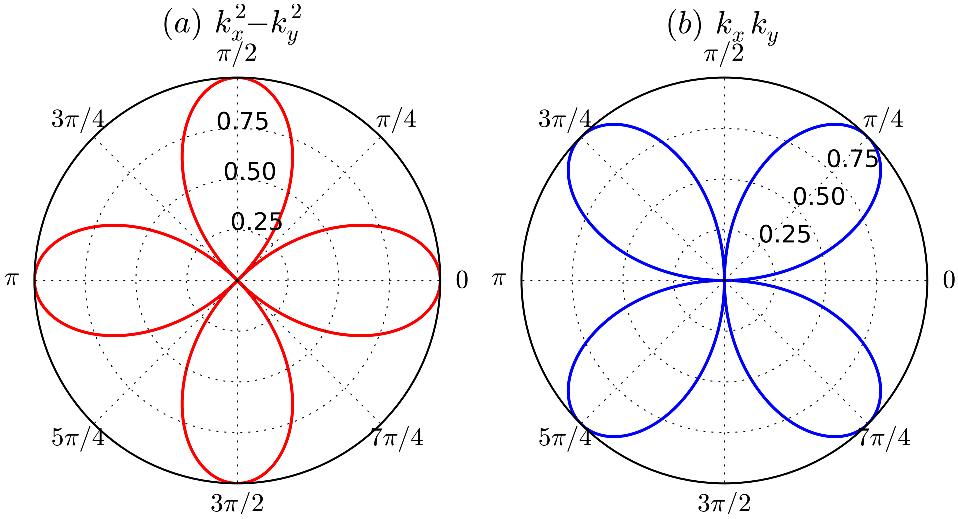

Figure 2.6: Plots of the two irreducible representations Γ_3^+ and Γ_4^+ of Table 2.2, characterized for possessing d-wave symmetry. Panel (a) shows nodes at $y=\pm x$ and panel (b) at $y=0$, and $x=0$.

invariant, unlike in the conventional case. This density component showed a four-lobe profile rather than the cylindrical symmetric structure of the Abrikosov vortices [107,108]. Huge efforts have been devoted to see this peculiar feature in HTSs, and thus confirm the $d+s$-wave pairing, however the task has been challenging due to the dominance of the cylindrical symmetric structure of the d-wave component.

In order to study phenomenologically $d+s$-wave superconductivity, one can start by finding the irreducible representations of the corresponding symmetry group. In this case, bearing in mind that the HTS $Bi_2Sr_2CaCu_2O_{8+\delta}$ possesses the tetragonal crystal symmetry and its pairing is of the singlet type, the symmetry group behind this analysis is the D_{4h}. The list of the irreducible representations of this group for the gap parameter ψ [see Eq. (2.78)] is shown in table 2.2. Among the five representations two have the d-wave symmetry and one the s-wave symmetry, namely the pair (Γ_3^+, Γ_4^+), and Γ_1^+, respectively. In Fig. 2.6, the plot of the two representations with the d-wave symmetry is shown. The figure clearly shows that both representations have line nodes, and that their locations correspond to those listed in the fourth column of Table 2.2.

According to the irreducible representations of the D_{4h} symmetry group, the expansion of the superconducting gap for a $d+s$-wave superconductor reads [108]

$$\psi(\mathbf{k}) = \eta_s + \eta_d(k_x^2 - k_y^2), \tag{2.95}$$

where η_s and η_d are the order parameters transforming like coordinates according to the irreducible representations Γ_1^+ and Γ_3^+, respectively. These order parameters are obtained following the same process that was applied to Ψ_x and Ψ_y in the chiral p-wave case, i.e. using Landau's theory of second order phase transitions. The condensation free energy density for $d+s$-wave superconductivity thus

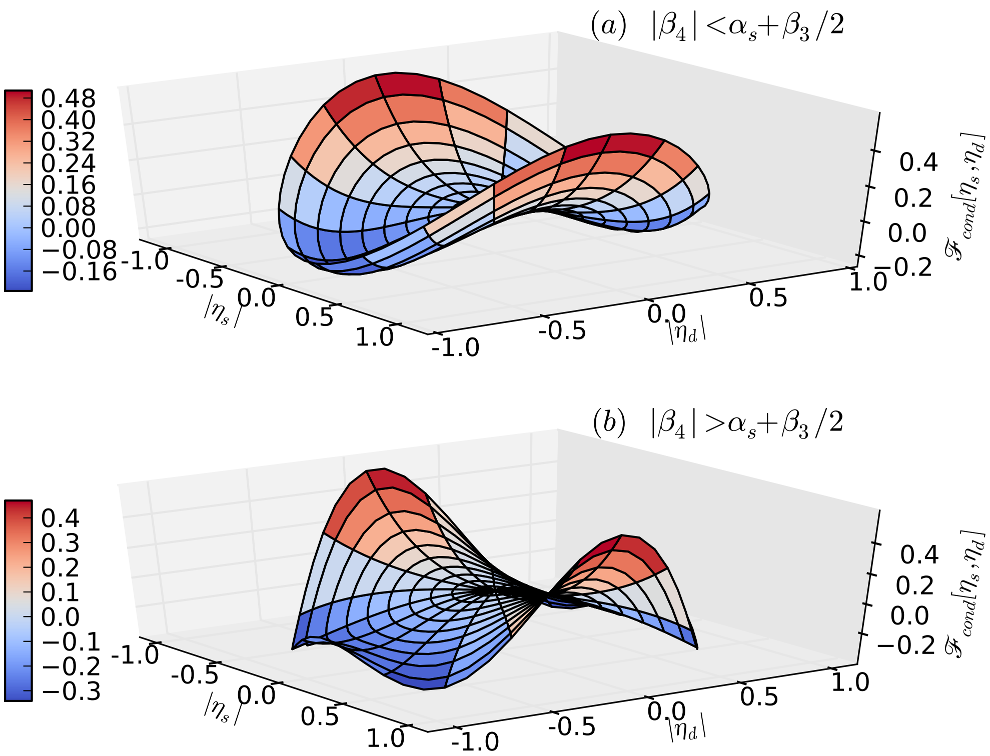

Figure 2.7: Contour plot of the condensation free energy density ($\mathscr{F}_{\rm cond}$) for $d+s$-superconductors. The energy density in panel (a) is bound from below and has its minimum at ($\eta_d = 0$,$|\eta_s| = \alpha_s + \beta_3$). On the other hand the energy density of panel (b) is not bound from below.

reads

$$\mathscr{F}_{\rm cond} = \alpha_s|\eta_s|^2 + \alpha_d|\eta_d|^2 + \beta_1|\eta_s|^4 + \beta_2|\eta_d|^4 + \beta_3|\eta_s|^2|\eta_d|^2 + \beta_4\big(\eta_s^{*2}{\eta_d}^2 + \eta_d^{*2}{\eta_s}^2\big). \tag{2.96}$$

The coefficients α_s, α_d, and β_i with $i = 1-4$, are treated here phenomenologically. However they can be related to microscopic quantities such as the shape of the Fermi surface, the Fermi velocity and the electronic density of states [109]. Since the order parameter η_d is the dominant one [107, 108], one assumes that its T_c is higher than the corresponding one to η_s. That means that while α_d is considered negative, α_s is either positive or negative provided that it can be larger than α_d. In Fig. 2.7 the contour plot of the condensation energy is shown for two different combination of phenomenological coefficients. For simplicity it has been chosen that $\beta_1 = \alpha_s$ and $\beta_2 = |\alpha_d|$. In panel (a) one can see that for the condition $|\beta_4| < \alpha_s + \beta_3/2$, $\mathscr{F}_{\rm cond}$ is bound from below and has one physical minimum at $\eta_s = 0$ and $|\eta_d| = \beta_3/\beta_1 + \alpha_s$. On the other hand, panel (b) shows that $\mathscr{F}_{\rm cond}$ has a saddle point when $|\beta_4| > \alpha_s + \beta_3/2$. The local minimum of panel (a) will be considered further in this work since we are interested only in stable solutions of the d-wave at zero external field.

The terms of the kinetic energy density for $d+s$-wave superconductivity have been reported extensively in the literature [106–109]. They are calculated such as the corresponding terms for chiral p-wave superconductors, outlined in the previous section. They read

$$\mathscr{F}_{\rm kin} = \gamma_s|\mathbf{D}\,\eta_s|^2 + \gamma_d|\mathbf{D}\,\eta_d|^2 + \gamma_\nu\big[(D_y\eta_s)^*(D_y\eta_d) - (D_x\eta_s)^*(D_x\eta_d) + \text{c.c.}\big], \tag{2.97}$$

where the coefficients γ_s, γ_d, and γ_ν are treated phenomenologically here, although one can relate them to the inverse masses of the electrons in the s and d bands, and their corresponding coupling

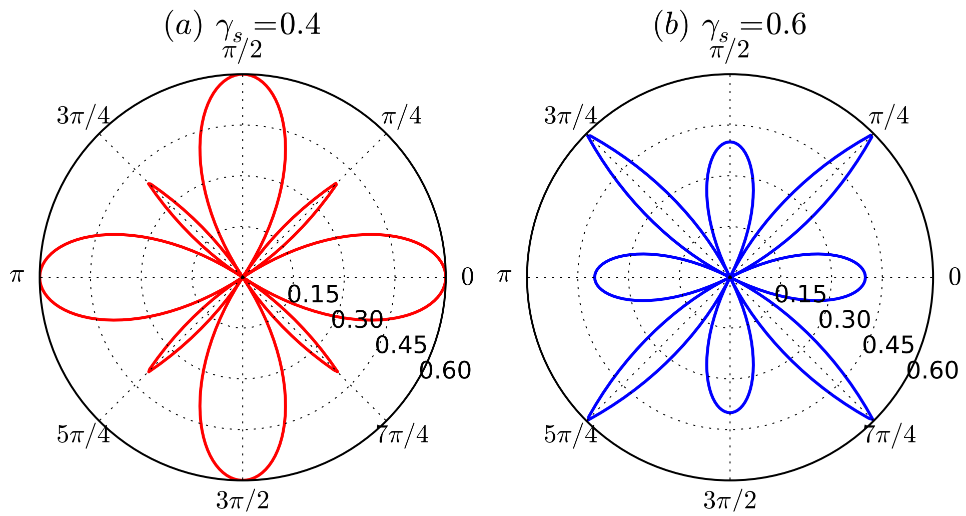

Figure 2.8: Plots of one of the eigenvalues stemming from the bilinear form of the kinetic energy density for d+s-superconductors after Fourier transformation (see main text). The eigenvalue has the four lobe estructure of the Γ_3^+ irreducible representation, but it also has other four lobes at the line nodes of this representation due to the admixture of the s-wave component.

[106, 107]. In order to see that these terms indeed reflect the d+s-wave symmetry, one can calculate the kinetic free energy (F_{kin}) using the Fourier transform, as done in Eq. (2.91) and the text therein,

$$F_{\text{kin}} = \hbar^2 \int d^2\mathbf{k} \left(\tilde{\eta}_s^*(\mathbf{k}), \tilde{\eta}_d^*(\mathbf{k})\right) \begin{bmatrix} \gamma_s \mathbf{k}^2 & \gamma_\nu (k_y^2 - k_x^2) \\ \gamma_\nu (k_y^2 - k_x^2) & \gamma_d \mathbf{k}^2 \end{bmatrix} \begin{pmatrix} \tilde{\eta}_s(\mathbf{k}) \\ \tilde{\eta}_d(\mathbf{k}) \end{pmatrix}, \tag{2.98}$$

where

$$\tilde{\eta}_{s(d)}(\mathbf{k}) = \frac{1}{2\pi} \int d^2\mathbf{r} e^{i\mathbf{k}\cdot\mathbf{r}} \eta_{s(d)}(\mathbf{r}). \tag{2.99}$$

The roots of the secular equation derived from the eigenvalue problem $\widehat{B}\,Y = \omega^{d+s} Y$, where $Y = (\tilde{\eta}_s(\mathbf{k}), \tilde{\eta}_d(\mathbf{k}))^T$, and $\widehat{B} = \begin{bmatrix} \gamma_s \mathbf{k}^2 & \gamma_\nu (k_y^2 - k_x^2) \\ \gamma_\nu (k_y^2 - k_x^2) & \gamma_d \mathbf{k}^2 \end{bmatrix}$, are

$$\omega_\pm^{d+s} = \pm\gamma_s \mathbf{k}^2 - \gamma_\nu |k_y^2 - k_x^2|, \tag{2.100}$$

where for ilustrative reasons $\gamma_s = \gamma_d$ was chosen. In Fig. 2.8 we plot the eigenvalue ω_+^{d+s} in polar coordinates. There is shown that ω_+^{d+s}, and consequently F_{kin}, has the four lobes symmetry of the Γ_3^+ irreducible representation plus another four lobes arising at the line nodes of this representation and owing to the admixture of an s-wave component.

2.3.4 Relevance to other superconductors with multi-component order parameter

The Fermi surface of the iron-based superconductor $Ba_{1-x}K_xFe_2As_2$ is complex and contains many sheets, as shown in Fig. 1.5 for $x = 0.4$. Theoretical and experimental works suggest that at moderate doping ($x \approx 0.4$) the superconductor possesses s-wave symmetry, and at maximum doping ($x = 1$) it possesses both s-wave and d-wave symmetries [110, 111]. Many works have therefore claimed that at $x \leq 1$ an admixture of the two distinct pairings is possible [112, 113]. However, this particular combination of symmetries is distinct from the previously discussed case (d+s-wave), since it breaks the time-reversal symmetry. The community name it $s+id$ to distinguish it from the time-reversal preserving pairing $d+s$-type. On the other hand, the GL free energy for $s+id$ superconductivity resembles that of $d+s$-wave superconductors. It reads

$$\begin{aligned}\mathscr{F} &= \alpha_s|\eta_s|^2 + \alpha_d|\eta_d|^2 + \beta_1|\eta_s|^4 + \beta_2|\eta_d|^4 + \beta_3|\eta_s|^2|\eta_d|^2 + \beta_4\big(\eta_s^{*2}{\eta_d}^2 + \eta_d^{*2}{\eta_s}^2\big) \\ &+ \gamma_s|\mathbf{D}\,\eta_s|^2 + \gamma_d|\mathbf{D}\,\eta_d|^2 + \gamma_\nu\big[(D_x\eta_s)^*(D_x\eta_d) - (D_y\eta_s)^*(D_y\eta_d) + \text{c.c.}\big],\end{aligned} \tag{2.101}$$

where it is assumed that the parameters α_i and β_i of the condensate free energy density are such that the ground state is degenerate [113], i.e. breaks the time-reversal symmetry. The $s+id$ pairing is therefore another example of an unconventional superconductor with particular relevance in the study of multiband superconductivity in the iron-based superconductors and can be addressed using similar theoretical tools to the ones discussed in this thesis.

3
Numerical methods

3.1 Numerical solution of the Bogoliubov-de Gennes equations

The numerical solution of the Bogoliubov-de Gennes (BdG) equations for chiral p-wave superconductivity presented in this thesis follows the same procedure that was applied to conventional superconductivity in Refs. [114] and [115]. In this section a brief description of this procedure is provided. Instead of solving Eqs. (2.61) and (2.62), the BdG equations are solved in the representation where the components of the gap $\Delta_{x,y}$ are substituted by $\Delta_{\pm} = (\Delta_x \pm \Delta_y)/2$. They read

$$\begin{bmatrix} \mathscr{H}_0(\mathbf{r}) & \Pi(\mathbf{r}) \\ -\Pi^*(\mathbf{r}) & -\mathscr{H}_0^*(\mathbf{r}) \end{bmatrix} \begin{pmatrix} u_n(\mathbf{r}) \\ v_n(\mathbf{r}) \end{pmatrix} = \varepsilon_n \begin{pmatrix} u_n(\mathbf{r}) \\ v_n(\mathbf{r}) \end{pmatrix}, \tag{3.1}$$

where the single particle Hamiltonian $\mathscr{H}_0$ is

$$\mathscr{H}_0(\mathbf{r}) = \frac{1}{2m}\left[\frac{\hbar}{i}\nabla - \frac{e}{c}\mathbf{A}\right]^2 - E_{\mathrm{F}}, \tag{3.2}$$

and,

$$\Pi(\mathbf{r}) = -\frac{i}{k_{\mathrm{F}}}\left\{\Delta_+(\mathbf{r})\partial_+ + \Delta_-(\mathbf{r})\partial_- + \frac{1}{2}\Big[\partial_+\Delta_+(\mathbf{r}) + \partial_-\Delta_-(\mathbf{r})\Big]\right\}, \tag{3.3}$$

with $\mathbf{A}$ being the vector potential, $\partial_{\pm} = \partial_x \pm i\partial_y$, and k_{F} (E_{F}) being the Fermi wave length (energy), respectively. The self-consistent conditions (2.72) and (2.72) are correspondingly changed to the $\Delta_{\pm}$ representation, and yield

$$\Delta_{\pm}(\mathbf{r}) = -V_p\Omega\frac{i}{2k_{\mathrm{F}}}\sum_n \left[v_n^*(\mathbf{r})\partial_{\mp}u_n(\mathbf{r}) - u_n(\mathbf{r})\partial_{\mp}v_n^*(\mathbf{r})\right]\tanh\left(\frac{\varepsilon_n}{2T}\right). \tag{3.4}$$

The sample that we consider in this section is a cylinder of radius R and thickness d. However, in the limit of $d \ll \lambda$, physical quantities such as the superconducting current and the magnetic field remain constant along the sample (see Fig. 3.1). As a result, one can treat the system as a quasi-two dimensional sample. Therefore, we can choose polar coordinates for convenience, for this particular geometry. Moreover, we also assume that the cylindrical symmetry of the sample is imposed on the superconducting gap, i.e. we consider the following ansatz for the gap: $\Delta_{\pm}(\mathbf{r}) = \Delta_{\pm}(r)e^{iL_{\pm}\theta}$.

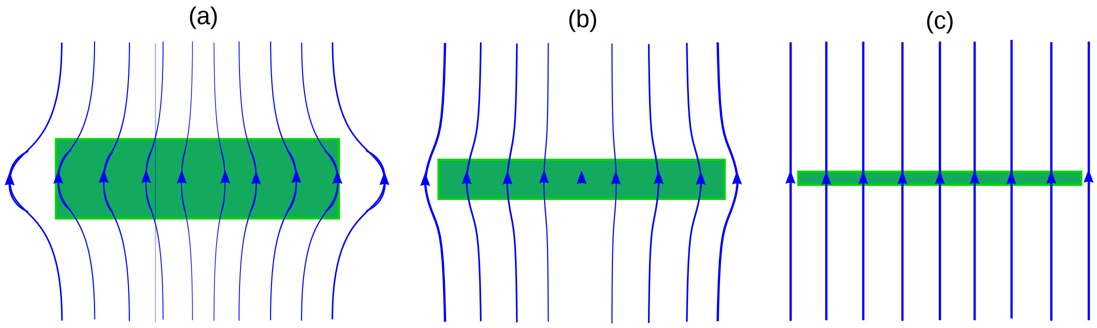

Figure 3.1: Cartoons of superconducting disks showing the side view of three samples with different thickness. The line profiles of their magnetic fields are also shown. The set of samples reveal that the demagnetization effects are smaller for the thinner disks.

This assumption leads to the subsequent expression for the non-diagonal operator $\Pi(\mathbf{r})$ in polar coordinates,

$$\begin{aligned}\Pi(\mathbf{r}) &= -\frac{i}{k_{\mathrm{F}}}\Big\{e^{i(L_{+}+1)\theta}\Big[\Delta_{+}\Big(\frac{\partial}{\partial r}+\frac{i}{r}\frac{\partial}{\partial\theta}\Big)+\frac{1}{2}\Big(\frac{\partial\Delta_{+}}{\partial r}-\frac{L_{+}}{r}\Delta_{+}\Big)\Big] \\ &+ e^{i(L_{-}-1)\theta}\Big[\Delta_{-}\Big(\frac{\partial}{\partial r}-\frac{i}{r}\frac{\partial}{\partial\theta}\Big)+\frac{1}{2}\Big(\frac{\partial\Delta_{-}}{\partial r}+\frac{L_{-}}{r}\Delta_{-}\Big)\Big]\Big\}. \end{aligned} \tag{3.5}$$

On the other hand, in the Coulomb gauge the single-particle Hamiltonian reads

$$\mathscr{H}_0(\mathbf{r}) = \frac{1}{2m}\Big[-\hbar^2\nabla^2 - \frac{2e\hbar}{ic}\mathbf{A}\cdot\nabla + \frac{e^2}{c^2}\mathbf{A}^2\Big] - E_{\mathrm{F}}, \tag{3.6}$$

where the set containing all the eigen-functions stemming from the Hamiltonian $h_0 = -\frac{\hbar^2}{2m}\nabla^2$ forms a complete basis that one can use for the expansion of the quasiparticle wavefunctions of the BdG equations,

$$u_n(\mathbf{r}) = \sum_{\mu,j} c_{n\,\mu,j}\phi_{j,\mu}(\mathbf{r}), \qquad v_n(\mathbf{r}) = \sum_{\mu',j'} d_{n\,\mu',j'}\phi_{j',\mu'}(\mathbf{r}). \tag{3.7}$$

The eigen-functions $\phi_{j,\mu}(\mathbf{r}) = \varphi_{j,\mu}(r)\frac{e^{i\mu\theta}}{\sqrt{2\pi}}$, which are composed of separate radial and azimuthal parts are demanded to be orthonormal, i.e. $\int d^2\mathbf{r}\,\phi^{*}_{j',\mu'}(\mathbf{r})\phi_{j,\mu}(\mathbf{r}) = \delta^{\mu'}_{\mu}\delta^{j'}_{j}$. They have the eigen-energies $\epsilon_{j,\mu} = \hbar^2\alpha^2_{j,\mu}/2mR^2$, where $\alpha_{j,\mu}$ are the zeros of the μth Bessel function of the first kind [$J_\mu(r)$]. The radial part of the eigen-functions reads

$$\varphi_{j,\mu}(r) = \frac{\sqrt{2}}{RJ_{\mu+1}(\alpha_{j,\mu})}J_\mu\Big(\alpha_{j,\mu}\frac{r}{R}\Big). \tag{3.8}$$

Replacing the expansions of the quasiparticle wavefunctions back into the BdG equations (3.1), and projecting the resultant quantum state into the base vector $\phi_{l,\nu}(\mathbf{r})$, one obtains the following set of linear equations

$$\begin{aligned}\sum_{\mu,j}\langle l,\nu|\mathscr{H}_0|j,\mu\rangle c_{n\,\mu,j} + \sum_{\mu',j'}\langle l,\nu|\Pi|j',\mu'\rangle d_{n\,\mu',j'} &= \sum_{\mu,j}\varepsilon_n c_{n\,\mu,j}\delta^{l}_{j}\delta^{\nu}_{\mu}, \\ -\sum_{\mu,j}\langle l,\nu|\Pi^{*}|j,\mu\rangle c_{n\,\mu,j} - \sum_{\mu',j'}\langle l,\nu|\mathscr{H}_0^{*}|j',\mu'\rangle d_{n\,\mu',j'} &= \sum_{\mu',j'}\varepsilon_n d_{n\,\mu',j'}\delta^{l}_{j'}\delta^{\nu}_{\mu'}, \end{aligned} \tag{3.9}$$

where

$$\langle l,\nu|\mathscr{H}_0|j,\mu\rangle = \int d^2\mathbf{r}\,\phi^*_{l,\nu}(\mathbf{r})\mathscr{H}_0(\mathbf{r})\phi_{j,\mu}(\mathbf{r}), \tag{3.10}$$

$$\langle l,\nu|\Pi|j',\mu'\rangle = \int d^2\mathbf{r}\,\phi^*_{l,\nu}(\mathbf{r})\Pi(\mathbf{r})\phi_{j,\mu}(\mathbf{r}), \tag{3.11}$$

and $\langle l,\nu|\Pi^*|j,\mu\rangle$, $\langle l,\nu|\mathscr{H}_0^*|j',\mu'\rangle$ can be obtained in a similar way straightforwardly.

In the quasi-two dimensional limit ($d \ll \lambda$) the magnetic field is constant along the sample and one can obtain that the vector potential becomes $\mathbf{A} = \frac{\mathbf{H}\times\mathbf{r}}{2}$, or $\mathbf{A} = \frac{Hr}{2}\hat{\theta}$, in polar coordinates. This expression reduces the complexity of the problem and facilitates the calculation of the matricial elements deriving from the single particle Hamiltonian and its complex conjugate,

$$\begin{aligned}\langle l,\nu|\mathscr{H}_0|j,\mu\rangle &= \Big\{\Big[\frac{\hbar^2\alpha^2_{j,\mu}}{2mR^2} - E_{\mathrm{F}} - \frac{\hbar e}{mc}\frac{H}{2}\mu\Big]\delta^l_j \\ &+ \frac{e^2}{2mc^2}\frac{H^2}{4}\int dr r^3\varphi_{l,\nu}(r)\varphi_{j,\mu}(r)\Big\}\delta^\nu_\mu,\end{aligned} \tag{3.12}$$

and

$$\begin{aligned}\langle l,\nu|\mathscr{H}_0^*|j',\mu'\rangle &= \Big\{\Big[\frac{\hbar^2\alpha^2_{j',\mu'}}{2mR^2} - E_{\mathrm{F}} + \frac{\hbar e}{mc}\frac{H}{2}\mu'\Big]\delta^l_{j'} \\ &+ \frac{e^2}{2mc^2}\frac{H^2}{4}\int dr r^3\varphi_{l,\nu}(r)\varphi_{j',\mu'}(r)\Big\}\delta^\nu_{\mu'}.\end{aligned} \tag{3.13}$$

On the other hand, the matricial elements deriving from the operator Π, and its complex conjugate Π^*, read

$$\begin{aligned}&\langle l,\nu|\Pi|j',\mu'\rangle = \\ &-\tfrac{i}{k_{\mathrm{F}}}\int dr r\varphi_{l,\nu}\Big[\Delta_+\tfrac{\partial\varphi_{j',\mu'}}{\partial r} + \tfrac{\varphi_{j',\mu'}}{2}\tfrac{\partial\Delta_+}{\partial r} - \Delta_+\tfrac{\varphi_{j',\mu'}}{r}\big(\mu' + \tfrac{L_+}{2}\big)\Big]\delta^\nu_{\mu'+L_++1} \\ &-\tfrac{i}{k_{\mathrm{F}}}\int dr r\varphi_{l,\nu}\Big[\Delta_-\tfrac{\partial\varphi_{j',\mu'}}{\partial r} + \tfrac{\varphi_{j',\mu'}}{2}\tfrac{\partial\Delta_-}{\partial r} + \Delta_-\tfrac{\varphi_{j',\mu'}}{r}\big(\mu' + \tfrac{L_-}{2}\big)\Big]\delta^\nu_{\mu'+L_--1},\end{aligned} \tag{3.14}$$

and,

$$\begin{aligned}&\langle l,\nu|\Pi^*|j,\mu\rangle = \\ &\tfrac{i}{k_{\mathrm{F}}}\int dr r\varphi_{l,\nu}\Big[\Delta^*_+\tfrac{\partial\varphi_{j,\mu}}{\partial r} + \tfrac{\varphi_{j,\mu}}{2}\tfrac{\partial\Delta^*_+}{\partial r} + \Delta^*_+\tfrac{\varphi_{j,\mu}}{r}\big(\mu - \tfrac{L_+}{2}\big)\Big]\delta^\nu_{\mu-L_+-1} \\ &+\tfrac{i}{k_{\mathrm{F}}}\int dr r\varphi_{l,\nu}\Big[\Delta^*_-\tfrac{\partial\varphi_{j,\mu}}{\partial r} + \tfrac{\varphi_{j,\mu}}{2}\tfrac{\partial\Delta^*_-}{\partial r} - \Delta^*_-\tfrac{\varphi_{j,\mu}}{r}\big(\mu - \tfrac{L_-}{2}\big)\Big]\delta^\nu_{\mu-L_-+1},\end{aligned} \tag{3.15}$$

where one can easily note that due to the separable form of the ansatz for the gap, $L_- - L_+ = 2$. This fact leads to the reduction of the number of independent parameters existing in the model and subsequently to the speed up of the numerical algorithm. Moreover, from the comparison of the nonzero elements of Eqs. (3.12) and (3.14) [or (3.13) and (3.15)], another reduction of independent parameters is obtained for the BdG equations. That reduction follows from the equation $\mu' = \mu - L_+ - 1$.

In order to demonstrate how the numerical algorithm works we calculate the Hamiltonian and the eigen-vector arising from the set of linear Eqs. (3.9) when $(L_+, L_-) = (0, 2)$. They read

$$\mathscr{H} = \left[\begin{array}{ccccc|ccccc} \hat{H}_0 & & & & & \ddots & & & & \\ & \hat{H}_1 & & & & \hat{\Pi}_{1,0} & \ddots & & & \\ & & \hat{H}_2 & & & & \hat{\Pi}_{2,1} & \ddots & & \\ & & & \hat{H}_3 & & & & \hat{\Pi}_{3,2} & \ddots & \\ & & & & \ddots & & & & \ddots & \ddots \\ \hline \ddots & -\hat{\Pi}^*_{0,1} & & & & -\hat{H}^*_0 & & & & \\ & \ddots & -\hat{\Pi}^*_{1,2} & & & & -\hat{H}^*_1 & & & \\ & & \ddots & -\hat{\Pi}^*_{2,3} & & & & -\hat{H}^*_2 & & \\ & & & \ddots & \ddots & & & & -\hat{H}^*_3 & \\ & & & & \ddots & & & & & \ddots \end{array}\right], \tag{3.16}$$

and

$$\psi_n = \left(\mathbf{c}_{n\,0},\, \mathbf{c}_{n\,1},\, \mathbf{c}_{n\,2},\, \mathbf{c}_{n\,3},\, \cdots, \mathbf{d}_{n\,0},\, \mathbf{d}_{n\,1},\, \mathbf{d}_{n\,2},\, \mathbf{d}_{n\,3}, \cdots\right)^T, \tag{3.17}$$

with $\hat{H}_\alpha$, $\hat{\Pi}_{\alpha,\alpha-1}$, $\hat{H}^*_\alpha$, and $\hat{\Pi}^*_{\alpha,\alpha+1}$, being the submatrices $\langle l,\alpha|\mathscr{H}_0|j,\alpha\rangle$, $\langle l,\alpha|\Pi|j',\alpha-1\rangle$, $\langle l,\alpha|\mathscr{H}_0^*|j',\alpha\rangle$, and $\langle l,\alpha|\Pi^*|j,\alpha+1\rangle$, respectively. Moreover, $\mathbf{c}_{n\,\alpha}$ and $\mathbf{d}_{n\,\alpha}$ are subvectors with the corresponding components $(c_{n\,\alpha,0}, c_{n\,\alpha,1}, c_{n\,\alpha,2}, \cdots)^T$ and $(d_{n\,\alpha,0}, d_{n\,\alpha,1}, d_{n\,\alpha,2}, \cdots)^T$, respectively. Owing to the particular block structure of the Hamiltonian (3.16), one can decompose this large matrix into a set of 2×2 matrices and write the BdG equations as

$$\begin{bmatrix} \hat{H}_\alpha & \hat{\Pi}_{\alpha,\alpha-1} \\ -\hat{\Pi}^*_{\alpha-1,\alpha} & -\hat{H}^*_{\alpha-1} \end{bmatrix} \begin{pmatrix} \mathbf{c}_{n\,\alpha} \\ \mathbf{d}_{n\,\alpha-1} \end{pmatrix} = \varepsilon_n \begin{pmatrix} \mathbf{c}_{n\,\alpha} \\ \mathbf{d}_{n\,\alpha-1} \end{pmatrix}. \tag{3.18}$$

The expansion of the quasiparticle wavefunctions [see Eq. (3.7)] is infinite, and consequently so is the dimension of matrix (3.16), rendering the BdG equations impractical to solve for any numerical algorithm. However, due to the instability of the Fermi surface toward the formation of Cooper pairs, only states within the Debye window make major contributions to the superconducting gap. Thus, one can select a finite number of basis states that lie within this window and obtain a reliable approximation of the gap. Precisely, this is obtained iteratively after the eigenvectors and eigenvalues of the set of BdG Eqs. (3.18) are calculated. The iteration starts with a trial gap and ends when the relative convergence between two neighbor iterations is below some limit, typically 10^{-5} meV. The BdG equations have a discrete symmetry that is worth mentioning since it allows one to speed up the numerical algorithm. It is the time reversal relation

$$\{u_{-\varepsilon_n}, v_{-\varepsilon_n}\} = \{v^*_{\varepsilon_n}, u^*_{-\varepsilon_n}\}, \tag{3.19}$$

which enables us to obtain the quasiparticle excitation spectrum for negative angular momenta from that with positive angular momenta.

3.2 Finite difference method for the Ginzburg-Landau equations of p-wave superconductivity

In this thesis the GL equations for chiral p-wave superconductivity are solved using the time-dependent (TDGL) approach. TDGL equations introduce temporal evolution in the stationary GL equations of conventional superconductors [see Eqs. (1.4) and (1.5)], and for chiral p-wave superconductivity they read

$$\frac{\hbar^2}{2m^*D}\Big(\frac{\partial}{\partial t}+i\frac{e^*}{\hbar}\varphi\Big)\mathbf{\Psi} = -\frac{\delta\mathscr{F}}{\delta\mathbf{\Psi}^*}, \tag{3.20}$$

$$\frac{\sigma}{c}\Big(\frac{1}{c}\frac{\partial\mathbf{A}}{\partial t}+\nabla\varphi\Big) = -\frac{\delta\mathscr{F}}{\delta\mathbf{A}}-\frac{1}{4\pi}\nabla\times\nabla\times\mathbf{A}\,, \tag{3.21}$$

where the free energy $\mathscr{F}=\mathscr{F}_{cond}+\mathscr{F}_{kin}$ is given by Eqs. (2.87) and (2.90), D is a phenomenological diffusion coefficient, σ the normal conductivity, and φ the electrostatic potential. The TDGL equations are strictly valid only for gapless superconductors [116]. However, for conventional superconductivity they have proven to describe well the slow moving vortices in the mixed state regime [117]. For dirty superconductors there exists another generalized TDGL equation, taking into account the inelastic scattering [118].

The TDGL equations are gauge invariant, i.e. under the transformation $\big(\mathbf{\Psi}',\mathbf{A}',\varphi'\big)=\big(\mathbf{\Psi}e^{\frac{ie^*}{\hbar c}\chi},\mathbf{A}+\nabla\chi,\varphi-\frac{1}{c}\frac{\partial\chi}{\partial t}\big)$ they remain invariant for any arbitrary function χ. That allows one to simplify the TDGL equations by properly chosing the arbitrary function (gauge fixing). In what follows we present the two gauge choices considered in this thesis.

3.2.1 Zero-electrostatic potential gauge

The zero-electrostatic potential gauge is the most convenient choice for the TDGL equations when neither charges nor external currents are considered in the superconducting sample. From the original fields $\big(\mathbf{\Psi},\mathbf{A},\varphi\big)$ the arbitrary function χ is required to satisfy the equation $\frac{1}{c}\frac{\partial\chi}{\partial t}=\varphi$. This choice imposes the transformed electrostatic potential to vanish, $\varphi'=0$, reducing considerably the complexity of the TDGL equations for the transformed fields:

$$\frac{\hbar^2}{2m^*D}\frac{\partial\mathbf{\Psi}'}{\partial t} = -\frac{\delta\mathscr{F}\big[\mathbf{\Psi}',\mathbf{\Psi}'^*,\mathbf{A}\big]}{\delta\mathbf{\Psi}'^*}, \tag{3.22}$$

$$\frac{\sigma}{c^2}\frac{\partial\mathbf{A}'}{\partial t} = -\frac{\delta\mathscr{F}}{\delta\mathbf{A}'}-\frac{1}{4\pi}\nabla\times\nabla\times\mathbf{A}'\,. \tag{3.23}$$

For the numerical algorithm that solves the TDGL equations it is convenient to work with dimensionless quantities. That is achieved by scaling the distance in units of the coherence length $\xi=\sqrt{\frac{\hbar^2}{2m^*|\alpha|}}$, time in units of the GL time $t_0=\xi^2/D$, the magnetic field in units of the bulk upper critical field $H_{c2}=\frac{\hbar c}{e^*\xi^2}$, the order parameter scaled to its bulk value in absence of magnetic field $\Delta_0=\sqrt{\frac{|\alpha|}{\beta_1-\beta_2}}$, and the free energy density to $\mathscr{F}_0=\frac{\hbar^2\Delta_0^2}{2m^*\xi^2}$. The dimensionless TDGL equations in the zero-electrostatic potential gauge thus become

$$\frac{\partial\mathbf{\Psi}}{\partial t} = -\frac{\delta\mathscr{F}}{\delta\mathbf{\Psi}^*}, \tag{3.24}$$

$$\sigma\frac{\partial\mathbf{A}}{\partial t} = -\frac{1}{2}\frac{\delta\mathscr{F}}{\delta\mathbf{A}}-\kappa^2\nabla\times\nabla\times\mathbf{A}\,, \tag{3.25}$$

where for convenience we have dropped all the primes and σ is the dimensionless normal conductivity, scaled to $\sigma_0=\frac{c^2t_0}{4\pi\lambda^2}$. The dimensionless free energy density reads

$$\mathscr{F} = \tfrac{k_0+k_1}{4}\left\{|\mathbf{D}\psi_+|^2+|\mathbf{D}\psi_-|^2\right\}+(k_2+k_3)\mathrm{Re}\left\{\Pi_+\psi_-(\Pi_-\psi_+)^*\right\} + \tag{3.26}$$
$$\tfrac{k_2-k_3}{2}\mathrm{Re}\left\{i\Big[D_x\psi_+(D_y\psi_+)^* - D_x\psi_-(D_y\psi_-)^*\Big]\right\}+\tfrac{k_4}{2}\left\{|D_z\psi_+|^2+|D_z\psi_-|^2\right\}$$
$$-\tfrac{1}{2}\left(|\psi_+|^2+|\psi_-|^2\right)+\tfrac{1+\tau}{4}\left(|\psi_+|^2+|\psi_-|^2\right)^2-\tfrac{\tau}{4}\left(|\psi_+|^2-|\psi_-|^2\right)^2,$$

where $\tau = \frac{\beta_2}{\beta_1-\beta_1}$, the dimensionless covariant derivative is $\mathbf{D} = \nabla - i\mathbf{A}$ and we took $\beta_3 = 0$ [103]. The geometry of the sample to be solved with TDGL equations of chiral p-wave superconductivity is rectangular and thin. Moreover, an external magnetic field is applied perpendicularly to the plane of the sample. Assuming the demagnetization field is vanishing due to the small thickness of the sample in comparison to λ, one can treat the system as quasi-two-dimensional. In this case the dimensionless TDGL equations read

$$\begin{aligned}
\frac{\partial \mathbf{\Psi}}{\partial t} &= \frac{1}{2}\begin{bmatrix} \frac{k_0+k_1}{2}\mathbf{D}^2+\frac{k_2-k_3}{2i}[D_x,D_y] & (k_2+k_3)\,\Pi_+^2 \\ (k_2+k_3)\,\Pi_-^2 & \frac{k_0+k_1}{2}\mathbf{D}^2-\frac{k_2-k_3}{2i}[D_x,D_y]\end{bmatrix}\begin{pmatrix}\psi_+\\ \psi_-\end{pmatrix} \\
&+ \mathbf{\Psi}\left(\frac{1}{2}-\frac{1+\tau}{2}|\mathbf{\Psi}|^2 \pm \frac{\tau}{2}\mathbf{\Psi}^*\hat{\sigma}_z\mathbf{\Psi}\right), \qquad (3.27)\\
\sigma\frac{\partial \mathbf{A}}{\partial t} &= \mathbf{J}-\kappa^2\nabla\times\nabla\times\mathbf{A}\,, \qquad (3.28)
\end{aligned}$$

where [ ] denotes the commutator and $\mathbf{J}$ the superconducting current density

$$\begin{aligned}
\mathbf{J} &= \mathrm{Im}\left\{\frac{k_0+k_1}{4}\Big(\psi_+^*\mathbf{D}\psi_+ + \psi_-^*\mathbf{D}\psi_-\Big)+\frac{k_2+k_3}{2\sqrt{2}}\Big(\mathbf{\Psi}^*\Big[\Pi_+\hat{\sigma}_+ + \Pi_-\hat{\sigma}_-\Big]\mathbf{\Psi}\hat{\imath}\right. \qquad (3.29)\\
&+ \left. i\,\mathbf{\Psi}^*\Big[\Pi_+\hat{\sigma}_+ - \Pi_-\hat{\sigma}_-\Big]\mathbf{\Psi}\,\hat{\jmath}\Big)\right\} - \frac{k_2-k_3}{4}\mathrm{Re}\left\{\hat{\mathrm{k}}\times\big(\psi_+^*\mathbf{D}\psi_+ - \psi_-^*\mathbf{D}\psi_-\big)\right\}.
\end{aligned}$$

Here $\hat{\sigma}_\pm = (\sigma_x \pm i\sigma_y)/2$ are pseudospin or chiral operators acting on the space span by $\psi_\pm$. The boundary conditions for the TDGL Eqs. (3.27) and (3.28), and compatible with the existence of spontaneous edge currents, are [94]

$$\begin{aligned}
&\left.\begin{aligned}\psi_+ - \psi_- &= 0\\ D_y\psi_+ + D_y\psi_- &= 0\end{aligned}\right\} \quad \text{at the north and south sides,}\\
&\left.\begin{aligned}\psi_+ + \psi_- &= 0\\ D_x\psi_+ - D_x\psi_- &= 0\end{aligned}\right\} \quad \text{at the east and west sides,}\\
&(\nabla\times\mathbf{A})\cdot\hat{n} = H, \qquad (3.30)
\end{aligned}$$

where $\hat{n}$ is the unitary vector normal to the sample surface. With these boundary conditions the problem is well posed and one can solve the TDGL equations with a numerical algorithm. In this thesis we use the finite difference method and the link variables technique. The discretization of kinetic terms such as $\mathbf{D}^2\psi_\pm$ has been reported elsewhere [119, 120], but that of $\mathbf{\Pi}_\pm^2\psi_a$ was not. It reads

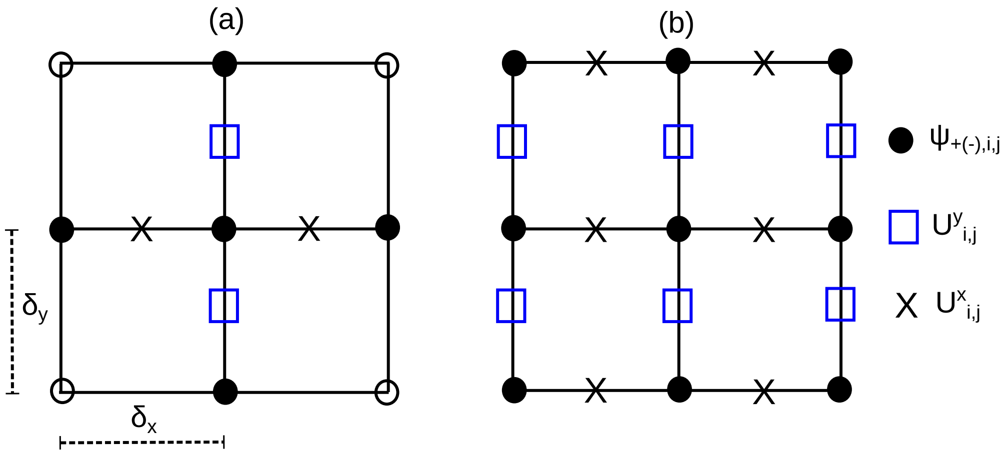

Figure 3.2: Comparison of (a) the five-point stencil discretization of the operator $\mathbf{D}^2$*, and (b) the nine-point stencil of* $\Pi_\pm^2$*.*

$$
\begin{aligned}
\mathbf{\Pi}_\pm^2 \psi_\mp &= \frac{1}{2}(D_x \pm iD_y)(D_x \pm iD_y)\psi_\mp, \qquad (3.31)\\
&= \frac{1}{2}\big(D_x^2 - D_y^2 \pm i\big[D_x D_y + D_y D_x\big]\big)\psi_\mp,\\
&= \frac{U_{i,j}^x \psi_{\mp,\,i+1,j} - 2\psi_{\mp,\,i,j} + \bar{U}_{i-1,j}^x \psi_{\mp,\,i-1,j}}{2\delta_x^2}\\
&- \frac{U_{i,j}^y \psi_{\mp,\,i,j+1} - 2\psi_{\mp,\,i,j} + \bar{U}_{i,j-1}^y \psi_{\mp,\,i,j-1}}{2\delta_y^2}\\
&\pm iU_{i,j}^x \frac{U_{i+1,j}^y \psi_{\mp,\,i+1,j+1} - \bar{U}_{i+1,j-1}^y \psi_{\mp,\,i+1,j-1}}{8\delta_x\delta_y}\\
&\mp i\bar{U}_{i-1,j}^x \frac{U_{i-1,j}^y \psi_{\mp,\,i-1,j+1} - \bar{U}_{i-1,j-1}^y \psi_{\mp,\,i-1,j-1}}{8\delta_x\delta_y}\\
&\pm iU_{i,j}^y \frac{U_{i,j+1}^x \psi_{\mp,\,i+1,j+1} - \bar{U}_{i-1,j+1}^x \psi_{\mp,\,i-1,j+1}}{8\delta_x\delta_y}\\
&\mp i\bar{U}_{i,j-1}^y \frac{U_{i,j-1}^x \psi_{\mp,\,i+1,j-1} - \bar{U}_{i-1,j-1}^x \psi_{\mp,\,i-1,j-1}}{8\delta_x\delta_y} + \mathcal{O}(\delta\mathbf{r}^3),
\end{aligned}
$$

where $U_{i,j}^x = e^{-i\delta_x A_{x,\,i,j}}$, and $U_{i,j}^y = e^{-i\delta_y A_{y,\,i,j}}$ are the link variables, $\bar{U}_{i,j}^x$ and $\bar{U}_{i,j}^y$ their complex conjugates, and δ_x, δ_y the widths of the mesh shown in Fig. 3.2. There one can see that the second-order finite difference approach for $\mathbf{\Pi}_\pm^2\psi_a$ contains nine grid points, unlike the five points stencil approach for $\mathbf{D}^2\psi_\pm$. The commutator term in Eq. (3.27) can be simplified further with a straightforward calculation, $[D_x, D_y] = -i(\partial_x A_y - \partial_y A_x) = -iB_z$, and thus its discretization becomes simpler. Finally, the discretization of Eq. (3.28) reads

$$
\begin{aligned}
A_{x,\,i,j}^{n+1} - A_{x,\,i,j}^n &= \frac{\Delta t}{\sigma} J_{x,\,i,j} - \frac{\kappa^2 \Delta t}{\sigma\delta_y}\big(B_{z,\,i,j}^n - B_{z,\,i,j-1}^n\big), \qquad (3.32)\\
A_{y,\,i,j}^{n+1} - A_{y,\,i,j}^n &= \frac{\Delta t}{\sigma} J_{y,\,i,j} + \frac{\kappa^2 \Delta t}{\sigma\delta_x}\big(B_{z,\,i,j}^n - B_{z,\,i-1,j}^n\big), \qquad (3.33)
\end{aligned}
$$

where

$$
\begin{aligned}
J_{x,i,j} &= \mathrm{Im}\sum_{\alpha=\pm}\Big\{\frac{k_0+k_1}{4}\psi^*_{\alpha,i,j}\Big[\frac{U^x_{i,j}\psi_{\alpha,i+1,j}-\bar{U}^x_{i-1,j}\psi_{\alpha,i-1,j}}{2\delta_x}\Big]+\frac{k_2+k_3}{4}\psi^*_{\alpha,i,j}\\
&\times \Big[\frac{U^x_{i,j}\psi_{-\alpha,i+1,j}-\bar{U}^x_{i-1,j}\psi_{-\alpha,i-1,j}}{2\delta_x}+i\alpha\frac{U^y_{i,j}\psi_{-\alpha,i,j+1}-\bar{U}^y_{i,j-1}\psi_{-\alpha,i,j-1}}{2\delta_y}\Big]\Big\}\\
&+ \mathrm{Re}\sum_{\alpha=\pm}\alpha\frac{k_2-k_3}{4}\psi^*_{\alpha,i,j}\frac{U^y_{i,j}\psi_{\alpha,i,j+1}-\bar{U}^y_{i,j-1}\psi_{\alpha,i,j-1}}{2\delta_y},
\end{aligned}
\tag{3.34}
$$

$$
\begin{aligned}
J_{y,i,j} &= \mathrm{Im}\sum_{\alpha=\pm}\Big\{\frac{k_0+k_1}{4}\psi^*_{\alpha,i,j}\Big[\frac{U^y_{i,j}\psi_{\alpha,i+1,j}-\bar{U}^y_{i-1,j}\psi_{\alpha,i-1,j}}{2\delta_x}\Big]+\frac{k_2+k_3}{4}\psi^*_{\alpha,i,j}\\
&\times \Big[\alpha\frac{U^x_{i,j}\psi_{-\alpha,i+1,j}-\bar{U}^x_{i-1,j}\psi_{-\alpha,i-1,j}}{2\delta_x}+i\frac{U^y_{i,j}\psi_{-\alpha,i,j+1}-\bar{U}^y_{i,j-1}\psi_{-\alpha,i,j-1}}{2\delta_y}\Big]\Big\}\\
&- \mathrm{Re}\sum_{\alpha=\pm}\alpha\frac{k_2-k_3}{4}\psi^*_{\alpha,i,j}\frac{U^x_{i,j}\psi_{\alpha,i,j+1}-\bar{U}^x_{i,j-1}\psi_{\alpha,i,j-1}}{2\delta_x},
\end{aligned}
\tag{3.35}
$$

and $B^n_{z,i,j}$ is the local magnetic field calculated using first-order finite differences,

$$
B_{z,i,j} = \frac{A_{y,i+1,j}-A_{y,i,j}}{\delta_x} - \frac{A_{x,i,j+1}-A_{x,i,j}}{\delta_y}. \tag{3.36}
$$

In Eqs. (3.32) and (3.33) the superindex n stands for the discretized time index. That means that $A^{n+1}_{x,i,j}$ and $A^n_{x,i,j}$ are two subsequent local values of the vector potential separated by the time interval Δt. The solution of these equations can be done within an implicit method e.g. the Crank-Nicolson one, semi-implicit or explicit. In this thesis we opted for an explicit method, where $\Delta t \leq \min\{\frac{\mathcal{O}^2}{4}, \frac{\mathcal{O}^2}{4\kappa^2}\}$, with $\mathcal{O}^2 = \frac{2}{\delta_x^{-2}+\delta_y^{-2}}$.

3.2.2 Coulomb gauge

The Coulomb gauge, unlike the zero-electrostatic potential gauge, is the most convenient choice when an external current is applied to the superconducting sample [121, 122]. In this case the arbitrary function is required to satisfy the equation $\Delta\chi + \nabla\cdot\mathbf{A} = 0$, which makes the transformed vector potential $\mathbf{A}'$ divergence-free. This fact, combined with the operation of taking the divergence of Eq. (4.3) leads to the TDGL equations in dimensionless units for the Coulomb gauge

$$
\Big(\frac{\partial}{\partial t}+i\varphi\Big)\mathbf{\Psi} = -\frac{\delta\mathscr{F}}{\delta\mathbf{\Psi}^*}, \tag{3.37}
$$

$$
\sigma\Delta\varphi = \nabla\cdot\mathbf{J}, \tag{3.38}
$$

where the second TDGL equation is for the electrostatic potential rather than the vector potential such as in Eq. (3.28). The vector potential in this case is obtained from the gauge choice $\nabla\cdot\mathbf{A} = 0$. The boundary conditions for the fields $\mathbf{\Psi}$ and φ in a superconducting nanobridge linking two normal leads located at the north and south sides, and which are used to apply current into the superconducting sample are

$$\left.\begin{array}{r}\psi_{\pm}=0\\ \partial_y\varphi+j_n=0\end{array}\right\}\quad\text{at north and south sides,}$$

$$\left.\begin{array}{r}\psi_{+}+\psi_{-}=0\\ D_x\psi_{+}-D_x\psi_{-}=0\\ \partial_x\varphi=0\end{array}\right\}\quad\text{at east and west sides,}\tag{3.39}$$

where j_n denotes the normal current density. The TDGL equations (3.37) and (3.38) are numerically solved with finite differences and the link variable technique, where the discretization of the operators appearing in the first TDGL equation follows that of the previous section. The second equation is solved using the highly optimized Intel MKL routines for Fourier transformation, with the discretization for the superconducting current density as given in Eqs. (3.34) and (3.35).

3.3 Finite difference method for the Ginzburg-Landau equations of $d+s$-wave superconductivity

Although this thesis is devoted to the study of chiral p-wave superconductivity, the GL equations for $d+s$-wave superconductors provide an example of a gap symmetry with admixture of two distinct Cooper pairings. These GL equations can be solved following a procedure similar to that for p-wave superconductors, and the description of the numerical algorithm has value to several superconducting compounds outside the ones considered in the thesis. In this case the TDGL equations in dimensionless units read

$$\begin{aligned}\gamma_d\left(\frac{\partial}{\partial t}+i\varphi\right)\eta_d &= \gamma_d\mathbf{D}^2\eta_d+\gamma_\nu(D_y^2-D_x^2)\eta_s\\ &+ \eta_d-|\eta_d|^2\eta_d-\frac{\tau_3}{2}|\eta_s|^2\eta_d-\tau_4\eta_s^2\eta_d^*\ , \qquad (3.40)\\ \gamma_s\left(\frac{\partial}{\partial t}+i\varphi\right)\eta_s &= \gamma_s\mathbf{D}^2\eta_s+\gamma_\nu(D_y^2-D_x^2)\eta_d\\ &- \nu\eta_s-\tau_1|\eta_s|^2\eta_s-\frac{\tau_3}{2}|\eta_d|^2\eta_s-\tau_4\eta_d^2\eta_s^*\ , \qquad (3.41)\\ \sigma\left(\frac{\partial\mathbf{A}}{\partial t}+\nabla\varphi\right) &= \mathbf{J}-\kappa^2\nabla\times\nabla\times\mathbf{A}\ , \qquad (3.42)\end{aligned}$$

where

$$\begin{aligned}\mathbf{J} &= \mathrm{Im}\left\{\gamma_d\eta_d^*\mathbf{D}\eta_d+\gamma_s\eta_s^*\mathbf{D}\eta_s\right\}\\ &- \mathrm{Im}\Big\{\gamma_\nu\left[\eta_d^*D_x\eta_s+\eta_s^*D_x\eta_d\right]\hat{\imath}-\gamma_\nu\left[\eta_d^*D_y\eta_s+\eta_s^*D_y\eta_d\right]\hat{\jmath}\Big\},\end{aligned}\tag{3.43}$$

and the dimensionless phenomenological parameters are: $\nu=\frac{\alpha_s}{|\alpha_d|}$, and $\tau_i=\frac{\beta_i}{\beta_2}$, with $i=1,3,4$. In Eqs. (3.40) - (3.42) the distance is measured in units of the coherence length $\xi_d=\sqrt{\frac{\hbar^2}{2m^*|\alpha_d|}}$, time in units of the GL time $t_{0d}=\frac{\xi_d^2}{D}$, the magnetic field is scaled to the bulk upper critical field $H_{c2}=\frac{\hbar c}{e^*\xi_d^2}$, the electrostatic potential to $\varphi_{0d}=\frac{\hbar}{e^*t_{0d}}$, the order parameter to its bulk value $\eta_{d0}=\sqrt{\frac{|\alpha_d|}{2\beta_2}}$, and the free energy density to $\mathscr{F}_{0d}=\frac{\hbar^2\eta_{d0}^2}{2m^*\xi_d^2}$. Moreover, $\kappa=\frac{\lambda_d}{\xi_d}$ is the GL parameter where $\lambda_d=\sqrt{\frac{m^*c^2}{4\pi e^{*2}\eta_{d0}^2}}$ is the London penetration depth. The boundary conditions for the components of the order parameter and the vector potential in the sample considered here, namely a thin rectangular sample with an external magnetic field applied perpendicularly, read

$$
\begin{aligned}
&\left.\begin{aligned}\gamma_d D_y \eta_d + \gamma_\nu D_y \eta_s = 0\\ \gamma_s D_y \eta_s + \gamma_\nu D_y \eta_d = 0\end{aligned}\right\} \quad \text{at the north and south sides,}\\
&\left.\begin{aligned}\gamma_d D_x \eta_d - \gamma_\nu D_x \eta_s = 0\\ \gamma_s D_x \eta_s - \gamma_\nu D_x \eta_d = 0\end{aligned}\right\} \quad \text{at the east and west sides,}\\
&\qquad\qquad (\nabla \times \mathbf{A}) \cdot \hat{n} = H.
\end{aligned} \tag{3.44}
$$

Finally, the discretization of the TDGL equations for $d+s$-wave superconductors in the zero-electrostatic potential gauge and within the finite-difference and the link-variable technique read,

$$
\begin{aligned}
\gamma_d \frac{\eta^{n+1}_{d,i,j} - \eta^n_{d,i,j}}{\Delta t} &= \gamma_d \left[\frac{U^x_{i,j}\eta^n_{d,i+1,j} - 2\eta^n_{d,i,j} + \bar{U}^x_{i-1,j}\eta^n_{d,i-1,j}}{\delta x^2} \right.\\
&+ \left. \frac{U^y_{i,j}\eta^n_{d,i,j+1} - 2\eta^n_{d,i,j} + \bar{U}^y_{i,j-1}\eta^n_{d,i,j-1}}{\delta y^2} \right]\\
&+ \gamma_\nu \left[\frac{U^y_{i,j}\eta^n_{s,i,j+1} - 2\eta^n_{s,i,j} + \bar{U}^y_{i,j-1}\eta^n_{s,i,j-1}}{\delta y^2} \right.\\
&- \left. \frac{U^x_{i,j}\eta^n_{s,i+1,j} - 2\eta^n_{s,i,j} + \bar{U}^x_{i-1,j}\eta^n_{s,i-1,j}}{\delta x^2} \right]\\
&+ \eta^n_{d,i,j} - |\eta^n_{d,i,j}|^2 \eta^n_{d,i,j} - \frac{\tau_3}{2} |\eta^n_{s,i,j}|^2 \eta^n_{d,i,j} - \tau_4 \eta^{n\,2}_{s,i,j} \eta^{n\,*}_{d,i,j},
\end{aligned} \tag{3.45}
$$

$$
\begin{aligned}
\gamma_s \frac{\eta^{n+1}_{s,i,j} - \eta^n_{s,i,j}}{\Delta t} &= \gamma_s \left[\frac{U^x_{i,j}\eta^n_{s,i+1,j} - 2\eta^n_{s,i,j} + \bar{U}^x_{i-1,j}\eta^n_{s,i-1,j}}{\delta x^2} \right.\\
&+ \left. \frac{U^y_{i,j}\eta^n_{d,i,j+1} - 2\eta^n_{d,i,j} + \bar{U}^y_{i,j-1}\eta^n_{d,i,j-1}}{\delta y^2} \right]\\
&+ \gamma_\nu \left[\frac{U^y_{i,j}\eta^n_{d,i,j+1} - 2\eta^n_{d,i,j} + \bar{U}^y_{i,j-1}\eta^n_{d,i,j-1}}{\delta y^2} \right.\\
&- \left. \frac{U^x_{i,j}\eta^n_{d,i+1,j} - 2\eta^n_{d,i,j} + \bar{U}^x_{i-1,j}\eta^n_{d,i-1,j}}{\delta x^2} \right]\\
&- \nu \eta^n_{s,i,j} - \tau_1 |\eta^n_{s,i,j}|^2 \eta^n_{s,i,j} - \frac{\tau_3}{2} |\eta^n_{d,i,j}|^2 \eta^n_{s,i,j} - \tau_4 \eta^{n\,2}_{d,i,j} \eta^{n\,*}_{s,i,j}.
\end{aligned} \tag{3.46}
$$

Publication The results of this chapter were published in:

- W. C. Gonçalves, E. Sardella, V. F. Becerra, M. V. Milošević, and F. M. Peeters, *Numerical solution of the time dependent Ginzburg-Landau equations for mixed $(d+s)$-wave superconductors*, Journal of Mathematical Physics **55**, 041501 (2014) (16 pages).

4

Multichiral ground states in mesoscopic p-wave superconductors

Using Ginzburg-Landau formalism we investigate the effect of confinement on the ground state of mesoscopic chiral p-wave superconductors in absence of magnetic field. We reveal stable multichiral states with domain walls separating the regions with different chiralities, as well as monochiral states with spontaneous currents flowing along the edges. We show that multichiral states can exhibit identifying signatures in the spatial profile of the magnetic field, if those are not screened by edge currents in the case of strong confinement. Such magnetic detection of domain walls in topological superconductors can serve as a long-sought evidence of broken time-reversal symmetry.

4.1 Introduction

In a topological superconductor besides the bulk gap that separates the normal and the superconducting phases, there exist gapless edge states carrying spontaneous currents along the boundaries of the sample [70]. Theoretical works have classified the topological superconductors in two types according to whether or not they break the time-reversal symmetry (TRS), namely (i) chiral, and (ii) helical [69, 73], respectively. In a chiral superconductor the Cooper pairs are spin polarized, i.e. spinless owing to the broken TRS, and its edge states resemble those of the quantum Hall state [73]. On the other hand, in a helical superconductor the Cooper pairs are in a spin-triplet state, i.e. spinful owing to the TRS, and its edge states resemble those of the quantum spin Hall state [73].

The archetypal example of a topological superconductor breaking (satisfying) the TRS in two dimensions is the chiral (helical) p-wave model of superconductivity. In a p-wave superconductor the orbital part of the superconducting gap (Δ) has odd parity, i.e. the Cooper pairs have angular momentum $l = 1$ since the parity (P) is defined by: $P = (-1)^l$. Moreover, the spin part of the gap is either spin polarized for the chiral case or spinful with a triplet state for the helical case. Microscopic and phenomenological models of chiral p-wave superconductivity in two dimensions (2D) have reported intriguing states comprising (i) the edge states arising from the topological nature of the model [77], (ii) chiral domain walls separating regions with different chiralities [76], and (iii) coreless vortices (skyrmions) with topology and electronic properties distinctly different from that of conventional Abrikosov vortices [123–125]. However, despite the numerous works revealing the vast novel physics behind chiral p-wave superconductivity, none of the three previously mentioned hallmarks have been confirmed experimentally in strontium ruthenate (SRO) [59–62], the leading candidate to display chiral p-wave superconductivity [101].

Strontium ruthenate, Sr_2RuO_4, is a layered perovskite with a Fermi surface containing three sheets [57, 96]. Among them two are one-dimensional (α and β) and arising from the d_{xz} and d_{yz} orbitals of Ru, whereas the remaining one is two-dimensional (γ) and arising from the d_{xy} orbitals of Ru. Chiral p-wave superconducting order was suggested to emerge in the γ band of SRO as a consequence of strong Hund's rule coupling [48]. The evidences of p-wave order in SRO to date comprise (i) the detection of spontaneous fields in muon spin resonance (μSR) experiments [52], (ii) the enhancement and suppression of the Josephson critical current depending on the direction of the junction plane [49, 126], and (iii) the observation of a state breaking the TRS in the polar Kerr effect (PKE) [53]. However, measurements of the spin susceptibility below the critical temperature (T_c) for magnetic fields applied either parallel or perpendicularly to the c axis could not demonstrate that the spins remained in the basal plane independently of the direction of the field [47, 100], as one expects in chiral p-wave superconductivity. Then, the debate about whether or not SRO is a chiral superconductor remains open, with an increasing number of works suggesting that superconducting order also develops in α and β bands and that those play an essential role in the physical properties of this material [55, 79–81].

In this chapter we employ the phenomenological Ginzburg-Landau (GL) model to describe chiral p-wave superconductors [94]. The set of coupled and nonlinear differential equations that we solve numerically for the two component superconducting order parameter, $\mathbf{\Psi} = (\psi_+, \psi_-)^T$, and the vector potential $\mathbf{A}$, depends on four phenomenological parameters, defined by the shape of the Fermi surface of the material under consideration [77, 102]. We then use the microscopic information available for SRO to calculate the four phenomenological parameters, and present striking results useful to explain the elusive detection of chiral domain walls (DWs). From our simulations we present the ground-state phase diagram as a function of the size and aspect ratio of the mesoscopic p-wave superconducting samples, in absence of any applied magnetic field. Among the stable phases, we reveal the multichiral states with domain walls separating the regions with different chiralities, as well as monochiral ones with spontaneous currents flowing along the edges.

The chapter is organized as follows. Sec. 4.2 presents the theoretical formalism and the discussion of the gauge invariance in the GL equations. From there we derive the equations that describe the considered system, namely mesoscopic rectangular samples without an external magnetic field. Sec. 4.3 then summons our findings, in a phase diagram of ground states, showing the stability and relationship between the superconducting configurations composed of multiple chiral domains as well as the monochiral states. Our findings and conclusions are summarized in Sec. 4.4.

4.2 Theoretical Formalism

Based on the point symmetry of the crystal structure under consideration, one can obtain the GL functional, and subsequently by its minimization, the time-dependent Ginzburg-Landau (TDGL) equations, which describe the spatial distribution of the magnetic induction $\mathbf{B}$, and the superconducting order parameter $\mathbf{\Psi}$. Within an analysis for unconventional superconductivity, a GL functional with a state breaking the TRS and of the p-wave type has already been reported for a tetragonal lattice [94]. Thus, the dimensionless GL functional, $\mathscr{F} = \mathscr{F}'/\mathscr{F}_0$, where $\mathscr{F}_0 = \hbar^2\Delta_0^2/2m\xi^2$, for chiral p-wave superconductors reads

$$
\begin{aligned}
\mathscr{F} &= \frac{K+k_1}{4}\left(\left|\mathbf{D}\,\psi_+\right|^2+\left|\mathbf{D}\,\psi_-\right|^2\right)\\
&+ \left(k_2+k_3\right)\mathrm{Re}\Big\{\Pi_+\psi_-(\Pi_-\psi_+)^*\Big\}\\
&- \frac{1}{2}\left|\mathbf{\Psi}\right|^2+\frac{1+\tau}{8}\left|\mathbf{\Psi}\right|^4-\frac{\tau}{8}(\mathbf{\Psi}^*\hat{\sigma}_z\mathbf{\Psi})^2\,, \qquad (4.1)
\end{aligned}
$$

where $\xi=\sqrt{\frac{\hbar^2}{2m\alpha}}$ is the superconducting coherence length, and $\Delta_0=\sqrt{\frac{\alpha}{2\beta_1}}$ is the magnitude of the degenerate zero-field solution, $\psi_0=\Delta_0(1,\pm i)/\sqrt{2}$, in the fields $\psi_x=(\psi_-+\psi_-)/2$ and $\psi_y=(\psi_+-\psi_-)/2i$. In Eq. (4.1), k_i, α, and $\tau=\beta_2/\beta_1$, with $i=1,2,3$, are parameters microscopically derived depending on the Fermi surface of the material. For SRO Refs. [77] and [102] give detailed calculation of these parameters assuming chiral superconductivity develops in the cylindrical γ band. $K=\sum k_i$, $\mathbf{D}$ is the covariant derivative, and $\Pi_\pm=\frac{1}{\sqrt{2}}(D_x\pm iD_y)$ are creation and annihilation operators of Landau levels, respectively. In dimensionless units where time is scaled to the GL time $t_0=\xi^2/D$, with D a diffusion phenomenological coefficient, distance to the coherence length ξ, the magnetic field to the upper critical field H_{c2}, and the electrostatic potential to $\varphi_0=H_{c2}\xi^2/ct_0$, where c is the speed of light, the TDGL equations become [119]

$$
\begin{aligned}
\left(\frac{\partial}{\partial t}+i\varphi\right)\mathbf{\Psi} &= -\frac{\delta\mathscr{F}}{\delta\mathbf{\Psi}^*}, \qquad (4.2)\\
\sigma\left(\frac{\partial\mathbf{A}}{\partial t}+\nabla\varphi\right) &= -\frac{\delta\mathscr{F}}{\delta\mathbf{A}}-\kappa^2\nabla\times\mathbf{B}\,. \qquad (4.3)
\end{aligned}
$$

In Eqs. (4.2) and (4.3) $\mathbf{B}$ is the magnetic induction, φ the electrostatic potential, σ the conductivity in units of $D/\alpha t_0$, and $\kappa=\lambda/\xi$ the GL parameter, where $\lambda=\sqrt{\frac{mc^2}{8\pi e^2\Delta_0^2}}$ is the London penetration depth.

The gauge invariance of the TDGL equations allows one to simplify them owing to the freedom of the arbitrary function χ in the transformation $\left(\mathbf{\Psi}',\mathbf{A}',\varphi'\right)=\left(\mathbf{\Psi}e^{i\chi},\mathbf{A}+\nabla\chi,\varphi-\frac{\partial\chi}{\partial t}\right)$. When χ is properly chosen (gauge fixed), it provides a supplementary equation for the transformed fields that simplifies the form of the TDGL equations. In what follows we present the gauge choice considered in this chapter.

4.2.1 Zero-electrostatic potential gauge

The zero-electrostatic potential gauge is the most convenient choice for the TDGL equations when neither charges nor external currents are considered in the superconducting sample [124]. From the original fields $\left(\mathbf{\Psi},\mathbf{A},\varphi\right)$ the arbitrary function χ is required to satisfy the equation $\frac{\partial\chi}{\partial t}=\varphi$. This choice renders vanishing the transformed electrostatic potential, $\varphi'=0$, reducing considerably the complexity of the TDGL equations for the transformed fields,

$$
\begin{aligned}
\frac{\partial\mathbf{\Psi}}{\partial t} &= \left(\frac{K+k_1}{2}\mathbf{D}^2+(k_2+k_3)\left[\Pi_+^2\hat{\sigma}_++\Pi_-^2\hat{\sigma}_-\right]\right)\mathbf{\Psi}\\
&+ \left(1-\frac{1+\tau}{2}|\mathbf{\Psi}|^2\pm\frac{\tau}{2}\mathbf{\Psi}^*\hat{\sigma}_z\mathbf{\Psi}\right)\mathbf{\Psi}, \qquad (4.4)\\
\sigma\frac{\partial\mathbf{A}}{\partial t} &= \mathbf{J}-\kappa^2\nabla\times\mathbf{B}, \qquad (4.5)
\end{aligned}
$$

where for convenience we have dropped all the primes and $\hat{\sigma}_\pm=(\hat{\sigma}_x\pm i\hat{\sigma}_y)/2$ are pseudo-spin or chiral operators acting on the space span by $\psi_\pm$. It is straightforward to show in Eq. (4.4) that by considering: (i) the stationary regime, i.e. $\frac{\partial \boldsymbol{\Psi}}{\partial t} = 0$, and (ii) the proximity of the superconducting to the normal phase, i.e. discarding the nonlinear terms, the first GL equation transforms to the eigenvalue problem: $\left[\frac{K+k_1}{2}\mathbf{D}^2 + (k_2+k_3)\left(\Pi_+^2\hat{\sigma}_+ + \Pi_-^2\hat{\sigma}_-\right)\right]\boldsymbol{\Psi} = -\boldsymbol{\Psi}$. The analytical solutions to the latter equation have been obtained from Landau level states (ϕ_n) satisfying the equations $\Pi_\pm\phi_n \propto \phi_{n\pm1}$ [94, 102, 127]. Thus, in the linearized case for chiral p-wave superconductors the order parameter is given by $\boldsymbol{\Psi} = (\phi_n, \phi_{n-2})^T$, where n becomes the vorticity.

Finally, with $\{\hat{\imath}, \hat{\jmath}\}$ being canonical base vectors in Cartesian coordinates, the dimensionless superconducting density current $\mathbf{J}$, given in units of $J_0 = \frac{e\hbar}{m\xi}\Delta_0^2$, reads

$$\begin{aligned}\mathbf{J} \;=\; & \mathrm{Im}\Bigg\{\frac{K+k_1}{4}\Big(\psi_+^*\mathbf{D}\psi_+ + \psi_-^*\mathbf{D}\psi_-\Big) \\ & + \frac{k_2+k_3}{2\sqrt{2}}\Big(\boldsymbol{\Psi}^*\Big[\Pi_+\hat{\sigma}_+ + \Pi_-\hat{\sigma}_-\Big]\boldsymbol{\Psi}\,\hat{\imath} + i\,\boldsymbol{\Psi}^*\Big[\Pi_+\hat{\sigma}_+ - \Pi_-\hat{\sigma}_-\Big]\boldsymbol{\Psi}\,\hat{\jmath}\Big)\Bigg\}.\end{aligned} \tag{4.6}$$

4.2.2 Boundary conditions

Eqs. (4.4) and (4.5) are solved in this chapter for mesoscopic rectangular samples with an external magnetic field H applied perpendicularly to the sample plane. The required boundary conditions that pose the problem well and that are compatible with the existence of spontaneous edge currents are: [77, 94, 124]

$$\begin{aligned} &\left.\begin{aligned}\psi_+ - \psi_- &= 0\\ D_y\psi_+ + D_y\psi_- &= 0\end{aligned}\right\} \quad \text{at north and south sides,}\\ &\left.\begin{aligned}\psi_+ + \psi_- &= 0\\ D_x\psi_+ - D_x\psi_- &= 0\end{aligned}\right\} \quad \text{at east and west sides.}\\ &(\nabla\times\mathbf{A})\cdot\hat{n} = H, \end{aligned} \tag{4.7}$$

where $\hat{n}$ is the unitary vector normal to the sample surface.

The equations (4.4) and (4.5) are numerically solved using finite differences and the link variables technique of Refs. ([119], [120]), with the corresponding boundary condition (4.7).

Before concluding this section, we give the reduced (hence more convenient) expression for the dimensionless free energy density, obtained by transformation of Eq. (4.1):

$$\frac{f}{f_0} = -\frac{1}{V}\int dV\left\{\frac{1+\tau}{8}|\boldsymbol{\Psi}|^4 - \frac{\tau}{8}(\boldsymbol{\Psi}^*\hat{\sigma}_z\boldsymbol{\Psi})^2 - \kappa^2\mathbf{B}^2\right\}. \tag{4.8}$$

The energetic considerations enable us to find not only the lowest energy (ground) states but also other stable states with higher energies (metastable states).

4.3 Ground-state phase diagram

In this section we solve the TDGL equations using the zero-electrostatic potential gauge for rectangular $w_x \times w_y$ mesoscopic samples with sizes in the range $[3.5\xi, 23\xi]$. We consider no external magnetic field and obtain the superconducting ground states according to the following procedure. (i) For taken size of the sample we numerically solve Eqs. (4.4) and (4.5) with different initials inputs, e.g. one domain wall (DW) at half-width of the sample,

$$\boldsymbol{\Psi} = \begin{pmatrix}1\\0\end{pmatrix} \quad 0 \le x \le 0.5\,w_x, \qquad \boldsymbol{\Psi} = \begin{pmatrix}0\\1\end{pmatrix} \quad 0.5w_x < x \le w_x.$$

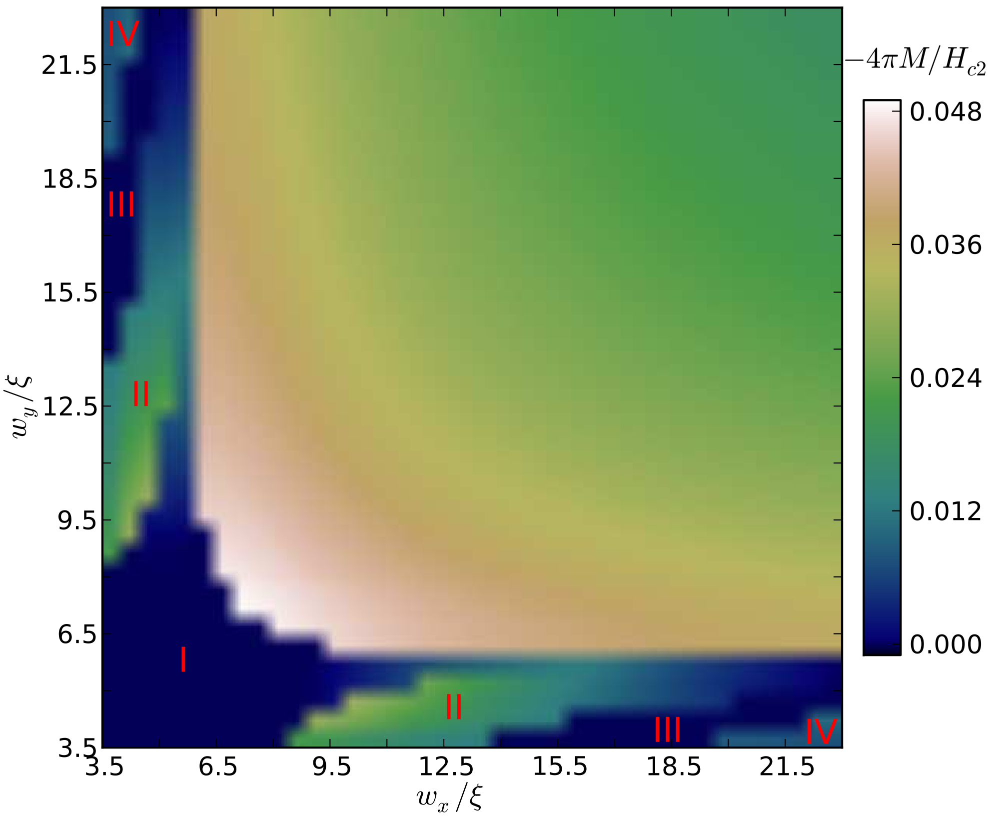

Figure 4.1: The phase diagram of the ground state of rectangular p-wave samples in absence of external magnetic field. Five (I)-(V) different phases are clearly distinguished and exhibit distinct magnetic responses. The phases are labeled according to the number of domain walls they contain, e.g. phases I and II have one and two domain walls, respectively. State V is an exception to the previous rule being free of domain walls (the monochiral state).

Other initial inputs in the set have two, three and four DWs distributed in the sample either horizontally or vertically. Moreover, initial inputs without DWs are considered as well, such as $\mathbf{\Psi} = (1, 0)^T$ and $\mathbf{\Psi} = (0, 1)^T$ throughout the sample. (ii) After the numerical simulations using different initial inputs, we compare the energies of all found solutions, using Eq. (4.8), and identify the lowest-energy solution. (iii) The process is repeated for all the samples with sizes in the range $w_x, w_y \in [3.5\xi,\, 23\xi]$.

Fig. 4.1 shows the phase diagram of the ground state at zero external magnetic field for mesoscopic rectangular samples of different sizes. For the phenomenological parameters, microscopic calculations have demonstrated that $k_1 = k_2 = k_3 = 1/3$ and $\tau = 1/2$, for chiral superconductivity developing in a cylindrical Fermi surface [77, 102]. The remaining two parameters (κ and σ) are taken 1.25 and 1, respectively. The value of κ was chosen to weakly deviate from the in-plane bulk GL parameter (κ_{ab}) of SRO [57, 96], in order to compare our results with previously reported works based on the BCS model for chiral p-wave superconductivity [77]. The value of σ was set to one as typically used [119]. This choice has weak implications on the stationary solution of the Eqs. 4.4 and 4.5, as it predominantly influences the dynamical regime by determining the distribution of the electrostatic potential in the presence of applied current. The diagram shows five different phases denoted by Roman numerals clearly distinguished according to their magnetization, and labeled according to the number of domains walls that they contain, the exception being phase V which is free of DWs.

Fig. 4.2 shows a superconducting state belonging to the phase I of the diagram of Fig. 4.1, i.e. a state with one domain wall as seen in the contour plots of $|\psi_\pm|^2$. Note that the two-component order parameter $\mathbf{\Psi}$ can also be expressed in terms of its Cartesian components ψ_x and ψ_y (as $\psi_x =$

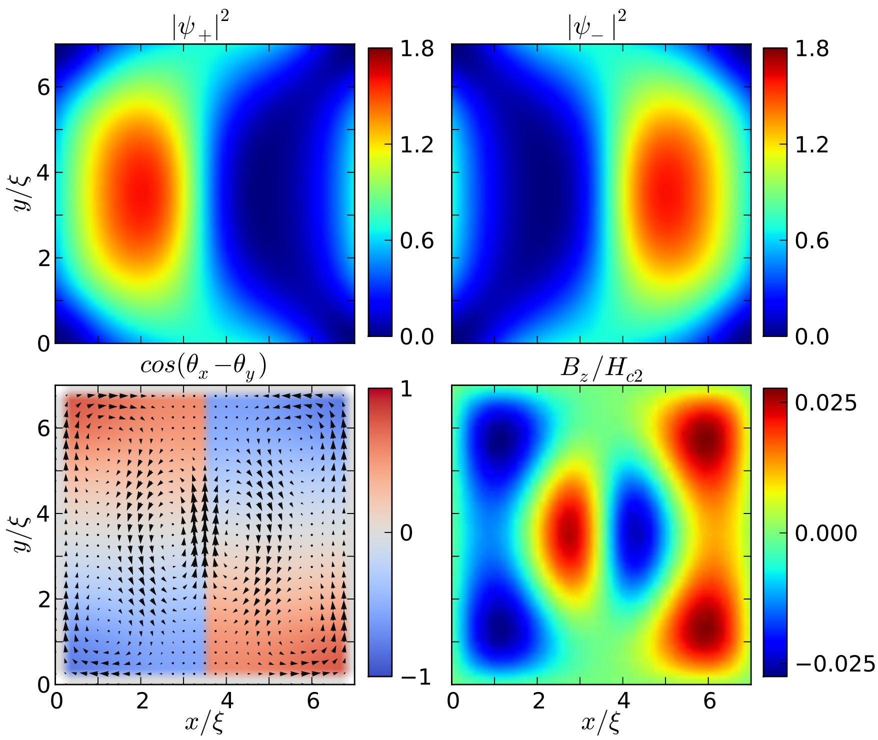

Figure 4.2: Contour plots of the superconducting density components $|\psi_\pm|^2$, the phase difference $\cos(\theta_x - \theta_y)$, and the magnetic induction B_z of a ground state with one domain wall. $\theta_{x,y}$ are the angular phases of $\psi_{x,y}$, where $\psi_x = (\psi_+ + \psi_-)/2$ and $\psi_y = (\psi_+ - \psi_-)/2i$. The spatial distribution of the superconducting current density **J** *is superimposed on the contour plot of* $\cos(\theta_x - \theta_y)$.

$\frac{\psi_+ + \psi_-}{2}$ and $\psi_y = \frac{\psi_+ - \psi_-}{2i}$), whose phases θ_x and θ_y can be employed for better identification of topological defects in p-wave superconductors (see Ref. [124]). The quantity $\cos(\theta_x - \theta_y)$, from now on simply called the phase difference, conveniently indicates the exact position of the DWs (the interface separating the regions where the chirality is dominated by ψ_+ in one side and by ψ_- in the other side). The spatial distribution of the superconducting current density **J** [see Eq. (5.7)] is also plotted in Fig. 4.2. It is superimposed on the contour plot of the phase difference, and it shows (i) the currents of the DW flowing from the south to the north side, and (ii) the spontaneous currents of the edge states flowing clockwise and counterclockwise on the west and east sides of the sample, respectively. Consequently, the contour plot of the magnetic induction B_z shows (i) the typical dipole profile expected from a DW at the sample center, and (ii) the magnetic induction arising from the spontaneous currents on the left and right sides [76, 77, 124]. It is noteworthy that by slightly increasing the ratio between the sample height (w_y) and width (w_x), one can shift the vertical position of the DW. This fact leads us to the discussion of the following states.

Changing the aspect ratio $r = w_y/w_x$ away from one, the phase II becomes the ground state. We show in Fig. 4.3 one of the ground states belonging to this phase. It exhibits in the contour plots of $|\psi_\pm|^2$ and $\cos(\theta_x - \theta_y)$ two horizontal DWs located close to the north and south sides of the sample. However, the contour plot of the magnetic induction, which is expected to show characteristic dipole-like profiles at each DW, does not show any clear signature of DWs. This is caused by (i) the vorticity of this state ($\nu_+ = 0$ and $\nu_- = -2$) and (ii) the shape of the superconducting sample (rectangular), which causes the two DWs to reside close to the north and south sides of the sample. As a consequence the current on one side of the DW interacts (annihilates) with the edge current, which diminishes the magnetic response on that side and the characteristic dipolar signature is lost.

When making the aspect ratio r of the sample more acute, one obtains as the ground state three

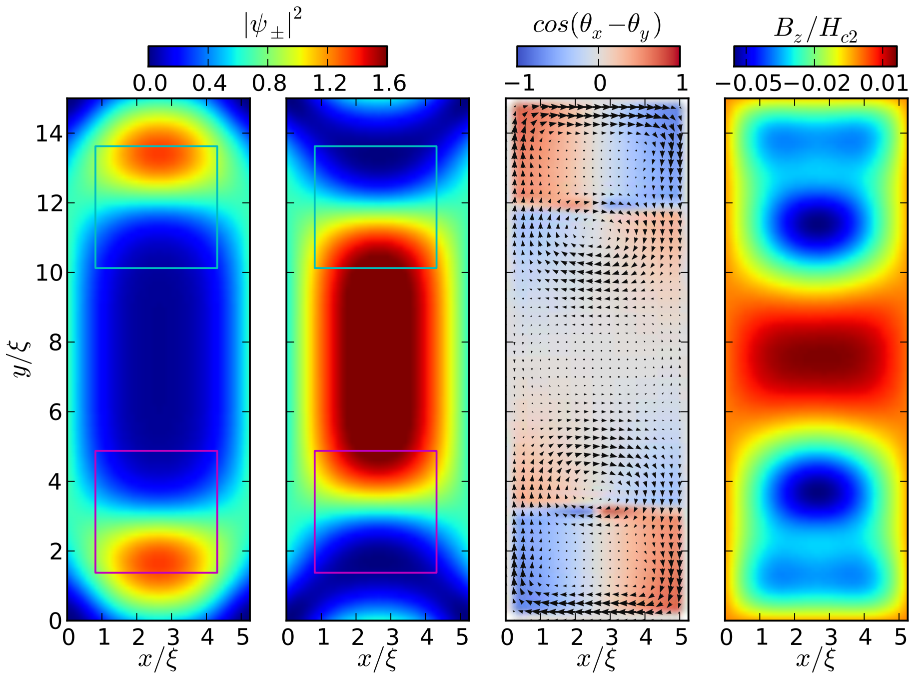

Figure 4.3: Same quantities as in Fig. 4.2 but for a ground state with two domain walls. The two pairs of boxes with different colors are displayed in the figure in order to highlight the regions where the shape of the sample strongly affects the order parameter components and breaks the mirror symmetry of the domain wall. Consequently, only one quasi-circular clockwise stream of current is preserved in the vicinity of the domain walls while the anticlockwise current on the other side of the wall (c.f. Fig. 4.2) is annihilated by the currents stemming from the sample edges.

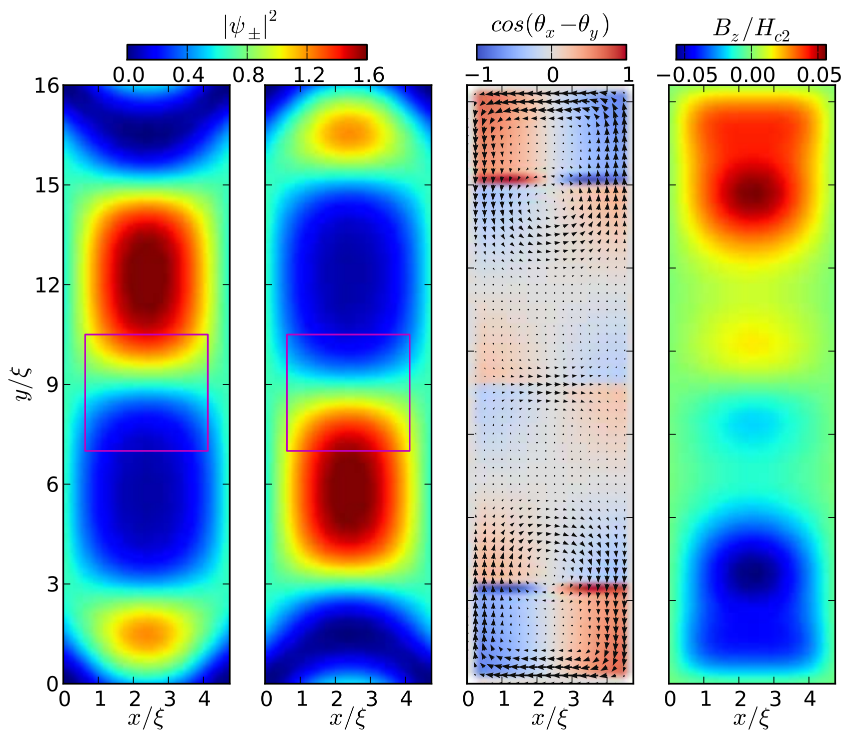

Figure 4.4: Same quantities as in Fig. 4.2 but for a state with three domain walls. A pair of boxes are displayed in the figure in order to highlight the local symmetry existing between the components, $|\psi_+|^2$ and $|\psi_-|^2$, related to the current distribution in the vicinity of the domain walls.

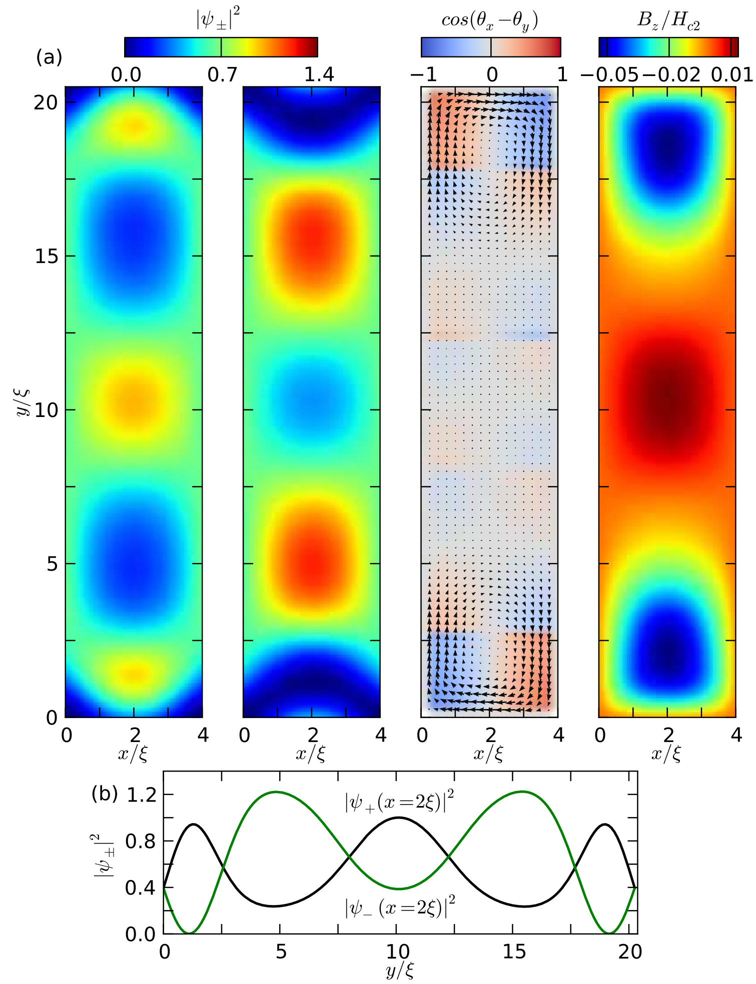

Figure 4.5: Row (a) shows the same quantities as in Fig. 4.2 but for a state with four domain walls. Row (b) shows the line profiles of the superconducting density components $|\psi_\pm|^2$ along the line defined by $x = 2\xi$.

DWs, i.e. phase III. In Fig. 4.4 we show a state belonging to this phase. Again, the contour plot of the magnetic induction confirms that top and bottom DWs do not show their characteristic dipole profiles, whereas the central DW does. The dipole profile on the central DW is maintained because of its weak interaction with the edge currents, so that the local symmetry between the two components $|\psi_+|^2$ and $|\psi_-|^2$ is maintained (see the regions enclosed by boxes in Fig. 4.4).

In the ground-state phase diagram of Fig. 4.1, the phase containing four DWs is obtained only for extreme aspect ratios of the sample ($r > 5$). One state belonging to this phase is shown in Fig. 4.5 for a narrow sample with $w_x = 4\xi$. According to the contour plot of the phase difference, the four DWs appear almost equidistantly distributed along the sample. However, the typical magnetic responses for the DWs expected in the contour plot of the magnetic induction are absent. The reason for this behavior is the imbalance between the superconducting components $|\psi_+|^2$ and $|\psi_-|^2$, which one can clearly see in the line profiles along $x = 2\xi$, shown in panel (b). Namely, the strong confinement in x direction has stronger influence on ψ_+ than ψ_-, which affects the balance between the two components required for the formation of the DW currents and consequently diminishes the dipolar profile of the DW in the magnetic induction.

Finally, in what follows we discuss the phase that is free of DWs, i.e. the phase V. It is the most present phase in the diagram of Fig. 4.1, as it spans samples ranging from size $(w_x \times w_y)$=(7ξ×7ξ) up to (23ξ×23ξ). Based on the transformation of dimensionless units to real units (using the temperature dependence of the coherence length $\xi = \xi(0)/\sqrt{1 - T/T_c}$, choosing $\xi(0)$ to fit SRO and $T =$

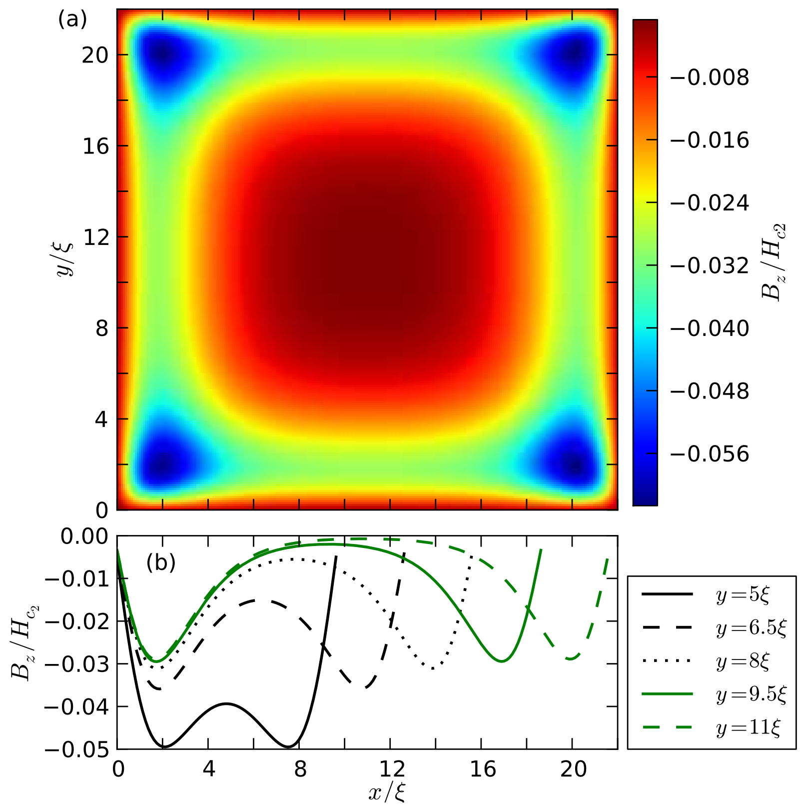

Figure 4.6: (a) Magnetic induction of a square sample with dimensions ($22\xi \times 22\xi$) at zero external magnetic field. The spontaneous currents flowing clockwise give rise to the negative values of B_z. (b) Line profiles of the magnetic induction of different square samples along the central cut through the sample.

$0.95T_c$), the ground state of a p-wave superconducting sample with size $20\xi \times 20\xi$ (approximately $6\mu\text{m}\times 6\mu\text{m}$) will be free of DWs in the ground state. However, this does not mean that the magnetic response of the ground states belonging to the phase V is negligible. On the contrary, the contour plot of the magnetic induction in Fig. 5.5(a) shows a significant magnetic response of this monochiral state, with spontaneous currents flowing along the edges. The characteristic scale for the magnetic response of the spontaneous currents is $\zeta = 1.6875\xi$, slightly different from the natural scale for the magnetic induction $\lambda = 1.25\xi$, presumably due to weak confinement effects. Then, in order to describe further the effects of confinement on the ground state in phase V, panel (b) shows line profiles of the magnetic induction of square samples with sizes 10ξ, 13ξ, 16ξ, 19ξ, and 22ξ. Here one can notice that owing to the confinement, the left and right edge currents interact strongly in the square samples smaller than $19\xi \times 19\xi$, i.e. in the central region of the sample the value of the magnetic induction becomes notably nonzero below certain sample size, due to the overlap and interaction of spontaneous currents stemming from opposite edges of the sample.

4.3.1 Influence of the parameters on the ground-state phase diagram

The phase diagram shown in Fig. 4.1 was obtained for the phenomenological parameters adjusted to represent a chiral p-wave superconductor with a cylindrical Fermi surface (presumably SRO falls in this category). However, the fact that the spontaneous currents in SRO have remained elusive so far, questions the emergence of chiral order in this material. Large efforts have been made to reconcile the experiments with theory, including works analyzing the effect of disorder on the spontaneous currents [82, 84], as well as the possibility of chiral non-p-wave order in SRO [83].

Recent works have also considered that superconductivity can develop in the other two bands of

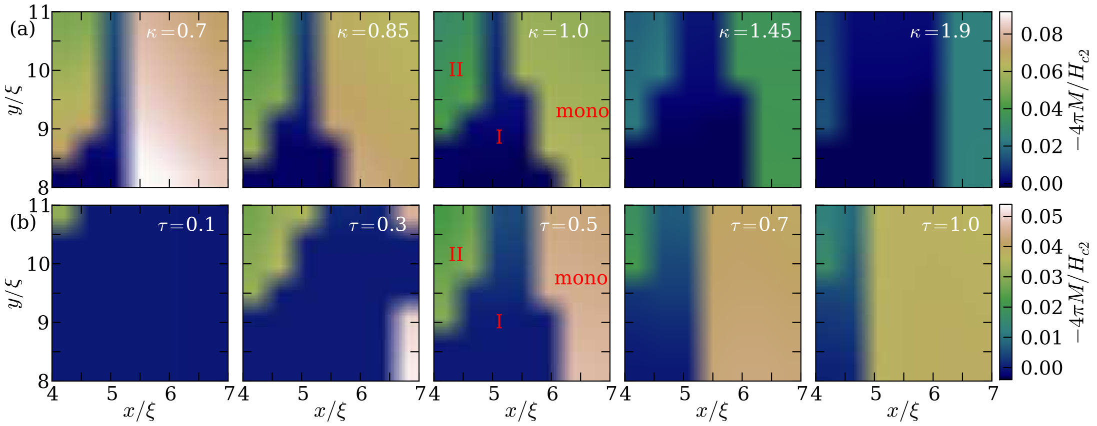

Figure 4.7: Diagram of ground states for different values of the phenomenological parameters κ and τ. The color scales indicate the corresponding magnetization of the ground states. The panels enclose a region containing the phases I, II, and V, and demonstrate the influence that the parameters have on these phases.

SRO (α and β) [55, 79–81]. Surprisingly, in this scenario of multi-band superconductivity one of the predictions is that the spontaneous currents are strongly suppressed owing to the existence of the α and β bands. Quantitatively, the suppression is due to a considerable reduction of the k_2 and k_3 parameters [81] (see in Eq. 5.7 that the term that supports the chiral currents is multiplied by the sum of k_2 and k_3). The effect of such changed values of k_i, i.e. $k_i \neq 1/3$, on the superconducting states of mesoscopic samples has already been discussed elsewhere [123, 124]. However, little is known about the robustness of multichiral states against the variation of parameters κ and τ. In Fig. 4.7 we focus on one part of the phase diagram to illustrate the influence that these parameters have on the transitions between states I, II, and V, and then draw generic conclusions. As a first important finding, one can see in the sequence of Fig. 4.7(a) that the phase having the multichiral state of Fig. 4.2 expands as κ is increased, i.e. the magnetic response of the sample is disfavored. The expansion of phase I occurs at the expense of phases II and V, since they become less favorable owing to their nonzero magnetization.

To understand the influence of the parameter τ on the phases I, II, and V, before looking at the actual results, one can analyze the condensation energy of Eq. (4.1) (the last three terms), to have an insight into the expected behavior. The minima of $\mathscr{F}_{\text{cond}} = -\frac{1}{2}\left|\mathbf{\Psi}\right|^2 + \frac{1+\tau}{8}\left|\mathbf{\Psi}\right|^4 - \frac{\tau}{8}(\mathbf{\Psi}^*\hat{\sigma}_z\mathbf{\Psi})^2$ are the degenerate states: ($|\psi_+| = \sqrt{2}$, $\psi_- = 0$) and ($\psi_+ = 0$, $|\psi_-| = \sqrt{2}$). These states are separated by a barrier which is proportional to τ. One can obtain the shape of this barrier by replacing $|\psi_+| = \sqrt{2}\cos\theta$, and $|\psi_-| = \sqrt{2}\sin\theta$, so the condensation energy expression becomes [$\mathscr{F}_{\text{cond}} = \frac{\tau-1}{2} - \frac{\tau}{4}\cos^2(2\theta)$]. One should notice that the barrier disappears when $\tau = 0$, leading to the removal of the degeneracy of the ground state. That means that one should not expect the formation of domain walls if τ is close to zero. However, in the sequence of Fig. 4.7(b) one sees that phase I is the most dominant one at $\tau = 0.1$. The reason of this seemingly counterintuitive result is that the last term of $\mathscr{F}_{\text{cond}}$ is not the only one that breaks TRS. In fact, the second term in the kinetic energy of Eq. (4.1) also breaks TRS and in this case is the term that favors the multichiral over the monochiral states.

From Fig. 4.7(b) one can also deduce that the effect on phase I of increasing τ is the opposite of increasing κ. As τ is increased, phases I and II give way to the expansion of phase V. This effect can be attributed to the increase of the barrier separating the degenerate ground states. When the barrier is high such that the spatial fluctuations (real or in our case numerical) can not overcome it, combination of degenerate states becomes energetically unfavorable, leading the system to prefer the monochiral state of phase V.

4.4 Conclusions

In summary, we have employed the time-dependent Ginzburg-Landau equations to study in detail chiral p-wave superconductivity in mesoscopic rectangular samples, with a goal to stabilize mono and multichiral states in the absence of any magnetic field. We have reported the ground-state phase diagram of rectangular mesoscopic samples with sizes ranging from 3.5ξ to 23ξ, where ξ is the superconducting coherence length, and classified the states according to the number of chiral domain walls they contain. The monochiral state has no domain walls, but contains spontaneous currents flowing along the edges. We also noticed that the multichiral phases are made stable owing to the strong confinement, but that same confinement can overshadow the typical dipole-like magnetic field profile of the domain walls. Nevertheless, the imaging of the reported spatial profile of stray magnetic field of the multichiral states can serve as a clear evidence of the time-reversal symmetry breaking in topological superconductors.

Publication The results of this chapter were published in:

- V. Fernández Becerra and M. V. Milošević, *Multichiral ground states in mesoscopic p-wave superconductors*, Phys. Rev. B **94**, 184517 (2016) (10 pages).

5

Vortical versus skyrmionic states in mesoscopic p-wave superconductors

In this chapter, we reveal the properties of the superconducting states that arise as a consequence of mesoscopic confinement and a multi-component order parameter in the Ginzburg-Landau model for p-wave superconductivity. Conventional vortices, but also half-quantum vortices and skyrmions are found as the applied magnetic field and the anisotropy parameters of the Fermi surface are varied. The solutions are well differentiated by a topological charge that for skyrmions is given by the Hopf invariant and for vortices by the circulation of the superconducting velocity. We show several unique states combining vortices and skyrmions, their possible reconfiguration with varied magnetic field, as well as the novel temporal and field-induced transitions between vortical and skyrmionic states.

5.1 Introduction

Strontium ruthenate, Sr_2RuO_4, is according to theoretical predictions the best candidate to date to host p-wave superconductivity. Generally speaking, the order parameter in superconductors describes the spatial profile of the gap function, $\Delta_{ij}(k)$. The order parameter in p-wave superconductivity is an odd function of the wave vector **k**, unlike the s-wave superconductors where it is an even function of **k** [101]. Following the notation of Balian and Werthamer, the p-wave order parameter reads [48, 94]

$$\hat{\mathbf{\Delta}}(k) = \begin{bmatrix} -d_x(k) + id_y(k) & d_z(k) \\ d_z(k) & d_x(k) + id_y(k) \end{bmatrix}, \tag{5.1}$$

or in a short notation $\hat{\mathbf{\Delta}}(k) = i\left(\mathbf{d}(k)\cdot\hat{\sigma}\right)\sigma_y$, where $\mathbf{d}(k)$ transforms as a vector under rotations and σ_i are Pauli matrices. Microscopic calculation of the superconducting gap is a highly demanding task that requires a detailed knowledge of the pairing mechanism which in many cases is not available. What remains then is to exploit all the symmetries (continuous and discrete) exhibited by the material under consideration and build a model that will depend on certain number of parameters. The possible superconducting order parameters that have been reported for p-wave superconductors required a detailed description of the crystal structure of the considered material [48, 94]. In that respect, strontium ruthenate (SRO) is a layered perovskite with a crystal structure similar to the well known high-T_c superconductor $(La,Sr)_2CuO_4$, where oxygen ions at the corners of an octahedron surround the body-centered Ru ion [57, 101]. The planar layers of RuO_2 are separated by Sr layers that stack along the highly symmetric axis c. The Fermi surface of strontium ruthenate contains three sheets arising from the binding of the Ru and O ions within the same layer [128]. Bindings between the RuO_2 layers are weak due to the long separation of the interplanar RuO_6 octahedra. The Fermi sheets α and β are both one dimensional (1D), while the γ sheet is two dimensional (2D). A rigorous analysis found that among the five irreducible representations for vector $\mathbf{d}(k)$ in the lattice point group D_{4h}, there are four 1D, $\mathbf{d} = k_x\hat{\mathbf{x}} \pm k_y\hat{\mathbf{y}}$ and $\mathbf{d} = k_y\hat{\mathbf{x}} \pm k_x\hat{\mathbf{y}}$, and one 2D, $\mathbf{d} = (k_x \pm ik_y)\hat{\mathbf{z}}$ [48, 94]. These 1D and 2D representations, namely helical and chiral, are the electronic analogues of the B and A phases of the superfluid ^{3}He [48], respectively. Knight shift measurements were not able to discern the chiral from the helical contributions, since they detected constant spin susceptibility (χ_c) for external field either within the RuO_2 plane or perpendicular to it [47, 100]. On the other hand, muon-spin relaxation (μSR) and the optical Kerr effect experiments have detected spontaneous magnetic fields [52, 53], only possible in the chiral phase that breaks the time-reversal symmetry (TRS) [76].

To confirm or discard SRO as a chiral superconductor, magnetic response experiments have been carried out on single crystals, but have failed to convincingly detect the spontaneous currents predicted to exist in chiral domain walls and close to sample edges [59–62]. In these works, numerical simulations of evenly distributed chiral domains estimated a minimal domain wall length of 2 μm $\approx 30\xi_0$ (where ξ_0 is the zero-temperature coherence length of SRO) to be detectable in scanning SQUID setup. Such domains are energetically costly in a bulk system, but are likely to stabilize in a mesoscopic sample of comparable size.

Therefore, to provide further insights in chiral physics of p-wave superconductors, in this work we employ the chiral p-wave GL model [77, 94, 102, 129], to report distinct mesoscopic effects of chirality in the superconducting state and related experimental observables, which in turn can serve to discriminate chiral from helical contributions in superconductors like SRO. We report the stabilization of various topological entities, full vortex (FV), half-quantum vortex (HQV) and skyrmion states. Skyrmion states, carrying topological charge defined by the Hopf invariant [123, 130, 131], are one of the distinct hallmarks of chiral superconductivity, and can be stable in bulk p-wave superconductors. It is well known in conventional s-wave superconductivity that confinement can stabilize superconducting configurations which in bulk systems are energetically unfavorable or even unattainable, e.g. non-Abrikosov vortex lattices, or vortices with phase winding $\phi = 2\pi n$, with $n > 1$ (giant vortices) [39–41, 132]. In mesoscopic spin-triplet superconductors HQVs have been predicted to exist, owing the reduction of their otherwise divergent energy to the low dimensionality of the system [133]. They carry unscreened spin currents and half the vorticity of a full vortex [133,134]. Despite of the fact that in the chiral phase vector $\mathbf{d}$ is locked to the $\hat{\mathbf{z}}$ axis [94,129], we found analogous HQVs defined by: (i) the $2\pi-$phase winding of one of the chiral superconducting components, and (ii) the anisotropic screening that causes their attraction to the edges of the mesoscopic sample. We present the found HQV states in multiple forms, but also FV and skyrmionic states and transitions between them as a function of the external magnetic field applied perpendicularly to the sample. We employed the time-dependent theoretical formalism, which allowed us to observe novel temporal transitions as well, related to peculiar entry and arrangement of HQVs and their temporal transformations into other topologies. The HQVs that were found to reside at the sample edges are the realization of the quasi-1D periodic array of domains discussed in Ref. [61].

The chapter is organized as follows. Sec. 5.2 presents the theoretical formalism and our analytical analysis of the first GL equation and the superconducting current. The boundary conditions imposed on our equations are derived from the latter expression. Sec. 5.3 then summarizes our findings for the superconducting configurations composed of HQV, FV and skyrmion states, obtained at weak coupling and considering a cylindrical Fermi surface. The transitions between states of interest as a function of the magnetic field are discussed in Sec. 5.4, while the temporal transformations are shown in Sec. 5.5. The effect of anisotropy on the topological, vortical and skyrmionic entities is analyzed in Sec. 5.6. Our findings and conclusions are summarized in Sec. 7.5.

5.2 Theoretical Formalism

After the above brief general description of strontium ruthenate, in what follows we show the Ginzburg-Landau (GL) equations that the order parameter, $\mathbf{\Psi} = (\psi_x, \psi_y)^T$ must satisfy. The order parameter has two components (is chiral) as a consequence of the 2 dimensional representation ($\Gamma_5^{\pm}$) of the tetragonal group D_{4h} [94]. The expansion of the GL free energy density up to fourth order in $\psi_{x,y}$, that fulfills the group symmetries, reads

$$\begin{aligned} \mathscr{F} &= K\left(|D_x\psi_x|^2 + |D_y\psi_y|^2\right) + k_1\left(|D_x\psi_y|^2 + |D_y\psi_x|^2\right) \\ &+ 2\,\mathrm{Re}\Big\{k_2 D_x\psi_x(D_y\psi_y)^* + k_3 D_x\psi_y(D_y\psi_x)^*\Big\} - \alpha\,|\mathbf{\Psi}|^2 \\ &+ \beta_1|\mathbf{\Psi}|^4 + \beta_2(\psi_x^*\psi_y - \psi_x\psi_y^*)^2 + \beta_3|\psi_x|^2|\psi_y|^2\,, \end{aligned} \tag{5.2}$$

where α, k_i and β_i, with $i = 1, 2, 3$, are parameters that depend on the details of the Fermi surface of the material under consideration. $K = \sum_i k_i$, and $D_{x,y}$ denote the components of the covariant derivative. The time-dependent Ginzburg-Landau (TDGL) equations, used in our numerical approach [120], are the set of coupled differential equations for the superconducting order parameter, $\mathbf{\Psi}$, and the vector potential $\mathbf{A}$, [119]

$$\frac{\hbar^2}{2m_s D}\Big(\frac{\partial}{\partial t} + \frac{2ie}{\hbar}\varphi\Big)\mathbf{\Psi} = -\frac{\delta\mathscr{F}}{\delta\mathbf{\Psi}^*}, \tag{5.3}$$

$$\frac{\sigma}{c}\Big(\frac{1}{c}\frac{\partial\mathbf{A}}{\partial t} + \nabla\varphi\Big) = -\frac{\delta\mathscr{F}}{\delta\mathbf{A}} - \frac{1}{4\pi}\nabla\times\mathbf{B}\,, \tag{5.4}$$

where φ is the scalar electric potential, $\mathbf{B}$ is the magnetic induction, m_s is the effective mass, D is the phenomenological diffusion coefficient, and σ the electrical conductivity. For convenience we set $\hbar = 1$ and $m_s = 1/2$. The second GL equation [Eq. (5.4)] is discarded in this work since the diamagnetic effects of superconductors are vanishingly small for a thin (effectively 2D) mesoscopic geometry. We use the symmetric gauge for the vector potential, $\mathbf{A} = (\mathbf{r}\times\mathbf{H})/2$, with the magnetic field ($\mathbf{H}$) directed along $\hat{\mathbf{z}}$. The scalar electric potential is set to zero since neither charges nor external currents are considered in this work. In dimensionless units, where distance is scaled to the coherence length, $\xi = \sqrt{\frac{1}{\alpha}}$, time to $t_0 = \frac{\xi^2}{D}$, magnetic field to the upper bulk critical field $H_{c2} = \frac{c}{2|e|\xi^2}$, and the superconducting order parameter to $\Delta_+ = \sqrt{\frac{\alpha}{2\beta_1}}$, the first TDGL equation becomes

$$\begin{aligned} \frac{\partial\mathbf{\Psi}}{\partial t} &= \begin{bmatrix} \frac{K+k_1}{2}\mathbf{D}^2 + \frac{k_2-k_3}{2i}[D_x, D_y] & (k_2+k_3)\,\Pi_+^2 \\ (k_2+k_3)\,\Pi_-^2 & \frac{K+k_1}{2}\mathbf{D}^2 - \frac{k_2-k_3}{2i}[D_x, D_y] \end{bmatrix} \begin{pmatrix} \psi_+ \\ \psi_- \end{pmatrix} \\ &+ \mathbf{\Psi}\Big(1 - \frac{1+\tau}{2}|\mathbf{\Psi}|^2 \pm \frac{\tau}{2}\mathbf{\Psi}^*\hat{\sigma}_z\mathbf{\Psi}\Big)\,, \end{aligned} \tag{5.5}$$

where $\Pi_\pm = \frac{1}{\sqrt{2}}(D_x \pm iD_y)$, $\psi_\pm = \psi_x \pm i\psi_y$, $\beta_3 = 0$ [103], and $\tau = \beta_2/\beta_1$. A straightforward calculation reveals the following important result, $[D_x, D_y] = iH$, which leads the operators $\Pi_\pm$ to satisfy the commutator: $[\Pi_+, \Pi_-] = H$. The external magnetic field, being constant, can be factored out from the above commutators, leading to $[\tilde{\Pi}_+, \tilde{\Pi}_-] = 1$, which defines the algebra behind the Landau levels; $\tilde{\Pi}_\pm = \Pi_\pm/\sqrt{H}$. This algebra is defined through the following commutators: $[\hat{N}, \tilde{\Pi}_+] = -\tilde{\Pi}_+$, $[\hat{N}, \tilde{\Pi}_-] = \tilde{\Pi}_-$; where $\hat{N} = \tilde{\Pi}_+\tilde{\Pi}_-$ is the particle number operator. Within the weak-coupling limit and considering a cylindrical Fermi surface (γ sheet), all the k_i parameters are equal to $\langle v_x^2 v_y^2\rangle/\langle v_x^4\rangle = 1/3$, where brackets $\langle\,\rangle$ denote averaging over the Fermi surface [103], and $\tau = 1/2$. For this case the first GL equation reads

$$\partial_t \mathbf{\Psi} = \frac{2}{3}\Big[\mathbf{D}^2 + \Pi_+^2\hat{\sigma}_+ + \Pi_-^2\hat{\sigma}_-\Big]\mathbf{\Psi} + \mathbf{\Psi}\Big(1 - \frac{3|\mathbf{\Psi}|^2}{4} \pm \frac{\mathbf{\Psi}^*\hat{\sigma}_z\mathbf{\Psi}}{4}\Big), \tag{5.6}$$

where $\hat{\sigma}_\pm = (\hat{\sigma}_x \pm i\hat{\sigma}_y)/2$, are pseudospin or chiral operators acting on the space span by $\psi_\pm$. Ignoring the nonlinear terms (linearized case), it is straightforward to show that the superconducting order parameter must be of the form: $\mathbf{\Psi} = (\phi_N, \phi_{N-2})^T$, where ϕ_N is the state corresponding to the Landau level N [77,102,103,127,129,135,136]. Within the superconducting formalism the number N turns out to be the vorticity of the order parameter. Then, one concludes that for chiral p-wave superconductors there is a vorticity difference two between the components of the superconducting order parameter. The full GL equations, i.e. the linearized equation plus the nonlinear terms, are a complicated set of partial differential equations with restricted analytical solutions [103, 127]. Therefore, in this work we solve this problem numerically. Due to the mesoscopic dimension of the sample under consideration, proper boundary conditions must be incorporated in the GL equations in order to pose the problem well. In what follows, the superconducting current is calculated for the general case, which includes the specific case where all k_i's are equal to 1/3, and from this expression the boundary conditions for the first GL equation are derived. The superconducting current density, defined as the negative functional derivative of the GL free energy density with respect to the vector potential, for chiral p-wave superconductors is

$$\begin{aligned} \mathbf{J} \;=\; & \mathrm{Im}\Big\{\frac{K+k_1}{4}\Big(\psi_+^*\mathbf{D}\psi_+ + \psi_-^*\mathbf{D}\psi_-\Big) + \frac{k_2+k_3}{2\sqrt{2}}\Big(\mathbf{\Psi}^*\Big[\Pi_+\hat{\sigma}_+ + \Pi_-\hat{\sigma}_-\Big]\mathbf{\Psi}\,\hat{\imath} \\ & + \; i\,\mathbf{\Psi}^*\Big[\Pi_+\hat{\sigma}_+ - \Pi_-\hat{\sigma}_-\Big]\mathbf{\Psi}\,\hat{\jmath}\Big)\Big\} - \frac{k_2-k_3}{4}\mathrm{Re}\Big\{\hat{\mathrm{k}}\times\big(\psi_+^*\mathbf{D}\psi_+ - \psi_-^*\mathbf{D}\psi_-\big)\Big\}, \end{aligned} \tag{5.7}$$

where $\hat{\imath}$, $\hat{\jmath}$ form the canonical base in Cartesian coordinates. The set of operators ($\hat{\sigma}_\pm$ and $\hat{\sigma}_z$) act on $\psi_\pm$, while $\hat{S}_y$ acts on $\{\hat{\imath},\hat{\jmath}\}$. The superconducting current contains mainly three contributions defined by the following factors, $(K+k_1)/4$, $(k_2+k_3)/2\sqrt{2}$, and $(k_2-k_3)/4$. The first one arises from the conventional term $\mathbf{D}^2$ in Eq. (5.5), the second one (we name chiral) is due to the internal degree of freedom (chirality) that appears in Eq. (5.5) in the form of two nondiagonal terms. Finally, the third contribution arises from the diagonal terms ($\pm[D_x, D_y]$) in Eq. (5.5), and accounts for the chiral polarization introduced by the orbital Zeeman interaction. Within the weak coupling limit k_2 and k_3 are equal [102, 127, 135, 136], but if the the density of states ($N(0)$) weakly depends on the energy derivative $(N'(0))$ at the Fermi surface, k_2 and k_3 slightly differ [77]. The boundary conditions imposed on Eq. (5.5) for our square mesoscopic sample are given as:

$$\begin{aligned} &\left.\begin{aligned} \psi_+ - \psi_- &= 0 \\ D_y\psi_+ + D_y\psi_- &= 0 \end{aligned}\right\} \quad \text{at north and south sides,} \\ &\left.\begin{aligned} \psi_+ + \psi_- &= 0 \\ D_x\psi_+ - D_x\psi_- &= 0 \end{aligned}\right\} \quad \text{at east and west sides.} \end{aligned} \tag{5.8}$$

It is straightforward to show that the boundary conditions of Eq. (7.5) set the perpendicular current at the edges to zero, i.e. they impose specular reflection in the chiral p-wave superconductor [77, 94, 135, 136]. It is important to remark also that they are parameter-independent, so they provide the proper boundary conditions for Eq. (5.6) but also for the most general case of Eq. (5.5). With Eq. (7.5) we have completed the set of equations needed for the GL description of a chiral p-wave mesoscopic superconductor. Eq. (5.5) is numerically solved using finite differences and the link variables technique of Ref. [119] on a square lattice with mesh grid $h_x = h_y = 0.1$. On the other hand, the temporal derivative is discretized using the Runge-Kutta method of first order. Before concluding this section, we give the reduced expression for the dimensionless free energy, since it allows us to find not only the lowest energy (ground) states but also the stable states with slightly higher energies (metastable states) The free energy reads:

$$\frac{F}{F_0} = \frac{1}{2}\int dV\Big\{(1+\tau)|\mathbf{\Psi}|^4 + \tau(\mathbf{\Psi}^*\hat{\sigma}_z\mathbf{\Psi})^2\Big\}, \tag{5.9}$$

where $F_0 = \Delta_+^2/\xi^2$ is the bulk free energy at zero field.

5.3 Isotropic Case (Cylindrical Fermi surface)

The results obtained using Eq. (5.6) for a square $8\xi\times8\xi$ sample are summarized in Fig. 5.1, showing the dimensionless free energy and the vorticity of vector $\mathbf{\Psi}$ as a function of the external magnetic field H. Panels (b) and (c) show the vorticity of the ground states of our superconducting sample, labeled *a-j* in Fig. 5.1 (a), where $\nu_{+(-)}$ is the vorticity of component $\psi_{+(-)}$. Note that both ν_+ and ν_- remain constant along the stability curves of each state in panel (a), and as such are good identification numbers for these states. Contour plots in Fig. 5.2 show the order parameter $\mathbf{\Psi}$ corresponding to the ground states *a* - *d*. While the left and central columns of Fig. 5.2 show contour plots of the superconducting density of each component, $|\psi_+|^2$ and $|\psi_-|^2$, respectively, the third column shows the difference between the angular phases of the components, i.e. $\theta_+ - \theta_-$.

The ground state *a* of Fig. 5.2 shows one anisotropic vortex in each component, i.e. vorticity $\nu_+ = -1$ in component ψ_+ and $\nu_- = 1$ in component ψ_-. The contour plots of the ground state *b* in Fig. 5.2, show the vortex free state in component ψ_+ and the giant vortex [39–41,132] with vorticity $\nu_- = 2$ in component ψ_-. The subsequent ground state *c* has vorticity $\nu_+ = 2$ and $\nu_- = 4$, where $|\psi_-|^2$ contains four vortices close to the corners, meanwhile $|\psi_+|^2$ shows a pronounced depletion around the center of the sample. The corresponding phase difference figure reveals that the depletion in component ψ_+ is a consequence of two vortices and two vortex-antivortex pairs there. The ground state *d* has six vortices in $|\psi_-|^2$ in full agreement with the vorticity reported in Figs. 5.1 (b) and (c) ($\nu_+ = 4$ and $\nu_- = 6$). However, the density $|\psi_+|^2$ fails to convincingly show any signature of a vortex. The vorticity $\nu_+ = 4$ of component ψ_+ is visible in the phase difference figure 2 (d), where 10 discontinuities are found along the edges as a consequence of six vortices from ψ_- and four from ψ_+. Four vortex-antivortex pairs at the center of the sample are also visible in this contour plot, but do not affect the total vorticity.

From the comparison between Figs. 5.2 (c) and (d) one sees that with increasing the magnetic field the component ψ_- dominates its partner component ψ_+. The dominance of ψ_- over ψ_+, especially at high fields impedes the proper description of the vortex configuration in the latter component. In order to describe the components of the order parameter on an equal footing, a more suitable representation is in terms of ψ_x and ψ_y. Fig. 5.3 show contour plots of $|\psi_x|^2$, $|\psi_y|^2$ and $\cos(\theta_x - \theta_y)$ for ground states *a* - *j* of Fig. 5.1. Fig. 5.3 (a) shows $\cos(\theta_x - \theta_y)$ for ground state *a* (from now on called the phase difference figure), and reveals a linear domain wall. Its extension across the sample coincides with the stripe where density $|\psi_y|^2$ vanishes. On the other hand, the partner component, ψ_x, is free of vortices. Ground states *b* and *c* look similar in both densities, although from the comparison between their phase difference figures in Fig. 5.3 (b) and (c) respectively, we see four domain walls in state *c* and none in state *b*. The domain walls (DWs) of ground state *c* define a path where the difference between the angular phases of components ψ_x and ψ_y are 0 or π, i.e. $\theta_x - \theta_y = 0, \pi$. Ground state *d* shows two vortices in density $|\psi_x|^2$ and none in $|\psi_y|^2$, while its corresponding phase difference figure shows the four domain walls of ground state *c* plus two other alternating domain walls that weakly connect the former ones. The contour plots of Fig. 5.3 (e), for

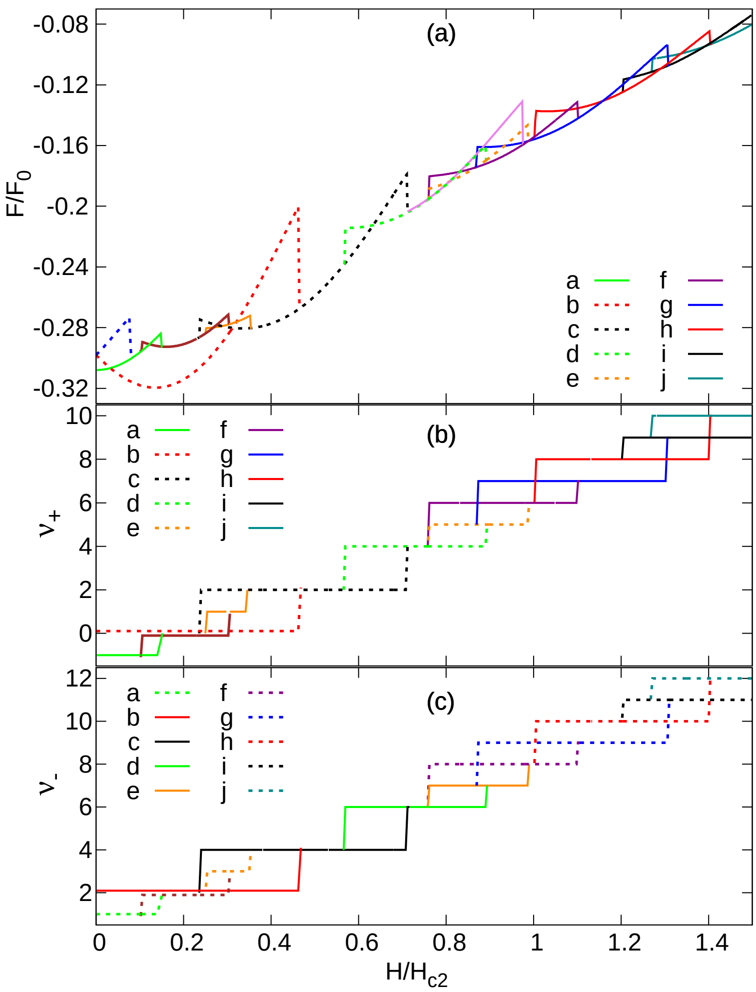

Figure 5.1: (a) Free energy in units of the bulk condensation energy at zero field (F_0) as a function of the external magnetic field in units of the bulk upper critical field (H_{c2}), for a square mesoscopic sample of size $8\xi\times8\xi$. Letter labels denote different found ground states. Some metastable states (not labeled) are also shown in this figure. Vorticity of components ψ_+ and ψ_- of the ground states of panel (a) are shown in (b) and (c) respectively. The difference in vorticity ($\nu_+ - \nu_- = 2$) between the components is in perfect agreement with the analytically predicted solution $\mathbf{\Psi} = (\phi_N, \phi_{N-2})^T$.

state *e* show clearly two vortices in each component. They look indistinguishable just from the analysis of their densities, but their phase difference figure reveals that there are two vortices, one in each component, that combine to produce a different signature from the remaining vortices. While the uncorrelated vortices lead to the formation of the alternating domain walls towards sample edges, the pair of correlated vortices align their cores and do not show any domain wall between them. The alternating domain wall is therefore the signature of a half quantum vortex (HQV) defined by the $2\pi-$phase winding of one of its superconducting components, in contrast to the other signature without domain wall that corresponds to the full vortex (FV).

The remaining ground states *f* - *j* of Fig. 5.1 are shown in the right column of Fig. 5.3. Both densities in ground state *f* clearly show two vortices in each component, which are indeed four HQVs according to the corresponding phase difference figure. Ground states *g* and *h* show one common feature, having different number of vortices per component, but all of them aligned vertically in component ψ_x and horizontally in component ψ_y. On the other hand, the corresponding phase difference figures for states *g* and *h* show that: (i) two vortices, one per component, combine to form one FV in state *g*, and (ii) four vortices, two per each component, combine to form one skyrmion

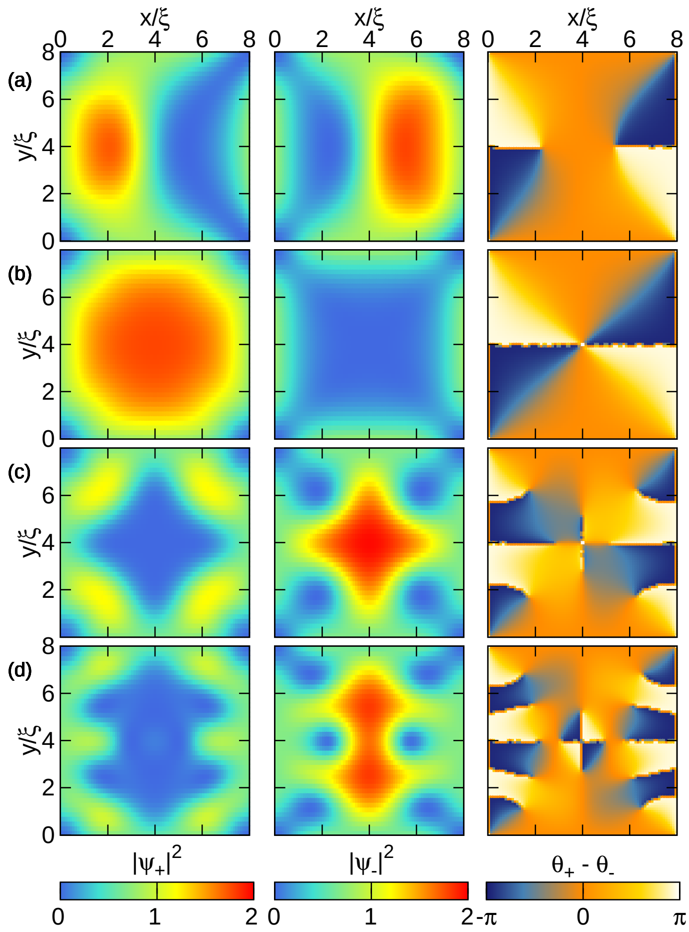

Figure 5.2: Ground states a - d *of Fig. 5.1. Left and central columns show the contour plots of the superconducting densities components* $|\psi_+|^2$ *and* $|\psi_-|^2$*, respectively. Right column shows the difference between the angular phases of the components, i.e.* $\theta_+ - \theta_-$.

in state *h*. The signature of the skyrmion is shown here for the first time: four alternating domain walls which are connected into a circular structure [137, 138]. The skyrmion state here of course differs from those of magnetic materials due in physics and the formation mechanism [131, 139, 140]. Nevertheless, their topological properties remain similar, as will be presented later. The phase difference figure of the ground state *i* shows four DWs around the corners, four HQVs close to the edges and three FVs in the center. What draws attention in all three contour plots of Fig. 5.3 (i) is that there are five vortices in each component (fractional vortices), and among them three align their cores to form FVs according to the corresponding phase difference figure. The triangular array formed by them resembles the consequences of vortex-vortex repulsion in conventional type II superconductors. Therefore, this supports our initial premise that the FV in our analysis is the usual Abrikosov vortex of conventional superconductivity. Finally, the phase difference figure of the ground state *j* shows four DWs, six HQVs and two FVs. One systematic comparison of the phase difference figure of ground states *f* - *j* clearly shows that HQV and FV are indeed very different states. While FVs are formed in the sample center, being favored by confinement, all the HQVs remain close to the sample edges. In order to explain this difference the following subsection discusses the calculated superconducting currents in the sample.

So far, DWs, HQVs, FVs and skyrmions have been distinguished in this work according to their signatures in the phase difference plots. The superconducting current, the physical quantity intertwined with the magnetic field, also allows us to identify more characteristic features of the novel topological solutions. Figs. 5.4 (a)-(d) show the supercurrents around one DW, HQV, FV and

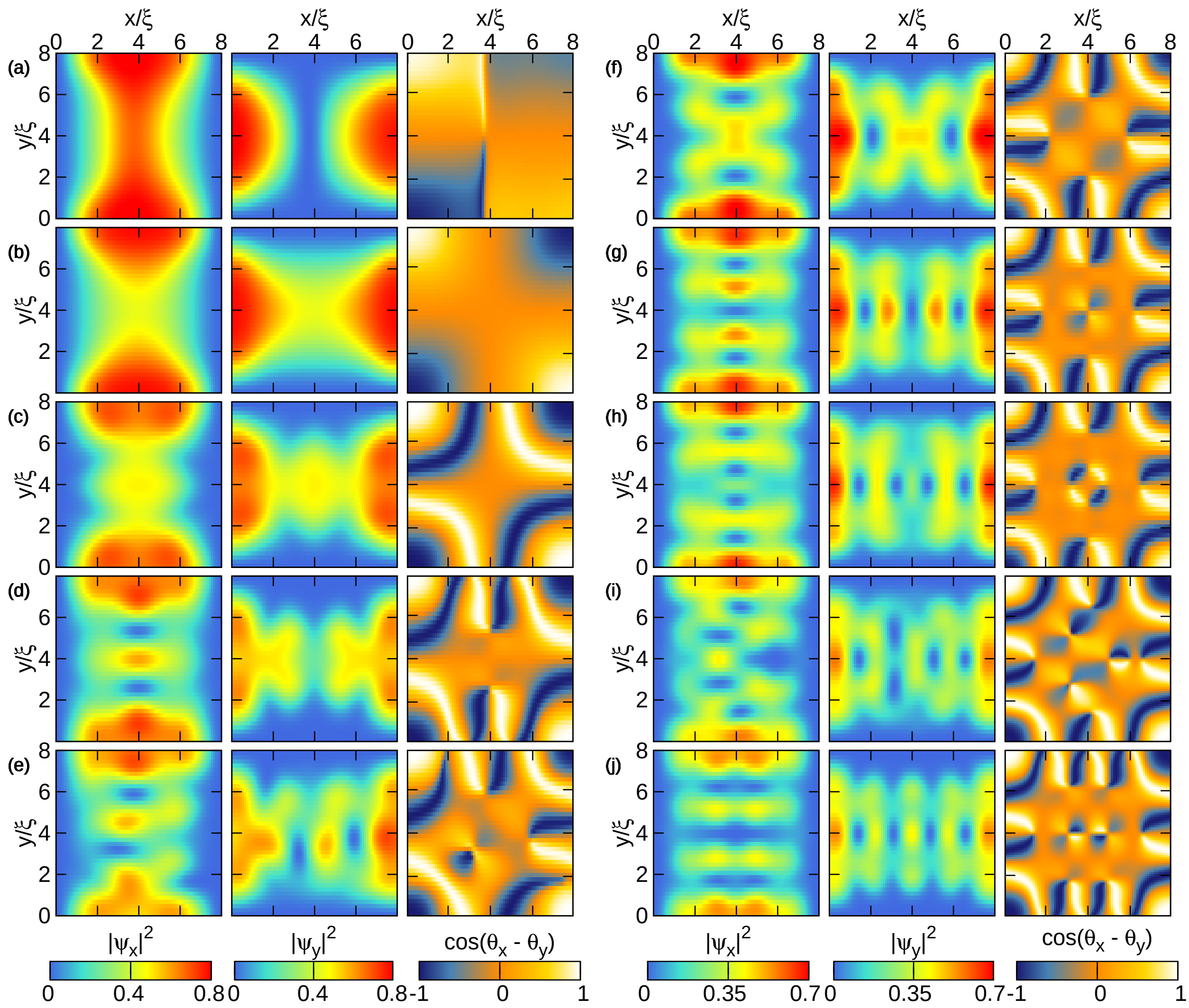

Figure 5.3: Ground states a - j *of Fig. 5.1, plotted correspondingly in panels (a) - (j). Left and central columns show the contour plots of the superconducting densities components* $|\psi_x|^2$ *and* $|\psi_y|^2$*, respectively. Right column shows* $\cos(\theta_x - \theta_y)$*, where* $\theta_{x,y}$ *are the angular phases of components* ψ_x *and* ψ_y*.*

skyrmion, respectively. Fig. 5.4 (a) zooms in the supercurrents around the right-top DW of Fig. 5.3(c). One can see two streams flowing in opposite senses at the upper right and lower left corners, respectively. The DW currents arise when these superconducting currents with opposite chiralities meet. In order to understand better the origin of the DW currents, Fig. 5.5(a) shows the line profiles of the corresponding superconducting densities $|\psi_\pm|^2$ along the diagonal line defined by $y = x$. Light (green) arrows point towards the already seen vortex cores of component ψ_- in Fig. 5.2(c). Dark (blue) arrows indicate the center of two DWs defined by the intersection where the densities $|\psi_-|^2$ and $|\psi_+|^2$ become equal. Where $\psi_+ = 0$, in the center of the sample, the other component (ψ_-) is non-zero and contributes to the chiral superconducting current. On the other hand, where $\psi_- = 0$, ψ_+ is non-zero and its current represents the chiral current flowing close to the corners of the sample.

The magnetic induction that corresponds to the DW supercurrents of Fig. 5.4(a) is shown in panel (a) of Fig. 5.6. It is calculated using the Maxwell equation,

$$\tilde{\kappa}^2 \nabla \times \mathbf{B} = \mathbf{J}, \tag{5.10}$$

where $\tilde{\kappa}^2 = \kappa^2/d$, with $\kappa = 2.3$ being the GL parameter reported for SRO along the *ab* plane [57], and d being the sample thickness which we suitably choose to be 2ξ. The contour plot of Fig.

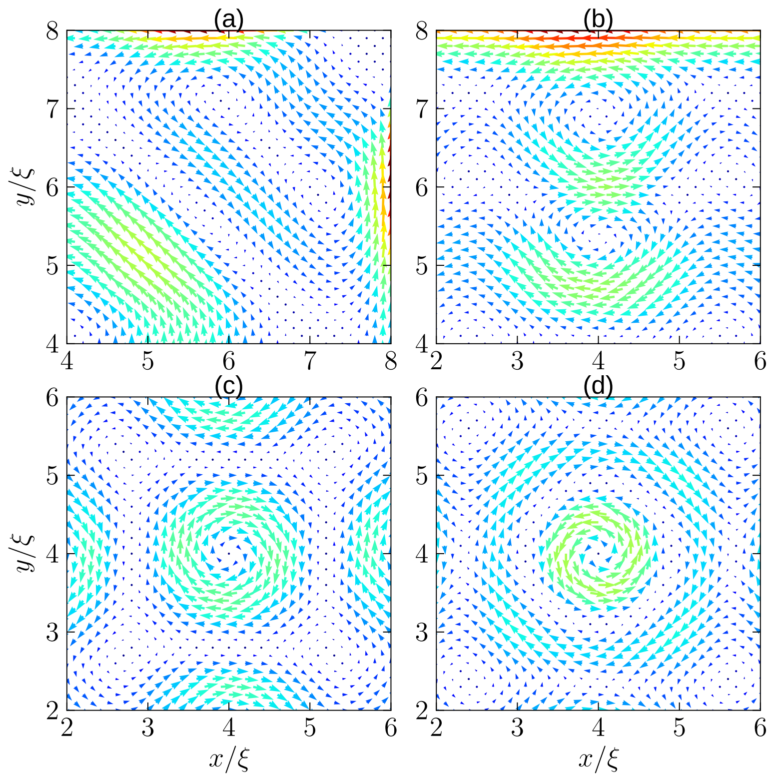

Figure 5.4: Superconducting currents around: (a) the upper right DW of Fig. 5.3(c), (b) the upper HQV of Fig. 5.3(d), (c) the FV of Fig. 5.3(g), and (d) the skyrmion of Fig. 5.3(h).

5.6(a) shows that the magnetic induction corresponding to the DW is weak and strongly screened by the Meissner effect. This fact represents an obstacle for the detection of DWs signatures in direct measurements of their magnetic response such as in magnetic force microscopy (MFM) or scanning Hall probe microscopy (SHPM).

Fig. 5.4(b) zooms in the supercurrents around the upper HQV of Fig. 5.3(d). It shows two adjacent counter-flowing streams with the bottom one flowing clockwise and belonging to the HQV supercurrents, while the top one flows counter-clockwise and represents the screening currents. The Meissner effect for the HQV is anisotropic due to the boundary conditions of Eq. (7.5). From the supercurrent equation (5.7), and the local approximation $\psi_y \approx 0$, or $\psi_+ \approx \psi_-$, drawn from Fig. 5.3(d), one easily obtains: $\mathbf{J} \approx \mathrm{Im}\{\psi_+^* D_x \psi_+ \hat{\imath} + \frac{1}{3}\psi_+ D_y \psi_+ \hat{\jmath}\}$. After straightforward calculations and replacing the covariant derivative once again one obtains: $\mathbf{J} \approx |\psi_+|^2 \left[(\partial_x \theta\, \hat{\imath} + \frac{1}{3}\partial_y \theta\, \hat{\jmath}) + \frac{Hr}{2}(\sin\phi\, \hat{\imath} - \frac{1}{3}\cos\phi\, \hat{\jmath})\right]$, which draws attention since the screening currents are defining elliptical equipotential lines. Thus, the anisotropic screening of the superconductor towards the HQVs causes them to move along the easy-screening direction which in this case is along $\hat{y}$. The contour plot of the magnetic induction corresponding to the supercurrents of Fig. 5.4(b) is shown in Fig. 5.6(b). As expected from the two counter-flowing streams seen in the HQV supercurrents, the magnetic induction also shows adjacent local maximum and local minimum.

Fig. 5.4(c) zooms in the superconducting currents around the FV of Fig. 5.3 (g), and shows that the FV currents flow clockwise and vanish as we move away from the FV core. This vanishing is due to the spatially isotropic Meissner effect, unlike in a HQV, that screens the FV currents. As expected, its magnetic induction signature [see Fig. 5.6(c)] agrees well with that of the Abrikosov vortex.

The superconducting currents around the skyrmion of Fig. 5.3 (h) are shown in Fig. 5.4 (d). Unlike the FV, the skyrmion supercurrents clearly show outer and inner structures. The supercurrents of the outer structure flow clockwise while the supercurrents of the inner flow counter-clockwise.

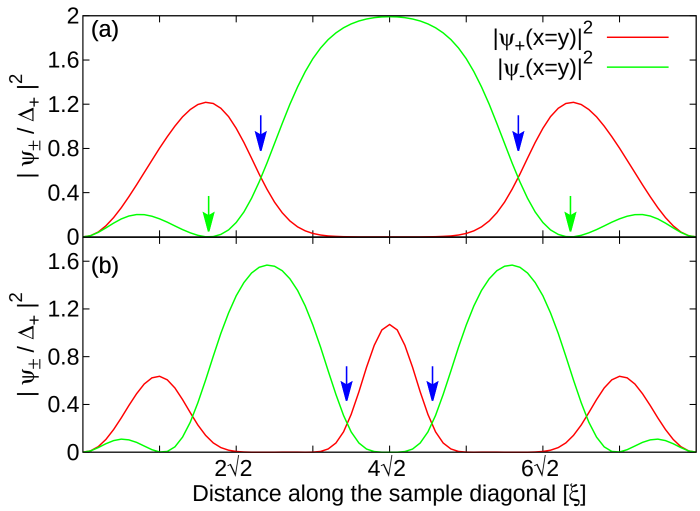

Figure 5.5: Diagonal profiles of the contour plots $|\psi_\pm|^2$ corresponding to ground states c *and* h *of Fig. 5.1, shown in panels (a) and (b), respectively. Blue and green arrows indicate the DW and vortex core locations, respectively.*

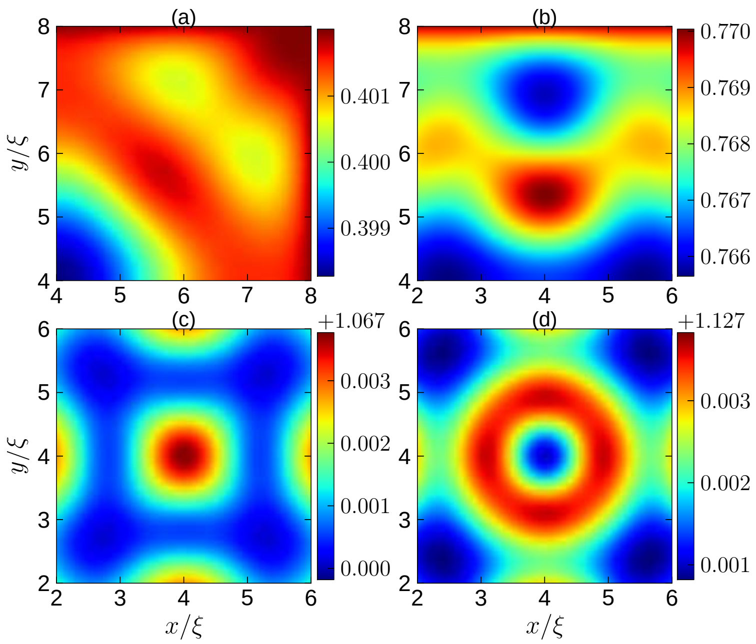

Figure 5.6: Contour plots of the magnetic induction corresponding to: (a) the supercurrents of the DW of Fig. 5.4(a), (b) the HQV of Fig. 5.4(b), the FV of Fig. 5.4(c), and (d) the skyrmion of Fig. 5.4(d).

The skyrmionic DW of Fig. 5.3(h) along with its supercurrents in Fig. 5.4(d) shows cylindrical symmetry, and one easily deduces that the same symmetry is present in densities $|\psi_\pm|^2$. Line profiles of $|\psi_\pm|^2$ then provide enough information to unveil the skyrmion supercurrents [see Fig. 5.5 (b)]. The inner structure of the skyrmion is defined by: $\psi_- = 0$ and $\psi_+ \neq 0$, i.e. the counter-clockwise currents at the core of the skyrmion arise from the chiral component ψ_+. However, away from the skyrmion core the scenario changes since the circular DW of Fig. 5.3 (h) is met, as indicated by arrows in Fig. 5.5 (b). Close beyond the circular DW, we find that while component ψ_+ drops to zero, ψ_- becomes non-zero. Replacing in Eq. (5.7) $\psi_+ = 0$ and bearing in mind that one giant vortex is hosted in component ψ_-, the supercurrent in cylindrical coordinates becomes: $\mathbf{J} \approx \frac{K+k_1}{4}|\psi_-|^2(-\frac{2}{r} + \frac{H}{2}r))\hat{\phi}$. The magnetic induction corresponding to the skyrmionic supercurrents of

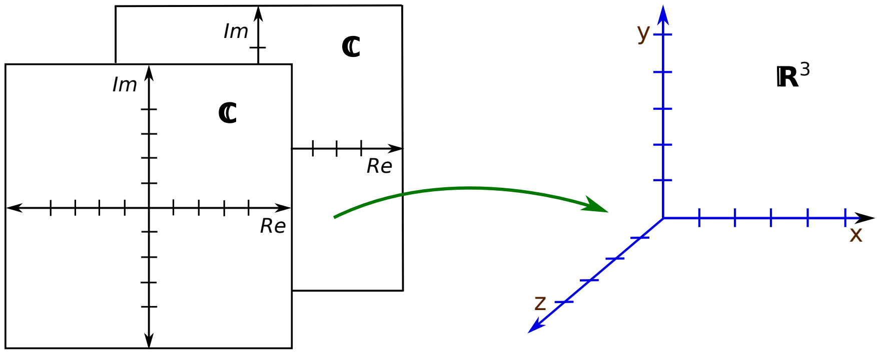

Figure 5.7: Representation of the spaces where the projection acts ($\mathbb{C} \times \mathbb{C}$) and where it projects ($\mathbb{R}^3$).

Fig. 5.4(d) is shown in the contour plot of Fig. 5.6(d). It clearly shows one local minimum at the skyrmion core surrounded by one circular stripe of local maxima, and as such can be directly imaged in magnetic measurements.

5.3.1 The topology of the skyrmion

In a two-component order parameter system, a 2D skyrmionic texture is not obviously seen in the order parameter configurations. However, it can be well understood by projecting the system onto a pseudospin space. This projection, defined by the Pauli matrices σ_i, with $i = x, y, z$, reads [123, 130, 141]

$$\mathbf{n} = (n_x, n_y, n_z) = \frac{\mathbf{\Psi}^\dagger \hat{\boldsymbol{\sigma}}\, \mathbf{\Psi}}{\mathbf{\Psi}^\dagger \cdot \mathbf{\Psi}}, \tag{5.11}$$

where the complex spaces $\mathbb{C} \times \mathbb{C}$ of components ψ_x, ψ_y are mapped into the real space $\mathbb{R}^3$ [see Fig. 5.7]. A straightforward calculation yields

$$\mathbf{n} = (\sin\alpha\cos\phi, \sin\alpha\sin\phi, \cos\alpha), \tag{5.12}$$

where $\sin\alpha = \frac{2|\psi_x||\psi_y|}{|\psi_x|^2+|\psi_y|^2}$, $\cos\alpha = \frac{|\psi_x|^2-|\psi_y|^2}{|\psi_x|^2+|\psi_y|^2}$, and $\phi = \theta_y - \theta_x$. As one can easily see from Eq. (5.12) the target space of mapping (5.11) is the 2-dim sphere of radius one, $\mathbb{S}^2$ [142, 143]. The topological invariant of the spaces that result from mapping (5.11) is defined by the integral [123, 130, 131]

$$\mathbb{Q} = \frac{1}{4\pi}\int \mathbf{n} \cdot (\partial_x \mathbf{n} \times \partial_y \mathbf{n})\, dx\, dy, \tag{5.13}$$

which is widely known as the Hopf invariant. One convenient interpretation of this topological invariant is that it counts the number of times that the 3-dim real field ($\mathbf{n}$) wraps around the 2-dim sphere ($\mathbb{S}^2$). Since the panel (h) of Fig. 5.3 reveals an additional topological possibility beyond the conventional vortex, the description of the superconducting configuration by the topological charge $\mathbb{Q}$ besides the vorticity per component of the order parameter (ν_+, ν_-), arises naturally.

Left and right panels of Fig. 5.8 show the texture $\mathbf{n}$ for ground states *h* and *g* of Fig. 5.3, respectively. The texture for the skyrmion (left panel) differs from the texture for the FV (right panel) owing to the alternating circular DW characteristic of the former state. While at the skyrmion core, field $\mathbf{n}$ points towards $-\hat{\jmath}$, outside the skyrmion it points towards $\hat{\jmath}$. Along the DW that separates the skyrmion core from the outside, the field texture whirls, therefore providing to the space the topological charge $\mathbb{Q} = -2$. The field texture that corresponds to the FV shows four lobes C4 symmetric profile where $\mathbf{n}$ changes smoothly. Unlike the skyrmion and in agreement with our earlier results, the field texture for the FV does not show any signature of a domain wall separating unequivalent outer and inner regions. Hence, its topological charge $\mathbb{Q}$ is zero.

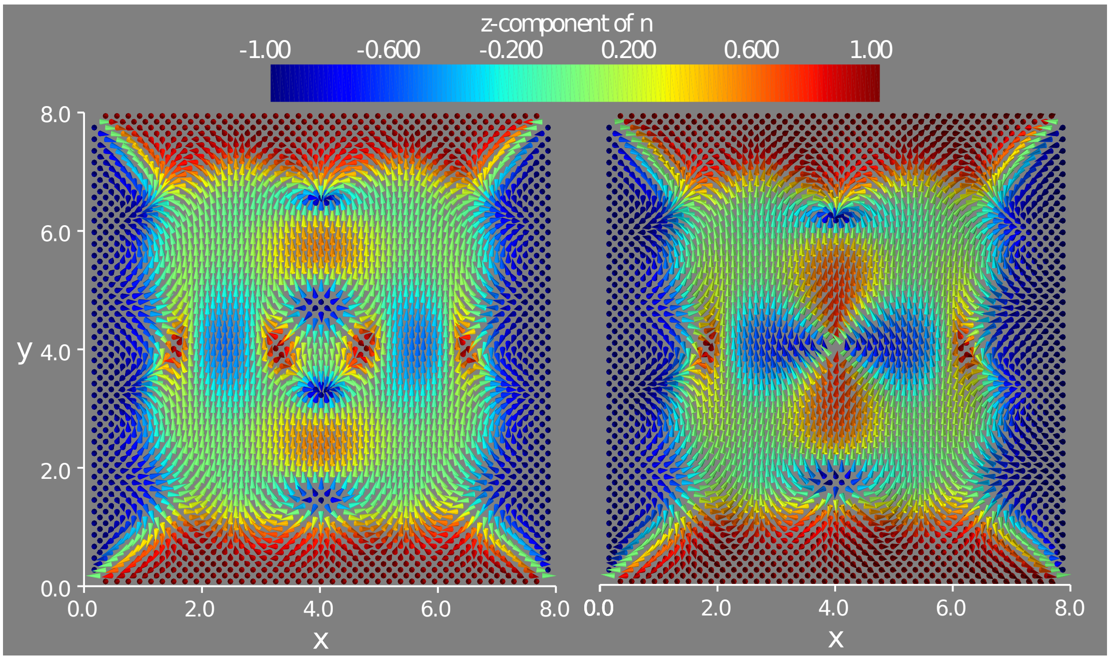

Figure 5.8: Textures of the ground states h *and* g *of Fig. 5.3, according to the mapping* $\mathbf{n} = \mathbf{\Psi}^\dagger\hat{\sigma}\mathbf{\Psi}/\mathbf{\Psi}^\dagger \cdot \mathbf{\Psi}$*, where* $\hat{\boldsymbol{\sigma}}$ *are the Pauli matrices. Colors show the amplitude of the z-component of* $\mathbf{n}$*.*

5.4 Field-driven transitions between skyrmionic and Vortical states

In bulk and type II superconducting samples vortices with phase windings higher than $2n\pi$, where n is integer, are energetically disfavored. The superconductor prefers two distant vortices each with phase winding 2π rather than one single vortex (giant vortex) with phase winding 4π. Nevertheless, in samples with dimensions of the order of the superconducting coherence length (mesoscopic samples), giant vortices can appear as stable configurations. The stabilization is provided mainly by the confinement due to the small sample size, although the external magnetic field also contributes through the screening currents and the confining force they exert on vortices. Field driven transitions from states with multiple distant vortices to giant vortices have been widely reported. [39–41, 132]

In this work we first report the field-driven transitions from HQV to FV states. Fig. 5.9 (a) shows the energy of state *f* of Fig. 5.1 (a), along with some of its neighboring states. Panel (b) shows the second derivative of the energy with respect to the external field only for state *f* . While the energy of state *f* is continuous, its second derivative shows discontinuities indicating transitions between distinct states. Three different states can be easily distinguished, which we labeled by a circle, square and triangle marker. The corresponding distributions of the superconducting order parameters are also shown in the figure: logarithmic contour plots of $|\psi_x|^2$ and $|\psi_y|^2$ are shown in the left and central columns, while the cosine of the phase difference is shown in the right column. State (◯) shows two fractional vortices in each component rendering four HQVs according to the phase difference contour plot. State (□) shows two HQVs and two FVs. The FVs are composed of two fractional vortices belonging separately to each component. The fractional vortices composing the FVs are slightly misaligned as can be seen in the density figures. This makes the FVs display a small closed domain wall in the phase difference contour plot. At high fields the screening currents confine even more the superconducting configuration of state (□) transforming it into one state with three HQVs and one FV (△). Due to the strong screening currents the upper FV of state (□) loses one of its fractional vortices which renders one HQV in state (△). The strong confinement also forces the alignment of the fractional vortices composing the FV of state (△).

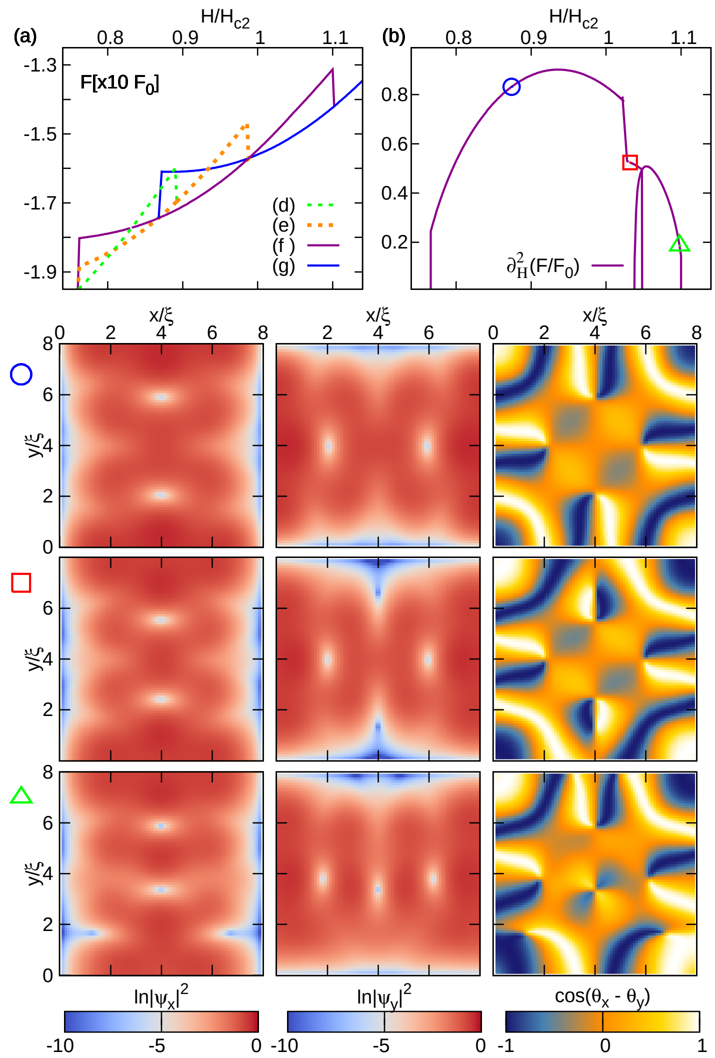

Figure 5.9: Field-driven transition from HQV to FV due to confinement in a square mesoscopic sample of size $8\xi\times8\xi$. (a) Energy of the state f *of Fig. 5.1 (a), along with some of its neighboring states. (b) Second derivative of the energy with respect to the external field showing three distinct states indicated by circular, squared and triangular symbols. The corresponding components of the superconducting order parameter are shown in panels (○), (□) and (△). Displayed quantities are logarithmic contour plots of $|\psi_x|^2$ and $|\psi_y|^2$ in left and central columns, respectively, while the cosine of the phase difference is shown at the right column.*

Another field-driven transition from skyrmion to FV state is presented in Fig. 5.10. Panel (a) shows the energy of state *j* of Fig. 5.1, along with some of its neighboring states. Panel (b) shows the first and second derivatives of the energy with respect to the external field only for state *j*. Unlike in Fig. 5.9 (b), here the second derivative is continuous as well as the first derivative. Nevertheless, this does not mean that there are no distinct states along the stability curve of state *j*. Circle, square and triangle markers (○, □ and △) indicate three states at weak, intermediate and strong confinement, respectively. At weak confinement the phase difference figure shows six HQVs and one skyrmion (see Fig. 5.10 (○)). At intermediate confinement, state (□) shows in $|\psi_x|^2$ that two out of the four fractional vortices composing the skyrmion of panel (○) have merged into one single discontinuity. This merger of initially distant fractional vortices renders the domain wall of the skyrmion asymmetric. At strong confinement (△) the former fractional vortices split their cores along the horizontal axis. According to the phase difference figure they join two other fractional vortices in density $|\psi_y|^2$ to form two horizontal FVs in the center of the sample. As can be easily seen, the vorticity of the

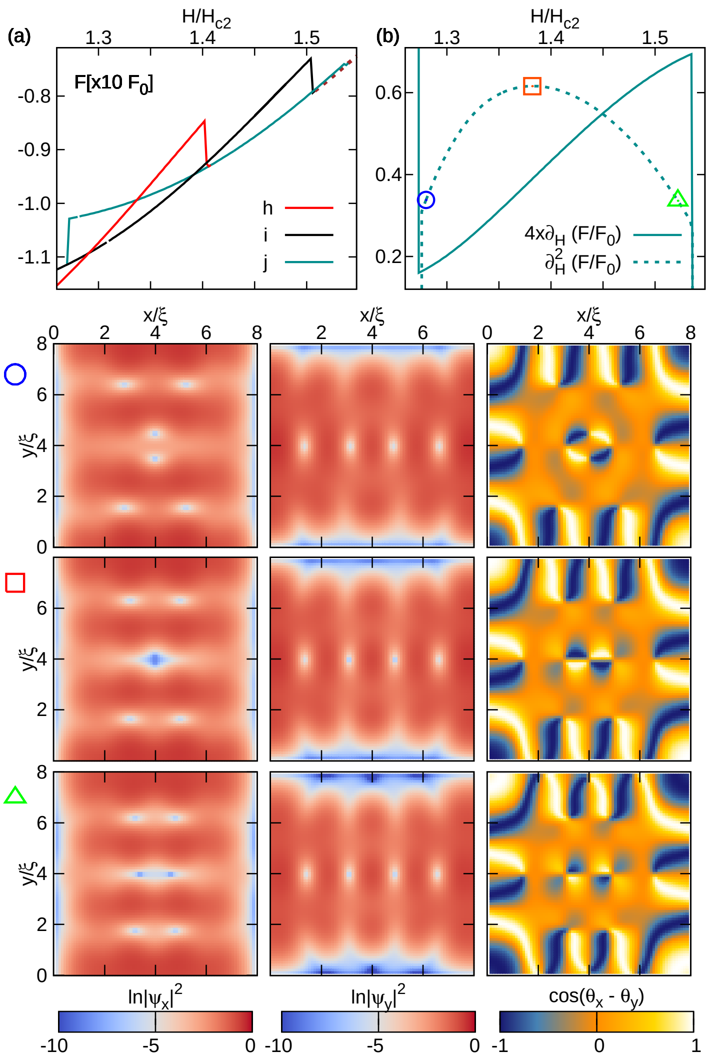

Figure 5.10: Another example of a field-driven transition between skyrmionic and vortical states along the state j *of Fig. 5.1. Displayed quantities are the same as in Fig. 5.9 with the only exception that in panel (b) the first derivative of the energy with respect to the external field is also shown.*

superconducting components along this field-driven transition is constant, unlike in Fig. 5.9 where it was not. This fact explains why the second derivative is continuous here and discontinuous in Fig. 5.9.

5.5 Temporal Dynamic transitions

To date, no works have treated the time-dependent phenomena within the GL formalism for chiral p-wave superconductors. Here we benefit from the temporal evolution included in the TDGL equations to report for the first time dynamic transitions involving vortices and skyrmions.

The dimensionless free energy as a function of the external field for states i and j is shown in panel (a) of Fig. 5.11. Unlike in Fig. 5.1 the sample size here is $12\xi\times12\xi$ rather than the $8\xi\times8\xi$, which was a suitable choice to study the evolution of the superconducting configuration. Panel (b) shows the temporal evolution of the free energy at the discontinuous step in energy in panel (a). Three states, initial, intermediate and final, are denoted by circle, square and triangle markers. The corresponding superconducting order parameters are shown in panels (○), (□) and

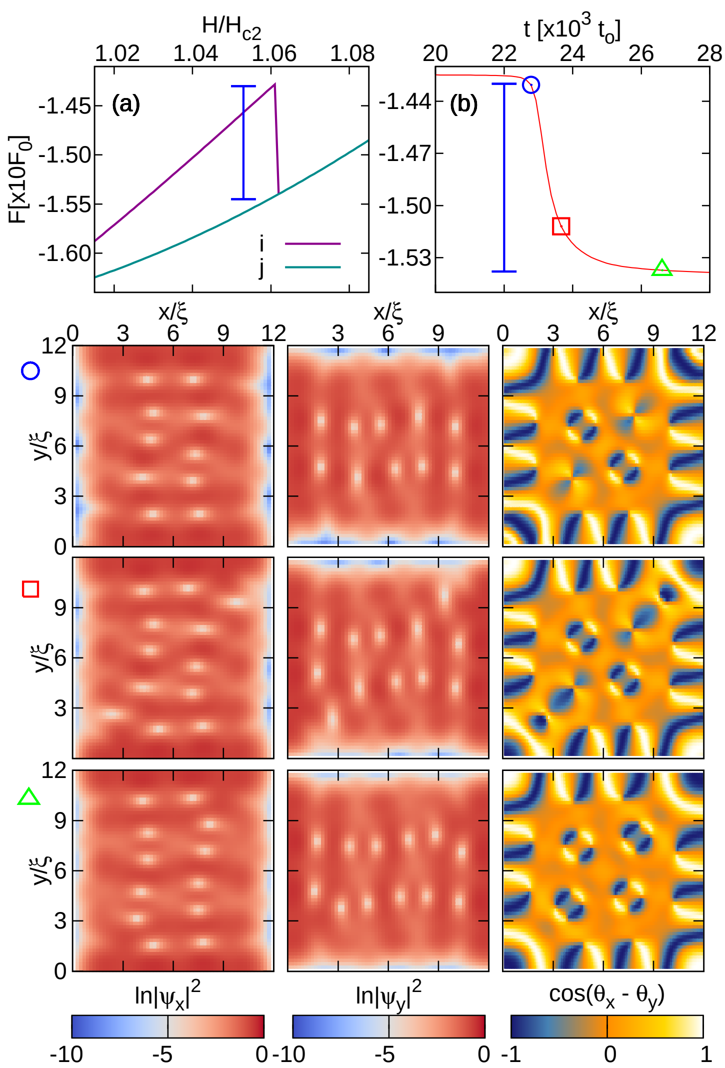

Figure 5.11: Temporal vortex-skyrmion transition in a square mesoscopic sample of size $12\xi\times12\xi$. Panel (a) shows the free energy of states i *and* j *containing 10 and 12 fractional vortices per component, respectively. The energy of state* i *is discontinuous at $H\approx 1.06H_{c2}$ reflecting a first order transition. Panel (b) shows the temporal evolution of the energy at the latter transition. Three states, initial, intermediate and final are denoted by circle, square and triangle markers, respectively. The components of the superconducting order parameter corresponding to each state are shown in panels (◯), (□) and (△).*

(△), respectively. The displayed quantities in the latter panels are the same as in those of Fig. 5.9. The initial state (◯) is a multi-vortex-skyrmion state containing two pairs of skyrmions and FVs, surrounded by eight HQVs at the sample edges. This state was not obtained for sample size $8\xi\times8\xi$ mainly due to the strong confinement there. At the intermediate state (□) two fractional vortices nucleate in each component of the superconducting order parameter forming two FVs according to the phase difference contour plot. The four FVs of the intermediate state then combine following the inverse process of the one described in Fig. 5.10, to form two skyrmions as depicted in state (△). It is noteworthy here that all field-driven transition from HQV or skyrmion to FV states and vice-versa are essentially driven by HQV penetration and recombination into other topological entities.

Finally we note that the above principles hold also for larger mesoscopic samples, though with more multi-vortex-skyrmion states found inside the sample, as well as more HQVs at the sample edges. Effectively, the edges of a large mesoscopic sample support realization of the quasi-1D periodic distribution of chiral domains discussed in Ref. [61], with domain walls of length $\approx 3\xi(T)$,

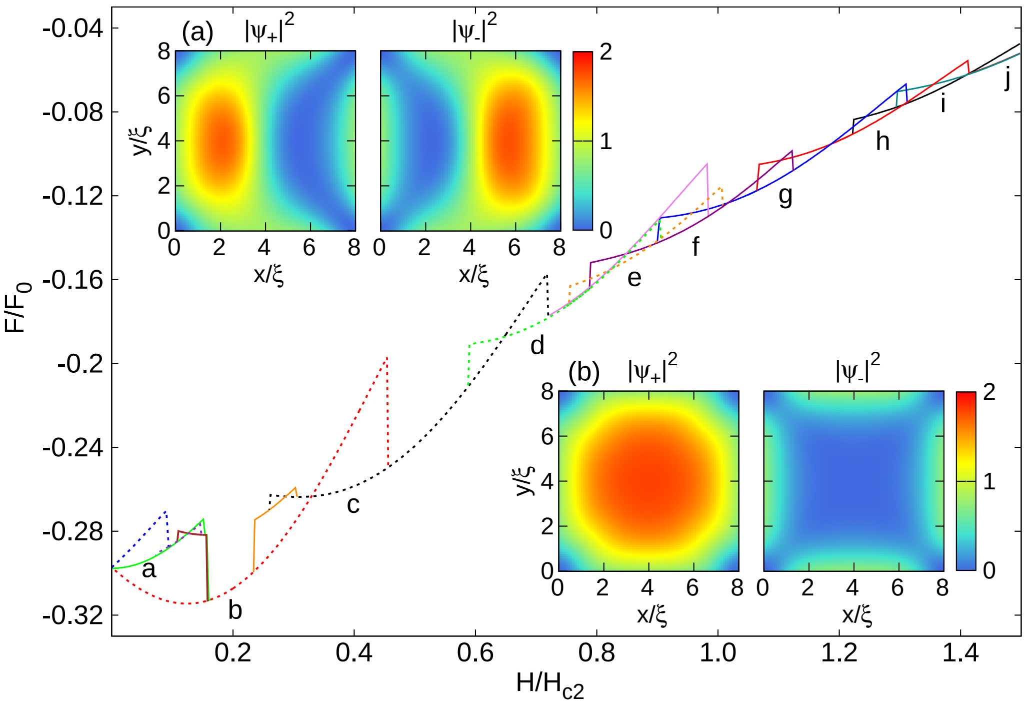

Figure 5.12: The free energy as a function of the external magnetic field, showing ground states b - j *plus one metastable state* a*, from the numerical simulations using Eq. (5.14) with $\delta_k = 0.03$. The parameters k_i thus only slightly deviate from the value $1/3$ obtained when a cylindrical Fermi surface is considered. Panels (a) and (b) show the superconducting density components $|\psi_+|^2$ and $|\psi_-|^2$ of the states* a *and* b*, respectively.*

i.e. ≈ 600 nm for $T = 0.9\,T_c$. This length is already matching the limits of scanning SQUID and Hall probe microscopies, explaining why spontaneous currents remained elusive in experiments to date, always performed on larger samples than considered in this work.

5.6 Anisotropic case

5.6.1 Strong chiral limit

This far, the ground states of a p-wave mesoscopic superconductor with size $8\xi \times 8\xi$ have been obtained under the assumption of weak coupling and with a cylindrical Fermi surface, which led us to set the k_i parameters to $1/3$ [77, 103, 135, 136]. However, several works have reported or suggested other scenarios for SRO such as: (i) multiband superconductivity with the 1D Fermi sheets developing superconducting order [63, 79, 80, 144], or (ii) anisotropy in the cylindrical Fermi surface [103, 123, 130]. In order to include just anisotropy in the Fermi surface, while preserving single-band superconductivity, and electron-hole symetry [77, 102, 127], in this section we introduce the parameter (δ_k), which sets the k_i's to: $k_1 = 1/3 + 2\delta_k$, and $k_2 = k_3 = 1/3 - \delta_k$. The motivation behind this choice is that the theoretical values for the k_i parameters corresponding to the three Fermi sheets (γ, α and β) lie between $1/3 < k_i^{\gamma} \leq 1$ and $0 \leq k_i^{\alpha,\beta} < 1/3$ [103], respectively. The GL equation for p-wave superconductors with anisotropy in the Fermi surface becomes:

$$\begin{aligned} \partial_t \mathbf{\Psi} &= \frac{2}{3}\Big[\mathbf{D}^2 + \Pi_+^2\hat{\sigma}_+ + \Pi_-^2\hat{\sigma}_-\Big]\mathbf{\Psi} + \mathbf{\Psi}\Big(1 - \frac{3|\mathbf{\Psi}|^2}{4} \pm \frac{\mathbf{\Psi}^*\hat{\sigma}_z\mathbf{\Psi}}{4}\Big) \\ &+ \delta_k\big[\mathbf{D}^2 - 2\big(\Pi_+^2\hat{\sigma}_+ + \Pi_-^2\hat{\sigma}_-\big)\big]\mathbf{\Psi}. \end{aligned} \tag{5.14}$$

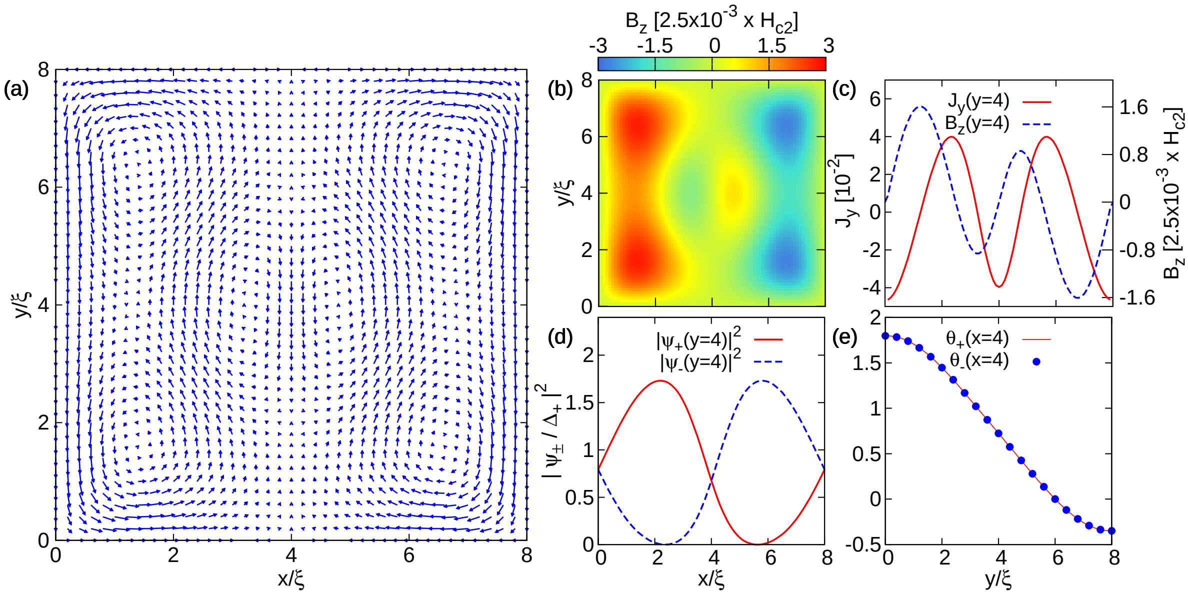

Figure 5.13: (a) Superconducting currents corresponding to the state a *of Fig. 5.12. These currents, which were obtained at zero field, are composed of two edge currents with different chiralities and flowing in opposite senses. (b) Contour plot of the magnetic induction (B_z) calculated from the supercurrents of panel (a). (c) Line profiles of J_y and B_z along the line $y = 4\xi$. (d) Line profiles of $|\psi_\pm|^2$ corresponding to the state* a *of Fig. 5.12. (e) Line profiles of the angular phases of components $\psi_\pm$ along the line $x = 4\xi$.*

By tuning δ_k within the interval $[0, 1/3]$, the strength of the non-diagonal (chiral) terms of Eq. (5.5) is changed, therefore driving the system between two limiting cases: the left limiting case being at $\delta_k = 0$ and given by Eq. (5.6), and the right limiting case being at $\delta_k = 1/3$ where the chiral coupling between the superconducting components is set to zero.

Fig. 5.12 summarizes the results obtained from the simulations that numerically approach Eq. (5.14) with $\delta_k = 0.03$. The energy against field plot of Fig. 5.12 shows nine ground states labeled by letters. The comparison between Figs. 5.12 and 5.1 reveals one important fact: the energy of the state *a* is higher than the energy of its adjacent state *b*. Actually, state *a* here is no longer the ground state at low fields $H \approx 0$, unlike in Fig. 5.1 where it was. Contour plots of the superconducting order parameter ($\mathbf{\Psi}$) that correspond to the states *a* and *b* of Fig. 5.12 are depicted in insets (a) and (b), respectively. The comparison between the insets of Fig. 5.12 and the corresponding states in Fig. 5.2 shows that despite of the small anisotropy introduced in the GL equation, the superconducting configuration of these states is practically identical in both cases.

Two decades have passed since the discovery of the unconventional properties of strontium ruthenate, but to date there has not been a consensus whether or not it is a chiral p-wave superconductor [59–62]. The main experimental results that support unconventional superconductivity in SRO are provided by the set of measurements carried out using techniques such as the Knight shift [47, 100], μSR [52], the optical Kerr effect [53], and cantilever magnetometry [134]. The smoking gun evidence that lacks, and which, if found, would convince the scientific community is the finding of the theoretically predicted spontaneous currents in Sr_2RuO_4 [71, 76, 77]. Interestingly, what we just found in this work is that the state with spontaneous currents is no longer the ground state when the GL model slightly deviates from the isotropic case at $H \approx 0$, i.e slightly deviated from the cylindrical Fermi surface. This energy lift of the state with spontaneous currents makes it even harder to be detected. Fig. 5.13(a) shows the supercurrent distribution corresponding to the state *a* of Fig. 5.12. We note that the currents displayed there were obtained at $H = 0$, thus those are the spontaneous currents widely sought in experiments. The spontaneous currents are composed mainly of two counter-flowing streams at left and right sides of our sample. They are the chiral edge currents predicted by Matsumoto and Sigrist [76]. Along the line $x = 4\xi$, the linear domain wall (DW) of Fig. 5.3(a) separates the left and right sides showing an enhancement in the supercurrents around the center. The magnetic induction corresponding to the supercurrents of panel (a) is shown in panel (b) of the same figure.

Panel (c) of Fig. 5.13 shows line profiles of the magnetic induction and the y-component of **J** along the line $y = 4\xi$. This plot agrees well with the result of Matsumoto and Sigrist which showed that J_y (B_z) is an even (odd) function of x along the line perpendicular to the DW [76]. Finally, panels (d) and (e) provide important information that allow us to calculate the supercurrent along the DW. From panel (d) the DW is defined by $|\psi_+| = |\psi_-|$ at $x = 4\xi$, but along this line panel (e) tells us that not only the magnitudes of the superconducting components are equal but also their angular phases. Then, from Eq. (5.7) our estimation for the superconducting current along the linear domain wall is simply $J_y(x = 4\xi) = k_1|\psi_+|^2\partial_y\theta_+$.

5.6.2 Strong Zeeman limit

Microscopy with superconducting quantum interference devices (SQUIDs) and scanning Hall probes (SHPs) have recently detected vortex coalescence in single crystals of strontium ruthenate [145, 146]. One possible explanation for this behavior is the existence of at least two different coherence lengths arising from multigap superconductivity, and which lead to attractive (repulsive) interaction at long (short) ranges [144]. Refs. [60] and [146] have reported that within their corresponding resolutions no convincing evidence for spontaneous currents and DWs has been found yet. In order to explore more superconducting configurations, comprising DWs, HQVs, FVs and skyrmions as the fundamental entities, in what follows a different set of the k_i parameters is defined by: $k_1 = 1/3$, $k_2 = 1/3 + \delta_k$ and $k_3 = 1/3 - \delta_k$. Such a choice of parameters enables one to keep constant the strength of the chiral terms while varying δk. The first GL equation for this particular choice of parameters reads

$$\begin{aligned}\partial_t\mathbf{\Psi} &= \frac{2}{3}\Big[\mathbf{D}^2 + \Pi_+^2\hat{\sigma}_+ + \Pi_-^2\hat{\sigma}_- - \frac{3\delta_k}{2}H\hat{\sigma}_z\Big]\mathbf{\Psi} \\ &+ \mathbf{\Psi}\Big(1 - \frac{3|\mathbf{\Psi}|^2}{4} \pm \frac{\mathbf{\Psi}^*\hat{\sigma}_z\mathbf{\Psi}}{4}\Big). \end{aligned} \quad (5.15)$$

The fourth term in the right side of Eq. (5.15) represents the orbital Zeeman interaction. It is zero whitin the weak-coupling limit where $k_2 = k_3$ [77, 127]. In this subsection, we consider a possible assymetry between electron and hole that leads to slightly different k_2 and k_3. In order to study the dependence of the superconducting configuration on the anisotropy parameter, in Eq. (5.15) the magnetic field is kept fixed while δ_k is varied. Fig. 5.14(a) plots the free energy of the states, solving Eq. (5.15), as a function of the anisotropy parameter δ_k. Circle, square and triangle markers denote three states whose $|\psi_+|^2$ and $|\psi_-|^2$ diagonal ($y = x$) line profiles are shown in panels (b) and (c), respectively. From panel (c), and unlike in panel (b), one clearly sees that for high values of δ_k the density $|\psi_-|^2$ diminishes. Our explanation for this behavior is through the definition of two effective coherence lengths, one for each superconducting component. Defining them as the coefficients in front of the linear terms ψ_+ and ψ_- in Eq. (5.15), they read: $\xi_+ = 1 - \delta_k H$ and $\xi_- = 1 + \delta_k H$, respectively. With H fixed and δ_k increasing, ξ_+ (ξ_-) becomes smaller (larger) therefore leading to an effective reduction (increase) of confinement in component ψ_+ (ψ_-). Concerning the phase, contour plots of θ_+, θ_- and $\cos(\theta_x - \theta_y)$ corresponding to the states denoted by circle, square and triangle markers are shown in rows (○), (□), and (△). According to the phase difference figure, state (○) is composed of two concentric skyrmions, one circular and one rhomboidal. From the contour plot of θ_- one sees that the circular skyrmion arises from the formation of one giant vortex in ψ_- with phase winding 4π. The phase difference figure corresponding to state (□) shows one irregular closed domain wall emerging from the intersection of the circular and rhomboidal skyrmions. Its formation

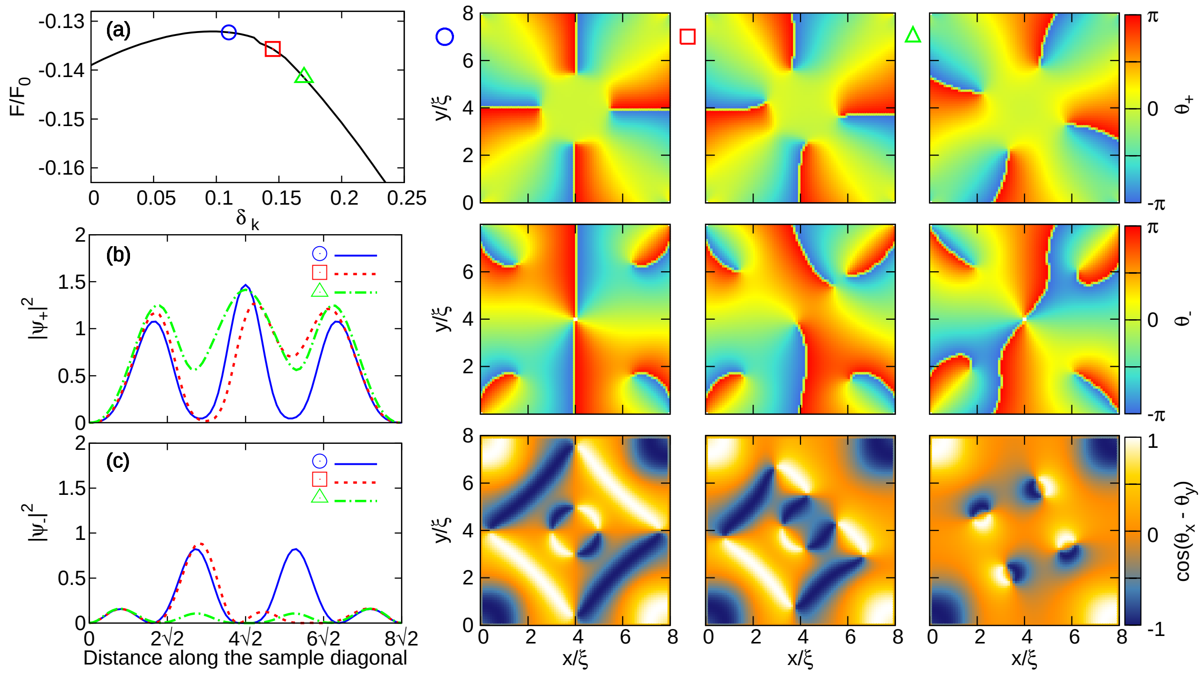

Figure 5.14: (a) Free energy as a function of the anisotropy parameter δ_k with the external magnetic field fixed at $H = 0.530[H_{c2}]$. Three distinct states are indicated by circular, square and triangular markers (◯, □ and △). (b) and (c) show line profiles of $|\psi_+|^2$ and $|\psi_-|^2$, respectively, along the diagonal line ($y = x$) corresponding to the states of panel (a). Columns (◯), (□) and (△) show contour plots of θ_+, θ_- and $\cos(\theta_x - \theta_y)$ corresponding to the denoted states of panel (a).

is determined by the annihilation of the giant vortex in θ_- that has split into two fractional vortices. Finally, the phase difference figure of state (△) shows four FVs with cores slightly asymmetric as can be seen from the small circular DWs present there. Due to the density $|\psi_-|^2$ has been substantially depleted at this value of δ_k, the superconducting state is completely defined by component ψ_+. Hence, what we have achieved by considering assymetry between electron and hole in the chiral p-wave model of Eq. (5.5), is a chiral polarization enhanced due to the strong confinement present in a mesoscopic sample.

5.7 Conclusions

In summary, we have studied in detail the Ginzburg-Landau model that describes chiral p-wave superconductors [77, 94, 102, 103, 129, 135, 136], and all the possible states of a mesoscopic superconducting sample as a function of the external magnetic field and the anisotropy parameters of the material. Due to odd parity and breaking of the time-reversal symmetry, the order parameter is a two-component complex vector [48, 94] and the fundamental solutions of the corresponding TDGL equations, that we obtained numerically, are fractional vortices, i.e. solutions where the phase winding 2π is found in one component but not in the other one. In two- and three-band superconductors similar fractional vortices were obtained between components, but for different reasons [147–149]. Fractional vortices in different components can combine to form a cored/full-vortex state, as well as a coreless/skyrmion state seen in phase difference and magnetic response figures. Skyrmions arise when same number of fractional vortices in each component combine to form a closed domain wall that separates distinct intercomponent phase difference $(\theta_x - \theta_y)$ regions [137, 138]. Alternating segments between 1 and -1 in the $\cos(\theta_x - \theta_y)$ between fractional vortices along the domain wall is the main signature for skyrmions. While for skyrmions the topological charge ($\mathbb{Q}$) is defined by the Hopf invariant [123, 130, 131], for vortices it is defined by the circulation of the superconducting velocity. Despite of the fact that vector $\mathbf{d}$ is strongly pinned along $\hat{\mathbf{z}}$ in the chiral representation $\mathbf{d} = (k_x \pm ik_y)\hat{\mathbf{z}}$ [94, 129], we also obtained half-quantum vortices analogous to those of spin-triplet superconductors [133]. The screening currents of half-quantum vortices are anisotropic and in Cartesian coordinates we have analytically shown that the equipotential lines of the screening currents are ellipsoidal rather than circular as in full vortices. This anisotropic screening causes the attraction of the half quantum vortex towards the sample edges. The mesoscopic size of our samples provides stability to the half quantum vortices and the $\mathbb{Q} = 2$ skyrmions, in contrast to larger systems where larger values of $\mathbb{Q}$ were considered [123, 130], and bulk systems where the half quantum vortices have been usually regarded as high-energy states. Actually the mesoscopic size of the sample plays a remarkable role in the stability of skyrmions as well as in the here reported novel transitions (e.g. from a skyrmion to a full vortex). At high external fields, above the H_{c1} critical field, states with different configurations of skyrmions and half quantum vortices gradually transform into full vortices owing to the increased screening currents and confinement effects.

To date, the only superconductor expected to be p-wave is strontium ruthenate, with enough evidence demonstrating its unconventional behavior [47, 52, 53, 100, 134]. Nevertheless, many works have failed to convincingly detect spontaneous currents, half-quantum vortices and skyrmions in large samples [59–62]. What we have demonstrated here is that: (i) even by slight anisotropy in the Fermi surface, the state with spontaneous currents is no longer the ground state at $H \approx 0$, (ii) for large mesoscopic samples quasi-1D periodic distribution of chiral domains is realized at the edges of the sample, with half-quantum vortices residing on domain walls with length of several coherence lengths, with magnetic features detectable in scanning SQUID and hall probe microscopy, and (iii) distinct field-driven transitions between half-quantum vortex, full vortex, and skyrmions, provide alternative method to indirectly prove the existence of these exotic states in magnetic measurements.

Publication The results of this chapter were published in:

- V. Fernández Becerra, E. Sardella, F. M. Peeters, and M. V. Milošević, *Vortical versus skyrmionic states in mesoscopic p-wave superconductors*, Phys. Rev. B **93**, 014518 (2016) (13 pages).

6

Electronic properties of emergent topological defects in chiral p-wave superconductivity

Chiral p-wave superconductors in an applied magnetic field can exhibit more complex topological defects than just conventional superconducting vortices, due to the two-component order parameter and the broken time-reversal symmetry. In this chapter, we show the electronic properties of those exotic states, all obtained as a self-consistent solution of the microscopic Bogoliubov-de Gennes equations. We reveal the link between the local density of states (LDOS) of the novel topological states and the behavior of the chiral domain wall between the components of the order parameter, enabling direct identification of those states in scanning tunneling microscopy. Finally, we present the magnetic field and temperature dependence of the properties of a skyrmion, indicating that this topological defect can be surprisingly large in size, and can be pinned by an artificially indented non-superconducting closed path in the sample. These features are expected to facilitate the experimental observation of skyrmionic states, thereby enabling experimental verification of chirality in emerging superconducting materials.

6.1 Introduction

Spin-triplet chiral p-wave superconducting states attract great interest because of their exotic properties and the possibility to have topologically protected quantum states [150]. Such unconventional pairing is realized in the A-phase of superfluid ^{3}He and may be attributed also to the layered ruthenate superconductor Sr_2RuO_4 [151]. The order-parameter (OP) of the p-wave pairing state is necessarily multi-component due to the nonzero orbital angular momentum of the Cooper pairs. This fact has profound consequences, namely the breaking of time-reversal symmetry [48, 152], and results in rich topological defect states, of different types, with often nontrivial vorticity.

First, there exist domain walls with spontaneous supercurrent separating domains with different degenerate time-reversal-symmetry-broken ground states [76]. Second, half-quantum vortices arise due to the extra spin freedom in OP and are predicted to be thermodynamically stable in mesoscopic samples and have been detected in Sr_2RuO_4 [134, 150]. It is also expected that the half-quantum vortices in two-dimensional superfluids will host Majorana states at exactly zero energy as bound states inside the vortex cores [153]. The Majorana zero mode gives rise to non-Abelian statistics and thus can be utilized to make topological quantum computation [154].

Third, in p-wave superconductivity, there exist two types of singly quantized vortices due to the broken time-reversal symmetry [155]. The Cooper pairs of chiral p-wave pairing have internal orbital angular momentum, i.e. the paired electrons are rotating. Then, the vortex can have either the vorticity in the same direction to the angular momentum of the rotating Cooper-pair (parallel vortex), or in the opposite direction (anti-parallel vortex). These two types of vortices have different angular momenta, causing different properties in electronic states [156] leading to different optical absorption [155], vortex charging effect [157], and surface sensitivity effect [158].

Lastly, the chiral p-wave pairing state allows the existence of coreless vortices (CLVs) with nonzero vorticity in only one OP component [159], which are very different from conventional singular-core vortices. The CLVs result from the extra orbital and spin degree of freedom in the OP. The CLV with doubly quantized flux has been detected in liquid ^{3}He [160]. In chiral p-wave superconductors, this doubly quantized vortex state is predicted to be energetically favorable when compared to the state with two singly quantized vortices [123, 130], and should be further stabilized in the presence of mesoscopic boundaries [124]. The Ginzburg-Landau simulations reported the magnetic field distributions of the CLV states [130], that are still to be been observed experimentally.

Such CLVs are extremely interesting, exhibiting a variety of different aspects: (i) they are analogous to a giant vortex in s-wave superconductors [39] since they contain multiple flux quanta, but exhibit a larger size. (ii) The CLV is similar to a domain wall separating domains where different OP components dominate [159]. (iii) The $\mathbf{l}$-vector texture of a coreless vortex was characterized as a 2D skyrmion [143], where a pseudo-spin texture $\mathbf{n}$ of a two-component OP exhibits 2D skyrmion texture for the coreless vortex [130, 141]. Although these previous studies revealed important aspects of the coreless vortices, there is still a need for a systematic study in order to enhance understanding on the coreless vortices and skyrmionic topological defects especially concerning their bound electronic states.

In this chapter, we study the possible topological defect states in chiral p-wave superconductors, ranging from domain walls, and vortices, to coreless vortices and skyrmions, by solving the microscopic Bogoliubov-de Gennes (BdG) equations self-consistently. The purpose of this chapter is to clarify their topological properties and also to reveal their detailed electronic properties. The bound electronic states in e.g. vortices are known to be important for many applications [161–165]. For example, they determine the low-temperature behavior of the specific heat [166]. In this chapter, the shown results on characteristic quasiparticle excitation spectra and details of the local density of states (LDOS) of each state (especially the states associated with the skyrmion), enable their identification in e.g. scanning tunneling microscopy (STM). Modern STM operates at spatial resolution up to 0.1 nm, and has successfully detected to date the zero bias conductance peak at the vortex core [167], phase transition between multi- and giant vortex states [41], proximity effect [168], Josephson vortices [169, 170], etc. Hence our results will provide valuable info for direct detection of novel topological states, which can in turn serve as a 'smoking gun' for p-wave superconductivity in the studied system.

The chapter is organized as follows. In Sec. 6.2 we introduce our theoretical methodology for chiral p-wave superconductors. In Sec. 6.3 we collect the results for three distinct states without a skyrmionic topology. Those are the vortex-free state, the parallel vortex state and the anti-parallel vortex state. In Sec. 6.4 we present results on coreless vortex states. Their OP structures, supercurrent distribution, energy spectra and LDOS are discussed. We show that they are associated with skyrmionic topological defects in relative OP space. In Sec. 6.5 we reveal the magnetic field and temperature dependence of the properties of the skyrmion, followed by the investigation of an effective skyrmion pinning in Sec. 6.6. Finally, our findings are summarized in Sec. 6.7.

6.2 Bogoliubov-de Gennes equations for chiral p-wave superconductors

We consider chiral p-wave superconductors whose order parameter (OP) is expressed as

$$\mathbf{\Delta}(\mathbf{r},\mathbf{k}) = \Delta_+(\mathbf{r})Y_+(\mathbf{k}) + \Delta_-(\mathbf{r})Y_-(\mathbf{k}). \tag{6.1}$$

Here the $\Delta_\pm(\mathbf{r})$ are the real spatial $p_x \pm ip_y$-wave OP and $Y_\pm(\mathbf{k}) = (k_x \pm ik_y)/k_\mathrm{F}$ are the pairing functions in relative momentum space. We consider a disk geometry with radius R. The corresponding $p_x \pm ip_y$-wave BdG equations are written as: [157]

$$\begin{bmatrix} H_e(\mathbf{r}) & \Pi(\mathbf{r}) \\ -\Pi^*(\mathbf{r}) & -H_e^*(\mathbf{r}) \end{bmatrix} \begin{bmatrix} u_n(\mathbf{r}) \\ v_n(\mathbf{r}) \end{bmatrix} = E_n \begin{bmatrix} u_n(\mathbf{r}) \\ v_n(\mathbf{r}) \end{bmatrix}, \tag{6.2}$$

where

$$H_e(\mathbf{r}) = \frac{1}{2m}\Big[\frac{\hbar}{i}\nabla - \frac{e}{c}\mathbf{A}(\mathbf{r})\Big]^2 - E_\mathrm{F} \tag{6.3}$$

is the single particle Hamiltonian with m being the electron mass, E_F the Fermi energy and $\mathbf{A}(\mathbf{r})$ the vector potential (we use the gauge $\nabla \cdot \mathbf{A} = 0$). For simplicity, we take the cylindrical two dimensional Fermi surface. The term $\Pi(\mathbf{r})$ is written as

$$\Pi(\mathbf{r}) = -\frac{i}{k_\mathrm{F}}\sum_\pm [\Delta_\pm \Box_\pm + \frac{1}{2}(\Box_\pm \Delta_\pm)], \tag{6.4}$$

with $\Box_\pm = e^{\pm i\theta}(\partial_r \pm \frac{i}{r}\partial_\theta)$ in cylindrical coordinates. $u_n(\mathbf{r})(v_n(\mathbf{r}))$ are electron(hole)-like quasiparticle eigen wavefunctions with the normalization condition

$$\int \big\{|u_n(\mathbf{r})|^2 + |v_n(\mathbf{r})|^2\big\} d\mathbf{r} = 1, \tag{6.5}$$

and E_n are the corresponding quasiparticle eigenenergies. The boundary conditions for the wavefunctions are $u_n(r = R) = 0$ and $v_n(r = R) = 0$. The $\Delta_\pm(\mathbf{r})$ satisfy the self-consistent gap equations

$$\Delta_\pm(\mathbf{r}) = -i\frac{g}{2k_\mathrm{F}} \sum_{E_n < \hbar\omega_D} [v_n^*(\mathbf{r})\Box_\mp u_n(\mathbf{r}) - u_n(\mathbf{r})\Box_\mp v_n^*(\mathbf{r})] \times [1 - 2f(E_n)], \tag{6.6}$$

where $k_\mathrm{F} = \sqrt{2mE_\mathrm{F}/\hbar^2}$ is the Fermi wave length, g the coupling constant and $f(E_n) = [1 + \exp(E_n/k_\mathrm{B}T)]^{-1}$ is the Fermi distribution function. The summations in Eq. (6.6) are over all the quasiparticle states with energies in the Debye window $\hbar\omega_D$. The supercurrent density is calculated by

$$\begin{aligned} \mathbf{j}(\mathbf{r}) =& \frac{e\hbar}{2mi}\sum_n \Big\{ f_n u_n^*(\mathbf{r})\Big[\nabla - \frac{ie}{\hbar c}\mathbf{A}(\mathbf{r})\Big]u_n(\mathbf{r}) \\ &+ (1 - f_n)v_n(\mathbf{r})\Big[\nabla - \frac{ie}{\hbar c}\mathbf{A}(\mathbf{r})\Big]v_n^*(\mathbf{r}) - \mathrm{h.c.}\Big\}. \end{aligned} \tag{6.7}$$

In order to perform the self-consistent simulation, we include the contribution of the supercurrent to the total magnetic field. Then, the vector potential $\mathbf{A}(\mathbf{r})$ in Eqs. (6.3) and (6.7) has two parts, i.e. $\mathbf{A}(\mathbf{r}) = \mathbf{A_0}(\mathbf{r}) + \mathbf{A_1}(\mathbf{r})$, where $\mathbf{A_0}(\mathbf{r}) = \frac{1}{2}H_0 r\mathbf{e}_\theta$ corresponds to the applied magnetic field $\mathbf{H} = H_0\mathbf{e}_z$ and the $\mathbf{A_1}(\mathbf{r})$ is induced by the supercurrent and obey the Maxwell equation

$$\nabla \times \nabla \times \mathbf{A_1}(\mathbf{r}) = \frac{4\pi}{c}\mathbf{j}(\mathbf{r}). \tag{6.8}$$

However, we find that the $\mathbf{A_1}(\mathbf{r})$ is negligible due to the very thin superconducting sample. As a result, the contribution of the supercurrent to the total magnetic field can be completely neglected in this type of simulation.

In this chapter, we only consider vortex and skyrmion states with cylindrical symmetry. Therefore, the $p_x \pm ip_y$ components of the order parameter are expressed as $\Delta_\pm(\mathbf{r}) = \Delta_\pm(r)e^{iL_\pm\theta}$ with winding numbers $L_\pm$, respectively. Due to operators $\square_\pm$ in Eqs. (6.2)-(6.6), $\Delta_\pm$ have a ±1 Cooper-pair phase winding, respectively, leading to $L_- = L_+ + 2$. This also breaks the time-reversal symmetry, resulting in chiral states.

In a cylindrical system, the quasiparticle wavefunctions $u_n(\mathbf{r})$ and $v_n(\mathbf{r})$ can be expanded in terms of the following Bessel set [114]:

$$\begin{pmatrix} u_n(\mathbf{r}) \\ v_n(\mathbf{r}) \end{pmatrix} = \sum_j \begin{pmatrix} c_{n\mu j}\varphi_{j\mu}(r)e^{i\mu\theta} \\ d_{n\mu' j}\varphi_{j\mu'}(r)e^{i\mu'\theta} \end{pmatrix}, \tag{6.9}$$

where $c_{n\mu j}$ and $d_{n\mu' j}$ are coefficients, μ,$\mu' \in \mathbb{Z}$ are angular quantum numbers corresponding to the angular momentum, and

$$\varphi_{j\mu}(r) = \frac{\sqrt{2}}{RJ_{\mu+1}(\alpha_{j\mu})} J_\mu(\alpha_{j\mu}\frac{r}{R}), \tag{6.10}$$

with J_μ the μth Bessel function and $\alpha_{j\mu}$ the jth zero of J_μ. Note that $\mu' = \mu - L_+ - 1$ because of the phase winding in $\Delta_\pm$, i.e. $L_- = L_+ + 2$. Then, the BdG equations are reduced to a matrix eigenvalue problem and can be solved separately in each subspace of fixed μ and μ'.

After the self-consistent solutions are obtained, we calculate the LDOS as usual

$$A(\mathbf{r}, E) = \sum_n [|u_n(\mathbf{r})|^2\delta(E - E_n) + |v_n(\mathbf{r})|^2\delta(E + E_n)]. \tag{6.11}$$

For each quasiparticle state, we can define the spectral weight Z_n:

$$Z_n = \int |u_n(\mathbf{r})|^2 d\mathbf{r}. \tag{6.12}$$

$Z_n \in [0, 1]$ and it represents the contribution of the electronic part of the wave function of a Bogoliubov quasiparticle state. A state with $Z_n < 0.5$ indicates a hole-like state while $Z_n > 0.5$ is an electron-like state. A Bogoliubov quasiparticle state is well formed when it couples between half-electron and half-hole, i.e. for $Z_n = 0.5$.

Next, we remark that the quasiparticle states have the following time-reversal relation:

$$\{u_{-E_n}, v_{-E_n}\} = \{v^*_{E_n}, u^*_{E_n}\}. \tag{6.13}$$

It indicates that a state having energy E_n and angular momentum (μ, μ') carries the same information as a state having energy $-E_n$ and angular momentum $(-\mu', -\mu)$. This allows us to reduce half of the computational time by only considering half of the angular momentum (μ, μ'). Due to this, it is sufficient to display the quasiparticle excitation spectrum with both positive and negative energy E_n but with only positive angular momentum μ or μ'.

We also remark that our chiral p-wave BdG equations are invariant under the time-reversal operations:

$$\{\Delta_\pm, \mathbf{B}\} \to \{\Delta^*_\mp, -\mathbf{B}\}, \tag{6.14}$$

where $\mathbf{B}$ is the magnetic field. In the bulk the two degenerate ground states are the $p_x + ip_y$ and $p_x - ip_y$-wave states. At zero temperature, their OP $(\Delta_+, \Delta_-) = \Delta_0(1, 0)$ and $\Delta_0(0, 1)$, respectively, where $\Delta_0 \in \mathbb{R}$ is the bulk OP at zero temperature. These two states can be mirrored by Eq. (6.14). The situation is the same for vortex states. For example, when one knows the Δ_+ dominant vortex

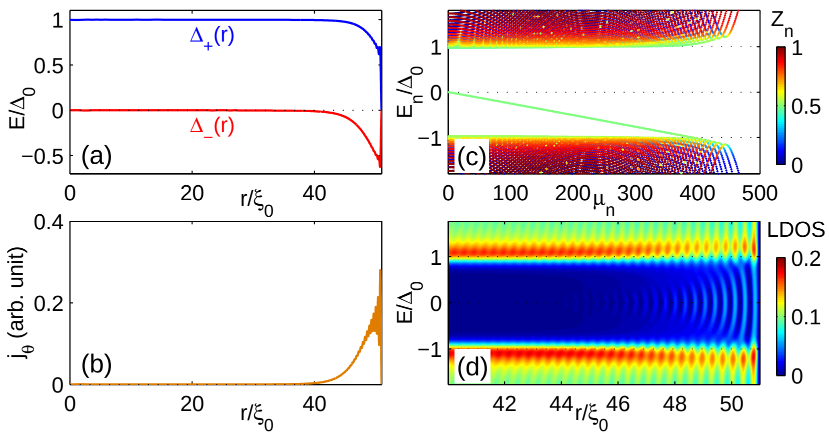

Figure 6.1: Vortex-free state $(L_+, L_-) = (0, 2)$ with Δ_+ dominant. (a) Profile of $\Delta_\pm(r)$ at $\theta = 0$. (b) Azimuthal supercurrent density $j_\theta(r)$. (c) The quasiparticle excitation spectrum E_n as a function of the positive angular momentum μ. The negative part of the spectrum can be obtained by the time-reversal relation of Eq. (6.13). The color coding indicates the spectral weight Z_n. (d) The LDOS near surface as a function of radius r and bias energy E.

states with winding numbers (L_+, L_-), one can easily obtain the Δ_- dominant vortex states with winding numbers $(-L_-, -L_+)$ by using Eq. (6.14). The complete study requires to consider both Δ_+ dominant and Δ_- dominant states for all possible (positive and negative) winding numbers. However, with the time-reversal operations of Eq. (6.14), it is equivalent to consider only half of the possible winding numbers but for both Δ_+ dominant and Δ_- dominant states.

Next we define the p_x and p_y-wave OP Δ_x and Δ_y. They often show interesting properties and can provide important information about the vortex and skyrmion states. The OP expressed by Δ_x and Δ_y can be written as

$$\mathbf{\Delta} = (\Delta_x k_x + \Delta_y k_y)/k_{\mathrm{F}}. \tag{6.15}$$

Eq. (6.1) can also be expressed as

$$\mathbf{\Delta} = \{[\Delta_+ + \Delta_-]k_x + i[\Delta_+ - \Delta_-]k_y\}/k_{\mathrm{F}}. \tag{6.16}$$

By comparing Eqs. (6.15) and (6.16), we find

$$\begin{aligned} \Delta_x &= \Delta_+ + \Delta_-, \\ \Delta_y &= i(\Delta_+ - \Delta_-). \end{aligned} \tag{6.17}$$

6.3 Structure of vortex states without skyrmionic topology

In this section, we investigate three prominent vortex states not exhibiting a skyrmionic topology: Vortex-free state $(L_+, L_-, \mathbb{Q}) = (0, 2, 0)$, parallel vortex state $(1, 3, 0)$ and anti-parallel vortex state $(-1, 1, 0)$. Since $\mathbb{Q}$, defined by Eq. 5.13, is zero for all these states, we omit it in this section. The OP structures, supercurrent density, quasiparticle excitation spectrum E_n, and LDOS for the considered states will be presented, where some findings coincide with previous works [72, 76]. In our analysis, we found that the p_x and p_y OP components Δ_x and Δ_y are very useful, and will be employed in the analysis of the found vortex states. The calculations are performed for the sample of radius $R = 51\xi_0$, where $\xi_0 = \hbar v_F/\pi\Delta_0$ is the BCS coherence length at zero temperature, with v_F the Fermi velocity and Δ_0 the bulk OP at zero temperature. $E_{\mathrm{F}} = \hbar\omega_D$ and $\hbar\omega_D/\Delta_0 \approx 14$, resulting in $k_{\mathrm{F}}\xi_0 = 9$. We also set the applied magnetic field to $\mathbf{H} = 0$, so the reported properties are surly not a consequence of the magnetic field. The considered temperature is $T = 0.1T_c$. The

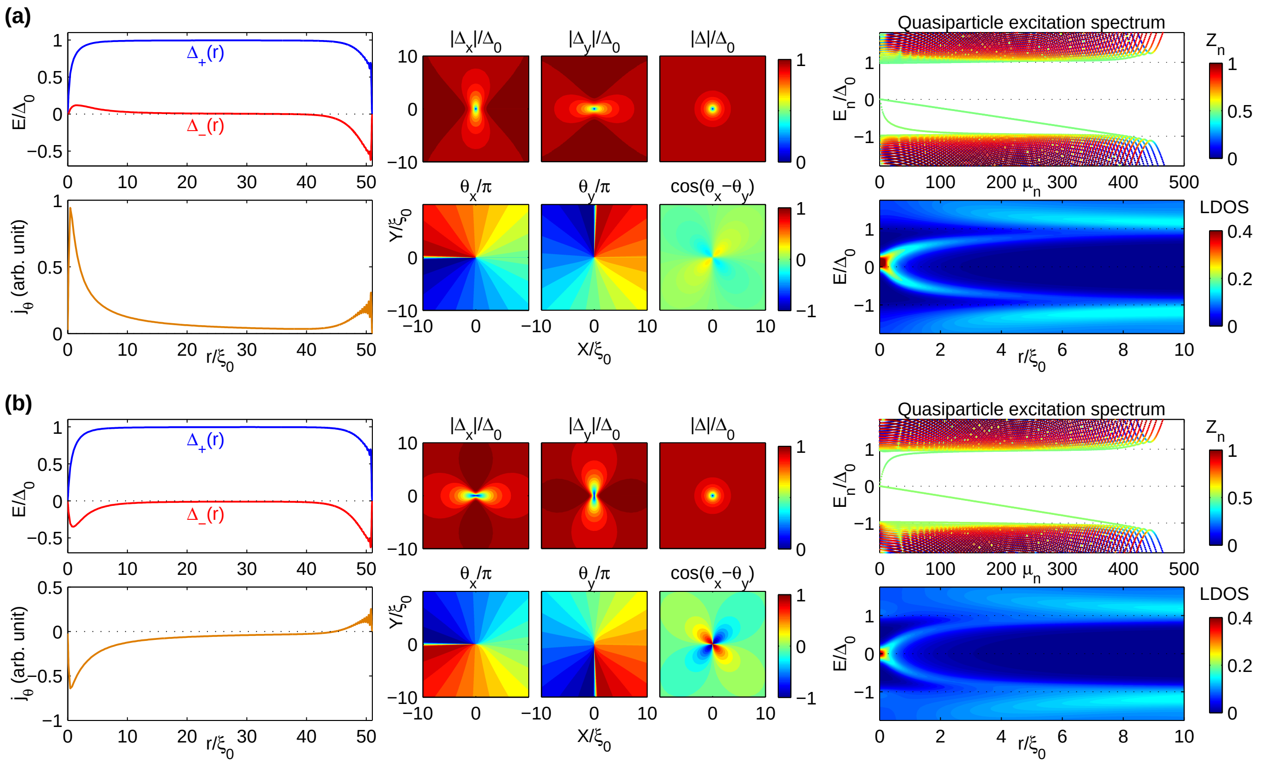

Figure 6.2: Two types of Δ_+-dominant singly-quantized vortex states: $(L_+, L_-) = (1, 3)$ and $(-1, 1)$, respectively shown in panels (a) and (b). Plots on the left show profiles of $\Delta_\pm(r)$ and the azimuthal supercurrent density $j_\theta(r)$. Central plots show both amplitude and phase of OP components $\Delta_x(\mathbf{r})$ and $\Delta_y(\mathbf{r})$, their relative phase $\cos(\theta_x - \theta_y)$, and the total OP amplitude $|\Delta(\mathbf{r})|$. Note that the winding numbers of Δ_x and Δ_y are $L_x = L_y = 1$ for the $(L_+, L_-) = (1, 3)$ state and $L_x = L_y = -1$ for the $(L_+, L_-) = (-1, 1)$ state. Plots on the right show the quasiparticle excitation spectrum E_n as a function of the angular momentum μ (with color coding indicating the spectral weight Z_n), and the LDOS around the vortex core as a function of radial distance r and bias energy E.

results remain qualitatively the same when we change the magnetic field $\mathbf{H}$ and temperature T. We first introduce the vortex-free state $(L_+, L_-) = (0, 2)$, with Δ_+ as a dominant component. The results are summarized in Fig. 6.1. The state is analogous to the Meissner state in s-wave superconductors, therefore it is the first step for understanding vortex and skyrmion states. In bulk, the ground state is $(\Delta_+, \Delta_-) = \Delta_0(1, 0)$. However, the physical properties significantly change near a surface [76]. As seen from Fig. 6.1(a), the $|\Delta_+|$ suppresses and $|\Delta_-|$ rises at the surface, where an anticlockwise supercurrent is also induced [see Fig. 6.1(b)]. The quasiparticle excitation spectrum shown in Fig. 6.1(c) reveals chiral surface states with a linear dispersion around the Fermi energy [71, 72, 76]. These are Andreev bound states induced by the chirality of the superconducting state [77]. The states cross the Fermi energy but there is no exact-zero energy Majorana mode [71]. They contribute to the low-bias LDOS distributions near the surface, as shown in Fig. 6.1(d). Note that the LDOS and the supercurrent $j_\theta(r)$ show Friedel-like oscillations with a wave vector $2k_\mathrm{F}$ near the surface.

Here we note that the spontaneous surface supercurrent is the major characteristic of the superconducting state with broken time-reversal symmetry. Experiments to date have observed the surface bound states [78] but failed to capture the surface supercurrent [59–62]. One possible explanation is that the supercurrent depends on exact geometry and band structure of the sample, [171] but that discussion is out of the scope of this paper.

Next we present the case of two types of singly quantized vortex states with Δ_+ dominant: the parallel vortex state $(L_+, L_-) = (1, 3)$ and the anti-parallel vortex state $(L_+, L_-) = (-1, 1)$, shown in Fig. 6.2(a) and (b), respectively. Here we remind the reader that the vortex and the anti-vortex states exhibit very different properties due to the broken time-reversal symmetry [72, 155, 157].

The left plots in Fig. 6.2(a,b) show $\Delta_\pm(r)$ and the supercurrent density profile $j_\theta(r)$. Compared to the vortex-free $(L_+, L_-) = (0, 2)$ state shown in Fig. 6.1, $\Delta_+(r)$ exhibits a singular vortex core in the center of the sample. At the same time, $\Delta_-(r)$ is induced near the vortex core and also exhibits singularity there, so the cores in $\Delta_\pm$ overlap. However, the two possible singly-quantized vortex states have different vortex core structures. For the parallel vortex $(1, 3)$ state, $\Delta_\pm(r)$ show different asymptotic behavior: $\Delta_+(r) \propto r$ while $\Delta_-(r) \propto r^3$. For the anti-vortex $(-1, 1)$ state, both $|\Delta_\pm(r)| \propto r$. In addition, the states have different supercurrent density distributions. The parallel vortex $(1, 3)$ state has the positive vorticity, leading to the clockwise $j_\theta(r)$ around the vortex. In contrast, the anti-vortex $(-1, 1)$ state has the negative vorticity, leading to the anti-clockwise $j_\theta(r)$ around the vortex core.

Previous works concerning vortex states in chiral p-wave superconductors rarely presented the p_x and p_y OP components Δ_x and Δ_y. We actually found that they can be very useful in the analysis of interesting properties, especially related to the vorticity of the sample. The central plots in Fig. 6.2 show the profiles of Δ_x, Δ_y, the relative phase between them $\theta_x - \theta_y$, and the total OP Δ. We find the winding numbers $L_x = L_y = 1$ for the parallel vortex $(1, 3)$ state and $L_x = L_y = -1$ for the anti-vortex $(-1, 1)$ state, thus better describing the vorticity of the sample than the angular momenta of $\Delta_\pm$. The vortex cores in Δ_x and Δ_y are at the sample center and they overlap. Unlike the cylindrical vortex core structures in $\Delta_\pm$, the vortex cores are deformed in Δ_x and Δ_y, and exhibit different profiles for the $(1, 3)$ and $(-1, 1)$ states. It is interesting that Δ_y can be obtained by rotating Δ_x with 90 degrees clockwise for the $(1, 3)$ state and anticlockwise for the $(-1, 1)$ vortex state. It is also interesting to note that the relative phase $\theta_x - \theta_y$ twirls twice for both cases, exhibiting a cloverleaf profile. For the $(-1, 1)$ vortex state, Δ_x and Δ_y alternate between being fully in-phase and fully out-of-phase around the vortex core.

The right hand side plots in Fig. 6.2 show the quasiparticle excitation spectrum $E_n(\mu_n)$ and the LDOS. Comparing to the vortex-free $(L_+, L_-) = (0, 2)$ state, one more branch of bound states appears within the gap energy Δ_0 in the excitation spectrum. Those are the vortex bound states, localized around the vortex core [155]. The vortex bound states for the $(1, 3)$ and $(-1, 1)$ states are different. For $(1, 3)$ vortex states, the bound states reside in the negative energy range for positive angular momentum μ_n. However, for the $(-1, 1)$ state they have positive energy for positive μ_n, due to opposite vorticity.

It was demonstrated in Refs. [172–174] that there exists a pair of zero-energy Majorana modes for a single vortex with odd vorticity in the chiral p-wave superconductivity. The energy levels of the vortex bound states appear at integer points $E_n \sim nE_\delta$, where n is an integer and E_δ is the level spacing of the order of Δ_0^2/E_F [175]. For the state with $E_n = 0$, the time-reversal relation of Eq. (6.13) prescribes the zero-energy state appearing as a pair, and the quasiparticle wave functions keep the relation $u_n(\mathbf{r}) = v_n^*(\mathbf{r})$. Thus, the quasiparticle creation operator is equivalent to the annihilation of a quasiparticle, which corresponds to the Majorana fermions [173]. However, the Majorana zero mode splits when there exists vortex-vortex interaction or/and vortex-surface interaction [176]. In our case where $R = 51\xi_0$, the energies of the lowest vortex bound state of both cases are of the order of $10^{-7}\Delta_0$. It indicates the existence of the Majorana zero mode and the vortex-surface interaction being negligible. With sample radius R decreasing, the energy of the lowest vortex bound state oscillates and its envelope increases with exponential law. The vortex bound states of both cases are the well-formed Bogoliubov quasiparticle states with $Z_n = 0.5$, which is also supporting the Majorana zero mode.

The LDOS showing in Fig. 6.2 reveals the zero-bias peak at the vortex core, corresponding to the same characteristic of vortex states with odd winding number in s-wave superconductors. It is worth noting that the LDOS is asymmetric for $E \leftrightarrow -E$ for the $(1, 3)$ state and symmetric for the

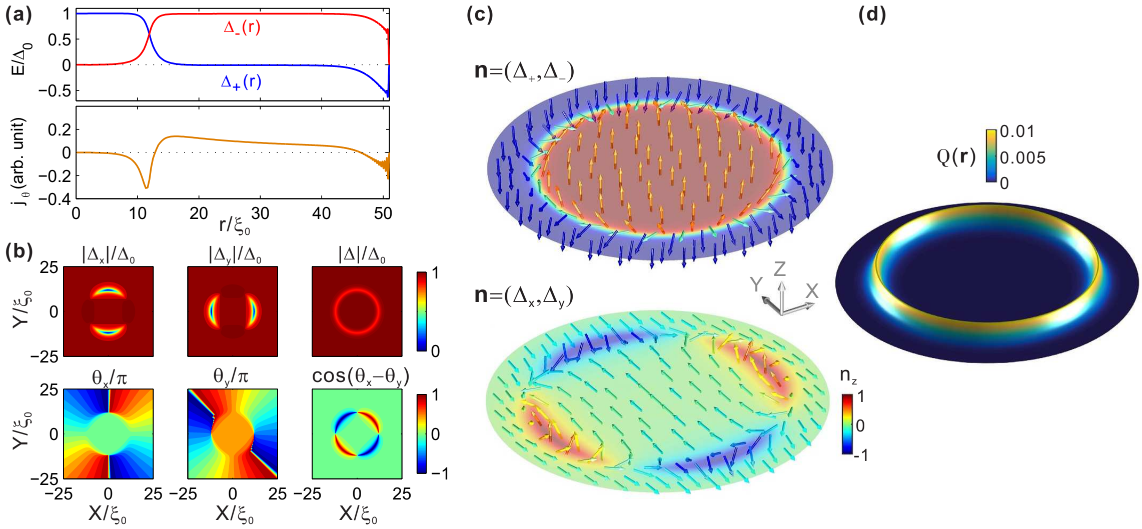

Figure 6.3: Topological structure of the skyrmion state $(L_+, L_-, \mathbb{Q}) = (0, 2, 2)$. (a) Profiles of $\Delta_\pm(r)$ and the azimuthal supercurrent density $j_\theta(r)$. (b) The amplitude and the phase of $\Delta_x(\mathbf{r})$ and $\Delta_y(\mathbf{r})$, their relative phase $\cos(\theta_x - \theta_y)$, and the total OP amplitude $|\Delta(\mathbf{r})|$. Note that the winding numbers of Δ_x and Δ_y are $L_x = L_y = 2$. (c) The texture $\mathbf{n}(\mathbf{r})$ of the relative OP space, calculated using $\Delta_\pm$ (upper panel), and using Δ_x and Δ_y (lower panel). The colors show the amplitude of the z-component of $\mathbf{n}(\mathbf{r})$. Both shown pseudospin textures give topological charge density $Q(\mathbf{r})$ shown in panel (d) and the topological charge $\mathbb{Q} = 2$.

$(-1, 1)$ state.

6.4 Structure of skyrmionic topological defects

Coreless vortices are one of the most striking states emerging in the chiral p-wave superconductivity. They exhibit an additional topology which is skyrmionic. The one known coreless vortex state is the doubly quantized one [156, 159], having the topological charge $\mathbb{Q} = 2$ [123]. In this section, we investigate the topological structure and the electronic properties of the doubly quantized coreless vortex state (skyrmion state) $(L_+, L_-, \mathbb{Q}) = (0, 2, 2)$ and the vortex-skyrmion coexisting state $(L_+, L_-, \mathbb{Q}) = (1, 3, 2)$. We set parameters the same as in the previous section to facilitate the direct comparison of the results. Note that we choose the Δ_--dominant states for convenience, so that the skyrmion corresponds to positive vorticity. The Δ_+-dominant counterpart with negative vorticity can be obtained equivalently by using Eq. (6.14).

We first present the topological structures of the state $(L_+, L_-, \mathbb{Q}) = (0, 2, 2)$ in Fig. 6.3. Fig. 6.3(a) shows $\Delta_\pm(r)$ and the supercurrent density profile $j_\theta(r)$. Comparing to the results for the vortex free state $(L_+, L_-, \mathbb{Q}) = (0, 2, 0)$ shown in Fig. 6.1, a domain wall appears in $\Delta_\pm(r)$ at $r = 12\xi_0$ separating outer Δ_- and inner Δ_+ regions. In addition, the winding numbers of $\Delta_\pm$ are $L_+ = 0$ and $L_- = 2$, respectively. There is therefore a 4π-phase difference between $\Delta_\pm$ along the domain wall, which breaks the time reversal symmetry leading to the *chiral domain wall*. A supercurrent $j_\theta(r)$ is induced around the chiral domain wall, and changes sign at the domain wall - flowing clockwise inside the domain wall but anti-clockwise outside of it [124].

The region inside the chiral domain wall is sometimes thought of as a vortex core. However, this is not correct. Different from the singular vortex which is a point-like topological defect, the coreless vortex is a loop-like topological defect. Fig. 6.3(b) shows the results expressed using Δ_x and Δ_y. We found that Δ_x and Δ_y components of the OP contain two vortices each, thus having winding numbers $L_x = L_y = 2$, so this state carries a total of 2 flux quanta. The vortices are not at the sample center but on the chiral domain wall and align orthogonally in Δ_x compared to Δ_y. All four

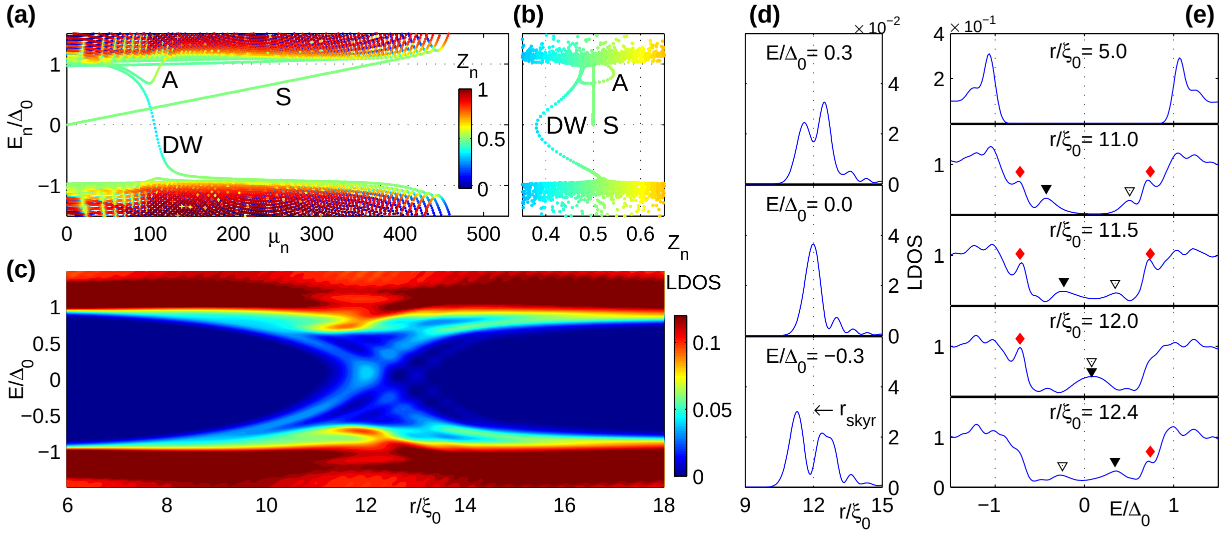

Figure 6.4: Electronic structure of the skyrmion state $(L_+, L_-, \mathbb{Q}) = (0, 2, 2)$. (a) The quasiparticle excitation spectrum E_n as a function of the angular momentum μ_n (color coding indicates the spectral weight Z_n). S, DW and A represent the surface bound state, domain-wall bound state and the Andreev bound state associated with the domain wall, respectively. Their spectral weights Z_n are shown in panel (b). (c) The LDOS(r, E) around the skyrmion as a function of radial distance r and bias energy E. (d) The profiles of the LDOS(r) around the domain wall at bias energies $E = 0.3, 0$ and -0.3. The chiral domain wall is at $r_{\rm skyr}/\xi_0 = 12$. (e) The profiles of the LDOS(E) as a function of bias energies E at several radial distances. The peaks labeled by triangles (diamonds) are induced by the domain-wall bound states (Andreev bound states).

vortices are spatially separated and play the same role in this $(0, 2, 2)$ state, as seen from Fig. 6.3(b). Therefore they are the one-component vortices (in Δ_x-Δ_y space) and each of them carries half of the flux quantum, analogously to the half-quantum vortex [154]. Finally, the chiral domain wall is formed by an *enclosed chain of all one-component vortices* and carries 2 flux quanta. The total OP is cylindrically symmetric, and it is suppressed (though not completely) on the chiral domain wall. The relative phase $\theta_x - \theta_y$ alternates between 0 and π along the domain wall, indicating that Δ_x and Δ_y are respectively in- and out of phase. Note that the relative phase alternates exactly 4 times along the domain wall, where each node corresponds to the location of one-component vortices on the chiral domain wall.

Actually, the *chiral domain wall* in $\Delta_\pm$ and the *enclosed chain of one-component vortices* in Δ_x and Δ_y are two different but both relevant aspects of a *skyrmionic topological defect* in the relative OP space. This can be seen clearly from Fig. 6.3(c) where we map both $\Delta_\pm$ and $\Delta_{x,y}$ decompositions of the OP onto the pseudo-spin fields $\mathbf{n}$. As seen from the upper panel, where the results are obtained by using OP components $\Delta_\pm$, the field $\mathbf{n}$ rotates at the domain wall which separates the central region where $\mathbf{n}$ points up and the region outside of the domain wall where $\mathbf{n}$ points down. In addition, the field $\mathbf{n}$ rotates along the domain wall by 4π, resulting in the nontrivial topological charge density on the chiral domain wall [see Fig. 6.3(d)]. The net topological charge $\mathbb{Q} = 2$ indicates that the field $\mathbf{n}$ wraps twice on the surface of the sphere. The lower panel of Fig. 6.3(c) shows the results obtained by using OP components Δ_x and Δ_y. The field $\mathbf{n}$ also rotates at the domain wall. In this case, the domain wall separates the central region where $\mathbf{n}$ points in positive y-direction and the outside region where $\mathbf{n}$ points in negative y-direction. $\mathbf{n}$ also rotates by 4π along the domain wall, leading to the net topological charge $\mathbb{Q} = 2$. In fact, this pattern can be reached by rotating the previous n field by an angle 90° about the y-axis. The topological charge density and the net topological charge are invariant under this operation. As a result, one concludes that $(0, 2, 2)$ state is a skyrmionic topological defect with $\mathbb{Q} = 2$ in the relative OP space, and that such topological structures retain the skyrmionic character under the transformation between (Δ_+, Δ_-) and (Δ_x, Δ_y) representations.

Next we present the electronic properties of this skyrmionic topological defect in the $(0, 2, 2)$ state in Fig. 6.4. Previous studies revealed low energy excitations at the domain wall [156, 159]. However, the complete picture of excitations and LDOS is still lacking. Here, our self-consistent calculations provide the more details of the quasiparticle excitation spectra and LDOS, enabling their identification in e.g. scanning tunneling microscopy (STM).

Fig. 6.4(a) shows the quasiparticle excitation spectrum $E_n(\mu_n)$ and the corresponding LDOS(r, E) near the domain wall. As seen from Fig. 6.4(a), there are three distinct branches of bound states. These are the surface bound states (S), the domain-wall bound states (DW) and the Andreev bound states (A). The surface bound states are the same as those found in the vortex free states $(0, 2, 0)$, which were shown in Fig. 6.1. The domain-wall bound states and the Andreev bound states are typical for the skyrmion, i.e. chiral domain wall.

The domain-wall bound states cross zero energy with the lowest energy level having a small gap of the order $\Delta_0^2/E_{\mathrm{F}}$ [156, 174]. Thus, the zero-energy Majorana states do not appear. However, the domain-wall bound states cause two effects in LDOS: a zero-bias peak at the domain wall, and the peak splitting with increasing or decreasing the bias. One of those peaks shifts towards the interior of the domain wall, while the other shifts outward. This feature can be seen clearly in Fig. 6.4(d), where we display the profile of the LDOS(r) for bias energies $E/\Delta_0 = 0.3$, 0, and -0.3.

The Andreev bound states are induced near the gap energies $E \approx |\Delta_0|$, leading to peaks in LDOS at the domain wall, as seen from Fig. 6.4(c). They are essentially similar to the quantum rotor state which is induced by multiple Andreev reflections at the normal/superconducting interface [177]. In that case, due to the time-reversal symmetry, Andreev bound states appear near both $E = \pm|\Delta_0|$. However, the chiral domain wall breaks the time-reversal symmetry so that the Andreev bound states near $E = -|\Delta_0|$ are suppressed.

In addition, we found that the domain-wall bound states are electron-dominant (with spectral weight $Z_n < 0.5$) when they cross the zero bias, while the Andreev bound states are hole-dominant (with spectral weight $Z_n > 0.5$), as seen from Fig. 6.4(a) where the color coding indicates the spectral weight Z_n. This feature can be seen clearly in Fig. 6.4(b), where we displayed the spectral weight Z_n for all three types of bound states. The domain wall bound states and the Andreev bound states are different from the surface bound states whose spectral weight is $Z_n = 0.5$. These two branches of bound states are also different from the singly-quantized vortex bound states of $(L_+, L_-, \mathbb{Q}) = (1, 3, 0)$ and $(L_+, L_-, \mathbb{Q}) = (-1, 1, 0)$ shown in Fig. 6.2, which are fully coupled Bogoliubov quasiparticles with spectral weight $Z_n = 0.5$.

Due to the electron-dominant domain-wall bound states and the hole-dominant Andreev bound states, the LDOS near the domain wall exhibits asymmetry for bias energy $E \leftrightarrow -E$, as visible in Fig. 6.4(c). This feature can be seen clearly in Fig. 6.4(e), where we displayed the LDOS(E) as a function of bias energy at several radial distances r. When we scan the LDOS far away from the chiral domain wall, e.g. at $r/\xi_0 = 5$, the superconducting coherence peaks are well established at the gap energy Δ_0 and there is no LDOS peak when $|E| < \Delta_0$. When $r/\xi_0 = 11$ (near the domain wall at $r_{\mathrm{skyr}}/\xi_0 = 12$), there are four peaks inside the gap energy $|E| < \Delta_0$. Two of them are induced by the domain wall bound states [labeled by solid and open triangles in Fig. 6.4(e)]. The other two are induced by the Andreev bound states [labeled by diamonds in Fig. 6.4(e)]. Due to the electron-dominant domain-wall bound states, the peaks labeled by solid triangle have a higher amplitude than the ones labeled by the open triangle, which results in the asymmetric profile in LDOS. At larger r, the two peaks labeled by triangles move towards each other and merge at the domain wall where $r/\xi_0 = 12$. Simultaneously, the Andreev peak in negative E labeled by diamond is significant due to the hole-dominant Andreev bound states, leading to another asymmetric profile in the LDOS. When r is further increased, the peaks labeled by triangles continue shifting and finally merge into the coherence peaks at gap energy $|E| = \Delta_0$.

Since the skyrmionic topological defect appears in the relative OP space, whereas the vortex

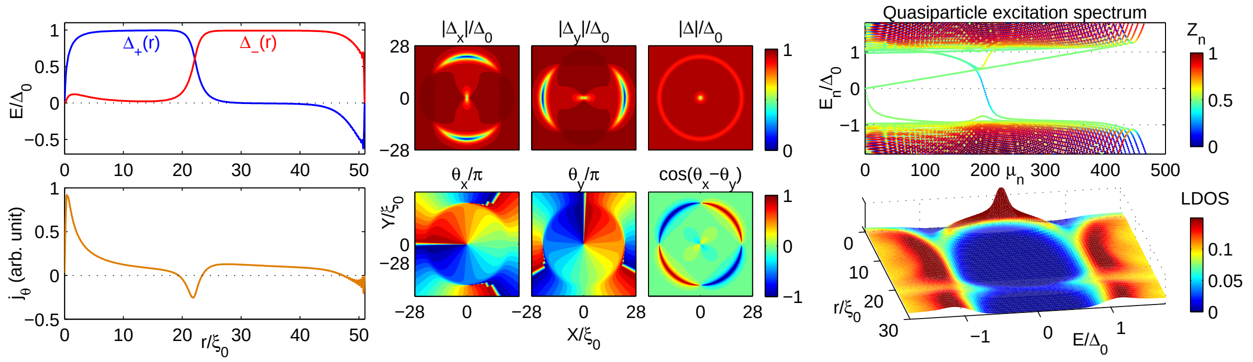

Figure 6.5: The skyrmion-vortex coexisting state $(L_+, L_-, \mathbb{Q}) = (1, 3, 2)$*. Plots on the left show profiles of* $\Delta_\pm(r)$ *and the azimuthal supercurrent density* $j_\theta(r)$*. Central plots show both amplitude and phase of OP components* $\Delta_x(\mathbf{r})$ *and* $\Delta_y(\mathbf{r})$*, their relative phase* $\cos(\theta_x - \theta_y)$*, and the total OP amplitude* $|\Delta(\mathbf{r})|$*. Note that the winding numbers of* Δ_x *and* Δ_y *are* $L_x = L_y = 3$*. Plots on the right show the quasiparticle excitation spectrum* E_n *as a function of the angular momentum* μ *(with color coding indicating the spectral weight* Z_n*), and the LDOS around the vortex core as a function of radial distance* r *and bias energy* E*.*

appears in the OP space, a vortex can be added to the $(L_+,L_-,\mathbb{Q}) = (0, 2, 2)$ state leading to the skyrmion-vortex coexisting state $(L_+, L_-, \mathbb{Q}) = (1, 3, 2)$. The results for such a topological "hybrid" are presented in Fig. 6.5(b). Comparing to the skyrmion $(0, 2, 2)$ state, one sees the superposition of a singly quantized vortex and the chiral domain wall, with the vortex being located at center of the sample. The supercurrent $j_\theta(r)$ flows clockwise around the vortex core, gradually changing to anti-clockwise on the inner side of the domain wall, and flips the direction again to clockwise outside the domain wall. Δ_x and Δ_y have winding numbers $L_x = L_y = 1 + 2 = 3$ in this case, 1 for the central vortex, and 2 for the one-component vortices on the domain wall. The chiral domain wall is larger than that of the skyrmion in the $(0, 2, 2)$ state, because of the repulsion between the vortex at the center and the one-component vortices on the domain wall.

The quasiparticle excitation spectrum $E_n(\mu_n)$ also shows the superposition of the vortex bound states and the chiral domain wall bound states. Since the domain wall is now larger, the domain wall bound states and the Andreev bound states shift to larger μ_n. In addition, we find that the domain wall bound states become even more electron-dominant and the Andreev ones more hole-dominant, resulting in more pronounced electron-hole asymmetry in LDOS around the domain wall compared to the skyrmion $(0, 2, 2)$ state. The LDOS of the coexisting skyrmion-vortex state exhibits distinctly strong zero-bias peak at the vortex core, and a significantly weaker one at the domain wall.

Finally, we mention that the skyrmion-anti-vortex coexisting state $(L_+,L_-,\mathbb{Q})= (-1, 1, 2)$ is unstable. Due to the attractive interaction between the anti-vortex and the skyrmion, such state evolves into the parallel vortex state $(L_+, L_-, \mathbb{Q}) = (1, 3, 0)$.

6.5 Magnetic field and temperature dependence of the properties of the skyrmion

The skyrmion is a chiral domain wall in $\Delta_\pm$ and an enclosed chain of one-component vortices in Δ_x, Δ_y representation of the two component OP. In either case, the skyrmion is a loop-like structure in OP space and it has very different properties from the vortex as a point-like defect. For example, the size of the vortex depends solely on the superconducting coherence length ξ. However, the size of the skyrmion depends also on the applied magnetic field because the chiral domain wall is expected to move under the influence of the magnetic field. We therefore report in this section the magnetic field and temperature dependence of the size of the skyrmion in the $(L_+, L_-, \mathbb{Q}) = (0, 2, 2)$ state,

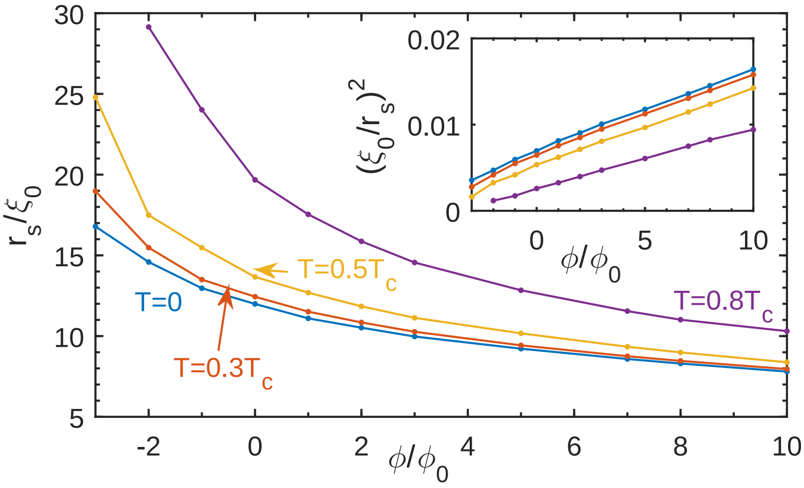

Figure 6.6: The radius of the skyrmion r_s as a function of the applied magnetic flux ϕ through the sample, at temperatures $T = 0,\ 0.3,\ 0.5,$ and $0.8T_c$. The inset shows that the area of the skyrmion shrinks linearly with magnetic field, being maximal for negative magnetic field.

and the consequences of varied skyrmion size on the energy spectrum.

Fig. 6.6 shows the radius r_s of the Δ_--dominated $(0, 2, 2)$ skyrmion, as a function of the magnetic flux ϕ through the sample, at temperatures $T = 0,\ 0.3,\ 0.5,$ and $0.8T_c$. The $\phi = H_0 S$ where H_0 is the magnetic field strength and $S = \pi R^2$ the area of the sample. We find that the skyrmion expands with increasing temperature T, but shrinks with increasing applied magnetic field. The skyrmion consists of the one-component vortices, with size related to the coherence length ξ. Since ξ increases with temperature, so does the vortex-vortex interaction, and the size of the skyrmion can duly increase. However, it is crucial here that the skyrmion is a chiral domain wall, balanced by the clockwise supercurrnt j_θ in the interior and the anti-clockwise at the exterior of the domain wall. With increasing applied magnetic field, the anti-clockwise part of j_θ is enhanced and the clockwise part is weakened, shrinking the domain wall to smaller equilibrium radius r_s. Inversely, the skyrmion expands with ϕ decreasing. Interestingly, the skyrmion survives even at negative magnetic field, i.e. for $\phi < 0$, likely due to the finite energy needed to break the domain wall so that vortices can leave the sample. As a consequence, at negative fields, the skyrmion continues to expand to surprisingly large sizes. The inset in Fig. 6.6 shows that actually the square of $r_\mathrm{s}(\phi)$ depends linearly on ϕ, i.e. $\propto 1/\phi^2$, so that magnetic flux inside the skyrmion is roughly constant. This is a very important finding, indicating that existing skyrmions in a given sample can be made larger, hence easier to detect in experiment, if the polarity of the applied magnetic field is reversed. Furthermore, the stability at reversed field clearly distinguishes skyrmions from vortices, since there is nothing preventing individual vortices from leaving the sample (apart from the ever-present disorder) if the polarity of the field is changed. Last but not least, our findings indicate that skyrmions are in general *an order of magnitude larger* than the conventional vortices.

The electronic structure is of course affected by the change in the size of the skyrmion. Fig. 6.7 shows the quasiparticle excitation spectrum $E_n(\mu_n)$ of the skyrmion at zero temperature, for magnetic flux through the sample $\phi/\phi_0 = 10$, 0, and -3, for which $r_\mathrm{s}/\xi_0 = 8, 11.7$ and 17.1, respectively. The domain-wall bound states move to large angular momentum μ when r_s increases, which is expected since the bound states are confined to the domain wall. In addition, the cusped energy lines of the Andreev bound states become more significant around $E = |\Delta_0|$. The continuous spectrum above the gap energy $|E| > |\Delta_0|$ tilts as a function of μ_n because of the supercurrent induced by the applied magnetic field favoring one chirality over the other.

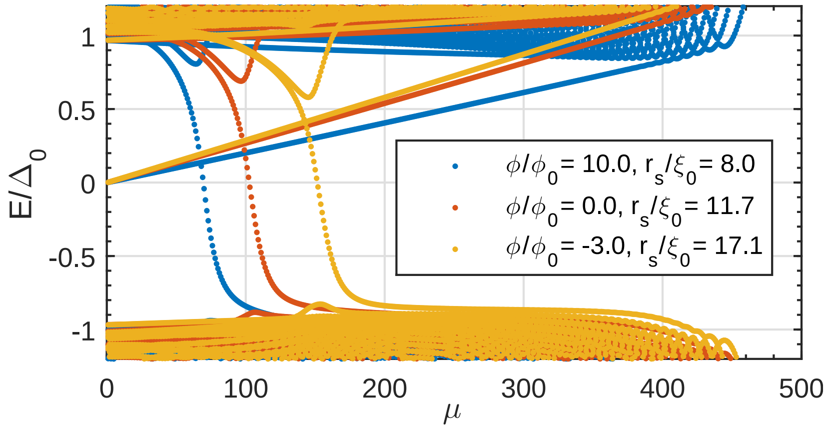

Figure 6.7: Quasiparticle excitation spectrum E_n of the skyrmion studied in Fig. 6.6, as a function of angular momentum μ_n, at zero temperature and for applied magnetic flux through the sample $\phi/\phi_0 = -3$, 0, and 10.

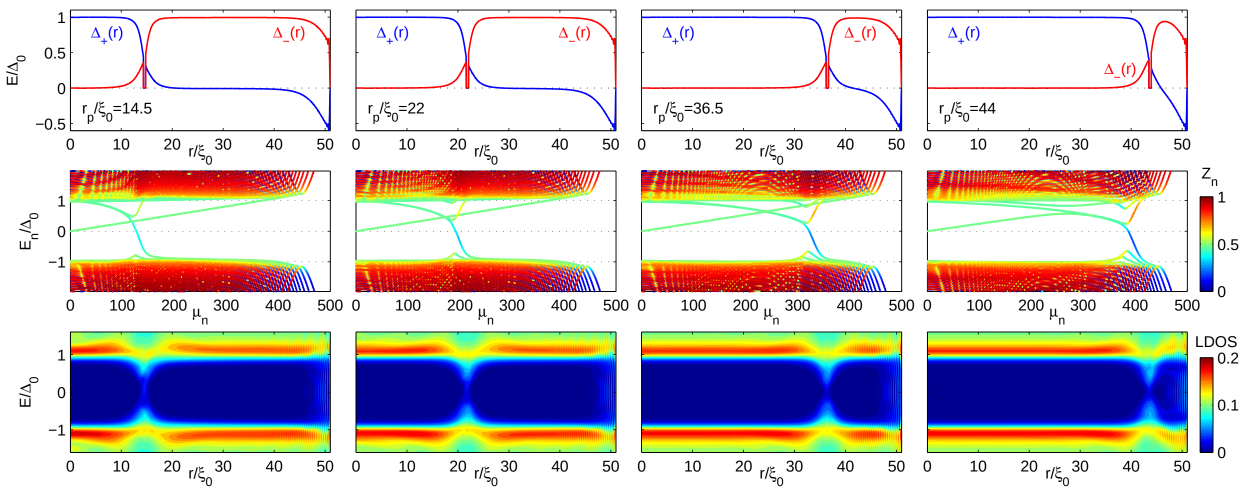

Figure 6.8: Skyrmion $(L_+, L_-, \mathbb{Q}) = (0, 2, 2)$ state trapped by a normal-metal ring. The radius of the pinning rings increases as $r_{\rm p}/\xi_0 = 14.5, 22, 36.5, 44$ from left to right panels, respectively. The top row of plots shows the OP profiles. The central row shows the corresponding quasiparticle excitation spectrum as a function of angular momentum μ_n, and the bottom row shows the LDOS as a function of radial distance r.

6.6 Pinning the skyrmion

Vortex matter in superconductivity is known to be pinned where the OP is suppressed, which can have technological relevance for e.g. increasing the maximal current a superconductor can sustain without the onset of vortex motion and related onset of resistance and heating. The skyrmion matter is a chain of enclosed one-component vortices according to the OP representation using Δ_x and Δ_y, implying that skyrmions can be pinned in an analogy to vortices. If so, then the size and the position of the skyrmion could be controlled artificially, which may be beneficial for the observation of skyrmions and for further fluxonic manipulations. In this section, we therefore consider the possibility to pin the skyrmion by an embedded normal-metal ring in the superconductor, where the superconducting coupling constant g is suppressed to zero, leading to $|\Delta| = 0$ inside the ring. The median radius of the ring is labeled $r_{\rm p}$, and the width of the ring is $0.5\xi_0$. Such narrow rings do not break the phase coherence between the superconductivity inside and outside of the ring. We investigate the OP profile, energy spectrum and LDOS when the skyrmion is pinned by such a normal-metal ring. The calculations are performed self-consistently for $T = 0.1T_c$ and in absence of the magnetic field, since we do not want the competing effects to shadow the conclusions.

Fig. 6.8 presents the OP profiles (top row), quasiparticle excitation spectrum (central row) and LDOS (bottom row) for the radii of the normal-metal ring $r_\mathrm{p}/\xi_0 = 14.5, 22, 36.5, 44$ (from left to right respectively). A seen in the OP profiles in Fig. 6.8, the chiral domain walls are trapped in the normal-metal ring in every considered case. With increasing radius of the ring r_p, the skyrmion correspondingly expands. As a result, the domain wall bound states shift to larger angular momentum μ_n in the energy spectrum, and the zero-bias peak in LDOS shifts as well. Note that the domain wall bound states become increasingly hole-dominant with the expansion of the skyrmion. At the same time, the Andreev bound states around $E = |\Delta_0|$ become more significant and increasingly electron-dominant.

The surface bound states are not affected by our exercise until the skyrmion gets close to the sample surface. As seen from the panels for $r_\mathrm{p}/\xi_0 = 44$, the OP profiles at the surface are strongly affected by the domain wall. The supercurrents induced by the domain wall and ones running near the surface combine, causing interactions between the domain wall bound states and the surface bound states. As seen from the energy spectrum $E_n(\mu_n)$, these two branches of bound states avoid crossing each other. Finally, we note that the quasiparticles interference above the gap energy $|E| > \Delta_0$ is enhanced with the r_p increasing. The quasiparticles interference effect is known to result in additional BCS-like energy gaps and more Bogoliubov quasiparticle states with $Z_n = 0.5$ above the gap energy Δ_0 [178]. Here, it is induced by the inhomogeneous OP profile stemming from the normal-metal ring, the skyrmion and the surface.

6.7 Summary

In summary, we have studied the topological and electronic properties of characteristic vortical and skyrmionic states in chiral p-wave superconductors, by solving Bogoliubov-de Gennes equations self-consistently. We have presented the distribution of the two-component order parameter, the supercurrent, quasiparticle excitation spectra, and LDOS, for each of the typical states. We pointed out that the chiral order parameter representation using components $\Delta_\pm = p_x \pm ip_y$ is ideal to study the properties of chiral domain walls in the given state, while the p_x- and p_y-components of the order parameter conveniently reveal the properties of vortices.

While conventional vortices are rather well understood in the literature (as point-like topological defects, with core in the order parameter, supercurrent flow around it, and the vortex bound states and LDOS peaks at the core), the topological defects comprising one-component vortices, and/or chiral domain walls as well as their interaction with conventional vortices, are an entirely new topic. Moreover, a chain of one-component vortices (half the vorticity of a complete vortex, analogous to half-quantum vortices of spin-triplet superconductors [133]) on a chiral domain wall can be characterized as a skyrmion, and can be seen in the total order parameter as loop-like topological defect without a fully developed core. Such defects carry multiple flux quanta, but are entirely different from “giant” vortices in s-wave superconductors [39, 41, 162]. Such skyrmion exhibits a chiral domain wall in $\Delta_\pm$, whereas a vortex does not. Unlike vortices, they are characterized not only by the angular momentum, but also by the topological charge in the relative order parameter space, where both the relative amplitude and relative phase between the two components of the order parameter play a role. A skyrmion traps bound states at the chiral domain wall, leading to zero-bias LDOS peaks at the domain wall. In addition, the LDOS exhibits electron-hole asymmetry, which is different from the electron-hole symmetric LDOS of usual multi-quanta vortex states. We also show the possibility to have a topological defect with a vortex inside a skyrmion, with superimposed features of both topological constituents.

Accounting for variations of the magnetic field and temperature, our analysis shows that the size of the skyrmion can be strongly tuned, being increased by increasing temperature and by decreasing applied magnetic field. The size of the skyrmion is typically an order of magnitude larger than a vortex. Furthermore, contrary to conventional vortices, a skyrmion survives changing the polarity of the applied magnetic field, due to the finite energy cost of breaking the chiral domain wall so that vortices within the skyrmion can leave the sample. As a consequence, the skyrmion can significantly increase in size at negative magnetic field, since the decreasing energy of currents flowing inside the skyrmion compensates the increasing energy of the longer chiral domain wall. Finally, we have shown that even in the absence of the magnetic field the size of the skyrmion can be manipulated by pinning on a normal-metal ring of prescribed size. Considering that due to recent experimental achievements in e.g. superconductor-ferroelectric hybrids one can draw practically at will the normal-metal paths inside the superconductor [179, 180], this opens up a broad playground for novel phenomena in fluxonics. We expect that our findings related to stability of skyrmionic topological defects in superconductors, manipulation of their size, and their distinct signatures in for example LDOS, will enable their experimental identification in scanning tunneling microscopy and spectroscopy, which can be further used to prove particular pairing symmetry in the superconductor of interest.

Publication The results of this chapter were published in:

- L.-F. Zhang, V. Fernández Becerra, L. Covaci, and M. V. Milošević, *Electronic properties of emergent topological defects in chiral p-wave superconductivity*, Phys. Rev. B **94**, 024520 (2016) (13 pages).

7

Dynamics of skyrmions and edge states in the resistive regime of mesoscopic *p*-wave superconductors

In a mesoscopic sample of a chiral p-wave superconductor, novel states comprising edge states, skyrmions, mono and multichiral states have been stabilized in out-of-plane applied magnetic field. Using the time-dependent Ginzburg-Landau equations we shed light on the dynamic response of such states to an external applied current, thereby providing new fingerprints for identification of p-wave superconductivity.

7.1 Introduction

Edge states, appearing where the condensate homogeneity is broken, and domain walls, separating regions with different chiralities, are the main characteristics of chiral p-wave superconductivity [76, 77]. They arise as a consequence of breaking the time-reversal symmetry in an order parameter with two components, i.e. $\mathbf{\Psi} = (\psi_+, \psi_-)^T$ [94]. Besides the edge states and the domain walls another topological entity (the skyrmion) has recently emerged in chiral p-wave superconductivity [123]. Unlike the Abrikosov vortex that has a core due to the discontinuity of its phase, the skyrmion is coreless and defined by a loop domain wall [124].

Chiral p-wave superconductivity is realized in spin-triplet superconductors. In such materials two electrons pair up forming a triplet rather than a singlet as in conventional superconductivity. In order to fulfil the Pauli principle, the orbital part of the wave function in spin-triplet superconductors has odd parity, i.e. angular momentum $L = 1$ (p-wave). As a consequence of the spin of the electronic pairs, another topological entity, the half-quantum vortex (HQV), arises in these materials. HQVs are expected to be unscreened by the Meissner effect due to their spin currents, i.e. they are likely to be found at the lateral borders of the sample [133].

Substantial evidence has been provided over the years that strontium ruthenate, Sr_2RuO_4 (SRO), is a chiral p-wave superconductor [49, 52, 53]. However, the lack of direct observation of states carrying spontaneous currents around space homogeneities undermines the candidacy of SRO to the p-wave class of superconducting materials [59–62]. In this chapter we study the electrical response of edge states, skyrmions, mono and multichiral states in a mesoscopic chiral p-wave superconductor sample when an external current is applied to the sample. The distinct behavior reported for the states with and without domain walls in the current-voltage characteristic provides an indirect method for their differentiation. Furthermore, the three different regimes, namely, superconducting, resistive and normal, seen in the current-voltage characteristic, coincides with those of conventional superconductivity. However, the temporal evolution of the two-component superconducting order parameter ($\mathbf{\Psi}$) is found to provide rich physics, and depending on the magnitude of applied-current, the skyrmionic and edge states must present different behavior from kinematic vortices in conventional superconductors [121, 181, 182]. This in turn provides new possibilities for resistive stages in the sample behavior, and indirect means to identify p-wave superconductivity.

7.2 Theoretical Formalism

Within the weak-coupling limit and considering a cylindrical Fermi surface, the dimensionless time-dependent Ginzburg-Landau (TDGL) equations for the two component order parameter $\mathbf{\Psi} = (\psi_+, \psi_-)^T$ and the vector potential $\mathbf{A}$, in chiral p-wave superconductors reads

$$\left(\frac{\partial}{\partial t}+i\varphi\right)\mathbf{\Psi} = \frac{2}{3}\begin{bmatrix} \mathbf{D}^2 & \Pi_+^2 \\ \Pi_-^2 & \mathbf{D}^2 \end{bmatrix}\begin{pmatrix} \psi_+ \\ \psi_- \end{pmatrix}+\mathbf{\Psi}\left(1-\frac{1+\tau}{2}|\mathbf{\Psi}|^2 \pm \frac{\tau}{2}\mathbf{\Psi}^*\hat{\sigma}_z\mathbf{\Psi}\right), \tag{7.1}$$

$$\kappa^2\nabla\times(\nabla\times\mathbf{A}) + \left(\nabla\varphi + \frac{\partial \mathbf{A}}{\partial t}\right) = \mathbf{J}\,, \tag{7.2}$$

where φ is the electrostatic potential, $\mathbf{D} = (\nabla - i\mathbf{A})$ is the covariant derivative, and $\Pi_\pm = (D_x \pm iD_y)/\sqrt{2}$ are creation and annihilation operators of Landau levels, satisfying the commutator $\frac{1}{H}[\Pi_+, \Pi_-] = 1$. τ is a phenomenological parameter that depends solely on the shape of the Fermi surface of the material under consideration (for SRO calculations yield $\tau = 1/2$, owing to cylindrical Fermi surface [77, 102]). Finally, $\hat{\sigma}_z$ is a Pauli matrix, κ is the GL parameter, and $\mathbf{J}$ is the superconducting current density,

$$\begin{aligned} \mathbf{J} &= \frac{1}{3}\,\mathrm{Im}\Big\{\psi_+^*\mathbf{D}\psi_+ + \psi_-^*\mathbf{D}\psi_-\Big\} \\ &+ \frac{1}{3\sqrt{2}}\,\mathrm{Im}\Big\{\mathbf{\Psi}^*\Big[\Pi_+\hat{\sigma}_+ + \Pi_-\hat{\sigma}_-\Big]\mathbf{\Psi}\,\hat{\imath} + i\,\mathbf{\Psi}^*\Big[\Pi_+\hat{\sigma}_+ - \Pi_-\hat{\sigma}_-\Big]\mathbf{\Psi}\,\hat{\jmath}\Big\}, \end{aligned} \tag{7.3}$$

where $\hat{\sigma}_\pm = (\hat{\sigma}_x \pm i\hat{\sigma}_y)/2$, and $\{\hat{\imath}, \hat{\jmath}\}$ is the canonical base in Cartesian coordinates. In Eqs. (7.1)-(7.3) distances are scaled to the superconducting coherence length ξ, time to the GL time t_0, and the vector and electrostatic potentials to $A_0 = \hbar c/2e\xi$ and $\varphi_0 = A_0/ct_0$, respectively. Similarly, the order parameter is scaled to its bulk zero-field value $|\mathbf{\Psi}(\mathbf{A}=0)|$, and the current density to $J_0 = (e\hbar/m\xi)|\mathbf{\Psi}_0|^2$. In order to study the dynamical properties of mesoscopic chiral p-wave superconductors, we adopt the Coulomb gauge, i.e. the arbitrary function of Sec. 3.2 is required to satisfy the equation $\Delta\chi = -\nabla\cdot\mathbf{A}$, which makes the transformed vector potential $\mathbf{A}'$ divergence-free at all times. This gauge choice thereby provides the equation for the electrostatic potential,

$$\nabla^2\varphi = \nabla\cdot\mathbf{J}\,. \tag{7.4}$$

For the vector potential and because of an out-of-plane applied magnetic field, we choose $\mathbf{A} = -(\mathbf{r}\times\mathbf{H})/2$. The boundary conditions imposed at the superconductor-vacuum and superconductor-normal-metal interfaces are,

$$\begin{aligned} &\left.\begin{aligned} \mathbf{\Psi} &= 0 \\ \partial_y\varphi + j &= 0 \end{aligned}\right\} \text{ at N and S sides,} \\ &\left.\begin{aligned} \psi_+ + \psi_- &= 0 \\ D_x\psi_+ - D_x\psi_- &= 0 \\ \partial_x\varphi &= 0 \end{aligned}\right\} \text{ at E and W sides,} \end{aligned} \tag{7.5}$$

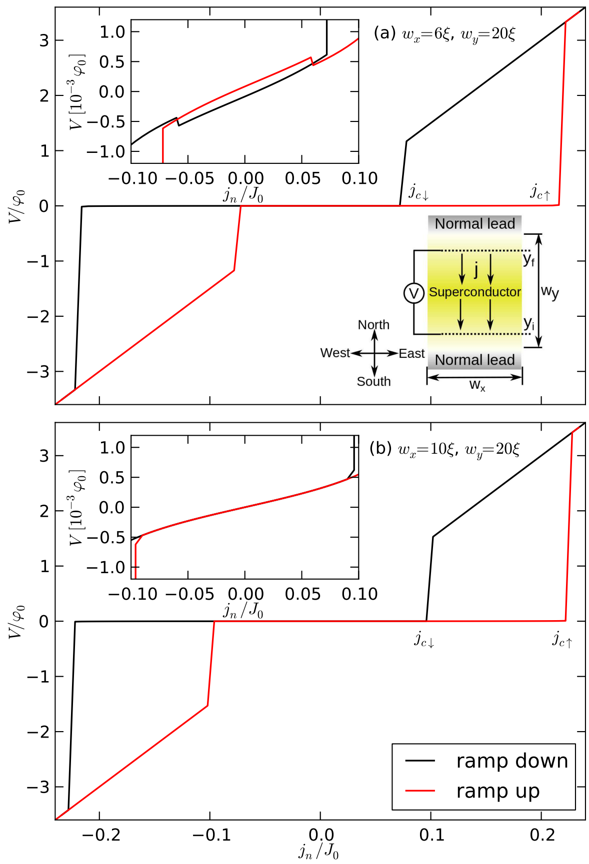

Figure 7.1: The voltage as a function of the applied current density for two nanobridges of same length ($w_y = 20\xi$), and with different widths: $w_x = 6\xi$ (a), and $w_x = 10\xi$ (b). The lower inset of panel (a) shows the nanobridge, along with the normal leads used to apply the current, and the points where the voltage is measured, namely, $y_\mathrm{f} = 17.5\xi$ and $y_\mathrm{i} = 2.5\xi$. Another two insets show the opening (a) and the absence (b) of the hysteretic loop of the voltage vs. current density in the superconducting phase, i.e. the phase with nearly zero voltage drop.

respectively. N, S, E and W stand for the cardinal points. Current j is applied at contacts located at N and S. Eq. (7.5) completes the TDGL equations for chiral p-wave superconductors which we solve using the finite-difference technique.

7.3 Transport signatures of domain walls in multichiral states

In this section we solve the TDGL equations using the Coulomb gauge, for nanobridges with normal leads at the north and south sides [see the lower inset of Fig. 7.1(a)]. These leads are used to apply an external current density j_n to the superconducting sample in order to measure the voltage drop between two voltage contacts, namely y_i and y_f. In dimensionless units and at zero external magnetic field, the voltage versus the current density (j_n-V characteristic) is plotted in Fig. 7.1 for two nanobridges of length 20ξ and widths 6ξ (a) and 10ξ (b), respectively. The obtained j_n-V characteristics are apparently similar, with two different critical currents for $j_n > 0$ ($j_{c\downarrow} < j_{c\uparrow}$) depending on whether j_n is decreased (ramped down) or increased (ramped up). However, a zoom in of the superconducting phase i.e. the phase with nearly zero measured voltage, shows a distinctly different behavior, as seen in the two upper insets. The hysteretic loop in the superconducting phase opens in Fig. 7.1(a), while being absent in Fig. 7.1(b). In order to understand the origin of the hysteresis within the superconducting phase, in what follows we describe the order parameters that

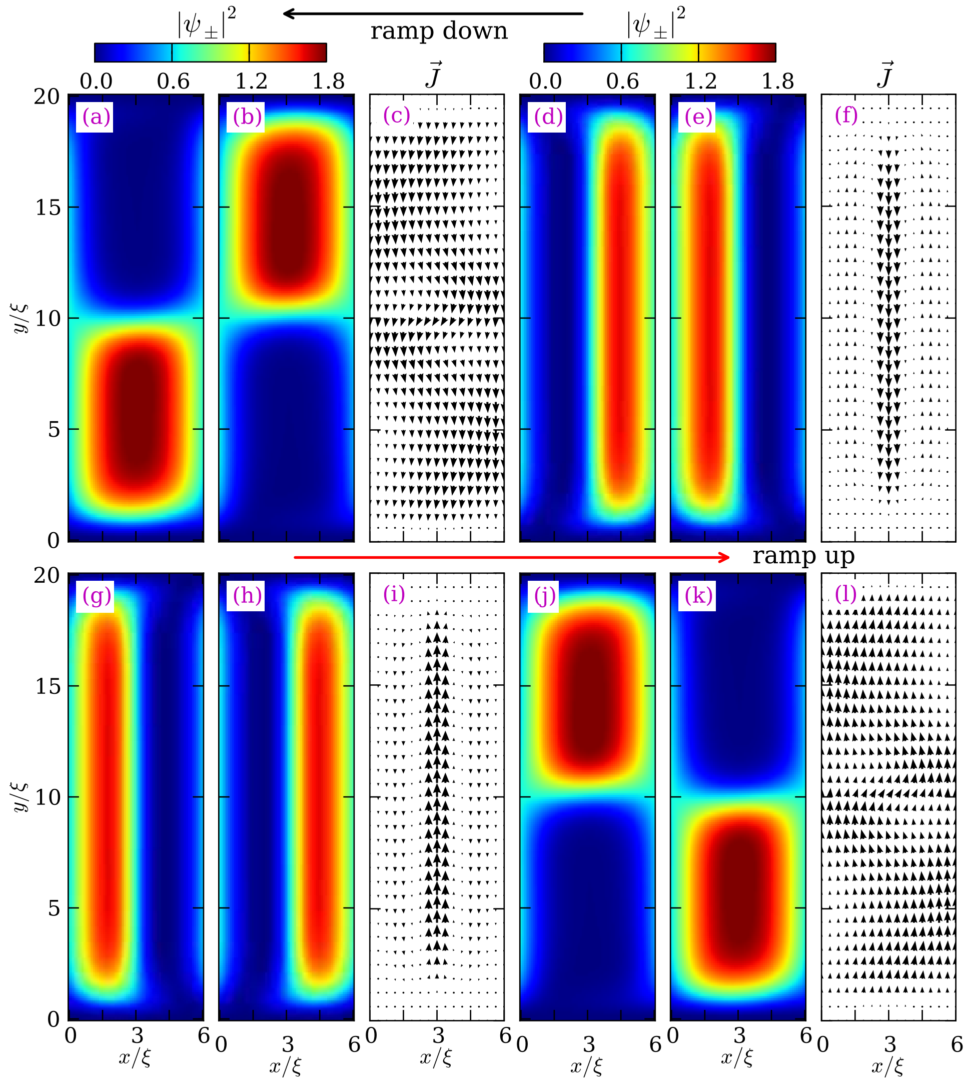

Figure 7.2: Four representative states during the ramp down (a-f) and ramp up (g-l) of the current in the V vs j plot of Fig. 7.1(a). The quantities shown are the contour plots of the superconducting order parameters ($|\psi_\pm|^2$) and the vectorial flow of the current density ($\mathbf{J}$).

correspond to these cases.

Fig. 7.2 directly shows the superconducting states responsible for the opening of the hysteretic loop in the j_n-V characteristic of Fig. 7.1(a). The top row in Fig. 7.2 shows two representative states corresponding to the ramp down of j_n, whereas the bottom row shows two representative states corresponding to the ramp up of j_n. From the top (bottom) row one can easily see that by ramping down (ramping up) the current from the normal phase, one vertical DW with chiral currents flowing downward (upward) is formed. Subsequently, as the external current is further decreased (increased) the vertical DW transforms to a horizontal DW with leftward (rightward) currents. Furthermore, one can also notice that the states with vertical DWs, as well as the states with horizontal DWs, form the pair of degenerate states owing to the broken TRS. That means that under the transformation $|\psi_+|_d \to |\psi_-|_h$ and $|\psi_-|_e \to |\psi_+|_g$, the reduced expression of the free energy [Eq. (4.8)] remains unchanged. Thus, we claim that the combination of degenerate superconducting states with opposite currents (vertical DWs), and the fact that the voltage in the nanobridge is measured transversally to them, leads to the hysteretic behavior seen in the inset of Fig. 7.1(a).

However, when the width of the nanobridge is changed, e.g. to $w = 10\xi$, the degenerate states become monochiral, allowing the formation of spontaneous currents flowing along the edges of the

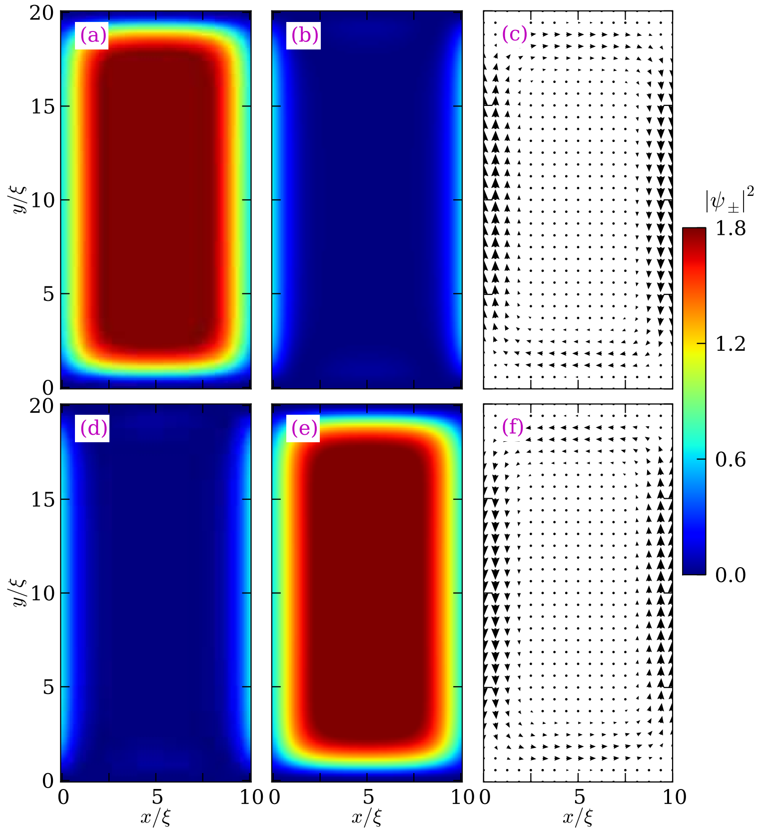

Figure 7.3: Same quantities as in Fig. 7.2 but for the states in the superconducting phase for the ramp down (top row) and ramp up (bottom row) paths of the V vs. j plot of Fig. 7.1(b).

sample for each case, but with opposite directions [clockwise as in Fig. 7.3(c) and counterclockwise as in Fig. 7.3(f)]. The corresponding voltage drop, reported in Fig. 7.1(b) for the latter case does not reveal any hysteretic opening of the j_n-V characteristic in the superconducting phase. Then, it is noteworthy that at zero external magnetic field hysteretic behavior can be used to distinguish monochiral states with spontaneous currents along the edges from multichiral states containing DWs.

Finally, we apply an external magnetic field perpendicularly to the nanobridge of width 6ξ and report the differential resistivity dV/dj_n as a function of the applied current density j_n/j_0, for several values of applied field. In Fig. 7.4 the differential resistivities for different external magnetic fields H have been linearly shifted for clarity. In all curves, at the critical current densities $\pm j_{c\downarrow}$, two discontinuities are clearly seen, indicating the transition point from the normal to the superconducting phase.

It is known that degenerate states such as those of Figs. 7.2 and 7.3 split up when an external magnetic field is turned on [124]. Thus, one expects that as a consequence of the lifted degeneracy, a nonzero field H can close the hysteretic loop of the inset of Fig. 7.1(a). We confirm this prediction in Fig. 7.4(a), although we notice that the hysteretic opening survives up to some threshold field, labeled $H_{\rm ch}$. Below $H_{\rm ch}$ one can see pronounced dips in the differential resistivity, a direct consequence of the discontinuities seen in the voltage plot of Fig. 7.1(a)(upper inset), arising due to applied current pushing the vertical DWs of Fig. 7.2 (f,i) out of the sample and allowing the formation of the horizontal DWs of Fig. 7.2(c,l). Since the sample is narrow ($w_x = 6\xi$), a weak applied magnetic field is sufficient to push out the vertical DWs and favor horizontal DWs as the ground state of the system, so that the hysteretic behavior in applied current is lost.

Above $H_{\rm ch}$ in Fig. 7.4(a) the applied current density j_n can only stabilize one ground state, i.e. one of the two non-degenerate states, independently of the polarity of applied current. As a

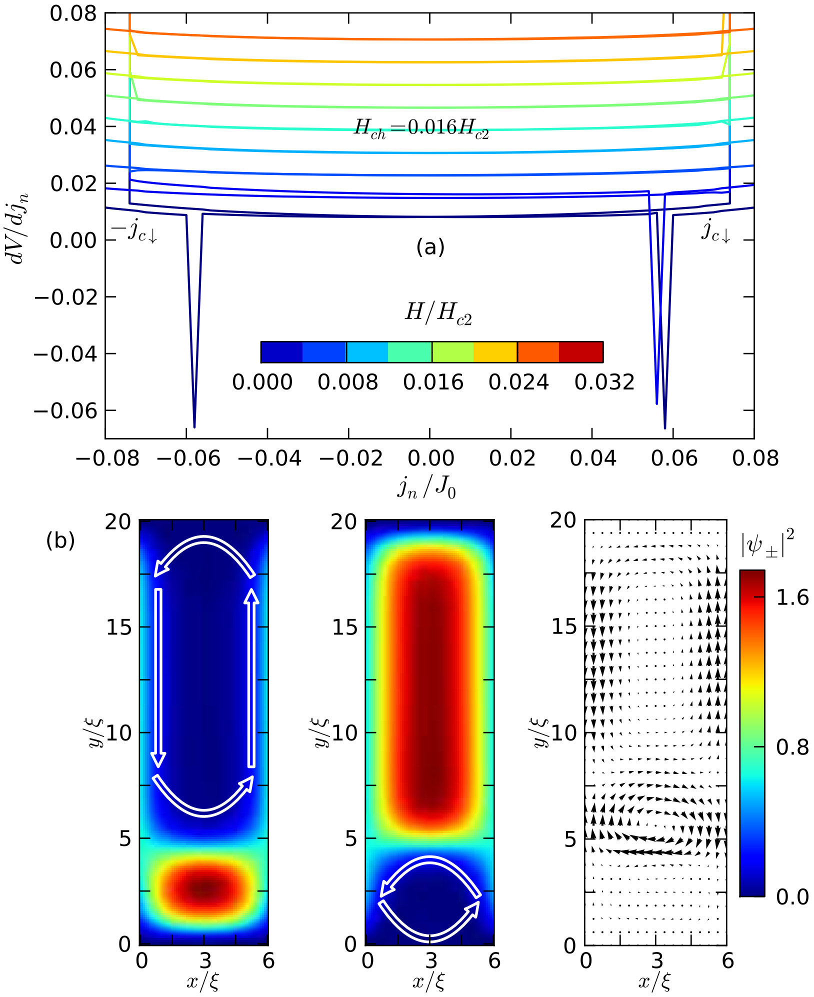

Figure 7.4: (a) Differential resistivity, dV/dj, as a function of the applied current density, j/j_0, for several values of the applied magnetic field H, for the nanobridge with size $6\xi \times 20\xi$. For clarity the differential resistivities have been linearly shifted as a function of the external field H. The visible dips in the curves arise due to the discontinuities in the voltage vs. current density characteristic [see upper inset in Fig. 7.1(a)]. (b) One representative state above $H_{\rm ch}$ at zero applied current density. The displayed quantities are the same as in Fig. 7.2.

consequence, the hysteretic loop in the voltage vs. current density characteristic is closed. In order to show the lifted degeneracy of the ground state, in Fig. 7.4(b) we show one representative non-degenerate state above $H_{\rm ch}$ at zero applied current. There one can see that the edge currents on one side of the DW are annihilated by the screening currents of the external magnetic field, and enhanced on the other side, so that it becomes energetically favorable to displace the horizontal DW off the center (downwards in this case).

7.4 Transport signatures of skyrmions and edge states

In Sec. 5.3 we saw that in mesoscopic samples an out-of-plane applied magnetic field stabilized states containing edge states, vortices and skyrmions. The skyrmion is the topological entity originally conceived in particle physics but appearing also as a characteristic topological defect in different areas of condensed matter physics, such as Bose-Einstein condensates (BEC) [183–185], unconventional superconductivity [123, 124], and magnetism [139, 186]. Strictly speaking, skyrmions are defined

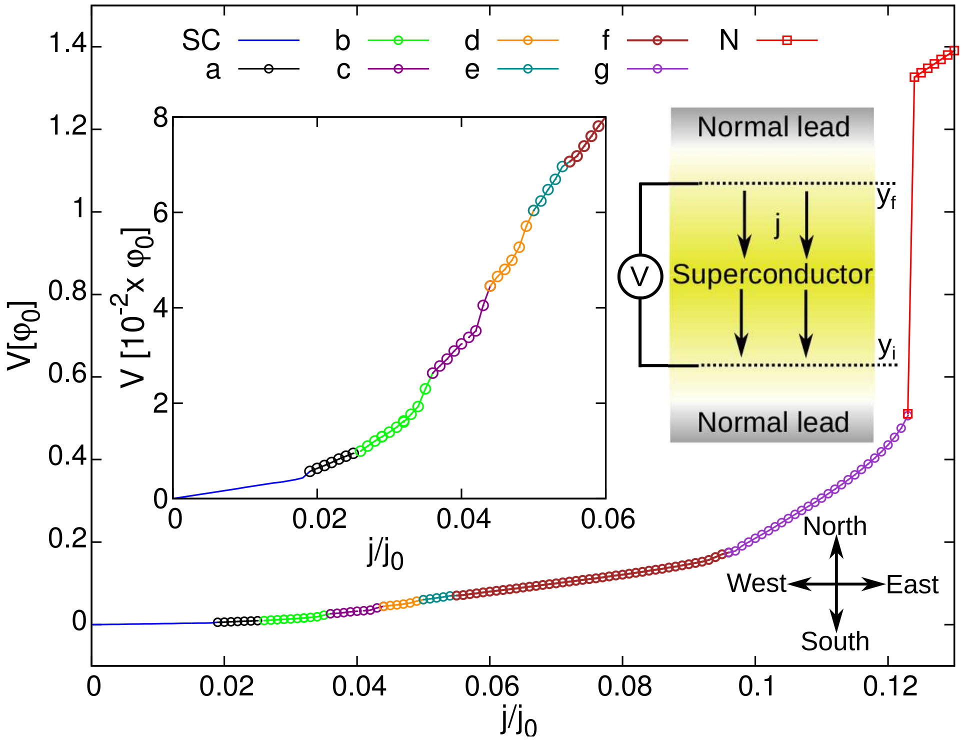

Figure 7.5: Measured voltage versus applied current in dimensionless units for a mesoscopic sample of size $10\xi\times 12\xi$ with normal contacts at north and south sides. An external magnetic field ($H = 0.8H_{c2}$) applied perpendicularly to the sample stabilizes domain walls, skyrmions and half-quantum vortices. Three different regimes can be identified, namely the superconducting (SC), resistive and normal regime (N). The resistive regime contains different states labelled here by (a) - (g).

by the integral

$$\mathbb{Q} = \frac{1}{4\pi}\int \mathbf{n}\cdot(\partial_x\mathbf{n}\times\partial_y\mathbf{n})\,dxdy, \tag{7.6}$$

which measures in discrete units their topological charge. In magnetic materials, more specifically in chiral magnets [139, 186], $\mathbf{n}$ stands for the magnetization density, while in unconventional superconductivity and BECs $\mathbf{n}$ is a pseudospin field obtained from the projection of the superfluid (superconducting) order parameters into the Pauli matrices [123, 124, 183, 185]

$$\mathbf{n} = \frac{\mathbf{\Psi}^{\dagger}\hat{\boldsymbol{\sigma}}\,\mathbf{\Psi}}{\mathbf{\Psi}^{\dagger}\cdot\mathbf{\Psi}}\,. \tag{7.7}$$

In this work we stabilize skyrmions with topological charge two and the edge states in a mesoscopic sample of size $10\xi\times 12\xi$ by applying an external magnetic field $H = 0.8H_{c2}$ out of plane of the sample. Although skyrmions can be stabilized also in bulk samples [123], the edge states (containing one vortex just in component ψ_+, i.e. a half-quantum vortex for the system [1]) appear only where the space homogeneity is broken, thus are characteristic of mesoscopic samples [124]. In what follows, we examine the response of such states to applied current. In our study, the external

[1]In the literature half-quantum vortices arise in p-wave spin-triplet superconductors when only one of the two spin components hosts a quantum of flux, i.e. $\Psi = \Delta(\mathbf{p})\left[e^{i\theta}|\uparrow\uparrow> + |\downarrow\downarrow>\right]$. In the chiral p-wave model considered here the spin of the Cooper paris has been polarized and subsequently they behave as spinless particles. Nevertheless, nucleation of vortices only in one component (half-quantum vortices) is still possible due to the nonzero orbital angular momentum of the Cooper pairs now playing the role of the spin and requiring an order parameter with two components, i.e. $\mathbf{\Psi} = (\psi_+, \psi_-)^T$.

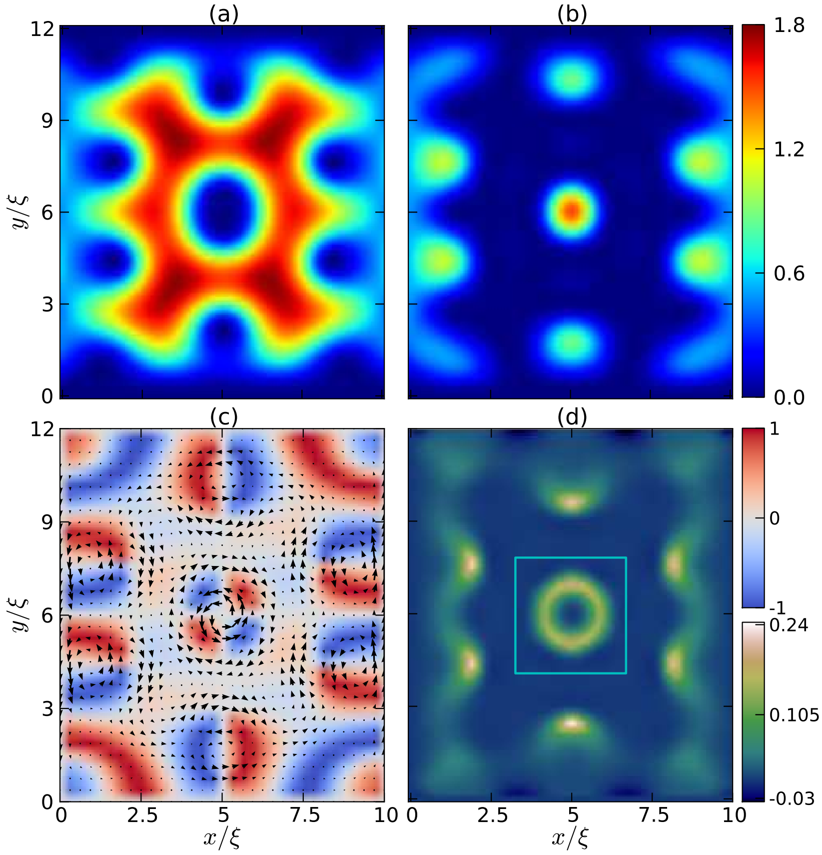

Figure 7.6: Contour plots of $|\psi_+|^2$ (a), $|\psi_-|^2$ (b), the cosine of the intercomponent phase difference $\cos(\theta_x - \theta_y)$ (c), and the density of the topological charge (d) [see Eq. (7.6)]. The current distribution $\mathbf{J}$ is superimposed over the contour plot of panel (c), where the phase difference $(\theta_x - \theta_y)$ was obtained from the fields: $\psi_x = (\psi_+ + \psi_-)/2$ and $\psi_y = (\psi_+ - \psi_-)/2i$. According to panels (c) and (d) the superconducting state is composed of one skyrmion inside the sample and the edge state formed by the connection of six half-quantum vortices at the borders and four chiral domain walls around the corners.

current density j is increased adiabatically from zero up to certain value j_f, streaming from the north to the south side of the sample.

The plot of voltage against current for a mesoscopic chiral p-wave superconductor is shown in Fig. 7.5, with the voltage defined as: $V = \bar{\varphi}|_{y_\mathrm{i}} - \bar{\varphi}|_{y_\mathrm{f}}$, where the bar over the electrostatic potential denotes average, and $y_\mathrm{i} = 1.5\,\xi$ and $y_\mathrm{f} = 10.5\,\xi$. To date, for chiral p-wave superconductors only the stationary GL equations have been derived either phenomenologically or microscopically [77, 94, 102]. The TDGL equations (7.1) and (7.2), obtained as an extension of the stationary ones after imposing full gauge invariance are conceived for gapless superconductors, but are expected to capture the evolution of static and dynamic states in the here studied cases.

Three different regimes can be identified from the current-voltage characteristics of Fig. 7.5, namely the superconducting (stationary), resistive (non-stationary), and normal (ohmic) regime. At low currents the superconducting regime can exhibit weak resistance, consequence of the normal contacts (see the inset of Fig. 7.5). Fig. 7.6 shows the superconducting phase at $j = 0$ in contour plots of $|\psi_+|^2$ (a), $|\psi_-|^2$ (b), the cosine of the intercomponent phase difference $\cos(\theta_x - \theta_y)$ (c) [from here on called the phase difference], and the density of the topological charge (d) [see Eq. (7.6)]. For clarity the current distribution $\mathbf{J}$ is superimposed over the contour plot of the phase difference, where the angular phases θ_x and θ_y were obtained from the redefined order parameters $\psi_x = (\psi_+ + \psi_-)/2$ and $\psi_y = (\psi_+ - \psi_-)/2i$, respectively.

The superconducting state, according to panels (c) and (d) of Fig. 7.6 and the pseudospin texture

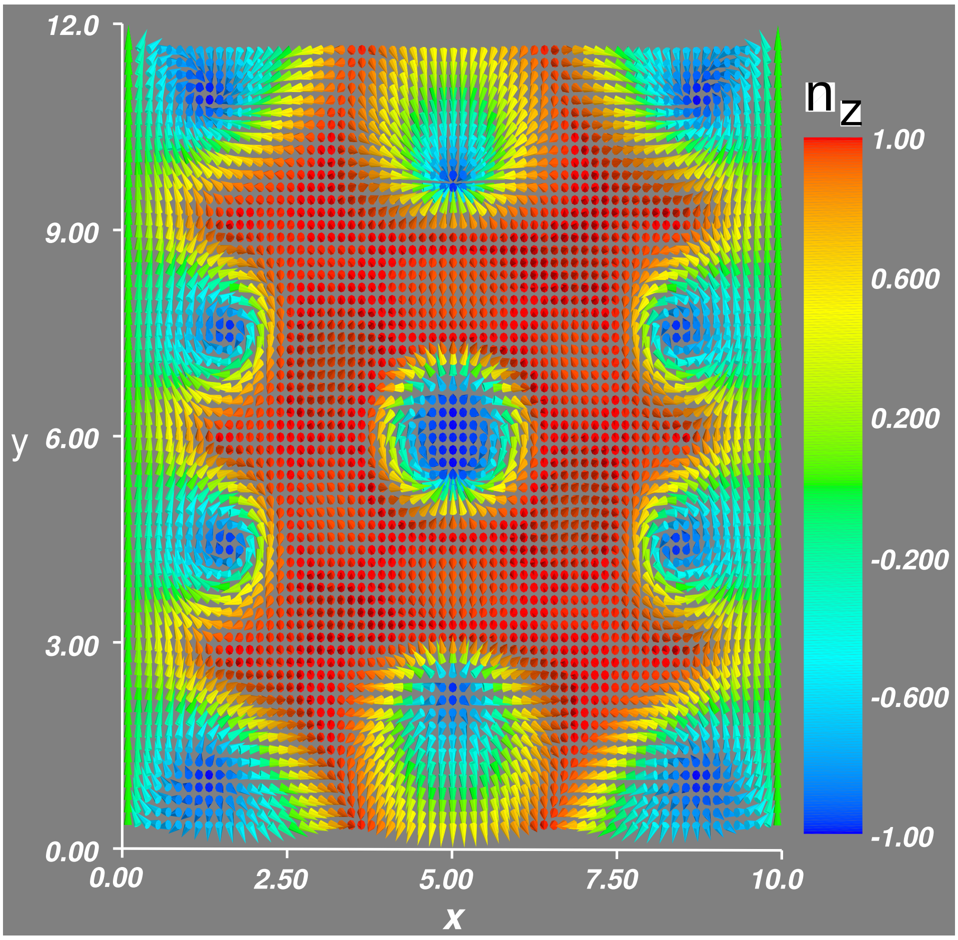

Figure 7.7: Texture of the pseudospin field $\mathbf{n}$ *corresponding to the superconducting state of Fig. 7.6 and obtained from the projection of the superconducting order parameter* $\boldsymbol{\Psi}$ *into the Pauli matrices* $\{\hat{\boldsymbol{\sigma}}_x, \hat{\boldsymbol{\sigma}}_y, \hat{\boldsymbol{\sigma}}_z\}$ *[see Eq. (7.7)].*

of Fig. 7.7 is composed of (i) one skyrmion inside the sample, and (ii) the edge state enclosing the sample and formed by the connection of six HQVs at the borders and four chiral domain walls around the corners. The topological charge of the skyrmion is 2 as obtained from Eq. (7.6) with the domain area indicated by the rectangle in Fig. 7.6 (d). Unlike the skyrmion, the topological charge of one isolated HQV is difficult to estimate due to the ill definition of its boundaries in the edge state (see in Fig. 7.6(d) that delimiting one single HQV is not straightforward). However, by comparing qualitatively the local density of the topological charge of one HQV with that of the skyrmion and with that of a vortex molecule, composed of a vortex-antivortex pair in different components, i.e. a meron pair [183, 185], one realizes that all those topological defects are distinctly different. This suggest that a convenient general description of the superconducting state is in terms of the bulk and surface states, namely the skyrmion/vortex and the edge state.

As one increases the external current the superconducting state of Fig. 7.6 shifts to the right due to the reduction of the superconducting currents in the east side compared to the west side (due to compensation of the Meissner currents with applied current, see e.g. [187]). The resistive regime thus appears at currents where the flux motion drives the superconductor to a non-stationary state. From Fig. 7.5 one can see that such regime exhibits sequential jumps in the voltage as current is increased, which we attribute to different non-stationary states (labelled there by letters). In order to study the temporal evolution of the two-component superconducting order parameter in the resistive regime, we choose the state a of Fig. 7.5 since it summarizes all the rich properties that a mesoscopic chiral p-wave superconductor presents.

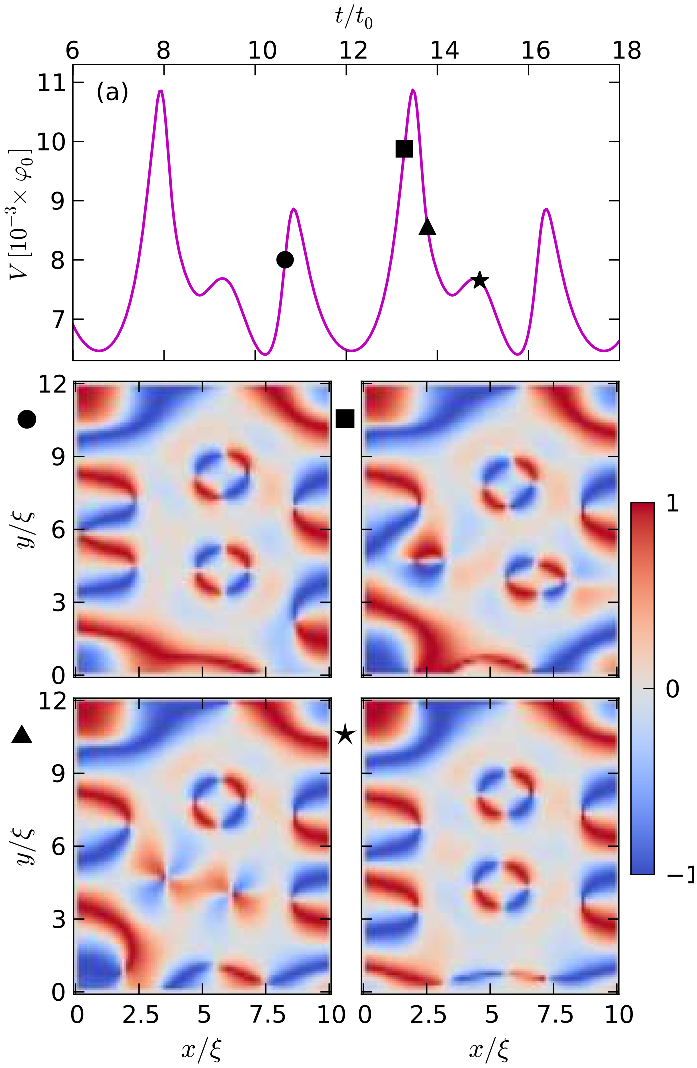

Figure 7.8: Temporal evolution of the non-stationary state a of Fig. 7.5 ($j=0.022j_0$), seen in the voltage vs. time plot (a), and four snapshots of the phase difference $\cos(\theta_x-\theta_y)$, (●), (■), (▲) and (⋆), respectively. The snapshots describe the states associated with the three peaks clearly seen in the voltage plot (a).

The plot of Fig. 7.8(a) reveals that the voltage in state a of Fig. 7.5 is a periodic function of time. Moreover, one can clearly see that there exist three distinct modes that correspond to a special flux motion. Contour plots of the phase difference show the superconducting state at these modes. From panel (●) to (■) one can distinguish three events: (i) the bottom skyrmion is heading towards the E side, (ii) one HQV at the E side left the sample at the south-east corner, and (iii) one HQV at the W side acquired a quantum of flux from component ψ_- to form a full vortex. Next, the skyrmion having two quanta of flux broke into two HQVs and one of these went to the E side while the other fused with another quantum of flux to form a second full vortex [see panels (■) and (▲)]. Another mechanism of skyrmion annihilation, displayed in state f (see the supplementary section), consist of one skyrmion losing its two quanta of flux in the form of two concentric HQVs. Finally, panels (▲) to (⋆) show the fusion of two full vortices into a skyrmion and the nucleation of a HQV at the W side from the west-south corner. There exists another mechanism of skyrmion creation, consisting of two quanta of flux being pumped inside the sample from the edge state, more precisely the W side.

The role of the normal contacts in the one dimensional movement of the HQVs is crucial. Owing to the superconducting-normal-metal interfaces the barrier for HQV exit/entry is cancelled on the

N/S sides of the sample. Further, there also exists a barrier formed by Meissner currents on the E/W sides, that prevents the HQVs to leave the edge state or conversely that prevent the HQV to get in the sample. Altogether, the HQV at the E and W sides experience the easy direction for motion along the superconducting-vacuum interfaces.

7.5 Conclusions

In summary, using the time-dependent Ginzburg-Landau equations for chiral p-wave superconductors, we have shown some characteristic dynamics of the edge state, skyrmions, mono and multichiral states in a mesoscopic p-wave superconductor. When an external current is applied to the sample, we reported novel features in the voltage versus current characteristics, which show a hysteretic behavior in the superconducting phase when domain walls are formed due to confinement. This behavior persisted even when a weak out of plane magnetic field was applied, providing a useful new hallmark for indirect confirmation of the presence of domain walls in the superconducting state and thereby offering a proof of chiral p-wave superconductivity in the material of interest. Furthermore, the resistive state shows much richer behavior compared to conventional s-wave superconductors. For example, depending on the strength of the external current, we found that the half-quantum vortices in the edge state can move along the direction of the applied current, contrary to standard kinematic vortices which always move perpendicularly to the current flow [121, 181, 182]. We also observe in the resistive regime that under the applied current skyrmions either nucleate the sample directly from the edge state or arise from the recombination of two full vortices. These findings combinatorially increase the possibilities for different resistive states in mesoscopic superconductors, worthy of further exploration.

Publication The results of this chapter were published as:

- V. Fernández Becerra and M. V. Milošević, *Multichiral ground states in mesoscopic p-wave superconductors*, Phys. Rev. B **94**, 184517 (2016) (10 pages).

- V. Fernández Becerra and M. V. Milošević, *Dynamics of skyrmions and edge states in the resistive regime of mesoscopic p-wave superconductors*, Physica C **533**, 91 (2017) (4 pages).

8 Summary and Outlook

8.1 Summary

Strontium ruthenate is an unconventional superconductor where the Cooper pairs form spin-triplets and break the time-reversal symmetry (TRS). Moreover, evidence suggests the symmetry of the gap is of the chiral p-wave type. Interestingly, this type of gap is proven to be the archetypal example of a topological superconductor breaking TRS. Vortex cores in chiral p-wave superconductors are expected to host zero-energy modes (the condensed-matter equivalent of Majorana fermions), that are predicted to be the key element for the future quantum computation. Then, the interest in SRO to develop a technological application from its topological properties appears well justified. However, the materialization of a quantum computer based on the topological superconductivity of SRO is yet to be confirmed since the spontaneous magnetic fields predicted to exist in this superconductor due to TRS breaking remained elusive so far.

In this thesis, we studied chiral p-wave superconductivity to reveal the novel superconducting configurations that emerge in mesoscopic samples where confinement is of importance. The approach used in this thesis comprises the phenomenological Ginzburg-Landau theory and the microscopic Bogoliubov-de Gennes formalism, solved self-consistently. We discussed the novel magnetic, electronic and electric properties of the emergent states in order to facilitate the identification of chiral p-wave superconductivity in a candidate material. These features, namely the magnetic profile, the density of states, and the voltage-current characteristic, can be compared with results from Hall probe microscopy, scanning tunneling microscopy, and resistance measurements.

With these goals, we first studied chiral p-wave superconductivity in mesoscopic rectangular samples in absence of any applied magnetic field, in order to stabilize mono and multichiral states. We reported the ground-state phase diagram of rectangular mesoscopic samples with sizes ranging from 3.5ξ to 23ξ, where ξ is the superconducting coherence length. We classified the states according to the number of domain walls separating the regions with different chiralities. The monochiral state has no domain walls, but contains spontaneous currents flowing along the edges. We also noticed that the multichiral phases are made stable owing to the strong confinement, but that same confinement can overshadow the typical dipole-like magnetic field profile of the domain walls. Nevertheless, the imaging of the reported spatial profile of stray magnetic field of the multichiral states can serve as a clear evidence of the time-reversal symmetry breaking in topological superconductors. Finally, we show that our conclusions and results are robust as a function of the phenomenological parameters

τ and κ, describing the possible variation of fermiology and magnetic properties in a given material.

After describing the multichiral states, as an entirely novel configuration compared to the available studies of mesoscopic s-wave superconductors, we have studied in detail all other possible states that arise in a mesoscopic chiral p-wave superconductor, as a function of out-of-plane applied magnetic field and the anisotropy parameters of the material. Due to odd parity and breaking of the time-reversal symmetry the fundamental solutions of the TDGL equations are fractional vortices, i.e. solutions where the phase winding 2π is found in one component of the order parameter but not in the other one. Fractional vortices in different components can combine to form a cored/full-vortex state, as well as a coreless/skyrmion state -clearly seen in the spatial profiles of the phase difference and the magnetic response. Skyrmions arise when same number of fractional vortices in each component combine to form a closed domain wall that separates the outer and inner region with different chiralities. On the other hand, we also obtained half-quantum vortices analogous to those of spin-triplet superconductors, despite of the fact that vector $\vec{d}$ is strongly pinned along $\hat{\mathbf{z}}$ in the chiral representation $\vec{d} = (k_x \pm ik_y)\hat{\mathbf{z}}$. Actually the mesoscopic size of the sample plays a remarkable role in the stability of skyrmions as well as in the here reported novel transitions (e.g. formation of skyrmions from the edge states, or transitions from a skyrmion to a full vortex).

Once we have identified these novel states and configurations, we have studied the topological and electronic properties of characteristic vortical and skyrmionic states in chiral p-wave superconductors. The distribution of the two-component order parameter, the supercurrent, quasiparticle excitation spectra, and LDOS, for each of the typical states have been presented. Special attention is devoted to the skyrmion, exhibiting a closed domain wall where the Cooper-pair density is suppressed, but core is not fully developed, unlike conventional vortices. Moreover, the skyrmion is found to be characterized not only by the angular momentum, but also by its topological charge, and the bound states that are trapped at the chiral domain wall. These bound states lead to zero-bias LDOS peaks at the domain wall, and electron-hole asymmetry in the LDOS, which is different from the electron-hole symmetric LDOS of usual multi-quanta vortex states. We also show the possibility to have a topological defect with a vortex inside a skyrmion, with superimposed features of both topological constituents. Finally, the analysis in varied magnetic field and temperature shows that the size of the skyrmion can be strongly tuned, being increased by increasing temperature and by decreasing applied magnetic field. Moreover, contrary to conventional vortices, a skyrmion survives changing the polarity of the applied magnetic field, that leads to the significant enlargement of skyrmions at negative magnetic field. Nonetheless, skyrmions can be manipulated also in the absence of the magnetic field, by pinning on a normal-metal ring of prescribed size, opening a broad playground for novel phenomena in fluxonics. We expect that our findings will enable the experimental identification of these novel states in scanning tunneling microscopy and spectroscopy, and that those can be further used to prove particular pairing symmetry in the superconductor of interest.

Finally, we addressed some characteristic dynamics of the edge state, skyrmions, mono and multichiral states in a mesoscopic p-wave superconductor. When an external current is applied to the sample, we reported novel features in the voltage versus current characteristics, which show a hysteretic behavior in the superconducting phase when domain walls are formed due to confinement. This behavior persisted even when a weak out-of-plane magnetic field was applied, providing a useful new hallmark for indirect confirmation of the presence of domain walls in the superconducting state and thereby offering a proof of chiral p-wave superconductivity in the material of interest. Furthermore, the resistive state shows much richer behavior compared to conventional s-wave superconductors. For example, depending on the strength of the external current, we found that the half-quantum vortices can move along the direction of the applied current, contrary to standard kinematic vortices which always move perpendicularly to the current flow. We also observe in the resistive regime that under the applied current skyrmions either nucleate the sample directly from the edge state or arise from the recombination of two full vortices. These findings combinatorially increase the possibilities for different resistive states in mesoscopic superconductors, worthy of further exploration.

In conclusion, this thesis shows a comprehensive analysis of novel vortical and skyrmionic states in mesoscopic p-wave superconductors, with emphasis on their experimentally verifiable properties, magnetic and electronic, as well as their behavior under applied current. The shown new features are potentially useful in technology, either for detection and manipulation of Majorana states, or by creation of more versatile nanoengineered circuits and devices. More importantly, we hope that this thesis presents the opening chapter in the further investigation of novel states in superconducting systems with a multicomponent order parameter, where p-wave case is only a particular example.

8.2 Outlook

In **chapters** 4 - 7, I investigated the novel superconducting configurations that appear in mesoscopic chiral p-wave superconductors. I revealed not only monochiral and multichiral states in absence of an out-of-plane applied field, but also skyrmions, conventional vortices and edge states in a non-zero external magnetic field. These novel states, characterized owing to their magnetic, electronic and dynamic properties, emerged as the signature of superconductivity of the p-wave type and breaking the TRS. However, superconductivity breaking the TRS can also manifest in other pairing symmetries, as for example $s+id$ and $s+is$. These symmetries are worthy of investigation since theoretical and experimental works have suggested that in the iron-based superconductor $Ba_{1-x}K_xFe_2As_2$, between the moderate ($x \approx 0.4$) and maximum ($x = 1$) doping, the $s+id$ and $s+is$ pairing symmetries are the leading candidates [112, 113]. Therefore, as a future continuation of my work it will be interesting to investigate these pairing symmetries phenomenologically and microscopically in mesoscopic samples, in order to reveal magnetic, electronic and dynamic properties of their superconducting configurations.

In **chapters** 5 and 7, I reported edge states containing half-quantum vortices (HQVs) analogous to those of spin-triplet superconductors where the direction of the $\vec{d}$ vector is allowed to rotate, unlike chiral p-wave superconductivity where $\vec{d}$ remains fixed along the $\hat{\mathbf{z}}$ axis. HQVs have been predicted to be more favorable than conventional vortices when an in-plane field is applied [133, 188, 189]. However, the theoretical approach for the study of these HQVs is not chiral, and I plan to upgrade the methods to address the emergent physics.

In **chapter** 7, I showed some characteristic dynamics of the edge state, skyrmions, mono and multichiral states in a nanobridge of a mesoscopic p -wave superconductor linking two normal leads. I revealed novel features in the voltage versus current characteristics when an external current was applied. The extension to a doubly connected superconductor, although not finished and included in this thesis, is already developed. The importance of this lies in our collaboration with experimental teams in Leiden and Penn State University, working on measurements of the nontrivial oscillation of the superconducting transition temperature with the applied magnetic flux (the Little-Parks effect), as well as the magnetoresistance of the ring-like SRO samples. Therefore, the study of the magnetoresistance in a doubly connected mesoscopic chiral p-wave superconductor is the immediate extension of this work.

9
Samenvatting

9.1 Samenvatting

Strontium ruthenaat (SRO) is een onconventionele supergeleider waarin de Cooper paren spin-triplets vormen en de tijdsomkeersymmetrie (TRS) breken. Bewijs suggereert dat de symmetrie van de bandgap van het chirale p-golf type is. Het is bewezen dat dit type van gap een archetypisch voorbeeld is van een topologische supergeleider die de TRS breekt. Er wordt verwacht dat vortices in een chirale p-golf supergeleider modes met energie nul bevatten (het gecondenseerd materie equivalent van Majorana fermionen), waarvan voorspeld wordt dat ze een sleutelelement zijn in toekomstige kwantum computationele berekeningen. Daarnaast lijkt de interesse in SRO, voor de ontwikkeling van toekomstige technologische applicaties, omwille van zijn topologische eigenschappen gerechtvaardigd. De materialisatie van een kwantumcomputer, gebaseerd op de topologische supergeleiding van SRO, moet echter nog steeds bewezen worden, aangezien het spontane magnetisch veld, dat voorspeld werd te moeten bestaan in deze supergeleider omwille van de breking van de TRS, echter afwezig blijft.

In deze thesis bestuderen we de chirale p-golf supergeleiding om de nieuwe supergeleidende configuraties die zich voordoen in mesoscopische samples, waar opsluiting belangrijk is, te onthullen. De methode die in deze thesis toegepast wordt, omvat de fenomenologische Ginzburg-Landau theorie en het microscopische Bogliubov-de Gennes formalisme. De vergelijkingen worden daarbij op een zelf-consistente manier opgelost. We bespreken de nieuwe magnetische, elektronische en elektrische eigenschappen van de toestanden, om de identificatie van de chirale p-golf supergeleiding in een kandidaat materiaal mogelijk te maken. Deze eigenschappen, zoals het magnetisch profiel, de toestandsdichtheid, en de spanning-stroom eigenschappen, kunnen vergeleken worden met resultaten van Hall probe microscopie, scanning tunneling microscopie, en weerstandsmetingen.

Met deze doelstellingen in het achterhoofd, bestudeerden we eerst de chirale p-golf supergeleiding in rechthoekige mesoscopische samples, in afwezigheid van een magnetisch veld, om zo de mono- en multi-chirale toestanden te stabiliseren. We rapporteren het grondtoestand fasediagram van rechthoekige mesoscopische samples met groottes gaande van 3.5ξ tot 23ξ, waarbij ξ de supergeleidende coherentie lengte is. We classificeerden de toestanden volgens het aantal domeingrenzen die de regio's met verschillende chiraliteit van elkaar scheiden. De monochirale toestand heeft geen domeingrens, maar bevat spontante stromen die langs de rand vloeien. We hebben ook ontdekt dat de multichirale fasen stabiel gehouden worden dankzij de sterke opsluiting, maar dat deze opsluiting het typische dipool magnetisch veld profiel van de domein grenzen kan overschaduwen. Toch kunnen afbeeldingen van het ruimtelijk profiel van het demagnetiserend veld van de multichirale toestanden dienen als een duidelijk bewijs van de tijdsomkeersymmetrie breking in topologische supergeleiders. Uiteindelijk tonen we dat onze conclusie en resultaten robuust zijn als functie van de fenomenologische parameters τ en κ, die de mogelijke variaties van fermiologie en magnetische eigenschappen van een bepaald materiaal beschrijven.

Na het beschrijven van de multichirale toestanden, als een volledig nieuwe configuratie in vergelijking met de beschikbare studies van mesoscopische s-golf supergeleiders, maakten we een gedetailleerde studie van andere mogelijke toestanden die ontstaan uit mesoscopische chirale p-golf supergeleiders, als functie van een loodrecht aangelegd magnetisch veld en de anisotropische parameters van het materiaal. Dankzij oneven pariteit en een breking van de tijdsomkeersymmetrie zijn de fundamentele oplossingen van de TDGL vergelijkingen fractionele vortices, i.e. oplossingen waar de fase omwinding 2π teruggevonden wordt in één van de componenten van de ordeparameter, maar niet in de andere. Fractionele vortices in verschillende componenten kunnen combineren om *cored*/*full* vortex toestanden te vormen, net zoals kernloze/skyrmion toestanden, duidelijk geobserveerd in het spatiale profiel van het faseverschil en de magnetische reactie. Skyrmionen komen voor wanneer een gelijke hoeveelheid van fractionele vortices in elke component combineren om gesloten domeingrens te vormen die de binnenste en buitenste regio's met verschillende chiraliteit van elkaar gaat scheidt. Langs de andere kant verkregen we ook half-kwantum vortices, analoog aan de spin-triplet supergeleiders, ondanks het feit dat de vector $\mathbf{d}$ sterk vastgepind is langs $\hat{\mathbf{z}}$ in de chirale voorstelling $\mathbf{d} = (k_x \pm ik_y)\hat{\mathbf{z}}$. De mesoscopische grootte van het sample lijkt een merkwaardige rol te spelen in de stabiliteit van de skyrmionen, alsook in de hier gerapporteerde nieuwe overgangen (bv. vorming van skyrmionen van randtoestanden, of overgangen van skyrmion tot een volledige vortex)

Eens we de nieuwe toestanden en configuraties hebben geïdentificeerd, bestudeerden we de topologische en elektronische eigenschappen van karakteristieke vortex en skyrmion toestanden in chirale p-golf supergeleiders. De distributie van de twee-component ordeparameter, de superstroom, quasideeltje excitatie spectra en LDOS worden voor elk van de typische toestanden voorgesteld. Er wordt extra aandacht besteed aan het skyrmion, dat een gesloten domeingrens heeft waar de cooperpaar dichtheid onderdrukt wordt, maar waar de kern niet volledig ontwikkeld is, in tegenstelling tot conventionele vortices. Bovendien werd er ontdekt dat het skyrmion niet enkel door angulair moment gekarakteriseerd kan worden, maar ook door zijn topologische lading, en de gebonden toestanden die vast zitten aan de chirale domeingrens. Deze gebonden toestanden leiden tot *zero-bias* LDOS pieken aan de domein grens, en elektron-gat asymmetrie in de LDOS, dat verschillend is van de elektron-gat symmetrische LDOS van gebruikelijke multi-kwanta vortex toestanden. We tonen ook de mogelijkheid om een topologisch defect te verkrijgen met een vortex binnenin een skyrmion, met gesuperponeerde kenmerken van beide topologische constituenten. Ten slotte toont de analyse in verschillende magnetische velden en bij verschillende temperaturen aan dat de grootte van het skyrmion sterk gevarieerd kan worden, waarbij deze toeneemt bij toenemende temperatuur en bij afnemend aangelegd magnetisch veld. Daar tegenover kunnen skyrmionen ook gemanipuleerd worden in afwezigheid van een magnetisch veld, dankzij pinning op een normaal-metaal ring van bepaalde grootte, waarbij een groot veld van nieuwe fenomenen in *fluxonics* geopend kan worden. We verwachten dat onze bevindingen een experimentele identificatie van deze nieuwe toestanden met behulp van scanning tunneling microscopie en spectroscopie in staat kunnen stellen, en dat deze verder gebruikt kunnen worden om specifieke paringssymmetrie in een relevante supergeleider te kunnen bewijzen.

Ten slotte bestudeerden we enkele karakteristieke dynamieken van de randtoestanden, skyrmionen, mono- en multichirale toestanden in een mesoscopische p-golf supergeleider. Wanneer een externe stroom wordt aangelegd op het sample, rapporteerden we nieuwe eigenschappen in de spanning versus stroom karakteristieken, die een hysteresisch gedrag vertonen in de supergeleidende fase, wanneer de domeinsgrens gevormd worden door opsluiting. Dit gedrag bleef behouden wanneer een zwak loodrecht magnetisch veld aangelegd werd, zorgend voor een handig nieuw keurmerk voor indirecte bevestiging van de aanwezigheid van domein grenzen in de supergeleidende toestand en daarbij bewijs leverend voor chirale p-golf supergeleiding in het beschouwde materiaal. Verder toont de resistieve toestand een veel rijker gedrag in vergelijking met de conventionele s-golf supergeleiders. Zo vonden we bijvoorbeeld dat, afhankelijk van de kracht van de externe stroom, de half-kwantum vortices kunnen bewegen langs de richting van de aangelegde stroom, in tegenstelling tot standaard kinematische vortices die altijd loodrecht bewegen ten opzichte van de richting van de stroom. We observeerden in het resistieve regime ook dat onder aangelegde stroom skyrmionen het sample ofwel direct vanuit de randtoestanden kunnen nucleëren, ofwel ontstaan vanuit de recombinatie van twee *full vortices*. Deze bevindingen zullen de mogelijkheden in het vormen van resestieve toestanden in mesoscopische supergeleiders combinatorisch doen toenemen, en zijn daarbij verder onderzoek waardig.

In conclusie, deze thesis toont een uitgebreide analyse van nieuwe vortex en skyrmion toestanden in mesoscopische p-golf supergeleiders, waarbij de nadruk gelegd wordt op hun experimenteel te verifiëren eigenschappen, magnetisch en elektronisch, alsook hun gedrag onder aangelegde stroom. De getoonde nieuwe kenmerken zijn potentieel van belang in technologie, ofwel voor de detectie en manipulatie van Majorana toestanden, ofwel bij de creatie van meer veelzijdige nano-ontworpen circuits en apparaten. Verder hopen we dat deze thesis een openingshoofdstuk is in toekomstig onderzoek naar nieuwe toestanden in supergeleidende systemen met een multicomponent ordeparameter, waarbij het p-golf geval enkel een specifiek voorbeeld is.

9.2 Toekomstperspectieven

In **hoofdstuk** 4 - 7, onderzoek ik de nieuwe supergeleidende configuraties die zich voordoen in mesoscopische chirale p-golf supergeleiders. Ik onthul niet enkel monochirale en multichirale toestanden in afwezigheid van een loodrecht aangelegd veld, maar ook skyrmionen, conventionele vortices en randtoestanden in externe magnetische velden verschillend van nul. Deze nieuwe toestanden, gekarakteriseerd door magnetische, elektronische en dynamische eigenschappen, komen naar voor als de signatuur van supergeleiding van het p-golf type en de breking van de TRS. Echter, supergeleiding die de TRS breekt kan zich ook manifesteren in andere paringssymmetrieën, zoals bijvoorbeeld $s+id$ and $s+is$. Deze symmetrieën zijn verder onderzoek waardig, aangezien theoretisch en experimenteel werk suggereert dat in ijzer-gebaseerde supergeleider $Ba_{1-x}K_xFe_2As_2$, tussen de gematigde ($x \approx 0.4$) en de maximum ($x = 1$) doping, de $s+id$ and $s+is$ pairingssymmetrieën de leidende kanidaten zijn [112, 113]. Als een toekomstige voortzetting van mijn werk zou het interessant zijn om deze paring symmetrieën verder fenomenologisch en microscopisch te bestuderen in microscopische samples, om zo de magnetische, elektronische, en dynamische eigenschappen van hun supergeleidende configuraties te kunnen onthullen.

In **hoofdstukken** 5 en 7 rapporteerde ik over randtoestanden die half-kwantum vortices (HQVs) bevatten, analoog aan deze van spin-triplet supergeleiders waar de richting van de $\mathbf{d}$ vector kan roteren, tegengesteld aan chirale p-golf supergeleiding waar $\mathbf{d}$ gefixeerd blijft langs de $\hat{\mathbf{z}}$ as. Er wordt voorspeld dat HQVs gunstiger zijn dan conventionele vortices wanneer een parallel veld aangelegd wordt [133, 188, 189]. De theoretische aanpak voor de studie van deze HQVs is echter niet chiraal en ik ben van plan om deze methodes te verbeteren om de nieuwe fysica te kunnen behandelen

In **hoofdstuk** 7 toon ik karakteristieke dynamica van de randtoestanden, skyrmionen, mono- en multichirale toestanden in een nanobrug van een mesoscopisch p-golf supergeleider die twee metalen met elkaar verbindt. Ik onthulde nieuwe kenmerken in de spanning versus stroom eigenschappen wanneer een extern veld aangelegd werd. De uitbreiding naar een dubbele aaneengesloten supergeleider, hoewel nog niet afgewerkt en ingesloten in deze thesis, is reeds ontwikkeld. Het belang hiervan ligt in onze samenwerking met experimentele teams in Leiden en Penn State University, waar zowel gewerkt wordt aan metingen van niet-triviale oscillaties van de supergeleidende transitie-temperatuur met aangelegde magnetische flux (het Little-Parks effect), alsook aan magnetoresistentie van ringachtige SRO samples. Daarom is de studie van de magnetoresistentie in een dubbel verbonden mesoscopische chirale p-golf supergeleider een directe extensie van dit werk.

Bibliography

[1] H. K. Onnes, “The resistance of pure mercury at helium temperatures,” *Commun. Phys. Lab. Univ. Leiden*, vol. 12, pp. 120+, 1911.

[2] H. K. Onnes, “The resistance of pure mercury at helium temperatures,” *Commun. Phys. Lab. Univ. Leiden*, vol. 12, pp. 133+, 1913.

[3] W. Meissner and R. Ochsenfeld, “Ein neuer effekt bei eintritt der supraleitfähigkeit,” *Naturwissenschaften*, vol. 21, no. 44, pp. 787–788, 1933.

[4] M. Tinkham, *Introduction to Superconductivity: Second Edition (Dover Books on Physics) (Vol i)*. Dover Publications, second edition ed., June 2004.

[5] F. London and H. London, “The electromagnetic equations of the supraconductor,” *Proceedings of the Royal Society of London A: Mathematical, Physical and Engineering Sciences*, vol. 149, no. 866, pp. 71–88, 1935.

[6] V. L. Ginzburg and L. D. Landau, “On the theory of superconductivity,” *Zh. Eksp. Teor. Fiz.*, vol. 20, pp. 1064–1082, 1950.

[7] A. A. Abrikosov, “On the Magnetic properties of superconductors of the second group,” *Sov. Phys. JETP*, vol. 5, pp. 1174–1182, 1957. [Zh. Eksp. Teor. Fiz.32,1442(1957)].

[8] U. Essmann and H. Truble, “The direct observation of individual flux lines in type II superconductors,” *Physics Letters A*, vol. 24, no. 10, pp. 526 – 527, 1967.

[9] H. F. Hess, R. B. Robinson, R. C. Dynes, J. M. Valles, and J. V. Waszczak, “Scanning-tunneling-microscope observation of the abrikosov flux lattice and the density of states near and inside a fluxoid,” *Phys. Rev. Lett.*, vol. 62, pp. 214–216, Jan 1989.

[10] J. Bardeen, L. N. Cooper, and J. R. Schrieffer, “Theory of superconductivity,” *Phys. Rev.*, vol. 108, pp. 1175–1204, Dec 1957.

[11] L. N. Cooper, “Bound electron pairs in a degenerate fermi gas,” *Phys. Rev.*, vol. 104, pp. 1189–1190, Nov 1956.

[12] H. Fröhlich, “Theory of the superconducting state. I. the ground state at the absolute zero of temperature,” *Phys. Rev.*, vol. 79, pp. 845–856, Sep 1950.

[13] E. Maxwell, “Isotope effect in the superconductivity of mercury,” *Phys. Rev.*, vol. 78, pp. 477–477, May 1950.

[14] L. P. Gor’kov, “Microscopic derivation of the Ginzburg-Landau equations in the theory of superconductivity,” *Sov. Phys. JETP*, vol. 36, pp. 1364–1367, 1959. [Zh. Eksp. Teor. Fiz.36,1918(1959)].

[15] N. E. Phillips, "Heat capacity of aluminum between 0.1^{o}K and 4.0^{o}K," *Phys. Rev.*, vol. 114, pp. 676–685, May 1959.

[16] J. G. Bednorz and K. A. Müller, "Possible high-Tc superconductivity in the BaLaCuO system," *Zeitschrift für Physik B Condensed Matter*, vol. 64, no. 2, pp. 189–193, 1986.

[17] A. Schilling, M. Cantoni, J. D. Guo, and H. R. Ott, "Superconductivity above 130 K in the Hg-Ba-Ca-Cu-O system," *Nature*, vol. 363, pp. 56–58, 1993.

[18] D. A. Wollman, D. J. Van Harlingen, W. C. Lee, D. M. Ginsberg, and A. J. Leggett, "Experimental determination of the superconducting pairing state in YBCO from the phase coherence of YBCO-Pb dc SQUIDs," *Phys. Rev. Lett.*, vol. 71, pp. 2134–2137, Sep 1993.

[19] C. C. Tsuei and J. R. Kirtley, "Pairing symmetry in cuprate superconductors," *Rev. Mod. Phys.*, vol. 72, pp. 969–1016, Oct 2000.

[20] J. F. Annett, "Symmetry of the order parameter for high-temperature superconductivity," *Advances in Physics*, vol. 39, no. 2, pp. 83–126, 1990.

[21] J. F. Zasadzinski, L. Ozyuzer, L. Coffey, K. E. Gray, D. G. Hinks, and C. Kendziora, "Persistence of strong electron coupling to a narrow boson spectrum in overdoped tunneling data," *Phys. Rev. Lett.*, vol. 96, p. 017004, Jan 2006.

[22] J. P. Carbotte, T. Timusk, and J. Hwang, "Bosons in high-temperature superconductors: an experimental survey," *Reports on Progress in Physics*, vol. 74, no. 6, p. 066501, 2011.

[23] J. Nagamatsu, N. Nakagawa, T. Muranaka, Y. Zenitani, and J. Akimitsu, "Superconductivity at 39 K in magnesium diboride," *Nature*, vol. 410, p. 63, Mar 2001.

[24] Y. Kamihara, H. Hiramatsu, M. Hirano, R. Kawamura, H. Yanagi, T. Kamiya, and H. Hosono, "Iron-based layered superconductor: LaOFeP," *Journal of the American Chemical Society*, vol. 128, no. 31, pp. 10012–10013, 2006. PMID: 16881620.

[25] Y. Kamihara, T. Watanabe, M. Hirano, and H. Hosono, "Iron-based layered superconductor La[$O_{1-x}F_x$]FeAs ($x = 0.05 - 0.12$) with Tc = 26 K," *Journal of the American Chemical Society*, vol. 130, no. 11, pp. 3296–3297, 2008. PMID: 18293989.

[26] F.-C. Hsu, J.-Y. Luo, K.-W. Yeh, T.-K. Chen, T.-W. Huang, P. M. Wu, Y.-C. Lee, Y.-L. Huang, Y.-Y. Chu, D.-C. Yan, and M.-K. Wu, "Superconductivity in the PbO-type structure α-FeSe," *Proceedings of the National Academy of Sciences*, vol. 105, no. 38, pp. 14262–14264, 2008.

[27] H. Ding, P. Richard, K. Nakayama, K. Sugawara, T. Arakane, Y. Sekiba, A. Takayama, S. Souma, T. Sato, T. Takahashi, Z. Wang, X. Dai, Z. Fang, G. F. Chen, J. L. Luo, and N. L. Wang, "Observation of Fermi-surface-dependent nodeless superconducting gaps in $Ba_{0.6}K_{0.4}$ Fe_2 As_2," *EPL (Europhysics Letters)*, vol. 83, no. 4, p. 47001, 2008.

[28] C. Day, "Iron-based superconductors," *Physics Today*, vol. 62, no. 8, pp. 36–40, 2009.

[29] A. P. Drozdov, M. I. Eremets, I. A. Troyan, V. Ksenofontov, and S. I. Shylin, "Conventional superconductivity at 203 kelvin at high pressures in the sulfur hydride system," *Nature*, vol. 525, p. 73, Sep 2015.

[30] P. G. De Gennes, *Superconductivity of Metals and Alloys*. Advanced book classics, Cambridge, MA: Perseus, 1999.

[31] J. Ketterson and S. Song, *Superconductivity*. Cambridge University Press, 1999.

[32] R. Prozorov, "Equilibrium topology of the intermediate state in type-I superconductors of different shapes," *Phys. Rev. Lett.*, vol. 98, p. 257001, June 2007.

[33] B. Josephson, "Possible new effects in superconductive tunnelling," *Physics Letters*, vol. 1, no. 7, pp. 251 – 253, 1962.

[34] B. J. Baelus and F. M. Peeters, "Dependence of the vortex configuration on the geometry of mesoscopic flat samples," *Phys. Rev. B*, vol. 65, p. 104515, Feb 2002.

[35] A. K. Geim, I. V. Grigorieva, S. V. Dubonos, J. G. S. Lok, J. C. Maan, A. E. Filippov, and F. M. Peeters, "Phase transitions in individual sub-micrometre superconductors," *Nature*, vol. 390, p. 259, Nov 1997.

[36] P. Singha Deo, V. A. Schweigert, and F. M. Peeters, "Hysteresis in mesoscopic superconducting disks: The Bean-Livingston barrier," *Phys. Rev. B*, vol. 59, pp. 6039–6042, Mar 1999.

[37] G. R. Berdiyorov, L. R. E. Cabral, and F. M. Peeters, "Surface barrier for flux entry and exit in mesoscopic superconducting systems," *Journal of Mathematical Physics*, vol. 46, no. 9, 2005.

[38] C. P. Bean and J. D. Livingston, "Surface barrier in type-II superconductors," *Phys. Rev. Lett.*, vol. 12, pp. 14–16, Jan 1964.

[39] V. A. Schweigert, F. M. Peeters, and P. S. Deo, "Vortex phase diagram for mesoscopic superconducting disks," *Phys. Rev. Lett.*, vol. 81, pp. 2783–2786, Sep 1998.

[40] B. Xu, M. V. Milošević, S.-H. Lin, F. M. Peeters, and B. Jankó, "Formation of multiple-flux-quantum vortices in mesoscopic superconductors from simulations of calorimetric, magnetic, and transport properties," *Phys. Rev. Lett.*, vol. 107, p. 057002, Jul 2011.

[41] T. Cren, L. Serrier-Garcia, F. Debontridder, and D. Roditchev, "Vortex fusion and giant vortex states in confined superconducting condensates," *Phys. Rev. Lett.*, vol. 107, p. 097202, Aug 2011.

[42] N. Barišić, M. K. Chan, Y. Li, G. Yu, X. Zhao, M. Dressel, A. Smontara, and M. Greven, "Universal sheet resistance and revised phase diagram of the cuprate high-temperature superconductors," *Proceedings of the National Academy of Sciences*, vol. 110, no. 30, pp. 12235–12240, 2013.

[43] W. N. Hardy, D. A. Bonn, D. C. Morgan, R. Liang, and K. Zhang, "Precision measurements of the temperature dependence of λ in $YBa_2Cu_3O_{6.95}$: Strong evidence for nodes in the gap function," *Phys. Rev. Lett.*, vol. 70, pp. 3999–4002, Jun 1993.

[44] H. Ding, M. R. Norman, J. C. Campuzano, M. Randeria, A. F. Bellman, T. Yokoya, T. Takahashi, T. Mochiku, and K. Kadowaki, "Angle-resolved photoemission spectroscopy study of the superconducting gap anisotropy in $Bi_2Sr_2CaCu_2O_{8+x}$," *Phys. Rev. B*, vol. 54, pp. R9678–R9681, Oct 1996.

[45] A. Damascelli, Z. Hussain, and Z.-X. Shen, "Angle-resolved photoemission studies of the cuprate superconductors," *Rev. Mod. Phys.*, vol. 75, pp. 473–541, Apr 2003.

[46] A. Damascelli, D. H. Lu, K. M. Shen, N. P. Armitage, F. Ronning, D. L. Feng, C. Kim, Z.-X. Shen, T. Kimura, Y. Tokura, Z. Q. Mao, and Y. Maeno, "Fermi surface, surface states, and surface reconstruction in Sr_2RuO_4," *Phys. Rev. Lett.*, vol. 85, pp. 5194–5197, Dec 2000.

[47] K. Ishida, H. Mukuda, Y. Kitaoka, K. Asayama, Z. Q. Mao, Y. Mori, and Y. Maeno, "Spin-triplet superconductivity in Sr_2RuO_4 identified by $^{17}0$ Knight shift," *Nature*, vol. 396, pp. 658–660, Dec 1998.

[48] T. M. Rice and M. Sigrist, "Sr_2RuO_4 : an electronic analogue of ^{3}He?," *Journal of Physics: Condensed Matter*, vol. 7, no. 47, p. L643, 1995.

[49] K. D. Nelson, Z. Q. Mao, Y. Maeno, and Y. Liu, "Odd-parity superconductivity in Sr_2RuO_4," *Science*, vol. 306, no. 5699, pp. 1151–1154, 2004.

[50] V. B. Geshkenbein and A. I. Larkin, "The Josephson effect in superconductors with heavy fermions," *JETP Lett.*, vol. 43, pp. 395–399, Mar 1986.

[51] A. Millis, D. Rainer, and J. A. Sauls, "Quasiclassical theory of superconductivity near magnetically active interfaces," *Phys. Rev. B*, vol. 38, pp. 4504–4515, Sep 1988.

[52] G. M. Luke, Y. Fudamoto, K. M. Kojima, M. I. Larkin, J. Merrin, B. Nachumi, Y. J. Uemura, Y. Maeno, Z. Q. Mao, Y. Mori, H. Nakamura, and M. Sigrist, "Time-reversal symmetry-breaking superconductivity in Sr_2RuO_4," *Nature*, vol. 394, pp. 558–561, Agu 1998.

[53] J. Xia, Y. Maeno, P. T. Beyersdorf, M. M. Fejer, and A. Kapitulnik, "High resolution polar Kerr effect measurements of Sr_2RuO_4: Evidence for broken time-reversal symmetry in the superconducting state," *Phys. Rev. Lett.*, vol. 97, p. 167002, Oct 2006.

[54] H. Suderow, V. Crespo, I. Guillamon, S. Vieira, F. Servant, P. Lejay, J. P. Brison, and J. Flouquet, "A nodeless superconducting gap in $\mathrm{Sr_2RuO_4}$ from tunneling spectroscopy," *New Journal of Physics*, vol. 11, no. 9, p. 093004, 2009.

[55] I. A. Firmo, S. Lederer, C. Lupien, A. P. Mackenzie, J. C. Davis, and S. A. Kivelson, "Evidence from tunneling spectroscopy for a quasi-one-dimensional origin of superconductivity in Sr_2RuO_4," *Phys. Rev. B*, vol. 88, p. 134521, Oct 2013.

[56] I. Bonalde, B. D. Yanoff, M. B. Salamon, D. J. Van Harlingen, E. M. E. Chia, Z. Q. Mao, and Y. Maeno, "Temperature dependence of the penetration depth in Sr_2RuO_4: Evidence for nodes in the gap function," *Phys. Rev. Lett.*, vol. 85, pp. 4775–4778, Nov 2000.

[57] A. P. Mackenzie and Y. Maeno, "The superconductivity of $\mathrm{Sr_2RuO_4}$ and the physics of spin-triplet pairing," *Rev. Mod. Phys.*, vol. 75, pp. 657–712, May 2003.

[58] K. Deguchi, Z. Q. Mao, and Y. Maeno, "Determination of the superconducting gap structure in all bands of the spin-triplet superconductor $\mathrm{Sr_2RuO_4}$," *Journal of the Physical Society of Japan*, vol. 73, no. 5, pp. 1313–1321, 2004.

[59] P. G. Björnsson, Y. Maeno, M. E. Huber, and K. A. Moler, "Scanning magnetic imaging of $\mathrm{Sr_2RuO_4}$," *Phys. Rev. B*, vol. 72, p. 012504, Jul 2005.

[60] J. R. Kirtley, C. Kallin, C. W. Hicks, E.-A. Kim, Y. Liu, K. A. Moler, Y. Maeno, and K. D. Nelson, "Upper limit on spontaneous supercurrents in $\mathrm{Sr_2RuO_4}$," *Phys. Rev. B*, vol. 76, p. 014526, Jul 2007.

[61] C. W. Hicks, J. R. Kirtley, T. M. Lippman, N. C. Koshnick, M. E. Huber, Y. Maeno, W. M. Yuhasz, M. B. Maple, and K. A. Moler, "Limits on superconductivity-related magnetization in Sr_2RuO_4 and $PrOs_4Sb_{12}$ from scanning SQUID microscopy," *Phys. Rev. B*, vol. 81, p. 214501, Jun 2010.

[62] P. J. Curran, S. J. Bending, W. M. Desoky, A. S. Gibbs, S. L. Lee, and A. P. Mackenzie, "Search for spontaneous edge currents and vortex imaging in $\mathrm{Sr_2RuO_4}$ mesostructures," *Phys. Rev. B*, vol. 89, p. 144504, Apr 2014.

[63] K. Deguchi, Z. Q. Mao, H. Yaguchi, and Y. Maeno, "Gap structure of the spin-triplet superconductor $\mathrm{sr_2ruo_4}$ determined from the field-orientation dependence of the specific heat," *Phys. Rev. Lett.*, vol. 92, p. 047002, Jan 2004.

[64] Y. Krockenberger, M. Uchida, K. S. Takahashi, M. Nakamura, M. Kawasaki, and Y. Tokura, "Growth of superconducting $\mathrm{Sr_2RuO_4}$ thin films," *Applied Physics Letters*, vol. 97, no. 8, p. 082502, 2010.

[65] Y. Maeno, T. Ando, Y. Mori, E. Ohmichi, S. Ikeda, S. NishiZaki, and S. Nakatsuji, "Enhancement of superconductivity of $\mathrm{Sr_2RuO_4}$ to 3 K by embedded metallic microdomains," *Phys. Rev. Lett.*, vol. 81, pp. 3765–3768, Oct 1998.

[66] M. Sigrist and H. Monien, "Phenomenological theory of the 3 kelvin phase in $\mathrm{Sr_2RuO_4}$," *Journal of the Physical Society of Japan*, vol. 70, no. 8, pp. 2409–2418, 2001.

[67] Y. A. Ying, Y. Xin, B. W. Clouser, E. Hao, N. E. Staley, R. J. Myers, L. F. Allard, D. Fobes, T. Liu, Z. Q. Mao, and Y. Liu, "Suppression of proximity effect and the enhancement of p-wave superconductivity in the $\mathrm{Sr_2RuO_4}$-Ru system," *Phys. Rev. Lett.*, vol. 103, p. 247004, Dec 2009.

[68] Y. A. Ying, N. E. Staley, Y. Xin, K. Sun, X. Cai, D. Fobes, T. J. Liu, Z. Q. Mao, and Y. Liu, "Enhanced spin-triplet superconductivity near dislocations in $\mathrm{Sr_2RuO_4}$," *Nat. Commun.*, vol. 4, pp. 2596–2603, Nov 2013.

[69] B. Bernevig and T. Hughes, *Topological Insulators and Topological Superconductors*. Princeton University Press, 2013.

[70] M. Z. Hasan and C. L. Kane, "*Colloquium* : Topological insulators," *Rev. Mod. Phys.*, vol. 82, pp. 3045–3067, Nov 2010.

[71] M. Stone and R. Roy, "Edge modes, edge currents, and gauge invariance in p_x+ip_y superfluids and superconductors," *Phys. Rev. B*, vol. 69, p. 184511, May 2004.

[72] J. A. Sauls, "Surface states, edge currents, and the angular momentum of chiral p-wave superfluids," *Phys. Rev. B*, vol. 84, p. 214509, Dec 2011.

[73] X.-L. Qi, T. L. Hughes, S. Raghu, and S.-C. Zhang, "Time-reversal-invariant topological superconductors and superfluids in two and three dimensions," *Phys. Rev. Lett.*, vol. 102, p. 187001, May 2009.

[74] G. C. Ménard, S. Guissart, C. Brun, M. Trif, F. Debontridder, R. T. Leriche, D. Demaille, D. Roditchev, P. Simon, and T. Cren, "Two-dimensional topological superconductivity in Pb/Co/Si(111)," *ArXiv e-prints*, July 2016.

[75] H.-J. Chen and K.-D. Zhu, "Surface plasmon enhanced sensitive detection for possible signature of majorana fermions via a hybrid semiconductor quantum dot-metal nanoparticle system," *Sci. Rep.*, vol. 5, pp. 13518–13529, Aug 2015.

[76] M. Matsumoto and M. Sigrist, "Quasiparticle states near the surface and the domain wall in a $p_x \pm ip_y$ -wave superconductor," *Journal of the Physical Society of Japan*, vol. 68, no. 3, pp. 994–1007, 1999.

[77] A. Furusaki, M. Matsumoto, and M. Sigrist, "Spontaneous Hall effect in a chiral *p*-wave superconductor," *Phys. Rev. B*, vol. 64, p. 054514, Jul 2001.

[78] S. Kashiwaya, H. Kashiwaya, H. Kambara, T. Furuta, H. Yaguchi, Y. Tanaka, and Y. Maeno, "Edge states of $\mathrm{Sr_2RuO_4}$ detected by in-plane tunneling spectroscopy," *Phys. Rev. Lett.*, vol. 107, p. 077003, Aug 2011.

[79] S. Raghu, A. Kapitulnik, and S. A. Kivelson, "Hidden quasi-one-dimensional superconductivity in $\mathrm{Sr_2RuO_4}$," *Phys. Rev. Lett.*, vol. 105, p. 136401, Sep 2010.

[80] T. Scaffidi, J. C. Romers, and S. H. Simon, "Pairing symmetry and dominant band in $\mathrm{Sr_2RuO_4}$," *Phys. Rev. B*, vol. 89, p. 220510, Jun 2014.

[81] T. Scaffidi and S. H. Simon, "Large Chern number and edge currents in $\mathrm{Sr_2RuO_4}$," *Phys. Rev. Lett.*, vol. 115, p. 087003, Aug 2015.

[82] S. Lederer, W. Huang, E. Taylor, S. Raghu, and C. Kallin, "Suppression of spontaneous currents in Sr_2RuO_4 by surface disorder," *Phys. Rev. B*, vol. 90, p. 134521, Oct 2014.

[83] W. Huang, E. Taylor, and C. Kallin, "Vanishing edge currents in non-p-wave topological chiral superconductors," *Phys. Rev. B*, vol. 90, p. 224519, Dec 2014.

[84] W. Huang, S. Lederer, E. Taylor, and C. Kallin, "Nontopological nature of the edge current in a chiral p-wave superconductor," *Phys. Rev. B*, vol. 91, p. 094507, Mar 2015.

[85] L. Fu and C. L. Kane, "Superconducting proximity effect and Majorana fermions at the surface of a topological insulator," *Phys. Rev. Lett.*, vol. 100, p. 096407, Mar 2008.

[86] R. M. Lutchyn, J. D. Sau, and S. Das Sarma, "Majorana fermions and a topological phase transition in semiconductor-superconductor heterostructures," *Phys. Rev. Lett.*, vol. 105, p. 077001, Aug 2010.

[87] Y. Oreg, G. Refael, and F. von Oppen, "Helical liquids and majorana bound states in quantum wires," *Phys. Rev. Lett.*, vol. 105, p. 177002, Oct 2010.

[88] V. Mourik, K. Zuo, S. M. Frolov, S. R. Plissard, E. P. A. M. Bakkers, and L. P. Kouwenhoven, "Signatures of Majorana fermions in hybrid superconductor-semiconductor nanowire devices," *Science*, vol. 336, no. 6084, pp. 1003–1007, 2012.

[89] W. Frank, "Majorana returns," *Nat. Phys.*, vol. 5, p. 614, Sep 2009.

[90] A. Y. Kitaev, "Unpaired Majorana fermions in quantum wires," *Physics-Uspekhi*, vol. 44, no. 10S, p. 131, 2001.

[91] D. A. Ivanov, "Non-abelian statistics of half-quantum vortices in p-wave superconductors," *Phys. Rev. Lett.*, vol. 86, pp. 268–271, Jan 2001.

[92] S. Das Sarma, C. Nayak, and S. Tewari, "Proposal to stabilize and detect half-quantum vortices in strontium ruthenate thin films: Non-abelian braiding statistics of vortices in a $p_x + ip_y$ superconductor," *Phys. Rev. B*, vol. 73, p. 220502, Jun 2006.

[93] S. D. Sarma, M. Freedman, and C. Nayak, "Majorana zero modes and topological quantum computation," *Npj Quantum Information*, vol. 1, p. 15001, Oct 2015.

[94] M. Sigrist and K. Ueda, "Phenomenological theory of unconventional superconductivity," *Rev. Mod. Phys.*, vol. 63, pp. 239–311, Apr 1991.

[95] D. Vollhardt and P. Woelfle, *The Superfluid Phases Of Helium 3*. Taylor & Francis, 1990.

[96] Y. Maeno, S. Kittaka, T. Nomura, S. Yonezawa, and K. Ishida, "Evaluation of spin-triplet superconductivity in $\mathrm{Sr_2RuO_4}$," *Journal of the Physical Society of Japan*, vol. 81, no. 1, p. 011009, 2012.

[97] J. J. Wiman and J. A. Sauls, "Superfluid phases of $^3\mathrm{He}$ in nanoscale channels," *Phys. Rev. B*, vol. 92, p. 144515, Oct 2015.

[98] L. V. Levitin, R. G. Bennett, A. Casey, B. Cowan, J. Saunders, D. Drung, T. Schurig, and J. M. Parpia, "Phase diagram of the topological superfluid $^3\mathrm{He}$ confined in a nanoscale slab geometry," *Science*, vol. 340, no. 6134, pp. 841–844, 2013.

[99] M. Sigrist, D. Agterberg, A. Furusaki, C. Honerkamp, K. Ng, T. Rice, and M. Zhitomirsky, "Phenomenology of the superconducting state in $\mathrm{Sr_2RuO_4}$," *Physica C: Superconductivity*, vol. 317318, pp. 134 – 141, 1999.

[100] H. Murakawa, K. Ishida, K. Kitagawa, Z. Q. Mao, and Y. Maeno, "Measurement of the $^{101}\mathrm{Ru}$-knight shift of superconducting $\mathrm{Sr_2RuO_4}$ in a parallel magnetic field," *Phys. Rev. Lett.*, vol. 93, p. 167004, Oct 2004.

[101] Y. Maeno, T. M. Rice, and M. Sigrist, "The intriguing superconductivity of strontium ruthenate," *Physics Today*, vol. 54, p. 42, Jan 2001.

[102] J.-X. Zhu, C. S. Ting, J. L. Shen, and Z. D. Wang, "Ginzburg-Landau equations for layered p-wave superconductors," *Phys. Rev. B*, vol. 56, pp. 14093–14101, Dec 1997.

[103] D. F. Agterberg, "Vortex lattice structures of $\mathrm{sr_2ruo_4}$," *Phys. Rev. Lett.*, vol. 80, pp. 5184–5187, Jun 1998.

[104] P. I. Soininen, C. Kallin, and A. J. Berlinsky, "Structure of a vortex line in a $d_{x^2-y^2}$ superconductor," *Phys. Rev. B*, vol. 50, pp. 13883–13886, Nov 1994.

[105] Y. Wang and A. H. MacDonald, "Mixed-state quasiparticle spectrum for d-wave superconductors," *Phys. Rev. B*, vol. 52, pp. R3876–R3879, Aug 1995.

[106] A. J. Berlinsky, A. L. Fetter, M. Franz, C. Kallin, and P. I. Soininen, "Ginzburg-Landau theory of vortices in d-wave superconductors," *Phys. Rev. Lett.*, vol. 75, pp. 2200–2203, Sep 1995.

[107] M. Franz, C. Kallin, P. I. Soininen, A. J. Berlinsky, and A. L. Fetter, "Vortex state in a d-wave superconductor," *Phys. Rev. B*, vol. 53, pp. 5795–5814, Mar 1996.

[108] R. Heeb, A. van Otterlo, M. Sigrist, and G. Blatter, "Vortices in d-wave superconductors," *Phys. Rev. B*, vol. 54, pp. 9385–9398, Oct 1996.

[109] Y. Ren, J.-H. Xu, and C. S. Ting, “Ginzburg-landau equations and vortex structure of a $d_{x^2-y^2}$ superconductor,” *Phys. Rev. Lett.*, vol. 74, pp. 3680–3683, May 1995.

[110] S. Graser, T. A. Maier, P. J. Hirschfeld, and D. J. Scalapino, “Near-degeneracy of several pairing channels in multiorbital models for the fe pnictides,” *New Journal of Physics*, vol. 11, no. 2, p. 025016, 2009.

[111] S. Maiti, M. M. Korshunov, T. A. Maier, P. J. Hirschfeld, and A. V. Chubukov, “Evolution of symmetry and structure of the gap in iron-based superconductors with doping and interactions,” *Phys. Rev. B*, vol. 84, p. 224505, Dec 2011.

[112] W.-C. Lee, S.-C. Zhang, and C. Wu, “Pairing state with a time-reversal symmetry breaking in feas-based superconductors,” *Phys. Rev. Lett.*, vol. 102, p. 217002, May 2009.

[113] S. Maiti, M. Sigrist, and A. Chubukov, “Spontaneous currents in a superconductor with $s + is$ symmetry,” *Phys. Rev. B*, vol. 91, p. 161102, Apr 2015.

[114] F. Gygi and M. Schlüter, “Self-consistent electronic structure of a vortex line in a type-II superconductor,” *Phys. Rev. B*, vol. 43, pp. 7609–7621, Apr 1991.

[115] N. Hayashi, T. Isoshima, M. Ichioka, and K. Machida, “Low-lying quasiparticle excitations around a vortex core in quantum limit,” *Phys. Rev. Lett.*, vol. 80, pp. 2921–2924, Mar 1998.

[116] L. Gor’kov and G. Eliashberg, “Generalization of Ginzburg-Landau equations for non-stationary problems in the case of alloys with paramagnetic impurities,” *Zh. Eksp. Teor Fiz.*, vol. 54, no. 2, pp. 612–626, 1968. [Sov. Phys. JETP 27(2), 328-334 (1968)].

[117] I. Sadovskyy, A. Koshelev, C. Phillips, D. Karpeyev, and A. Glatz, “Stable large-scale solver for Ginzburg-Landau equations for superconductors,” *Journal of Computational Physics*, vol. 294, pp. 639 – 654, 2015.

[118] L. Kramer and R. J. Watts-Tobin, “Theory of dissipative current-carrying states in superconducting filaments,” *Phys. Rev. Lett.*, vol. 40, pp. 1041–1044, Apr 1978.

[119] W. D. Gropp, H. G. Kaper, G. K. Leaf, D. M. Levine, M. Palumbo, and V. M. Vinokur, “Numerical simulation of vortex dynamics in type-II superconductors,” *Journal of Computational Physics*, vol. 123, no. 2, pp. 254 – 266, 1996.

[120] M. Milošević and R. Geurts, “The Ginzburg-Landau theory in application,” *Physica C: Superconductivity*, vol. 470, no. 19, pp. 791 – 795, 2010. Vortex Matter in Nanostructured Superconductors.

[121] G. R. Berdiyorov, M. V. Milošević, and F. M. Peeters, “Kinematic vortex-antivortex lines in strongly driven superconducting stripes,” *Phys. Rev. B*, vol. 79, p. 184506, May 2009.

[122] G. R. Berdiyorov, A. K. Elmurodov, F. M. Peeters, and D. Y. Vodolazov, “Finite-size effect on the resistive state in a mesoscopic type-II superconducting stripe,” *Phys. Rev. B*, vol. 79, p. 174506, May 2009.

[123] J. Garaud and E. Babaev, “Properties of skyrmions and multi-quanta vortices in chiral p-wave superconductors,” *Scientific Reports*, vol. 5, p. 17540, Dec 2015.

[124] V. Fernández Becerra, E. Sardella, F. M. Peeters, and M. V. Milošević, “Vortical versus skyrmionic states in mesoscopic p-wave superconductors,” *Phys. Rev. B*, vol. 93, p. 014518, Jan. 2016.

[125] L.-F. Zhang, V. F. Becerra, L. Covaci, and M. V. Milošević, "Electronic properties of emergent topological defects in chiral p-wave superconductivity," *Phys. Rev. B*, vol. 94, p. 024520, Jul 2016.

[126] Y. Liu, "Phase-sensitive-measurement determination of odd-parity, spin-triplet superconductivity in $\mathrm{Sr_2RuO_4}$," *New Journal of Physics*, vol. 12, no. 7, p. 075001, 2010.

[127] M. E. Zhitomirskii, "Upper critical fields and corresponding phases in superconductors with multicomponent order parameters," *Zh. Eksp. Teor Fiz.*, vol. 97, pp. 1346–1361, 1990. [Sov. Phys. JETP 70, 760 (1990)].

[128] C. Bergemann, A. P. Mackenzie, S. R. Julian, D. Forsythe, and E. Ohmichi, "Quasi-two-dimensional fermi liquid properties of the unconventional superconductor sr2ruo4," *Advances in Physics*, vol. 52, no. 7, pp. 639–725, 2003.

[129] S. B. Chung, D. F. Agterberg, and E.-A. Kim, "Fractional vortex lattice structures in spin-triplet superconductors," *New Journal of Physics*, vol. 11, no. 8, p. 085004, 2009.

[130] J. Garaud and E. Babaev, "Skyrmionic state and stable half-quantum vortices in chiral p-wave superconductors," *Phys. Rev. B*, vol. 86, p. 060514, Aug. 2012.

[131] N. Nagaosa and Y. Tokura, "Topological properties and dynamics of magnetic skyrmions," *Nat. Nano.*, vol. 8, pp. 899–911, dec 2013.

[132] A. Kanda, B. J. Baelus, F. M. Peeters, K. Kadowaki, and Y. Ootuka, "Experimental evidence for giant vortex states in a mesoscopic superconducting disk," *Phys. Rev. Lett.*, vol. 93, p. 257002, Dec 2004.

[133] S. B. Chung, H. Bluhm, and E.-A. Kim, "Stability of half-quantum vortices in $p_x + ip_y$ superconductors," *Phys. Rev. Lett.*, vol. 99, p. 197002, Nov 2007.

[134] J. Jang, D. G. Ferguson, V. Vakaryuk, R. Budakian, S. B. Chung, P. M. Goldbart, and Y. Maeno, "Observation of Half-Height Magnetization Steps in $\mathrm{Sr_2RuO_4}$," *Science*, vol. 331, pp. 186–188, Jan. 2011.

[135] B.-L. Huang and S.-K. Yip, "Phase diagrams of a p-wave superconductor inside a mesoscopic disk-shaped sample," *Phys. Rev. B*, vol. 86, p. 064506, Aug 2012.

[136] B.-L. Huang and S.-K. Yip, "Mesoscopic p-wave superconductor near the phase transition temperature," *Phys. Rev. B*, vol. 87, p. 064507, Feb 2013.

[137] J. Garaud, J. Carlström, and E. Babaev, "Topological solitons in three-band superconductors with broken time reversal symmetry," *Phys. Rev. Lett.*, vol. 107, p. 197001, Nov 2011.

[138] J. Garaud, J. Carlström, E. Babaev, and M. Speight, "Chiral $\mathbb{C}P^2$ skyrmions in three-band superconductors," *Phys. Rev. B*, vol. 87, p. 014507, Jan 2013.

[139] P. Milde, D. Köhler, J. Seidel, L. M. Eng, A. Bauer, A. Chacon, J. Kindervater, S. Mühlbauer, C. Pfleiderer, S. Buhrandt, C. Schütte, and A. Rosch, "Unwinding of a skyrmion lattice by magnetic monopoles," *Science*, vol. 340, no. 6136, pp. 1076–1080, 2013.

[140] X. Z. Yu, Y. Onose, N. Kanazawa, J. H. Park, J. H. Han, Y. Matsui, N. Nagaosa, and Y. Tokura, "Real-space observation of a two-dimensional skyrmion crystal," *Nature*, vol. 465, pp. 901–904, June 2010.

[141] E. Babaev, L. D. Faddeev, and A. J. Niemi, “Hidden symmetry and knot solitons in a charged two-condensate Bose system,” *Phys. Rev. B*, vol. 65, p. 100512, Feb. 2002.

[142] E. Babaev, “Vortices with fractional flux in two-gap superconductors and in extended Faddeev model,” *Phys. Rev. Lett.*, vol. 89, p. 067001, July 2002.

[143] A. Knigavko and B. Rosenstein, “Magnetic skyrmion lattices in heavy fermion superconductor $\mathrm{UPt_3}$,” *Phys. Rev. Lett.*, vol. 82, pp. 1261–1264, Feb. 1999.

[144] J. Garaud, D. F. Agterberg, and E. Babaev, “Vortex coalescence and type-1.5 superconductivity in $\mathrm{sr_2ruo_4}$,” *Phys. Rev. B*, vol. 86, p. 060513, Aug 2012.

[145] V. O. Dolocan, C. Veauvy, F. Servant, P. Lejay, K. Hasselbach, Y. Liu, and D. Mailly, “Observation of vortex coalescence in the anisotropic spin-triplet superconductor $\mathrm{sr_2ruo_4}$,” *Phys. Rev. Lett.*, vol. 95, p. 097004, Aug 2005.

[146] P. J. Curran, V. V. Khotkevych, S. J. Bending, A. S. Gibbs, S. L. Lee, and A. P. Mackenzie, “Vortex imaging and vortex lattice transitions in superconducting $\mathrm{sr_2ruo_4}$ single crystals,” *Phys. Rev. B*, vol. 84, p. 104507, Sep 2011.

[147] L. F. Chibotaru and V. H. Dao, “Stable fractional flux vortices in mesoscopic superconductors,” *Phys. Rev. B*, vol. 81, p. 020502, Jan 2010.

[148] R. Geurts, M. V. Milošević, and F. M. Peeters, “Vortex matter in mesoscopic two-gap superconducting disks: Influence of josephson and magnetic coupling,” *Phys. Rev. B*, vol. 81, p. 214514, Jun 2010.

[149] S. Gillis, J. Jäykkä, and M. V. Milošević, “Vortex states in mesoscopic three-band superconductors,” *Phys. Rev. B*, vol. 89, p. 024512, Jan 2014.

[150] G. E. Volovik, *The Universe in a Helium Droplet*. Oxford: Oxford University Press, 1 edition ed., May 2009.

[151] Y. Maeno, H. Hashimoto, K. Yoshida, S. Nishizaki, T. Fujita, J. G. Bednorz, and F. Lichtenberg, “Superconductivity in a layered perovskite without copper,” *Nature (London)*, vol. 372, pp. 532–534, Dec. 1994.

[152] C. Kallin, “Chiral p-wave order in $\mathrm{Sr_2RuO_4}$,” *Rep. Prog. Phys.*, vol. 75, p. 042501, Apr. 2012.

[153] N. Read and D. Green, “Paired states of fermions in two dimensions with breaking of parity and time-reversal symmetries and the fractional quantum Hall effect,” *Phys. Rev. B*, vol. 61, pp. 10267–10297, Apr. 2000.

[154] D. A. Ivanov, “Non-Abelian statistics of Half-Quantum vortices in p-wave superconductors,” *Phys. Rev. Lett.*, vol. 86, pp. 268–271, Jan. 2001.

[155] M. Matsumoto and M. Sigrist, “Chiral optical absorption by a vortex in $p_x \pm ip_y$-wave superconductor,” *J. Phys. Soc. Jpn.*, vol. 68, pp. 724–727, Mar. 1999.

[156] T. Daino, M. Ichioka, T. Mizushima, and Y. Tanaka, “Odd-frequency cooper-pair amplitude around a vortex core in a chiral p-wave superconductor in the quantum limit,” *Phys. Rev. B*, vol. 86, p. 064512, Aug. 2012.

[157] M. Matsumoto and R. Heeb, “Vortex charging effect in a chiral $p_x \pm ip_y$-wave superconductor,” *Phys. Rev. B*, vol. 65, p. 014504, Nov. 2001.

[158] T. Yokoyama, C. Iniotakis, Y. Tanaka, and M. Sigrist, “Chirality sensitive effect on surface states in chiral p-wave superconductors,” *Phys. Rev. Lett.*, vol. 100, p. 177002, Apr. 2008.

[159] J. A. Sauls and M. Eschrig, “Vortices in chiral, spin-triplet superconductors and superfluids,” *New J. Phys.*, vol. 11, p. 075008, July 2009.

[160] R. Blaauwgeers, V. B. Eltsov, M. Krusius, J. J. Ruohio, R. Schanen, and G. E. Volovik, “Double-quantum vortex in superfluid 3He-A,” *Nature (London)*, vol. 404, pp. 471–473, Mar. 2000.

[161] C. Caroli, P. G. De Gennes, and J. Matricon, “Bound Fermion states on a vortex line in a type II superconductor,” *Physics Letters*, vol. 9, pp. 307–309, May 1964.

[162] S. M. M. Virtanen and M. M. Salomaa, “Multiquantum vortices in superconductors: Electronic and scanning tunneling microscopy spectra,” *Phys. Rev. B*, vol. 60, pp. 14581–14584, Dec. 1999.

[163] K. Tanaka, I. Robel, and B. Jankó, “Electronic structure of multiquantum giant vortex states in mesoscopic superconducting disks,” *PNAS*, vol. 99, pp. 5233–5236, Apr. 2002.

[164] A. S. Mel’nikov and V. M. Vinokur, “Mesoscopic superconductor as a ballistic quantum switch,” *Nature (London)*, vol. 415, pp. 60–62, Jan. 2002.

[165] A. S. Mel’nikov, D. A. Ryzhov, and M. A. Silaev, “Local density of states around single vortices and vortex pairs: Effect of boundaries and hybridization of vortex core states,” *Phys. Rev. B*, vol. 79, p. 134521, Apr. 2009.

[166] N. B. Kopnin, A. S. Mel’nikov, V. I. Pozdnyakova, D. A. Ryzhov, I. A. Shereshevskii, and V. M. Vinokur, “Enhanced vortex heat conductance in mesoscopic superconductors,” *Phys. Rev. B*, vol. 75, p. 024514, Jan. 2007.

[167] H. Suderow, I. Guillamón, J. G. Rodrigo, and S. Vieira, “Imaging superconducting vortex cores and lattices with a scanning tunneling microscope,” *Supercond. Sci. Technol.*, vol. 27, p. 063001, June 2014.

[168] L. Serrier-Garcia, J. C. Cuevas, T. Cren, C. Brun, V. Cherkez, F. Debontridder, D. Fokin, F. S. Bergeret, and D. Roditchev, “Scanning Tunneling Spectroscopy Study of the Proximity Effect in a Disordered Two-Dimensional Metal,” *Phys. Rev. Lett.*, vol. 110, p. 157003, Apr. 2013.

[169] D. Roditchev, C. Brun, L. Serrier-Garcia, J. C. Cuevas, V. H. L. Bessa, M. V. Milošević, F. Debontridder, V. Stolyarov, and T. Cren, “Direct observation of josephson vortex cores,” *Nat. Phys.*, vol. 11, pp. 332–337, Apr. 2015.

[170] S. Yoshizawa, H. Kim, T. Kawakami, Y. Nagai, T. Nakayama, X. Hu, Y. Hasegawa, and T. Uchihashi, “Imaging josephson vortices on the surface superconductor $\mathrm{Si}(111)$-$(\sqrt{7}\times\sqrt{3})$-In using a scanning tunneling microscope,” *Phys. Rev. Lett.*, vol. 113, p. 247004, Dec 2014.

[171] A. Bouhon and M. Sigrist, “Current inversion at the edges of a chiral p-wave superconductor,” *Phys. Rev. B*, vol. 90, p. 220511, Dec 2014.

[172] S. Tewari, S. Das Sarma, and D.-H. Lee, “Index theorem for the zero modes of Majorana fermion vortices in chiral p-wave superconductors,” *Phys. Rev. Lett.*, vol. 99, p. 037001, July 2007.

[173] V. Gurarie and L. Radzihovsky, “Zero modes of two-dimensional chiral p-wave superconductors,” *Phys. Rev. B*, vol. 75, p. 212509, June 2007.

[174] T. Mizushima and K. Machida, “Vortex structures and zero-energy states in the BCS-to-BEC evolution of p-wave resonant Fermi gases,” *Phys. Rev. A*, vol. 81, p. 053605, May 2010.

[175] M. Takigawa, M. Ichioka, K. Machida, and M. Sigrist, “Vortex structure in chiral p-wave superconductors,” *Phys. Rev. B*, vol. 65, p. 014508, Nov. 2001.

[176] T. Mizushima and K. Machida, “Splitting and oscillation of Majorana zero modes in the p-wave BCS-BEC evolution with plural vortices,” *Phys. Rev. A*, vol. 82, p. 023624, Aug. 2010.

[177] S.-H. Lin, M. V. Milošević, L. Covaci, B. Jankó, and F. M. Peeters, “Quantum rotor in nanostructured superconductors,” *Scientific Reports*, vol. 4, Apr. 2014.

[178] L.-F. Zhang, L. Covaci, and F. M. Peeters, “Tomasch effect in nanoscale superconductors,” *Phys. Rev. B*, vol. 91, p. 024508, Jan. 2015.

[179] J. E. Villegas, C.-P. Li, and I. K. Schuller, “Bistability in a superconducting Al thin film induced by arrays of Fe-nanodot magnetic vortices,” *Phys. Rev. Lett.*, vol. 99, p. 227001, Nov. 2007.

[180] C. Visani, P. J. Metaxas, A. Collaudin, B. Calvet, R. Bernard, J. Briatico, C. Deranlot, K. Bouzehouane, and J. E. Villegas, “Hysteretic magnetic pinning and reversible resistance switching in high-temperature superconductor/ferromagnet multilayers,” *Phys. Rev. B*, vol. 84, p. 054539, Aug. 2011.

[181] A. Andronov, I. Gordion, V. Kurin, I. Nefedov, and I. Shereshevsky, “Kinematic vortices and phase slip lines in the dynamics of the resistive state of narrow superconductive thin film channels,” *Physica C: Superconductivity*, vol. 213, no. 1, pp. 193 – 199, 1993.

[182] A. G. Sivakov, A. M. Glukhov, A. N. Omelyanchouk, Y. Koval, P. Müller, and A. V. Ustinov, “Josephson behavior of phase-slip lines in wide superconducting strips,” *Phys. Rev. Lett.*, vol. 91, p. 267001, Dec 2003.

[183] K. Kasamatsu, M. Tsubota, and M. Ueda, “Vortex molecules in coherently coupled two-component bose-einstein condensates,” *Phys. Rev. Lett.*, vol. 93, p. 250406, Dec 2004.

[184] L. S. Leslie, A. Hansen, K. C. Wright, B. M. Deutsch, and N. P. Bigelow, “Creation and detection of skyrmions in a bose-einstein condensate,” *Phys. Rev. Lett.*, vol. 103, p. 250401, Dec 2009.

[185] Y.-X. Hu, C. Miniatura, and B. Grémaud, “Half-skyrmion and vortex-antivortex pairs in spinor condensates,” *Phys. Rev. A*, vol. 92, p. 033615, Sep 2015.

[186] N. Romming, C. Hanneken, M. Menzel, J. E. Bickel, B. Wolter, K. von Bergmann, A. Kubetzka, and R. Wiesendanger, “Writing and deleting single magnetic skyrmions,” *Science*, vol. 341, no. 6146, pp. 636–639, 2013.

[187] G. R. Berdiyorov, M. V. Milošević, M. L. Latimer, Z. L. Xiao, W. K. Kwok, and F. M. Peeters, “Large magnetoresistance oscillations in mesoscopic superconductors due to current-excited moving vortices,” *Phys. Rev. Lett.*, vol. 109, p. 057004, Jul 2012.

[188] V. Vakaryuk and A. J. Leggett, “Spin polarization of half-quantum vortex in systems with equal spin pairing,” *Phys. Rev. Lett.*, vol. 103, p. 057003, Jul 2009.

[189] K. Roberts, R. Budakian, and M. Stone, “Numerical study of the stability regions for half-quantum vortices in superconducting $\mathrm{Sr_2RuO_4}$,” *Phys. Rev. B*, vol. 88, p. 094503, Sep 2013.

Curriculum Vitae

Name: **Victor Leonardo Fernandez Becerra**
Date of birth: **February 14, 1986**
Gender: **Male**
Nationality: **Colombian**
E-mail address 1: **victorleonardo.fernandezbecerra@uantwerpen.be**
E-mail address 2: **vickthor31@gmail.com**

Education

- **University of Antwerp**, Antwerp, Belgium — 2012 - present
  Ph.D. student in Condensed Matter Theory Group
  Area of study: Unconventional superconductivity, topological phases

- **Universidade Federal Fluminense**, Niteroi, Brazil — 2009 - 2011
  Master in Physics
  Area of study: Strongly correlated electron systems, Kondo effect

- **Universidad del Valle**, Cali, Colombia — 2002 - 2008
  Bachelor in Physics Magna cum Laude, Graduated with Honors
  Theoretical physics (emphasis on solid state)

List of publications

- V. Fernández Becerra, M. V. Milošević. Dynamics of skyrmions and edge states in the resistive regime of mesoscopic p-wave superconductors. *Physica C*, 533, 91, February 2017.

- V. Fernández Becerra, M. V. Milošević. Multichiral ground states in mesoscopic p-wave superconductors. *Phys. Rev. B*, 94, 184517, November 2016.

- L.-F. Zhang, V. Fernández Becerra, L. Covaci, M. V. Milošević. Electronic properties of emergent topological defects in chiral p-wave superconductivity. *Phys. Rev. B*, 94, 024520, July 2016.

- V. Fernández Becerra, E. Sardella, F.M., Peeters, M. V. Milošević. Vortical versus skyrmionic states in mesoscopic p-wave superconductors. *Phys. Rev. B*, 93, 014518, January 2016.

- W. C. Gonçalves, E. Sardella, V. F. Becerra, M. V. Milošević, F. M. Peeters. Numerical solution of the time dependent Ginzburg-Landau equations for mixed (d+s)-wave superconductors. *J. Math. Phys.*, 55, 041501, April 2014.

Conferences and other activities

- V. Fernández Becerra, E. Sardella, F. M. Peeters, M. V. Milošević. Vortical versus skyrmionic states in mesoscopic chiral p-wave superconductors. In: *Ninth International Conference on Vortex Matter in Nanostructured Superconductors*, Rhodes, Greece, September 12–17, 2015. Poster.

- V. Fernández Becerra, F. M. Peeters, M. V. Milošević. Vortical versus skyrmionic states in mesoscopic p-wave superconductors. In: *International Conference on Multi-Condensate Superconductivity and Superfluidity in Solids and Ultracold Gases*, Camerino, Italy, June 24–27, 2014. Poster.

- V. Fernández Becerra, M. V. Milošević F. M. Peeters. Stable half quantum vortices in mesoscopic p-wave superconductors. In: *General Scientific Meeting of the Belgian Physical Society*, Leuven, Belgium, May 28th, 2014. Poster.

- V. Fernández Becerra, E. Sardella, F. M. Peeters, M. V. Milošević. Vortex dynamics for p-wave mesoscopic superconductors. In: *Workshop Novel Materials: Adding Material-specific Reality in Physicists' Models*, Natal, Brazil, December 3–12, 2012. Poster.

- *Autumn College on Non-Equilibrium Quantum System.* International Center for Theoretical Physics (ICTP), Buenos Aires, Argentina, May 2–13, 2011.

- *Low Dimensional Condensed Matter, XII Giambiagi School.* Universidad de Buenos Aires, Buenos Aires, Argentina, July 19–23, 2010.

- *New Phenomena in Quantum Matter. The 4th I2CAM/FAPERJ Summer School.* Centro Brasileiro de Pesquisas Físicas (CBPF), Rio de Janeiro, Brazil, June 6–12, 2010.

- *Bosonization Techniques and Luttinger Liquids.* International Center for Condensed Matter Physics (ICCMP), Brasilia, Brazil, July 13–27, 2009.

Skills and personal features

- Languages:
  Spanish (native), **English** (fluent), **Portuguese** (fluent), **French** (intermediate)

- Programming (basic knowledge):
  Fortran (MKL), Python, FreeFem++, UNIX shell scripting.

- Scientific packages/programs:
  Matlab, Matplotlib, Gnuplot, Mathematica

- Desktop Editing and Productivity Software:
  Vim, Gedit, TeX(LaTeX, BibTeX, PSTricks), Microoft Office, OpenOffice.org, LibreOffice, MayaVi, InkScape

- Operating Systems:
  Linux (Ubuntu and Mint), and other UNIX variants